2007

Design of surface acoustic wave sensors with nanomaterial sensing layers: Application to chemical and biosensing

Subramanian K.R.S Sankaranarayanan
University of South Florida

Scholar Commons Citation

Sankaranarayanan, Subramanian K.R.S, "Design of surface acoustic wave sensors with nanomaterial sensing layers: Application to chemical and biosensing" (2007). *Graduate Theses and Dissertations.*
http://scholarcommons.usf.edu/etd/2351

Design of Surface Acoustic Wave Sensors with Nanomaterial Sensing Layers:

Application to Chemical and Biosensing

by

Subramanian K.R.S. Sankaranarayanan

A dissertation submitted in partial fulfillment
of the requirements for the degree of
Doctor of Philosophy
Department of Chemical and Biomedical Engineering
University of South Florida

Co-Major Professor: Venkat R. Bhethanabotla, Ph.D.
Co-Major Professor: Babu Joseph, Ph.D.
John Wolan, Ph.D.
Elias Stefanakos, Ph.D.
Darren Branch, Ph.D.

Date of Approval:
September 4, 2007

Keywords: Surface acoustic wave, Nanoclusters, Nanowires, Molecular dynamics, Finite element, Acoustic streaming

Dedication

To my wife Reetu and my parents. Without your unconditional love and support, none of this work would have been possible.

Acknowledgements

I would like to sincerely thank my advisors Dr. Venkat R. Bhethanabotla and Dr. Babu Joseph for their constant encouragement, guidance and support throughout the course of this study. This dissertation would not be possible without the intellectual support of my advisors as well as the committee members: Drs. John Wolan, Lee Stefanakos, Don Malocha and Darren Branch. I am also grateful for the useful insights that came through discussions with classmates Ling Miao, Stefan Cular and other friends during the course of my studies at USF. I would also like to gratefully acknowledge the computational resources provided by USF Academic Computing as well as the Engineering Computing Center at USF. As one of the users of their computational facilities, an unlimited time was granted for usage and a great support was provided for any technical problems, without which, none of this work would be possible. I would also like to thank all the funding agencies for providing the necessary financial support for conducting the research presented in this dissertation (NASA Grant # 16266038-2 to 1, NSF-IGERT grant DGE0221681, USF-IDRG, and the Department of Defense contract W81XWH-05-1-0585). Finally, I am forever indebted to my parents and my wife Reetu for their understanding, endless patience and encouragement when it was most required.

Table of Contents

List of Tables

List of Figures

Design of Surface Acoustic Wave Sensors with Nanomaterial Sensing Layers: Application to Chemical and Biosensing

Subramanian K.R.S. Sankaranarayanan

ABSTRACT

Surface acoustic wave (SAW) sensors detect chemical and biological species by monitoring the shifts in frequency of surface acoustic waves generated on piezoelectric substrates. Incorporation of nanomaterials having increased surface area as sensing layer have been effective in improving the sensitivity as well as miniaturization of SAW sensors. Selectivity, sensitivity and speed of response are the three primary aspects for any type of sensor. This dissertation focuses on design and development of SAW devices with novel transducer configurations employing nanomaterial sensing layers for enhanced sensing, improved selectivity, and speed of response. The sensing mechanism in these SAW sensors is a complex phenomenon involving interactions across several different length and time scales. Surface acoustic wave propagation at the macro-scale is influenced by several kinetic phenomena occurring at the molecular scale such as adsorption, diffusion, reaction, and desorption which in turn depend on the properties of nanomaterials. This suggests the requirement of a multi-scale model to effectively understand and manipulate the interactions occurring at different length scales, thereby improving sensor design. Sensor response modeling at multiple time and length scales forms part of this research, which includes perturbation theories, and simulation techniques from finite element methods to molecular-level simulations for interpreting the response of these surface acoustic wave chemical and biosensors utilizing alloy nanostructures as sensing layers. Molecular modeling of sensing layers such as transition metal alloy nanoclusters and nanowires is carried out to gain insights into their thermodynamic, structural, mechanical and dynamic properties. Finite element technique is used to understand the acoustic wave propagation at the macroscale for sensing devices operating at MHz frequencies and with novel transducer designs. The findings of this research provide insights into the design of efficient surface acoustic wave sensors. It is expected that this work will lead to a better understanding of surface acoustic wave devices with novel transducer configurations and employing nanomaterial sensing layers.

Chapter One

Introduction

Surface acoustic wave (SAW) sensors detect chemical and biological species by monitoring the shifts in frequency of surface acoustic waves generated on piezoelectric substrates. The frequency shifts and therefore the sensor response depend on material properties of the sensing layer. Incorporation of nanomaterials as the sensing layer has been effective in improving the sensitivity as well as miniaturization of SAW sensors. These devices are conveniently small, relatively inexpensive and highly sensitive.

1.1 Motivation and objectives

Selectivity, sensitivity and speed of response are the three primary aspects for any type of sensor. This thesis focuses on design and development of SAW devices with novel transducer configurations employing nanomaterial sensing layers for enhanced sensing, improved selectivity, and speed of response. The sensing mechanism in these SAW sensors is a complex phenomenon involving interactions across several different length and time scales. Acoustic wave propagation at the macro-scale is influenced by several kinetic phenomena occurring at the molecular scale such as adsorption, diffusion, reaction, and desorption which in turn depend on the properties of nanomaterials. This suggests the requirement of a multi-scale model to effectively understand and manipulate the interactions occurring at different length scales, thereby improving sensor design. This research has manifold aims: 1) Investigate the thermodynamic, structural and mechanical properties of the bimetallic nanomaterial sensing layers, 2) Understand the surface acoustic wave generation and propagation characteristics at the macro-scale for various novel transducer configurations in devices operating in gas and liquid media and, 3) Investigate the fluid-substrate interactions to eliminate biofouling in typical biosensing applications.

Although it is well known that bimetallic nanowires and nanoclusters are better suited for sensing and catalytic applications, the sensing mechanism involved with the use of nanoalloys in acoustic sensors is quite complicated and relatively less explored. The acoustic wave propagation is strongly dependent on the material properties of nanostructure sensing layers which in turn can be altered by the wave propagation itself. Therefore, a through understanding of both the wave propagation and nanomaterial properties is required to unravel the sensing mechanism and improve the performance of acoustic sensors.

Computational modeling is an important tool that allows one to gain insights into the material behavior at the nanoscale and acoustic wave propagation at the macro-scale. Molecular dynamics simulation is a technique in which Newton's laws are applied at the atomic level to propagate the system's motion through time. The thermodynamic and transport properties were obtained as time average over the particle positions and velocities. In this thesis, this technique is utilized to derive the material properties of finite sized structures such as alloy nanostructures. At the macro-scale, the finite element method is used to study the wave generation and propagation characteristics in SAW sensors. The finite element technique involves solving the systems equation of motion typically expressed as partial differential equations. The domain to be solved is discretized into elements connected by nodes and the equations of motion are solved at the nodes. The nodes are represented by spatially varying but temporally constant shape functions. In the present work, the coupled wave equations that relate the electrical and mechanical quantities in a piezoelectric media are solved using the finite element techniques to gain insights into the wave generation and propagation. Optimization of various design parameters is achieved by evaluating the transient response of the SAW device to various applied electrical input.

1.2 Organization of thesis

This dissertation is organized in the following manner:

1) Chapter two describes the various types of acoustic sensing devices with specific emphasis on surface acoustic wave sensor. The use of nanomaterial sensing layers is also discussed.

2) Chapter three discusses the molecular dynamics simulation study of thermal characteristics of bimetallic Pd-Pt nanoclusters of different sizes and compositions. The melting mechanism and the influence of temperature on the nanocluster microstructure are discussed in detail.

3) Chapter four discusses the thermal characteristics of bimetallic Pd-Pt nanowires of different sizes and compositions. The nanoscale phase diagram of alloy nanowires and nanoclusters is explored in detail.

4) Chapter five gives insights into the influence of substrate/support interaction on the structure and morphology of the bimetallic transition metal nanoclusters. The melting and evolution of graphite supported clusters are discussed.

5) Chapter six discusses the mechanical properties of bimetallic nanowires under the influence of high and low strain rates. The mechanism of deformation and rupture as well as the differences in the mechanical properties of single component and alloy nanowires is discussed.

6) Chapter seven involves development of coupled field 3-D finite element (FE) model to understand the sensor response of a typical SAW gas sensor.

7) Chapter eight focuses on the development of fluid-solid interaction model to investigate the acoustic streaming phenomenon induced by Rayleigh wave interaction with liquid medium. Optimization of design parameters leading to enhanced acoustic streaming to eliminate biofouling in SAW biosensors is discussed.

8) Chapter nine involves development of coupled field 3-D FE model of a novel hexagonal SAW device, which finds applications in materials characterization as well as chemical and biological sensing. The use of hexagonal SAW device based on $LiNbO_3$ for rapid and simultaneous extraction of

multiple film parameters (film material density, Lamé and shear modulii, sheet conductivity) of a thin film material is demonstrated.

9) Chapter ten investigates the acoustic wave propagation and generation in focused SAW devices with transducers shaped as concentric circular arc. Optimization of design parameters leading to enhanced amplitude fields & lower propagation losses, thereby increased device sensitivity are discussed.

10) Chapter eleven summarizes the main contributions of this thesis and provides suggestion for possible future studies.

Chapter Two

Surface Acoustic Wave Sensors and Nanomaterial Sensing Layers

2.1 Acoustic wave sensors

A sensor allows the transduction of chemical and/or physical properties at an interface into usable information (Fig. 2-1). A chemical sensor generates an output signal which is a function of the chemical entity and/or concentration. The transduction methods are usually classified as electrochemical, acoustic, optical, and thermal.

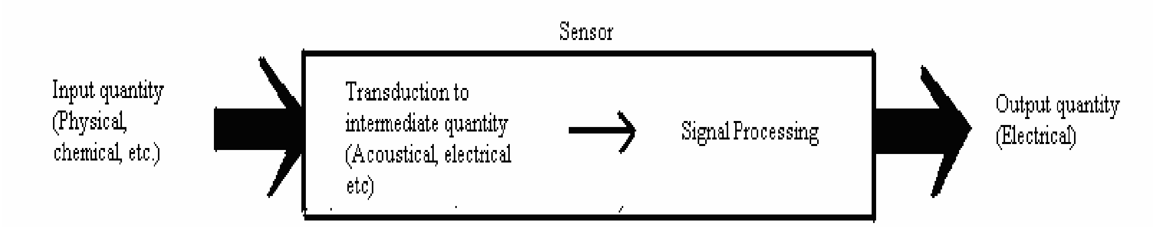

Figure 2-1. Schematic diagram of a sensor producing electrical output in response to analyte presence.

Acoustic wave sensors are devices which allow transduction between electrical and acoustical energies and are so named because they utilize a mechanical or acoustic wave as sensing mechanism[1]. As the acoustic wave propagates through or on the surface of a material, changes in the propagation path affect the amplitude and/or velocity of the wave. By monitoring the changes in wave velocity and amplitude, the frequency or phase characteristics of a sensor can be correlated to the corresponding physical quantity being measured. Virtually all acoustic wave devices and sensors use a piezoelectric material to generate the acoustic wave. Piezoelectricity refers to production of electrical charges on imposition of mechanical stress and occurs in crystals which lack center of symmetry[2]. The converse is also true which means that application of electrical field results in mechanical displacement.

Piezoelectric acoustic wave sensors apply an oscillating electric field to create a mechanical wave, which propagates through the substrate and is then converted back to an electric field for measurement. There are several piezoelectric substrates that can be used for acoustic wave generation. The most common are quartz (SiO_2), lithium niobate ($LiNbO_3$) and lithium tantalate ($LiTaO_3$). Other materials that have commercial applications include gallium arsenide (GaAs), silicon carbide (SiC), langasite (LGS), zinc oxide (ZnO), aluminum nitride (AlN), lead zirconium titanate (PZT), and polyvinylidene fluoride (PVF). Each of these materials has its own advantages and disadvantages, which include cost, temperature dependence, attenuation, and propagation velocity. The properties of these materials are influenced by the crystal cut and orientation[3,4].

The devices commonly used for sensor applications and materials characterization include thickness shear mode (TSM) resonator[5], the surface acoustic wave (SAW) device[6], the acoustic plate mode device (APM)[7] and the flexural plate wave (FPW)[8] device. In one port acoustic devices such as TSM, a single port serves as both the input and the output port whereas in two-port devices such as SAW, APM and FPW, one port is used for input and the other serves as an output port. The input signal generates an acoustic wave that propagates to a receiving transducer which regenerates a signal at the output port. The sensor response is determined based on the relative signal levels and phase delay between the input and the output ports.

Chemical sensitivity is imparted to the device by attaching a thin film to the acoustically active region[9,10]. The film serves as a chemical-to-physical transducer wherein one or more of its properties change in response to the presence of the species to be detected. Sensor response commonly relies on increased mass density of the film arising from the species accumulation. However, changes in other film parameters such as elastic and electrical properties also contribute to the response. Acoustic devices such as SAW with substantial surface normal displacement components are suitable for gas sensing applications[11]. On the other hand, acoustic devices generating shear motion in the liquid, e.g. TSM and shear horizontal SH-APM can operate with excessive damping when in contact with liquid and hence find applications in liquid sensing [12-15]. The interaction mechanism of SAW (Rayleigh) and SH-SAW devices[16] with their immediate environment (thin film, liquid or both) as well as the resulting response forms the focus of this chapter.

2.2 Surface acoustic waves: (SAW and SH-SAW)

Surface acoustic waves (SAW) are elastic waves which propagate along the surface of an elastic body, with most of the energy density confined to a depth of about one wavelength below the surface. There exist two main categories of surface waves, each with varying propagation characteristics:

2.2.1 Rayleigh wave (Gas sensing)

In 1885, Lord Rayleigh discovered the SAW mode of propagation and predicted the properties of these waves[17]. The Rayleigh waves have a longitudinal component and a vertical component that can couple with the medium placed in contact with the device's surface (Fig. 2-2). The Rayleigh mode surface acoustic wave has predominantly two particle displacement components in the sagittal plane[18-20]. The surface particles move in elliptical paths characterized by a surface normal and a surface parallel component. The surface parallel component is parallel to the wave propagation direction. The generated electromechanical field travels in the same direction. The velocity of the wave depends on the substrate material and the cut of the crystal. Typically, the energies of the SAW are confined to a zone close to the surface a few wavelengths thick. An example piezoelectric substrate is lithium niobate ($LiNbO_3$), where the dominant acoustic mode propagating on a Y-cut Z propagating $LiNbO_3$ is the Rayleigh mode. The use of Rayleigh SAW sensors is applicable only to gas media as the Rayleigh wave is severely attenuated in liquid media.

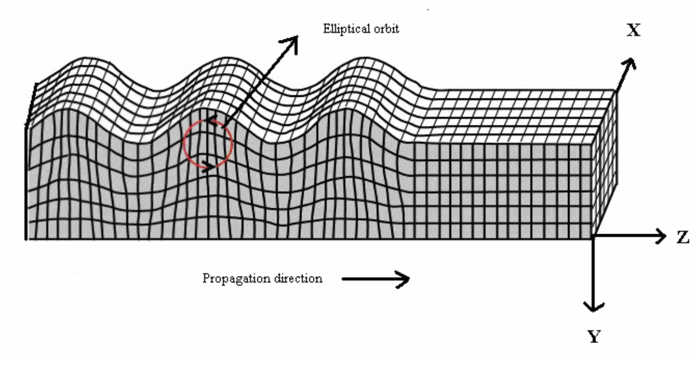

Figure 2-2. Rayleigh wave propagation in Y-Z $LiNbO_3$.

2.2.2 Shear horizontal wave (Bio-sensing)

The shear horizontal (SH) SAW devices shown in Fig. 2-3 are very similar to the SAW devices described above[21,22]. However, the selection of a different piezoelectric material and appropriate crystal cut yields shear horizontal waves instead of Rayleigh waves. An example piezoelectric substrate is lithium tantalate ($LiTaO_3$), where the dominant acoustic mode propagating on a 36^o-rotated Y-cut X propagating $LiTaO_3$ is the SH mode[23]. The particle displacements in this type of wave are transverse to the wave propagation direction and parallel to the plane of the surface. This makes SH-SAW devices suitable for operation in liquid media, where propagation at the solid-liquid media can be attained with minimal energy losses[14]. The appearances of these devices are very similar to that of Rayleigh mode devices, but a thin solid film or grating is added to prevent wave diffraction into the bulk.

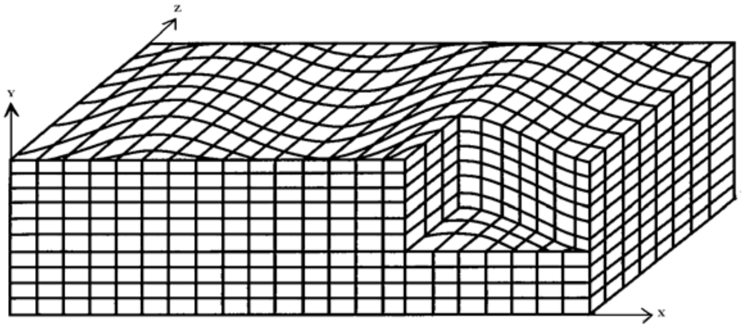

Figure 2-3. Shear Horizontal wave propagation in 36^o-rotated Y-X $LiTaO_3$. Adapted from Ref. (1).

2.3 Sensor response

Acoustic wave devices use piezoelectric materials for excitation and detection of acoustic waves. The nature of all of the parameters involved with sensor applications concerns either mechanical or electrical perturbations[24,25]. An acoustic device is sensitive mainly to the physical parameters which may interact with the mechanical properties of the wave and/or its associated electrical field. For chemical or bio-sensing applications, a transduction (sensing) layer is used to convert the value of desired parameter (for example: analyte concentration) into mechanical and electrical perturbation that can disturb the acoustic wave properties. One such surface acoustic wave sensor device is shown in Fig. 2-4.

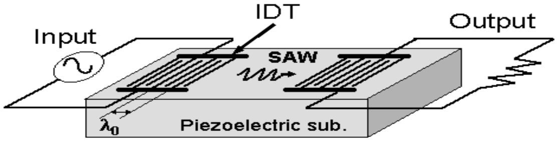

Figure 2-4. Surface acoustic wave device used in sensing applications.

The surface acoustic wave velocity is affected by several factors, each of which possesses a potential sensor response[11,26-28].

$$\frac{\Delta V}{V_0} \cong \frac{1}{V_0}\left(\frac{\partial V}{\partial mass}\Delta mass + \frac{\partial V}{\partial elec}\Delta elec + \frac{\partial V}{\partial mech}\Delta mech + \frac{\partial V}{\partial envir}\Delta envir \right) \qquad (2.1)$$

Eq. (2.1) illustrates the perturbation of acoustic velocity due to various factors. A sensor response may be due to a combination of these factors. Understanding the acoustic wave perturbation due to each of the above factors would help gain insights into the sensing mechanism as well as design efficient sensors.

2.4 Materials characterization

The recent progress in the area of materials science has resulted in newer materials being synthesized and used/developed for applications such as paints and coatings, corrosion protection, lubrication, electronics, chemical separations etc[29-31]. The properties of these materials are often complex. The ability of the material to meet the stringent specifications required for a specific application depends on its chemical and physical properties. Thus, characterizing the material properties plays a vital role in materials science.

Thin films form an important category of materials which find applications in a wide variety of industrial applications[32]. Optimization of thin film properties requires techniques which can directly characterize the same. SAW devices are ideally suited to thin film characterization due to their extreme sensitivity to thin film properties (Eq. (2.1)). The sensitivity of SAW devices to a variety of film properties such as mass density, viscoelasticity, and conductivity makes them versatile characterization tools. The ability of SAW devices to rapidly respond to changes in thin film properties allows for monitoring dynamic processes such as film deposition, chemical modification and diffusion of species in and out of the film. The thin film focus should not be viewed as a limitation of SAW devices. Bulk material properties can be derived from thin film data although such extrapolations should be performed with care[1]. In this thesis, a novel hexagonal surface acoustic wave device for nondestructive characterization of thin films is designed using 3-D coupled field finite element models.

2.5 Modeling of surface acoustic wave devices

Many models have been proposed for the analysis of SAW sensor response to the various mechanical and electrical perturbations[14,15,33-35]. The simplest of these rely on perturbation theory, or use analytical solutions based on approximations such as isotropic media with negligible piezoelectricity[36-38]. These techniques provide valuable insight into the effects of changes in parameters such as layer height, liquid viscosity or mass loading, but are limited by the assumptions made[39]. The response of SAW sensors have also been studied by Green's function methods using the quasi-static approximation[40]. This is appropriate for delay line devices where reflection, regeneration and bulk wave effects are negligible. Most existing studies assume that electrodes are located on the upper surface of the SAW, whereas in actual sensing applications they are often placed between the substrate and the guiding layer. Periodic Green's function yields a great deal of information for SAW signal processing components (e.g. Plessky and Thorvaldsson (1992) [41]). The models described above as well other simple models (Mason's model [42], equivalent circuit models[43]) either introduce simplifying assumptions or else handle only small segments of the SAW devices. For an accurate calculation of piezoelectric devices operating in the sonic and ultrasonic range, numerical methods such as finite element and/or boundary element methods are the preferred choice[34,44,45]. This thesis involves development of 3-D coupled field finite element structural models as well as 2-D fluid-solid interaction models to understand wave propagation characteristics in typical SAW gas and biosensor.

2.6 Nanomaterial sensing layers

The sensor type and sensing purpose dictate the choice of sensing material. Biosensors involve use of enzymes, antibodies or antigen, while gas sensors typically involve the use of transition metals and their oxides or polymers as sensing layers[46-49]. Chemical and biosensing applications mainly involve surface and interface interactions between the analyte molecules and the sensing materials. Therefore, nanomaterials such as nanoclusters and nanowires, with their large surface to bulk atom ratio are potentially very efficient sensing material. It is well known that bimetallic nanomaterials are better suited for sensing and catalytic applications than their single metal counterparts[50]. Therefore, in this thesis, we have focused on the use of bimetallic transition metal nanowires and nanoclusters such as those shown in Fig. 2-5.

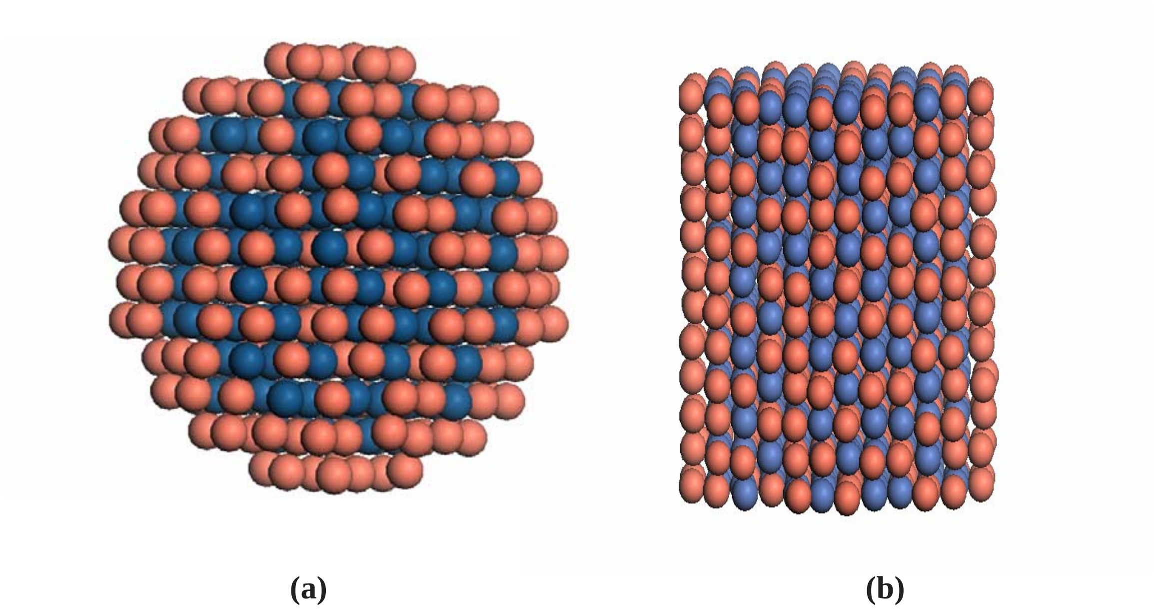
(a) **(b)**

Figure 2-5. Bimetallic nanomaterials for enhanced sensing (a) Pd-Pt nanocluster (b) Pd-Pt nanowire.

As brought out earlier, the acoustic wave propagation is strongly influenced by the material properties of the sensing layer as well as the piezoelectric substrate. While the properties of the piezoelectric substrates are fairly well established, those of nanomaterials particularly alloy nanoclusters and nanowires are relatively less explored. Owing to the finite size effect, the nanomaterial properties are expected to be very different from the bulk. In particular, the microstructure and morphological characteristics, which play a vital role in sensing applications, can be significantly different and are expected to vary with the size and composition of the alloy nanostructure. Knowledge of the influence of temperature, support interactions as well as mechanical stresses on the microstructure of the alloy nanomaterials is required before designing efficient sensors.

2.7 Modeling the properties of nanomaterial sensing layers

Molecular dynamics (MD) simulation is a technique which allows for calculation of equilibrium and transport properties of a classical many body system. The atomic positions and velocities are allowed to evolve according to Newton’s laws of motion. It takes advantage of the fact that statistical ensemble averages are equal to the time averages of the system. This is known as ergodic hypothesis. Therefore, the basic thermodynamic properties can be calculated as the time averages of atomic trajectories obtained from the MD simulations, after the system has equilibrated.

The thermal, structural and mechanical characteristics of bimetallic Pt-Pd nanoclusters and nanowires of different sizes and compositions were investigated through MD simulations using the Quantum Sutton-Chen (QSC) many-body potentials. Monte-Carlo (MC) simulations employing the bond order simulation model were used to generate minimum energy configurations, which were utilized as the starting point for molecular dynamics simulations. It is expected that the propagation of SAW as well as the presence of piezoelectric substrate would significantly alter the nanomaterial microstructure and properties. Similarly, the annealed structure obtained upon thermal processing also undergoes significant morphological changes. Insights into the influence of temperature, substrate/support interaction as well as mechanical stretching at various strain-rates on the properties of nanomaterial sensing layers are obtained by analyzing the atomic trajectories generated using MD simulations. The details are discussed in the subsequent chapters.

Chapter Three

Molecular Dynamics Simulation Study of Melting of Pd-Pt Nanoclusters

3.1 Abstract for chapter three

Bimetallic nanoclusters are of interest because of their utility in catalysis and sensors. The thermal characteristics of bimetallic Pt-Pd nanoclusters of different sizes and compositions were investigated through molecular dynamics simulations using the Quantum Sutton-Chen (QSC) many-body potentials. Monte-Carlo simulations employing the bond order simulation model were used to generate minimum energy configurations, which were utilized as the starting point for molecular dynamics simulations. The calculated initial configurations of Pt-Pd system consisted of surface segregated Pd atoms and a Pt rich core. Melting characteristics were studied by following the changes in potential energy and heat capacity as functions of temperature. Structural changes accompanying the thermal evolution were studied by the bond order parameter method (BOP). The Pt-Pd clusters exhibited a two-stage melting: surface melting of the external Pd atoms followed by homogeneous melting of the Pt core. These transitions were found to depend on the composition and size of the nanocluster. Melting temperatures of the nanoclusters were found to be much lower than those of bulk Pt and Pd. Bulk melting of Pd and Pt simulated using periodic boundary conditions compare well with experimental values, thus providing justification for the use of QSC potentials in these simulations. Deformation parameters were calculated to characterize the structural evolution resulting from diffusion of Pd and Pt atoms. The results indicate that in Pd-Pt clusters, Pd atoms prefer to remain at the surface even after melting. In addition, Pt also tends to diffuse to the surface after melting due to reduction of its surface energy with temperature. This mixing pattern is different from those reported in some of the earlier studies on melting of bimetallics.

3.2 Melting of Pd-Pt nanoclusters

Metal nanoparticles exhibit physical, chemical, and electronic properties different from those of bulk atoms and single molecules due to the large fraction of surface atoms. The large number of surface atoms, which depend on the size, shape, and composition of nanoparticles, leads to unique properties which make these nanoparticles suitable for applications in heterogeneous catalysis, sensors, as well as microelectronic devices. In catalysis and sensing applications, nanoclusters provide improved selectivity and sensitivity due to the high surface area offered. One such example is the palladium and palladium alloy nanostructure, which find use in hydrogen sensing.[51,52] Literature suggests that bimetallic nanoclusters of palladium exhibit superior activity, selectivity, stability, and resistance to poisoning when compared to their single metal counterparts.[50] Since the key to all applications of nanoclusters is their small size and structure, knowledge and control of their size and shape distribution, surface composition, and crystal structure is critical to improved designs of the same.

Considerable experimental and theoretical research has been dedicated to understanding the thermodynamics[53] and kinetics of nanoparticle growth and stabilization when subjected to thermal and other stresses.[54-57] Melting properties of the metal nanoclusters and their associated effect on shape and composition would have a bearing on the method of synthesis, processing and the performance of these nanoclusters in various areas of application. The melting points of nanoclusters decrease with decreasing cluster sizes and their values are much below the bulk melting temperatures.[58-62] This lowering effect is mainly attributed to the large percentage of weakly bound surface atoms which are less constrained in their thermal motions. However, there is very little quantitative data on the structure and energetics of bulk and surface regions governing the properties of such systems, and a comprehensive understanding of the same is needed. Computer simulations offer an effective tool to study properties of nanoclusters and complement ongoing experimental efforts.[63-65]

A molecular dynamics simulation study of melting, freezing, and coalescence of gold nanoclusters, in the size range of 135-3995 atoms, indicated that melting begins at the surface and proceeds inwards toward the core[66]. Several structural transformations are found to be precursors to cluster melting.[60] MD studies on melting of Ni nanoclusters up to 8007 atoms indicated a transition from molecular behavior below 500 atoms to a mesoscale regime above 750 atoms with well defined bulk and surface properties.[67] The final atomic arrangements in Au nanoclusters have been found to be strongly influenced by thermodynamic factors and growth kinetics[68]. Potential energy distribution of transition metal clusters showed the coexistence of a surface-melted phase with solid core for clusters larger than 200 atoms.[69] The phase change was mainly attributed to isomerization transitions, as no pre-melting peak was detected in the heat capacity curves. A non-monotonic variation of melting temperature with cluster size is found for very small sized clusters.[61] Experimental studies on tin nanoclusters having 10-30 atoms corroborate this finding[70].

While single component metal clusters have been extensively investigated, much less attention has been devoted to the study of bimetallic nanoclusters. In addition to the inter-atomic interactions, the properties of bimetallics are influenced by relative concentrations. Additional complexity in these systems results from the surface segregation phenomenon and micro-mixing at the surface. Earlier work on MD simulations of bimetallic Cu-Ni nanocluster indicated a two staged melting process in which surface melting of Cu was followed by homogeneous melting of the Ni core[71]. A Cu-Au cluster does not experience a smooth transition from a pure Cu like behavior to a pure Au cluster with a decrease in the concentration of Cu.[72] Also, the thermal behavior of Cu-Au is mainly influenced by presence of Cu atoms in the bimetallic. Cluster melting of Al coated Pb suggested dependence of the two-stage melting process on the relative orientation of crystal core to that of coating[73]. MD studies on melting and freezing of Ni-Al clusters of various compositions indicated surface segregated Al to inhibit nucleation in Al-rich and equi-atomic bimetallic clusters leading to formation of amorphous aggregates[74]. However, in all previous studies, the size and composition effects on the melting behavior of bimetallic nanoclusters have not been addressed. In the present paper, we explore the melting behavior of Pd-Pt clusters of different compositions ranging from Pd rich system to a cluster rich in Pt employing MD simulations using the Quantum Sutton Chen (QSC) potential[75].

3.3 Initial configuration set-up

3.3.1 Nanocluster size and shape

Both palladium and platinum are metals having an FCC structure. An FCC block was first constructed from an FCC unit cell by replication in the ABC direction with centre located at (0, 0, 0). Nanoclusters were constructed from this large FCC block of Pd-Pt, using various spherical cut-off radii, leading to smooth but facetted surface structures. The cluster cut off radius is defined as

$$R_c = R_g \sqrt{\frac{5}{3}} + R_i \tag{3.1}$$

where the inter atomic radius for the Pd-Pt system, R_i =1.37 A and radius of gyration R_g is given by,

$$R_g^2 = \frac{1}{N}\sum_j (R_j - R_{cm}) \tag{3.2}$$

where, $(R_j - R_{cm})$ is the distance of atom j from the cluster center of mass.

This structure was then subjected to a Monte-Carlo simulation employing a bond order simulation (BOS) model[76], to generate the minimum energy initial configuration which was subsequently used for studying the melting phenomena. The BOS model has been tested rigorously over a range of bimetallics and comparisons with experimental data reveal close agreements with the microstructure predicted by the BOS model.[76-79] Although Monte-Carlo simulations employing Sutton-Chen potential have also been used to predict the global minima of transition clusters[76], our calculations indicate that the equilibrium structures obtained using BOS model are more stable compared to those obtained using Sutton-Chen potential model.

Molecular and mesoscale regimes were reported for Ni nanoclusters with atoms less than 500 and greater than 750, respectively. Hence, we consider clusters ranging from 456 atoms to 1088 atoms to take into account a variety of size ranges in both the molecular and mesoscale region.[67]

3.3.2 Bond order simulation model

The BOS theory developed by Strohl[81,82] (1989) forms the basis for this model. The theory, also known as surface modified pair potential method, uses the fact that the site energy of any atom depends upon the co-ordination (number of neighbors) and the type of neighbor. The original model did not give the change in interaction energy with the type and number of neighbors. It was modified to incorporate the same and predict the interaction energy change with co-ordination number.[76]

The total interaction energy ΔE, for a system of N atoms is given by

$$\Delta E(\{A_i\}) = \sum_{i=1}^{N} \varepsilon^{\mathrm{A_i}}_{Z_i,M_i\ of\ B} \qquad (3.3)$$

where A_i is either A or B type atom and ε is the site energy for an A-type atom surrounded by M of B type and total of Z neighbors given by

$$\varepsilon^{A}_{Z,M\ of\ B} = \varepsilon^{A}_{Z} + M_B \Delta E^{B}_{Z,A\ \ B} + \frac{M_B(M_B - 1)}{2} \lambda^{A}_{Z,A\ \ B} \qquad (3.4)$$

Similarly, for a B type atom, the site energy ε is given by

$$\varepsilon^{B}_{Z,M\ of\ A} = \varepsilon^{B}_{Z} + M_A \Delta E^{A}_{Z,A\ \ B} + \frac{M_A(M_A - 1)}{2} \lambda^{B}_{Z,A\ \ B} \qquad (3.5)$$

M_A and M_B are the number of unlike neighbors for atom type B and A, respectively. The parameters in the system are ε^{A}_{Z} , ε^{B}_{Z} , $\Delta E^{A}_{Z,A-B}$, $\Delta E^{B}_{Z,A-B}$, $\lambda^{A}_{Z,A-B}$, and $\lambda^{B}_{Z,A-B}$. The latter four are known as mixing parameters, and are evaluated from mixing energies for the bulk system. In the above Eq. (3.4), and (3.5), ε^{A}_{Z} is the interaction energy of an A type atom surrounded by Z neighbors of A type and varies linearly with co-ordination number Z as given below

$$\varepsilon_Z^A = \begin{cases} \varepsilon_1^A + (\varepsilon_9^A - \varepsilon_1^A)\dfrac{Z-1}{8} & 1 \le Z \le 9 \\ \varepsilon_9^A + (\varepsilon_{12}^A - \varepsilon_9^A)\dfrac{Z-9}{3} & 9 \le Z \le 12 \end{cases} \tag{3.6}$$

when Z=1, $\varepsilon_1^A = -D_0/2$ (3.7)

where, D_0 is the dimer dissociation energy.

when Z=9, $\varepsilon_9^A = -E_{coh} + \sigma(111)(3^{1/2}/4)a_0^2$ (3.8)

where, σ (111) is the (111) surface energy at 0 K, a_0 is lattice constant.

For Z=12, $\varepsilon_{12}^A = -E_{coh}$ (3.9)

The site energies of monometallic systems have been evaluated using density functional theory[83] and are listed in Table 3-1. The Pd-Pt mixing parameters were taken from Zhu[78] (1997), who calculated these using the LDA approximation in the density functional theory. Eq. (3.3) through (3.9) are used simultaneously, in conjunction with Monte-Carlo simulations, to evaluate the system energies for various configurations and arrive at the minimum energy configuration.

Table 3-1. Parameters for BOS model used in MC simulations[84].

Component	ε_1 (eV)	ε_9 (eV)	ε_{12} (eV)	ΔE_{12} (eV)	λ(eV)
Pd	-0.52	-2.999	-3.89	-0.08751	0
Pt	-1.55	-4.8	-5.84	0.0751	0

3.3.3 Monte Carlo simulation technique

Monte-Carlo (MC) simulations, combined with the BOS model, were used to predict the structure of clusters containing two different kinds of atoms for various cluster compositions. The state of the system was characterized by the energy of the system as given by Eq. (3.3). The system energy change was computed by switching pairs of atoms of different types in the lattice and the standard Metropolis MC method was used to generate the minimum energy configuration at 300K.

Convergence was obtained when the minimum energy obtained during the simulation steps becomes constant ($\Delta E < 0.00001$), and the state of the system corresponding to that minimum energy was retained. Large number of simulations (100), with random initial configurations, each having (1000 times the total number of atoms) steps were performed to ensure convergence.

The BOS model predicts 75% of surface sites to be occupied by Pd atoms at 300 K. This result is comparable to the one reported for a 201 atom cuboctahedran which showed 79 % segregation of Pd.[76] This small difference may be due to greater number of edge and corner sites in cuboctahedran as compared to a sphere or the different cluster sizes (456 and 1088 atoms) under consideration or both. The preference of edges and corners by lower surface energy atoms enhances segregation in structures having greater numbers of such sites.[76,79]

3.4 Computational details for the melting study

3.4.1 Potential function

Molecular Dynamics (MD) simulations using DLPOLY were used to gain insights into the melting process at the atomistic level. All the thermodynamic and transport properties were obtained as time average over the particle positions and velocities. The embedded atom potential[85] and other long range potentials like the Sutton-Chen potential[86] based on Finnis-Sinclair type of potentials have been used in the literature successfully to predict the properties of FCC based metals such as Pd and Pt. The local electronic density is included to account for the many body terms. Based on the Sutton-Chen potential, the potential energy of the finite system is given by,

$$U_{tot} = \sum_{i} U_i = \sum_{i} \varepsilon \left[\sum_{j \neq i} \frac{1}{2} V(r_{ij}) - c\rho_i^{1/2} \right] \tag{3.10}$$

Here, V (r_{ij}) is a pair potential to account for the repulsion resulting from Pauli's exclusion principle.

$$V(r_{ij}) = \left(\frac{a}{r_{ij}} \right)^n \tag{3.11}$$

The local density accounting for cohesion associated with any atom i is given by,

$$\rho_i = \sum_{j \neq i} \phi(r_{ij}) = \sum_{j \neq i} \left(\frac{a}{r_{ij}} \right)^m \tag{3.12}$$

Sutton and Chen restricted values of m to be greater than 6 and fitted it to give close agreements with bulk modulus and the elastic constants. The Sutton-Chen potential predicts properties involving defects, surfaces and interfaces poorly. The Quantum Sutton-Chen potential[87] (hereafter referred to as QSC), includes quantum corrections and takes into account the zero point energy allowing better prediction of temperature dependent properties. The QSC potential function was found to be better suited to melting and phase transformation studies of bulk Cu-Ni, Cu-Au, and Pd-Ni alloys[75,88,89]. Both the Sutton-Chen[90] and the QSC parameters for the Pd and Pt are listed in Table 3-2. The geometric mean was used to obtain the energy parameter ε and the arithmetic mean was used for the remaining parameters, to predict the nature of interaction between Pd and Pt.

Studies on Pd-Pt system, using Sutton-Chen potential, indicated an appreciable movement of atoms even at 300K for Pd-Pt system, which is physically unlikely. However, as shown in the subsequent sections, the QSC gives better temperature behavior for the Pd-Pt bimetallic. Bulk properties of Pd, Pt as well as the bimetallic were also predicted in good agreement with experiment. Therefore we have used QSC potential function in all our nanocluster studies presented here.

3.4.2 MD simulation details

The MD simulations were carried out in an ensemble approximating the canonical with a constant number of atoms N and volume V (much larger than the cluster size) without any periodic boundary conditions. A constant temperature Berendson thermostat[91] with a relaxation time of 0.4 ps was used. The equations of motion were integrated using Verlet leapfrog algorithm[63] with time step of 0.001 ps. The spherical cluster was initially subjected to mild annealing in the 0-300 K interval. This was followed by heating to 1800 K in increments of 100 K. Near the melting point, the temperature increments were reduced to 10 K to account for the large temperature fluctuations. The simulations were carried out for 400 ps of equilibration followed by production time of 200 ps for generating time averaged properties.

Table 3-2. Potential parameters used in MD simulations for Pd-Pt clusters.

Sutton-Chen	n	m	ε (eV)	c	a(Å)
QSC (Pd)	12	6	3.2864e-3	148.205	3.8813
SC(Pd)	12	7	4.126e-3	108.526	3.2900
QSC(Pt)	11	7	9.7894e-3	71.336	3.9163
SC(Pt)	10	8	1.9768e-3	34.428	3.9200

3.5 Results and discussion

3.5.1 Melting point identification

The transition temperature from solid to liquid phase and vice versa is usually identified by studying the variation in either the thermodynamic properties such as potential energy and specific heat capacity or some structural properties such as Bond Order Parameter and Wigner values. The present study employs both these methods to identify melting points for different cluster sizes and compositions. The details are discussed in subsequent sections.

3.5.1.1 Thermodynamic properties

Fig. 3-1 (a) shows the temperature dependence of potential energy for a $(Pd_{0\ 5}\text{-}Pt_{0\ 5})_{456}$ atom cluster. The phase transition from a solid to a liquid phase and vice-versa can be identified by a simple jump in the total potential energy curve. Consistent with literature, we define the melting point as the transition temperature corresponding to the temperature of observed phase change in the heating run, and the freezing point as the temperature of observed phase change in the cooling run.

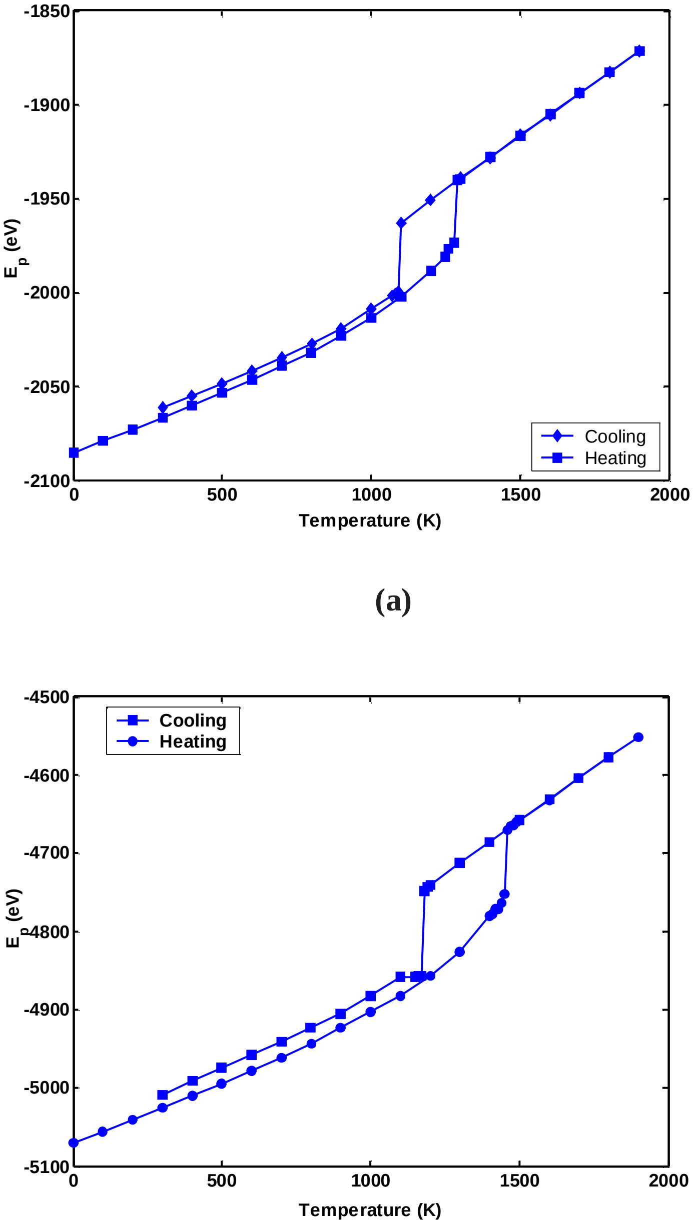

(a)

(b)

Figure 3-1. Variation of potential energy with temperature for (a) $(Pd_{0.5}\text{-}Pt_{0.5})_{456}$ (b) $(Pd_{0.5}\text{-}Pt_{0.5})_{1088}$ cluster.

This corresponds to a melting temperature of 1290 ±10K for $(Pd_{0\,5}\text{-}Pt_{0\,5})_{456}$ and 1460 ±10K for $(Pd_{0\,5}\text{-}Pt_{0\,5})_{1088}$, as seen in Fig. 3-1 (b). Upon cooling, the system undergoes a sharp liquid-solid transition and shows a rather strong hysteresis. The potential energy of the new solid phase is not very different from the initial one though structural differences prevail. The presence of hysteresis in melting/freezing transition is not unusual and is expected both theoretically[66,92] and experimentally as reported in the cases of Pb[93] and Na[56]. The structural changes resulting from cooling and melting also influence the phase transition and result in hysteresis as reported by Chausak and Bartell in their study on freezing of Ni-Al bimetallics[74]. The variation of potential energy with temperature for clusters with different compositions is discussed in subsequent sections.

The specific heat capacity in a weak coupling ensemble such as achieved with the Berendson thermostat can be written as a function of fluctuations in the potential energy $<(\delta E_p)^2>$.[94]

$$C_v = \frac{k < (\delta E_p)^2 >}{(kT)^2 - 2\alpha < (\delta E_p)^2 > / 3N} \tag{3.13}$$

Where, $< (\delta E_p)^2 > = < E_p^2 > - < E_p >^2$ and α is the ratio of the standard deviations of kinetic and potential energies.

$$\alpha = \sqrt{< (\delta KE)^2 > / < (\delta Ep)^2 >} \tag{3.14}$$

Morishita has proved that a weak coupling ensemble approaches a canonical ensemble for very short relaxation times ($\alpha \approx 0$) and to a microcanonical ensemble for longer relaxation times ($\alpha \approx 1$). In the present case, the Berendson thermostat with a coupling parameter of 0.4 ps leads to $\alpha \approx 10^{-4}$, making the calculations for specific heat capacity similar to that of a canonical ensemble as given in Eq. (3.16).

$$C_v = \frac{k \left\langle (\delta E_p)^2 \right\rangle}{(kT)^2} \tag{3.15}$$

To identify the melting/freezing temperature, the specific heat capacity at constant volume is plotted in Fig. 3-2. In case of $(Pd_{0\ 5}\text{-}Pt_{0\ 5})_{456}$ cluster, the maximum in the specific heat capacity corresponds to the temperature where a jump in potential energy is observed i.e. 1280-1290 K while heating and 1090-1100 K for cooling. This leads to a melting temperature $T_m=1290 \pm 10$ K and freezing temperature of 1090 ± 10 K. Similarly, we find that for $(Pd_{0\ 5}\text{-}Pt_{0\ 5})_{1088}$ melting and freezing temperature correspond to $Tm=1460 \pm 10$ K and 1170 ± 10 K respectively. As expected for the larger sized cluster, the peak in the case of $(Pd_{0\ 5}\text{-}Pt_{0\ 5})_{1088}$ is sharper compared to that for $(Pd_{0\ 5}\text{-}Pt_{0\ 5})_{456}$.

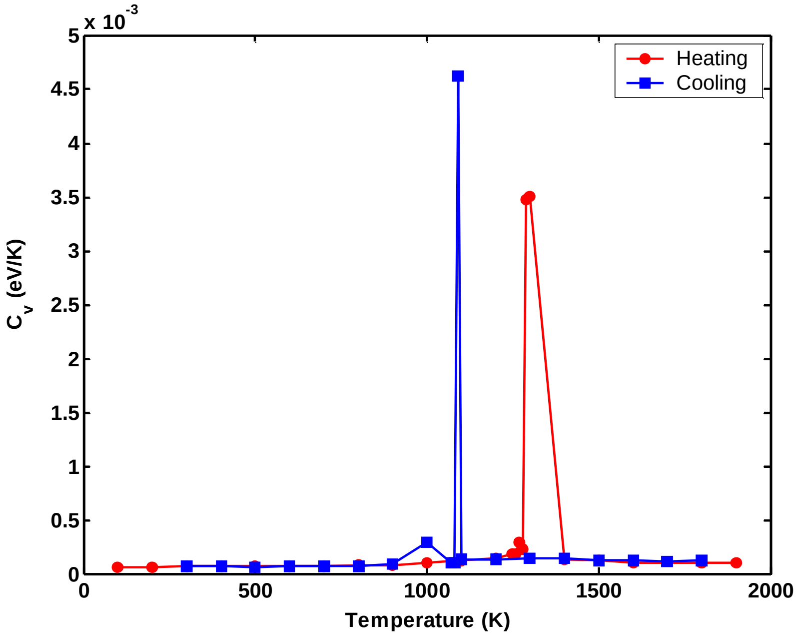

(a)

Figure 3-2. Variation of specific heat capacity at constant volume for (a) $(Pd_{0.5}\text{-}Pt_{0.5})_{456}$ and (b) $(Pd_{0.5}\text{-}Pt_{0.5})_{1088}$ cluster.

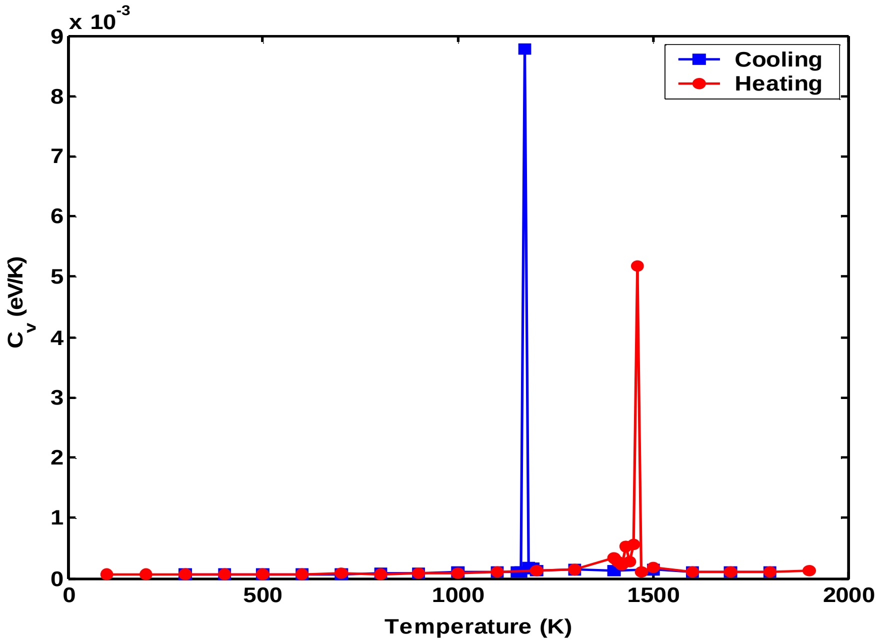

(b)

Figure 3-2: Continued

3.5.1.2 Bond orientational order parameters

There are several criteria used to identify local and extended orientational symmetries. One such method is the Bond Order Parameter method[95], which is used to analyze cluster structure as well as to distinguish between atoms in solid (closed pack) and liquid environment generated at the onset of melting. To determine the orientational order, spherical harmonic basis functions $Y_{lm}(\theta_{ij},\varphi_{ij})$ are associated with every bond joining an atom to its near neighbors. Here, Θ and Φ refer to polar and azimuthal angles of vector $\boldsymbol{r}_{ij}$ in a given reference frame. The term "bond" refers to the unit vector $\boldsymbol{r}_{ij}$ joining a reference atom i to any neighboring atom j within a cutoff radius r_{cut}. The cutoff radius is generally taken to be 1.2 times the first minimum in a in the radial distribution function. Fig. 3-3 shows one such function for a $(Pd_{0.5}\text{-}Pt_{0.5})_{456}$ cluster at 300 K, The function is calculated as an average over all atoms, surface and interior, and ensures all atoms in the first coordination shells are counted as near neighbors. To make the bonds independent of direction, only even l shaped harmonics are considered which are invariant under inversion. The local order around any atom i is an average over all its bonds with the neighboring N_{nb} atoms and given by

$$q_{lm}(i) = \frac{1}{N_{nb}(i)} \sum_{j=1}^{N_{nb}(i)} Y_{lm}(r_{ij}) \qquad (3.16)$$

A second order invariant can be constructed to give a local order parameter independent of the choice of reference system.

$$q_l(i) = \left(\frac{4\pi}{2l+1} \sum_{m=-l}^{l} | q_{lm}(i) |^2 \right)^{1/2} \qquad (3.17)$$

An average of q_{lm} over all N atoms in a cluster gives the global bond order parameter.

$$Q_l = \left(\frac{4\pi}{2l+1} \sum_{m=-l}^{l} \left| \overline{Q}_{lm} \right|^2 \right)^{1/2} \qquad (3.18)$$

where,

$$\overline{Q}_{lm} = \frac{\sum_{i=1}^{N} N_{nb} q_{lm}(i)}{\sum_{i=1}^{N} N_{nb}(i)} \qquad (3.19)$$

The value of the global bond order parameter Q_l in a solid cluster depends on the relative bond orientations and has a unique value for each crystal structure. Based on local solid symmetry, it was found that cubic and decahedral clusters have nonzero values of $q_l(i)$ for $l \geq 4$ and at $l = 6$ for those with icosahedral symmetry. All global order parameters vanish in isotropic liquids for $l > 0$. The global bond order values for different types of symmetry are reported in Table 3-3. The atoms in a solid undergo vibrations about their equilibrium positions leading to distortion of the crystal structure which is characterized by Q_4 and Q_6 values. The magnitude of the nonzero $\{Q_l\}$ values depends on the definition of nearest neighbors and can be changed by including surface bonds in the average. The cutoff distance (r_{cut}) for identifying the nearest neighbors was taken to be 3.6 A at 300 K. This corresponds to the position of the first minimum in the pair correlation function for FCC Pd-Pt. Similarly, r_{cut} at other temperatures were identified.

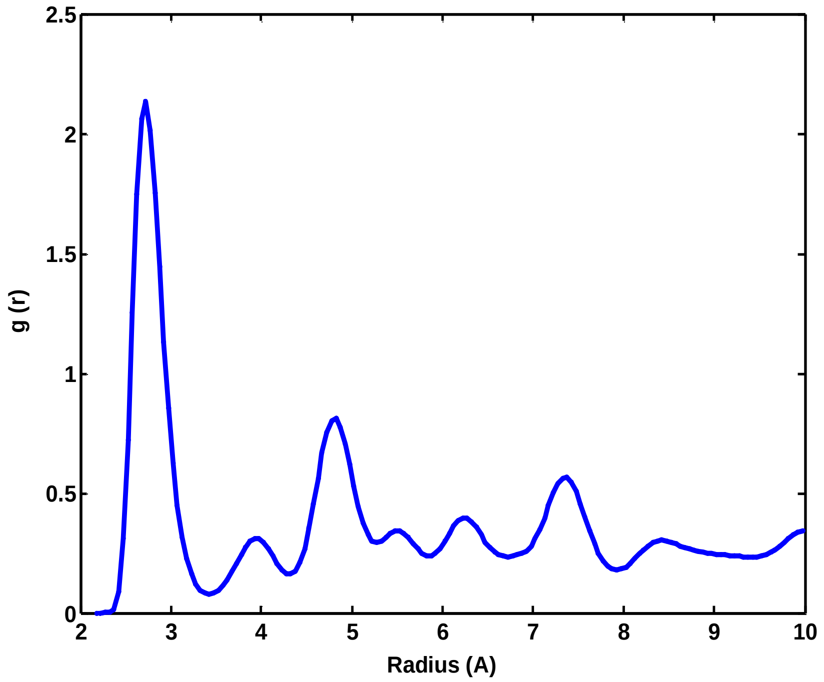

Figure 3-3. Radial distribution function for a $(Pd_{0.5}\text{-}Pt_{0.5})_{456}$ FCC cluster at 300 K.

A third order invariant which is less sensitive to the definition of the nearest neighbors can also be defined,

$$\hat{W}_l \equiv \frac{\sum\limits_{\substack{m_1,m_2,m_3\\ m_1+m_2+m_3=0}} \begin{bmatrix} l & l & l \\ m_1 & m_2 & m_3 \end{bmatrix} Q_{lm_1} Q_{lm_2} Q_{lm_3}}{\left[\sum\limits_{m} \left|Q_{lm}\right|^2\right]^{3/2}} \tag{3.20}$$

Table 3-3. Bond Order Parameter and Wigner values for various geometries.

Geometry	Q_4	Q_6	W_4	W_6
FCC	0.19094	0.57452	-0.159317	-0.013161
HCP	0.09722	0.48476	0.134097	-0.012442
Sc	0.76376	0.35355	0.159317	0.013161
Liquid	0	0	0	0

The Q_6 and W_6 values show transition from a FCC based cluster to a somewhat HCP symmetry near the melting point in the temperature range 1200-1290 K for both $(Pd_{0\ 5}\text{-}Pt_{0\ 5})_{456}$ and $(Pd_{0\ 5}\text{-}Pt_{0\ 5})_{1088}$ clusters. The melting point can be estimated from the variation in the bond order parameter values as shown in Fig. 3-4 (a). At the melting point, all the order parameters and Wigner values (Fig. 3-4 (b)) change rapidly to zero indicating a transition to isotropic liquid phase. Similar behavior is observed for the $(Pd_{0\ 5}\text{-}Pt_{0\ 5})_{1088}$ cluster. We find the melting point to be 1290 ± 10 K and 1460 ± 10 K for $(Pd_{0\ 5}\text{-}Pt_{0\ 5})_{456}$ and $(Pd_{0\ 5}\text{-}Pt_{0\ 5})_{1088}$ which is consistent with those obtained from the thermodynamic properties.

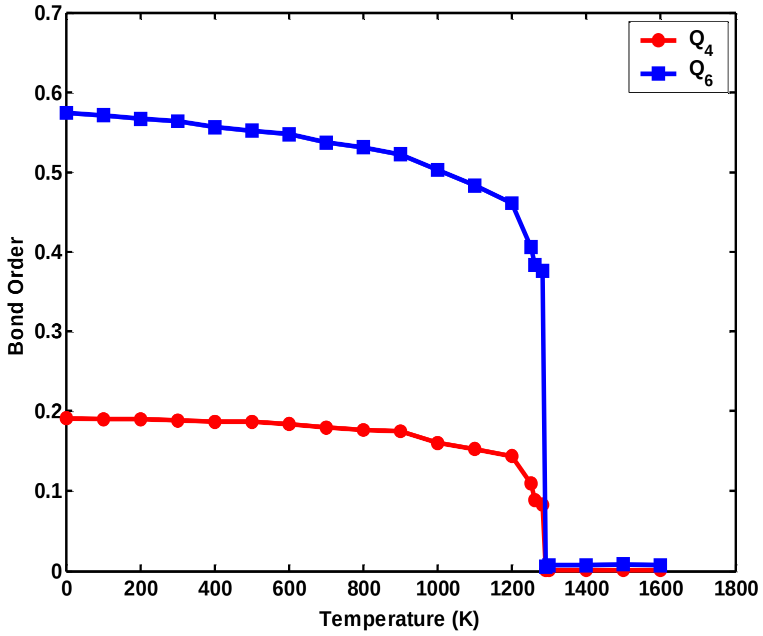

(a)

Figure 3-4. Temperature dependence of (a) global order parameter Q_4 (circles) and Q_6 (squares) and (b) global Wigner values W_4 (circles) and W_6 (squares) for $(Pd_{0\ 5}\text{-}Pt_{0\ 5})_{456}$ cluster.

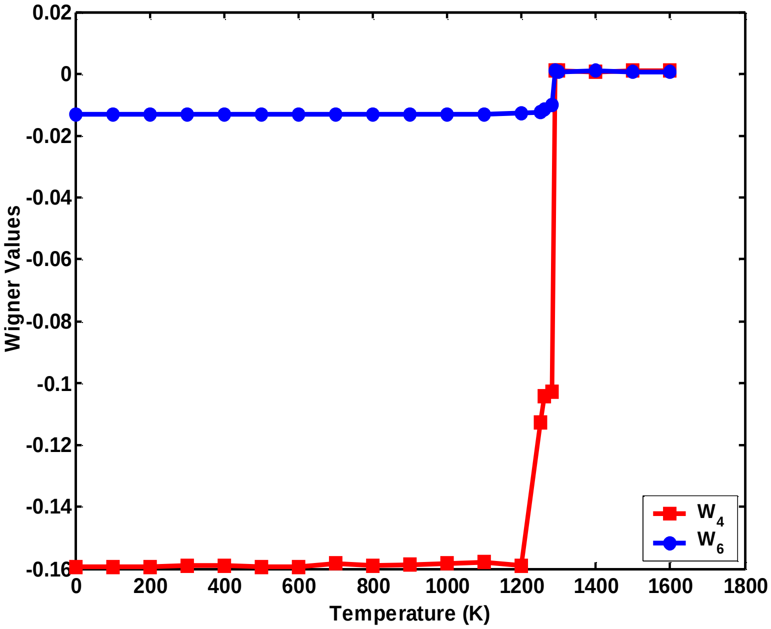

(b)

Figure 3-4: Continued

3.5.2 Understanding the melting phenomenon

3.5.2.1 Analysis of density profiles

Fig. 3-5 (a) shows the atomic distribution of Pd and Pt atoms, respectively, during the melting process for the $(Pd_{0.5}\text{-}Pt_{0.5})_{456}$ cluster along the z-axis. At lower temperatures, we find that the solid-like features are preserved as is indicated by the distinct peaks shown in Fig. 3-5 (b). As the temperature increases, the peaks merge and become broader, till the melting point when atomic distribution becomes smooth indicative of the liquid phase.

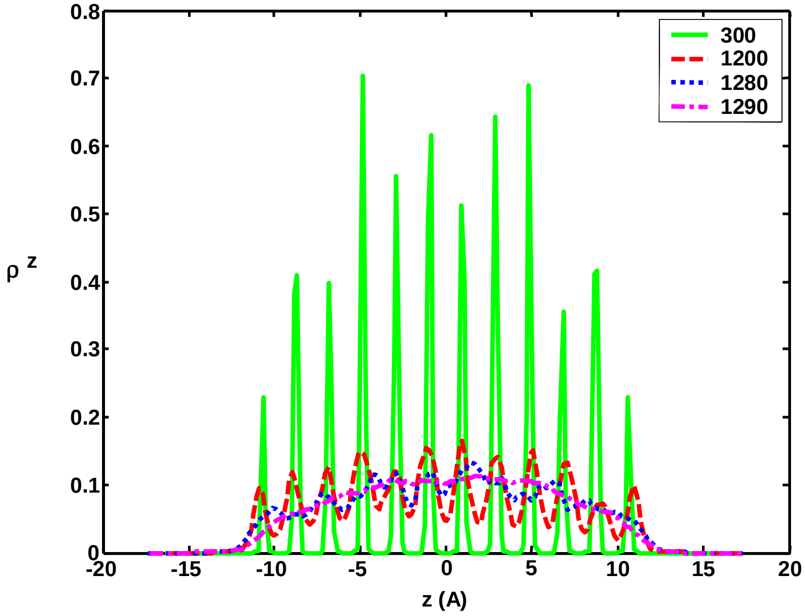

(a)

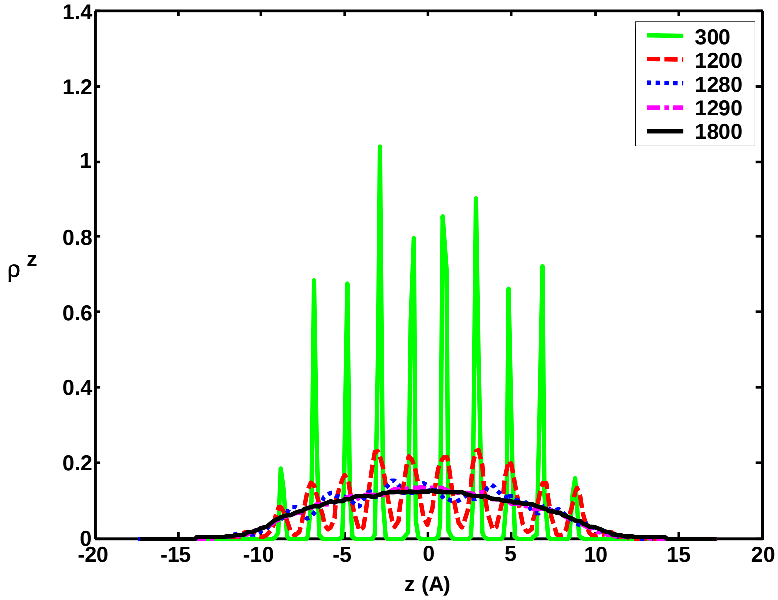

(b)

Figure 3-5. Z-density profiles for ($Pd_{0.5}$-$Pt_{0.5}$)$_{456}$ (a) Pd atomic distribution at various temperatures indicating melting transition (b) Pt atomic distribution at temperatures above and below melting transition.

To understand the melting characteristics of the bimetallics better, we analyzed the radial density profile of Pd and Pt, which are shown in Fig. 3-6. The surface segregation of Pd atoms is clearly visible from the initial density profile of Pd and Pt at 300 K (Fig. 3-6 (a)). As the temperature increases (900 K -1100 K), we find that the outer most peaks in the radial density profile of Pd merge and become broader suggesting surface melting (Fig. 3-6 (b)). However, the inner core consisting mostly of Pt is still crystalline which is evident from the well defined inner peaks in the Pt radial density profile in Fig. 3-6 (c). But above 1290 K we find liquid like behavior for Pt atoms which corresponds to the homogeneous melting temperature predicted for $(\mathrm{Pd}_{0\ 5}\text{-}\mathrm{Pt}_{0\ 5})_{456}$ (Fig. 3-6 (b) and (c)). Similar results were obtained for cluster melting at compositions other than 50% for both the cluster sizes under study.

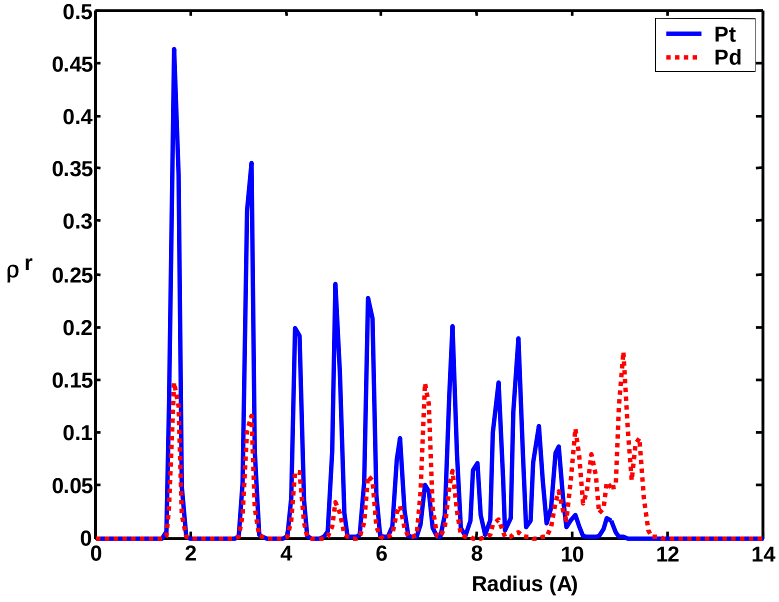

(a)

Figure 3-6. Radial density profile for $(\mathrm{Pd}_{0.5}\text{-}\mathrm{Pt}_{0.5})_{456}$ cluster. (a) Initial atomic distribution after annealing at 300 K. (b) Atomic distribution of Pd in radial direction before and after melting transition. (c) Atomic distribution of Pt in radial direction showing melting transition.

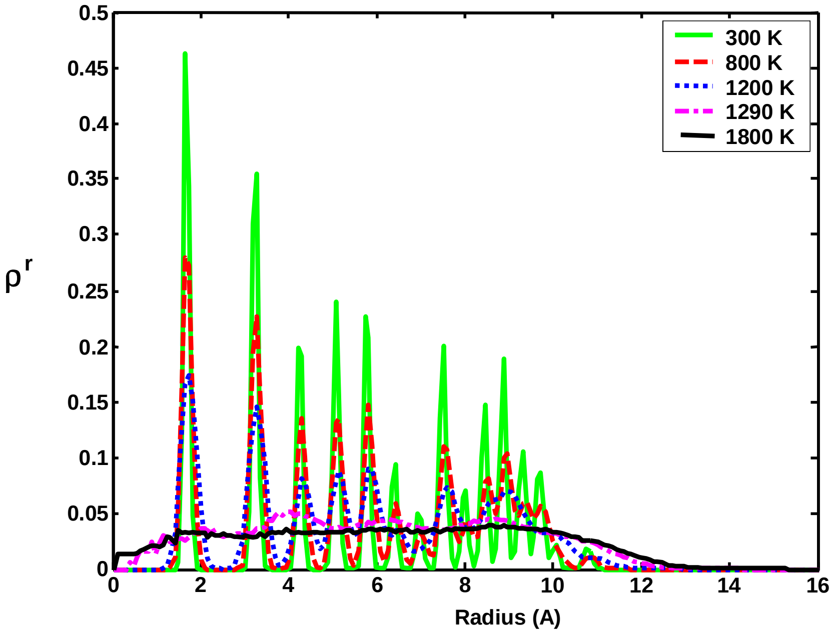

(b)

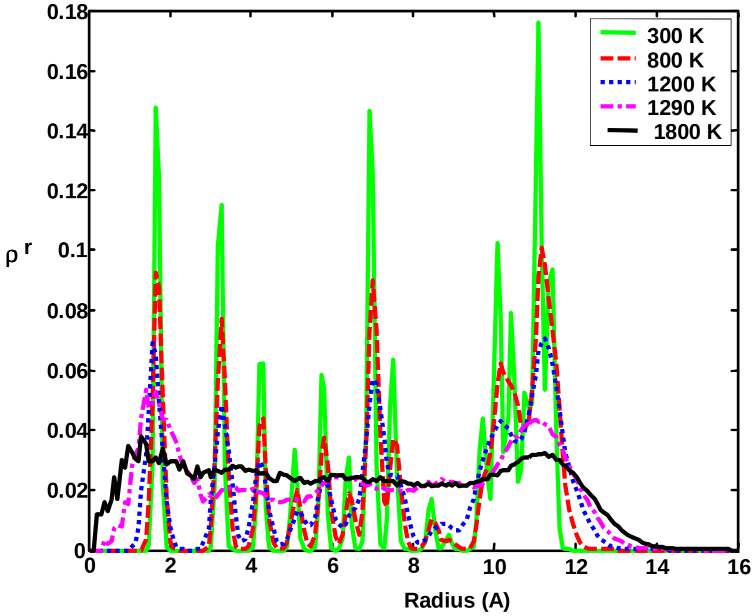

(c)

Figure 3-6: Continued

3.5.2.2 Deformation parameters

To explore the surface melting behavior and the associated shape changes, we use deformation parameters and shell based self diffusion coefficients. The melting phenomenon is associated with changes in nanocluster size and shape resulting from the diffusion of Pd and Pt atoms. The diffusion process in turn changes the number of Pd/Pt atoms on the surface and in the bulk. The bulk atoms in an FCC are identified as atoms having coordination number of 12, and the lesser coordinated atoms termed as surface atoms. However, this definition of bulk and surface atoms doesn’t hold strictly near and after the melting transition when the nanoclusters undergo shape and structural transformation. Therefore, in order to characterize these transformations, we use deformation parameters[96] given by,

$$\varepsilon_q = \frac{\sum_{i=1}^{N} | q_i - q_{cen} |}{N} \tag{3.22}$$

where, q_i refers to either the position coordinates of i^{th} atom in an N atom cluster along one of the three (x, y, z) directions, or the position vector **r**(x, y, z) and q_{cen} is the cluster center of mass. Eq. (4.9) can be used to track the structural changes accompanying melting of the cluster as a whole. However, the melting of nanoclusters proceeds in two stages, surface melting followed by the melting of the homogeneous core. In the first stage, most of the contribution to the deformation is from the surface atoms (mostly Pd), whereas in the second stage, there are contributions mostly from the bulk Pt atoms. To gain better insights into the structural changes in each of the two stages, partial deformation parameters for each of the element in the bimetallic (X=Pd, Pt) are defined as,

$$\varepsilon_q^x = \frac{\sum_{i=1}^{N_x} | q_i - q_{cen} |}{N_x} \tag{3.23}$$

The initial nanocluster shape is spherical at 300K. The atomic distribution of Pd is such that $\varepsilon_x^{Pd} \approx \varepsilon_y^{Pd} \approx \varepsilon_z^{Pd}$. The deformation parameters of Pt are lower than that of Pd indicating a preferential location of Pt at the cluster core.

Fig. 3-7 (a) depicts the evolution of the radial deformation parameters for $(Pd_{0\ 5}\text{-}Pt_{0\ 5})_{456}$. ε_r increases with temperature indicating an outward diffusion of both Pd and Pt up to 1100 K. However, near the melting point there is a sharp change in deformation parameters of both Pd and Pt. The deformation parameter for Pd (ε_r^{Pd}) shows a slight decrease, indicating diffusion into the nanoclusters core, whereas that for Pt atoms shows a rapid increase, indicating outward movement of Pt atoms. The overall deformation parameter increases rapidly because of the net outward diffusion of Pt atoms. This fact is further corroborated by Fig. 3-7 (b) and (c) which show the variation in partial deformation parameters (q=x, y, and z) for Pd and Pt.

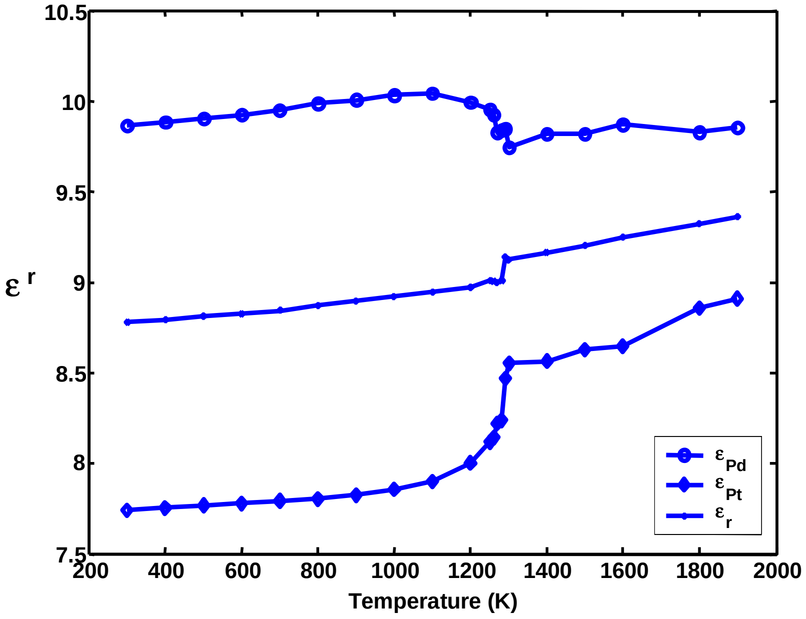

(a)

Figure 3-7. Variation of deformation parameters with temperature for $(Pd_{0.5}\text{-}Pt_{0.5})_{456.}$ (a) Radial deformation parameters ε_r, ε_r^{Pd}, ε_r^{Pt}. (b) Pd atomic partial deformation parameter in x, y, and z. (c) Pt atomic partial deformation parameter in x, y, and z.

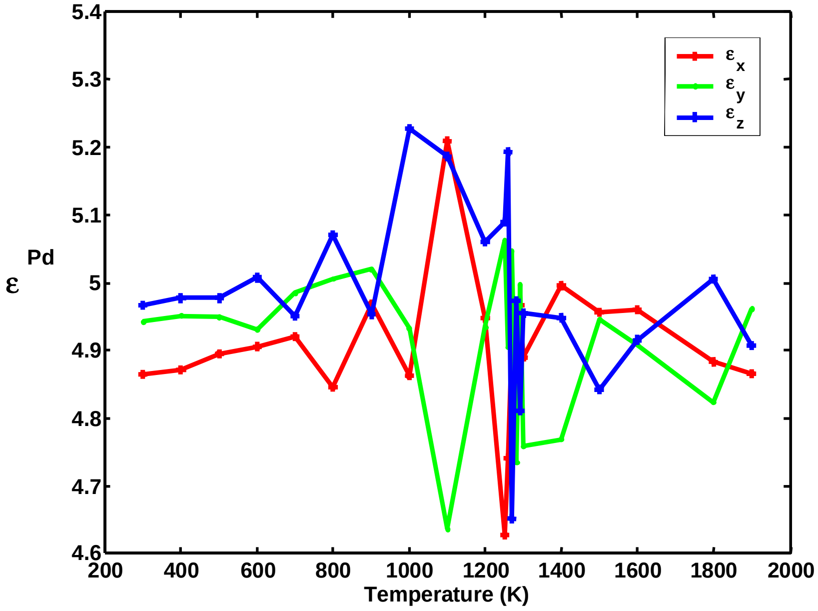

(b)

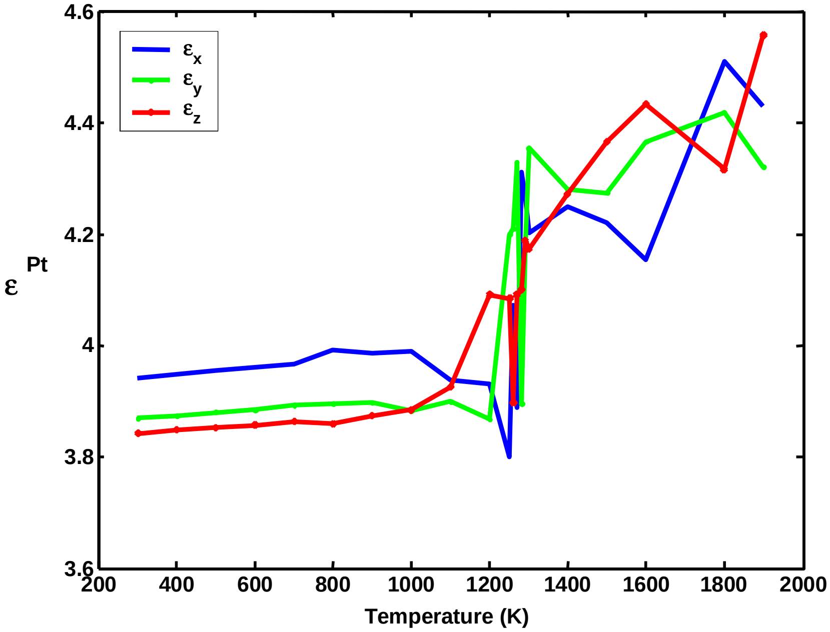

(c)

Figure 3-7: Continued

During the initial heating stage, the variation in ε_q^{Pd} is small. From 800 K to the melting temperature, there is lot of fluctuation in the deformation parameter of Pd in all the three directions. This atomic motion before the actual melting point signifies surface melting of the Pd atoms. The atomic motion starts first in z direction where a sharp increase is noticed in ε_z^{Pd} from 800 to 1000 K. At the melting point ε_z^{Pd} drops abruptly and becomes equal to ε_x^{Pd} and ε_y^{Pd}. This suggests that most of the Pd atoms still reside on the surface after cluster melting. The overall change in ε_q^{Pd} is small, again indicating the preference of Pd atoms to be located at the surface even after phase change.

On the other hand, ε_q^{Pt} shows a slight increase initially between 300 K and 1100 K. Between 1100 K and 1200 K, slightly larger changes are observed, followed by a rapid one near the melting point, which continues into the liquid phase. This indicates the tendency of the Pt atoms to move to the surface with increasing temperature. However, the decrease in ε_q^{Pd} is not the same as the increase in ε_q^{Pt}. The overall cluster shape has to change to accommodate the increased number of surface atoms. The shape of the cluster now changes from a spherical to a somewhat oval shape. This behavior is somewhat different from melting of Cu-Ni bimetallic clusters[96], where outward movement of Ni was countered by the inward movement of Cu maintaining an overall spherical shape. This difference in behavior is explained below on the basis of relative surface energy change with temperature for the two bimetallics.

3.5.2.3 Concept of surface energy

The surface energy is defined[76] as the difference between the site energy of surface and bulk sites ($\varepsilon_z - \varepsilon_{12}$), where ε_z is the site energy and Z (coordination number) 9, 8, 7, and 6 for (111), (110), edge and corner sites. ε_{12} is the site energy of bulk sites. Table 3-4 shows the surface energy difference at 0 K for a Pd-Pt system, when entropic factors are zero. The typical surface energy differences are between 15-45 KJ/mol depending on the coordination numbers.[97]

The mixing energy[76] (ΔEmix) is the heat of formation for a bimetallic alloy formed in the reaction

$xA+(1-x)B \rightarrow A_xB_{1-x}$ given by $\Delta E_{mix} = E\,(A_xB_{1-x}) - xE(A) - (1-x)\,E(B)$. The mixing energy values listed in Table 3-4 for Pd and Pt are -8.44 and 7.24 KJ/mol. A positive value of mixing energy indicates the tendency of an atom to be surrounded by its own kind, whereas negative valued atoms prefer neighbors of different type. The cluster microstructure at any temperature depends on the interplay among these three factors. At low temperatures, we find the segregation to be dependent primarily on the surface energy difference. For an ideal bimetallic alloy, with 50% composition, the entropy of mixing increases from 2 KJ/mol at 298 K to 7.4 KJ/mol near the melting point (1290 K for $(Pd_{0.5}$-$Pt_{0.5})_{456}$ cluster). The surface energy difference[97] between the two, however, increases with increasing temperature as shown in Fig. 3-8.

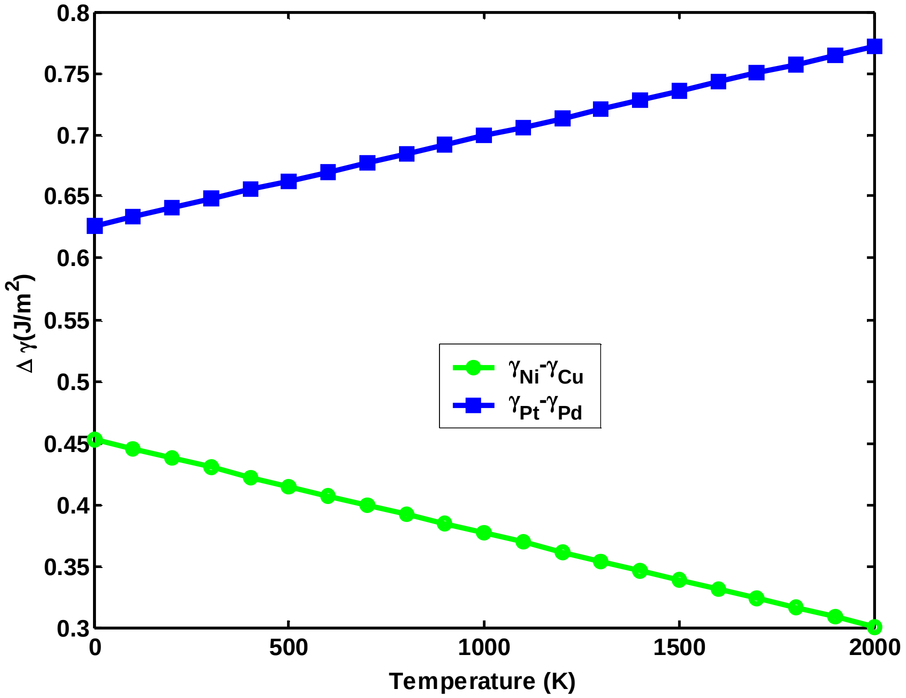

Figure 3-8. Variation of surface energy difference with temperature for Pd-Pt (squares) and Cu-Ni (circles) systems.

Table 3-4. Surface energy of Pd and Pt at various coordination sites.

Coordination Number	γ_{Pd}(KJ/mol)	γ_{Pt}(KJ/mol)
6 (corner)	175.6	218.1
7(edge)	145.7	178.5
8(fcc(100))	115.8	139.9
9(fcc(111))	85.9	100.3

The surface energies of both Pd and Pt decrease with temperature. Hence both Pd and Pt atoms would tend to locate themselves at the surface. However, an increase in the surface energy difference would mean that the decrease in surface energy of Pd atoms is much more than that of Pt. Hence Pd would continue to remain at the surface. Also, owing to the decrease in the absolute surface energy, Pt too prefers to move to the surface. The combined effect results in a net movement of atoms to the surface. This is clearly evident from the deformation parameter plot where ε^{Pt}_{r} increases sharply indicating the outward movement of Pt atoms. On the other hand, ε^{Pd}_{r} remains almost constant suggesting little movement of Pd atoms to the core. This behavior is different from a Cu-Ni bimetallic where the surface energy difference decreases with an increase in temperature showing that the decrease in surface energy of Ni overcomes that of Cu, resulting in migration of Ni atoms to the outside and that of Cu atoms to the inside.

3.5.2.4 Self diffusion coefficient and MSD

The self diffusion coefficients can be obtained from either the positions or velocities of molecules. MSD is proportional to the observation time in the limit as time tends to infinity. The proportionality constant relating the MSD to observation time is known as self diffusivity D which is given by,

$$D \equiv \frac{1}{2d} \lim_{t \to \infty} \frac{\left\langle [r(t_0+t) - r(t_0)]^2 \right\rangle}{t} \tag{3.24}$$

where d-dimensionality of the system and r(t) refers to the vector position of molecule at time t. The ensemble average is taken over all molecules in the system and over several time origins.[98] A linear least squares regression is performed on the MSD curve to give a slope (2dD) from which diffusivity at any temperature can be found.

Fig. 3-9 shows the variation of self diffusion coefficients of Pd and Pt. The diffusivity of Pd atoms shows an upward trend in the temperature range 800-1200 which corresponds to the surface melting stage. In this range, Pt which is mostly present in the bulk has diffusivity much smaller than that of Pd. At the melting point however, both Pd and Pt diffusivities show a sharp increase indicating a first order transition from solid to liquid phase. In the liquid phase, both the diffusion coefficients show a tendency to increase with temperature.

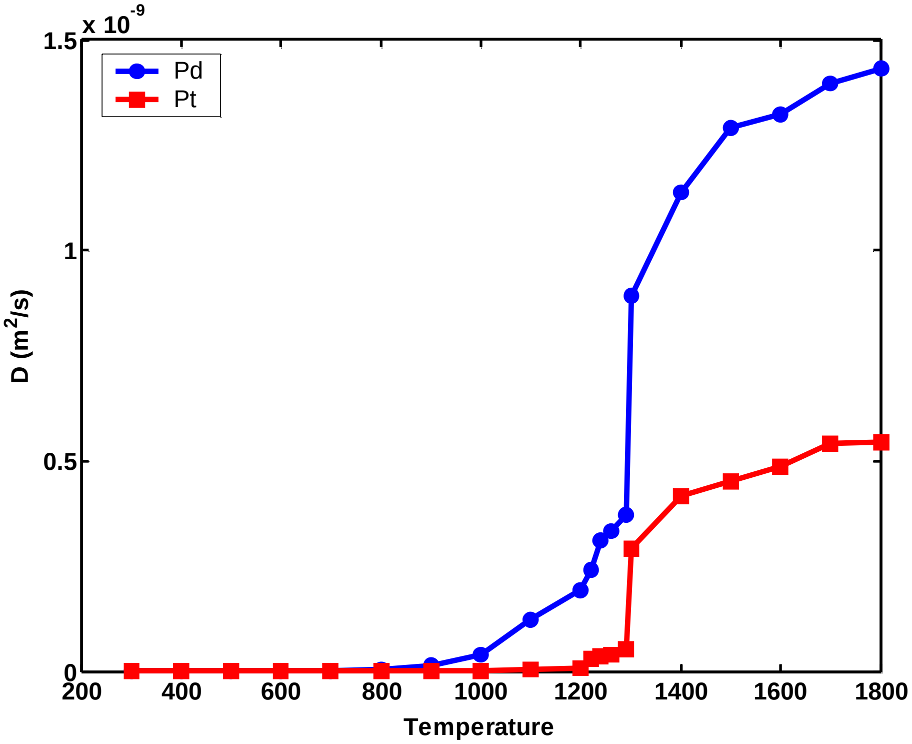

Figure 3-9. Variation of self diffusion coefficient with temperature for Pd (circles) and Pt (squares) in $(Pd_{0.5}\text{-}Pt_{0.5})_{456}$.

3.5.2.5 Surface melting and Lindemann criterion

Surface melting refers to the formation and propagation of a quasi-liquid film, which thickens with increasing temperature and ends with the melting of the solid core. The temperature at which the film thickness diverges to infinity corresponds to the bulk melting point. Although the surface melting behavior is somewhat captured in the atomic self diffusion coefficient variation of Pd and Pt, better insights into the same phenomenon could be obtained by partitioning the cluster into five radial shells of equal width dR. Mean square displacement calculated within each shell was used to calculate the self diffusion coefficients for atoms in that shell. The inter-atomic distance between atoms in the Pd-Pt bimetallic (2.75 Ǻ) was used as dR. The atoms were assigned to the bins based on their initial positions at the end of the equilibration period. The mean square displacements for each shell were then generated by averaging over a 25 ps trajectory with sampling done every 0.1 ps. Averages taken over 25ps trajectory with different origins gave the same result which is indicative of a system that is truly in equilibrium.

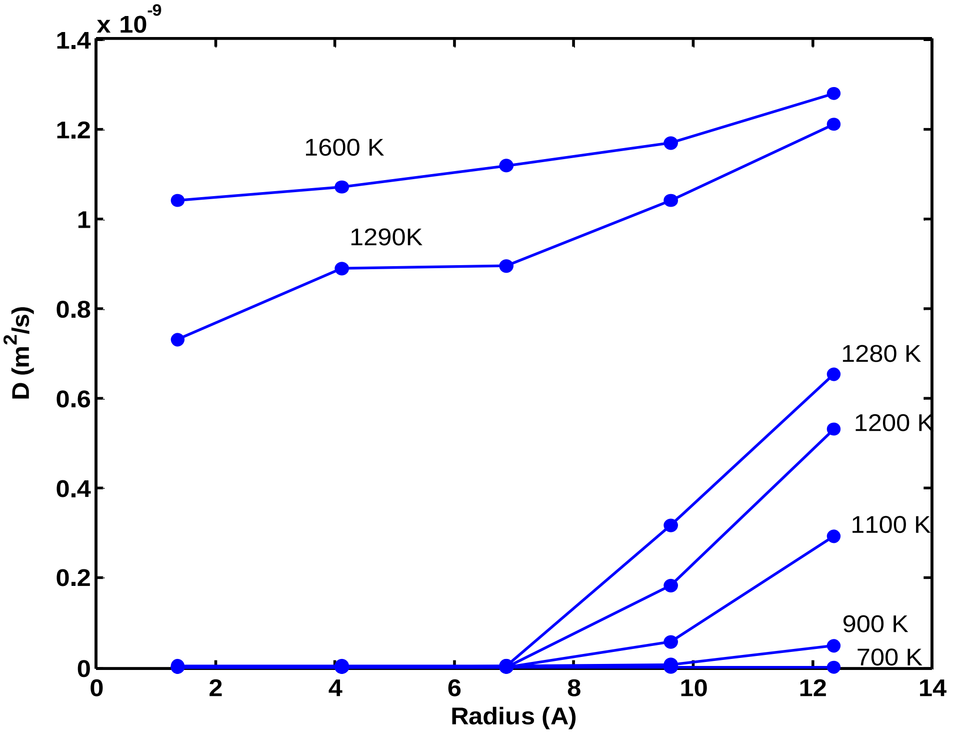

Figure 3-10. Diffusion coefficients calculated for atoms in various shells for $(Pd_{0.5}\text{-}Pt_{0.5})_{456}$ as a function of distance from the center of cluster.

The self diffusion coefficients calculated based on MSD was assigned to each shell and its dependence on distance from the center of cluster was carried out (Fig. 3-10). In all the cases, we find the diffusivities of outer shells to be higher than those of the inner ones. In accordance with the Lindemann criterion which predicts phase transition to occur when atomic motion exceeds 10-15% of inter-atomic distance (2.75 Ǻ), there exists a critical diffusivity (3e-10 m2/s) corresponding to root mean square (RMS) displacement ~ 0.6, which indicates transformation to a liquid phase. Based on this, we find that in the temperature range 900-1100, only the fifth bin is molten. As temperature increases (1200 K), atoms in the fourth and fifth bins reach the critical value, while those in the first three remain crystalline. At the melting point (1290 K), the diffusivity of the entire cluster exceeds the critical value. We can estimate the $R_{crystal}$ or the solid core remaining based on the shell diffusivity plot.

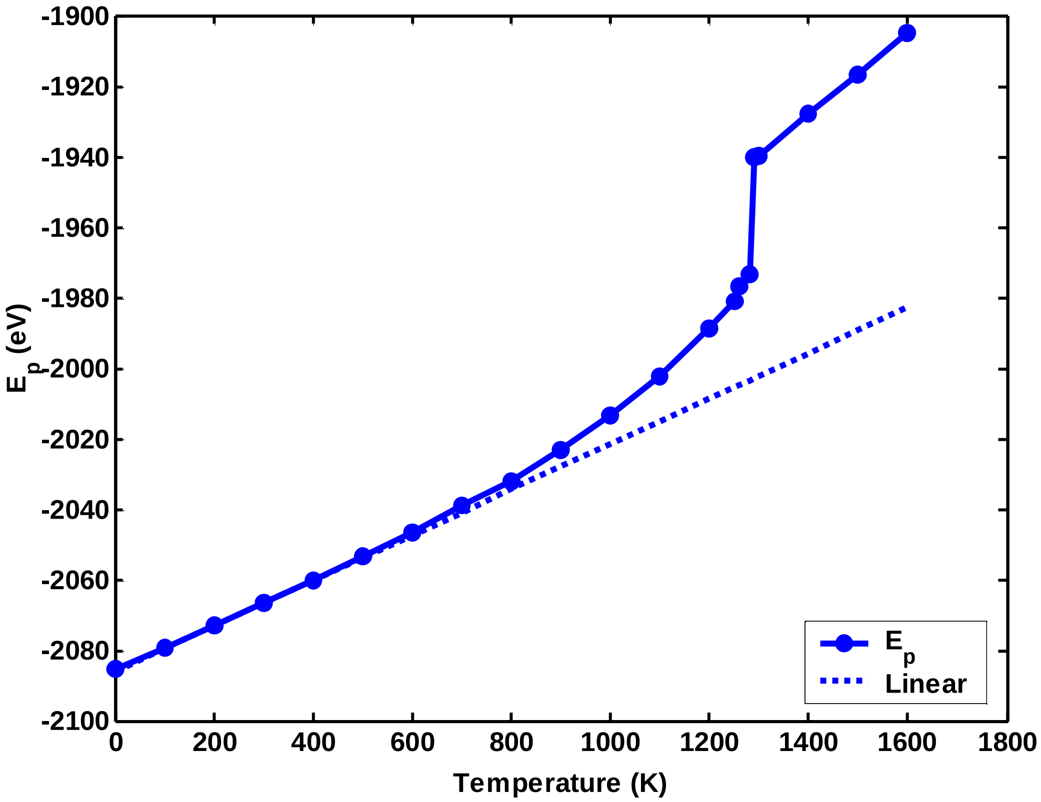

Figure 3-11. Surface melting characterized by deviation of potential energy curve from linearity for $(Pd_{0.5}-Pt_{0.5})_{456}$.

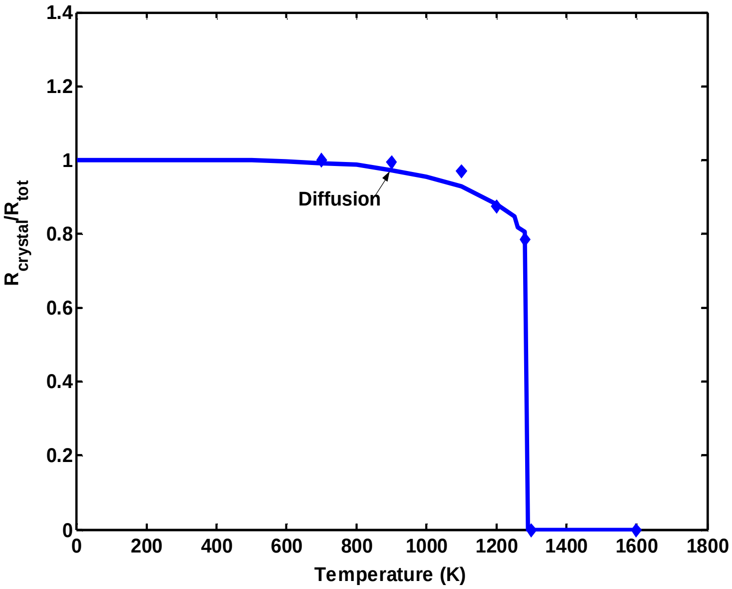

Figure 3-12. Radius of solid core in $(Pd_{0.5}\text{-}Pt_{0.5})_{456}$ cluster as a function of temperature during the melting process calculated from two procedures: The diamonds indicate values obtained by assuming a critical diffusivity of 3e-10 (m^2/s) similar to Lindemann criterion. The line is based on crystal radius obtained by calculated deviations from linearity in the potential energy curve (Figure 3-11).

The surface melting phenomenon is clearly evident from the snapshots taken at various temperatures (Fig. 3-13). The change in shape of the cluster is also observed. This behavior is also true for a $(Pd_{0.5}\text{-}Pt_{0.5})_{1088}$ cluster.

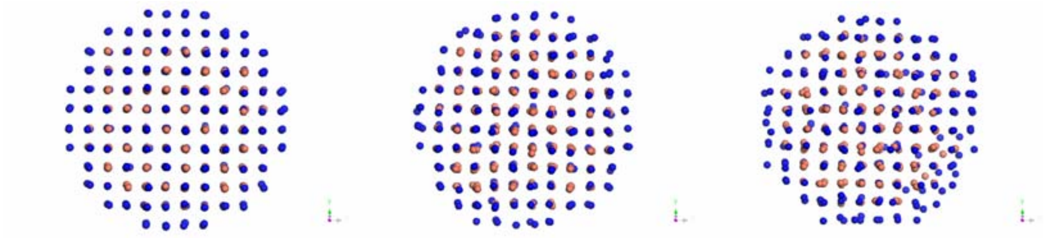

(a) **(b)** **(c)**

Figure 3-13. Snapshots of $(Pd_{0.5}\text{-}Pt_{0.5})_{456}$ cluster taken at various temperatures indicating surface melting of Pd (dark circles) followed by homogeneous melting of Pt (light circles) core. (a) 300 K (b) 700 K (c) 900 K (d) 1100 K (e) 1200 K (f) 1280 K (g) 1290 K (h) 1600 K.

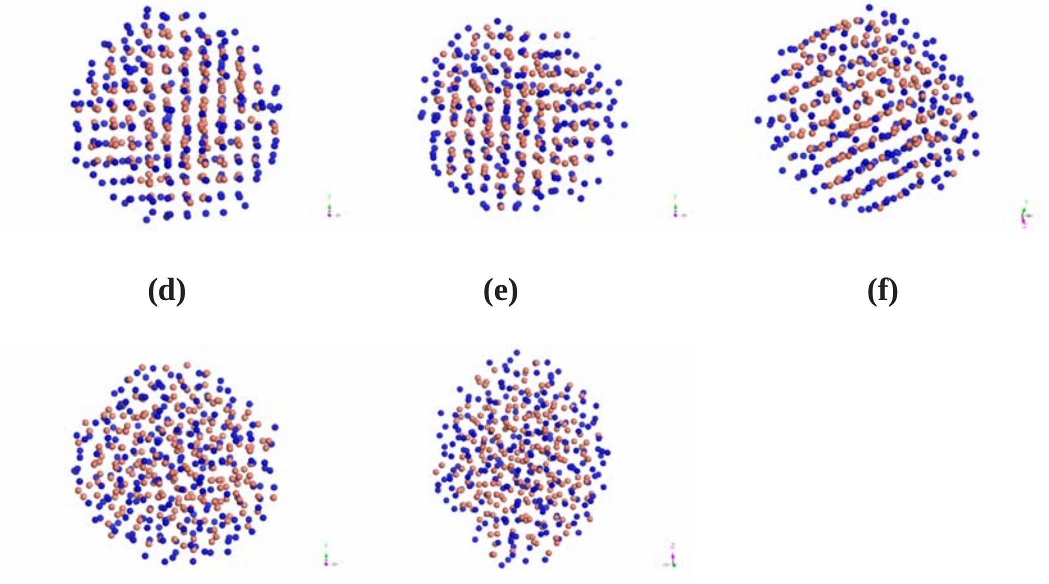

(d) **(e)** **(f)**

(g) **(h)**

Figure 3-13: Continued

$R_{crystal}$ can also be estimated from the heat of fusion.[67] The deviation from linearity in the potential energy curve (ΔPE) gives an extent of surface melting (Fig. 3-11). Radius of the solid core remaining at any point during the melting process can be given by,

$$\frac{R_{crystal}}{R_{total}} = \left(1 - \frac{\Delta PE}{L}\right)^{1/3} \tag{3.25}$$

Fig. 3-12 shows the radius of the remaining solid for $(Pd_{0\,5}\text{-}Pt_{0\,5})_{456}$ calculated using Eq. (3.25) and diffusion coefficients in Fig. 3-10. Similar investigations carried out for cluster compositions other than 50% reveal that surface melting is dictated by the composition of Pd in the bimetallic. This is clear from the greater deviations in the potential energy curve for clusters with higher Pd compositions (Fig. 3-16). The composition effect on the surface melting is studied in the subsequent sections.

3.5.3 Shape transformation during melting

Moment of inertia tensor (MI)[99] is a second rank tensor and has nine components as given in Eq. (3.26),

$$I_{jk} = \int_V \rho(r)(r^2\delta_{jk} - x_j x_k)dV \tag{3.26}$$

In order to better characterize the shape transformations associated with melting, a modified moment of inertia (Î), similar to that given by Eq. (3.26) can be defined in which all the atoms are assumed to be of unit mass. The atomic distribution could then be related to the nanocluster shape by comparing the principal components of Î. The change in Î depends only on the relative distance of the atoms from the cluster centre of mass. The tensor components calculated at different temperatures are summarized in Table 3-5. These can be used to gain insights into the changes in cluster shape.

Table 3-5. Tensor components of modified moment of inertia at different temperatures for ($Pd_{0.5}$-$Pt_{0.5}$)$_{456}$.

Temperature (K)	Î xx (Ǻ^2)	Î yy (Ǻ^2)	Î zz (Ǻ^2)	-Îxy=-Îyx (Ǻ^2)	-Îyz=-Îzy (Ǻ^2)	-Îzx=-Îxz (Ǻ^2)
300	24964.5312	24934.3347	24957.0824	-46.011	-55.205	41.815
900	25136.8223	25774.9342	26054.078	64.2382	-192.62	-199.69
1280	25803.8743	27379.5274	25844.8724	272.523736	264.252	1338.07
1290	26281.8507	27312.6066	27304.8483	-485.17	-1166.93	611.128
1800	28488.7811	28606.8318	26983.5971	-752.832	1861.20771	-1505.03

As shown in Table 3-5, the initial cluster shape is spherical with diagonal elements Ixx=Iyy=Izz and the off diagonal elements having much lower values. Î increases with temperature indicating that the atoms have a tendency to move away from the centre of mass. Near the melting point (1290K), the cluster has a shape closer to that of an ellipsoid (Îxx=Îzz) with the off-diagonal elements having higher values than before. At higher temperatures after phase transition occurs, the cluster remains more or less an ellipsoidal shape

(Îxx= Îyy). The same is indicated by principal moment of inertia as shown in Table 3-6, Fig. 3-14, and the snapshots in Fig. 3-13. It is difficult to predict the long term behavior of the shape changes. However, it is clear from Fig. 3-13 and Fig. 3-14 that the cluster is deformed from its initial spherical shape. Similar shape changes were obtained for (Pd$_{0\,5}$-Pt$_{0\,5}$)$_{1088}$ cluster. However, we find that clusters with higher Pt compositions (75 and 95%) maintain their spherical shape even after the phase transition. This is attributed to lesser surface melting at higher Pt compositions.

Table 3-6. Principal components of modified moment of inertia at different temperatures for (Pd$_{0.5}$-Pt$_{0.5}$)$_{456}$.

Temperature(K)	I$_1$ (1x10^4 Å^2)	I$_2$ (1x10^4 Å^2)	I$_3$ (1x10^4 Å^2)
300	2.4854	2.4998	2.5004
1280	2.4455	2.7183	2.7428
1290	2.5432	2.6988	2.8478
1800	2.4969	2.9231	2.9879

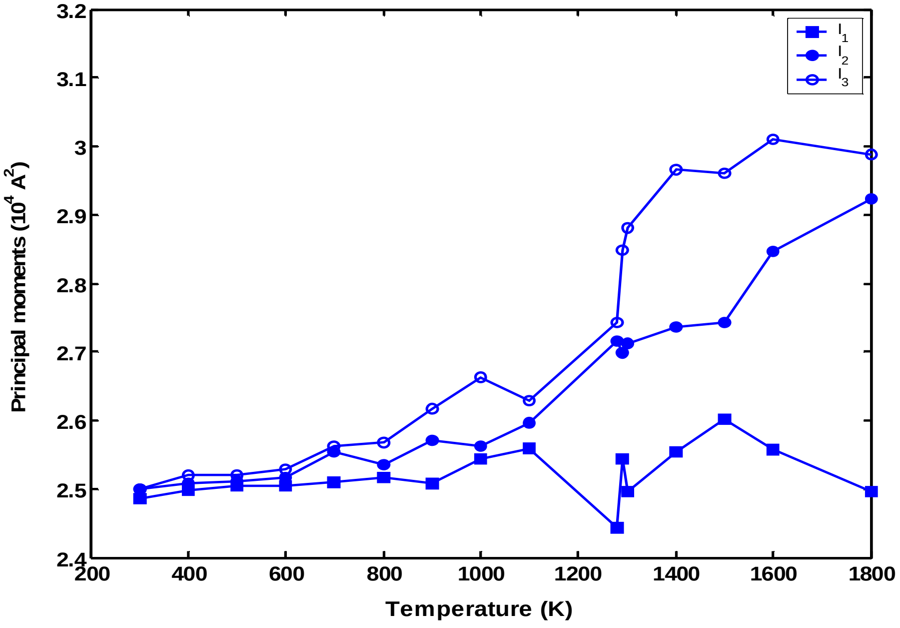

Figure 3-14. Variation of principal components of moment of inertia with temperature for (Pd$_{0.5}$-Pt$_{0.5}$)$_{456}$.

3.5.4 Effect of composition on melting

The melting characteristics were investigated for different compositions of the bimetallic, namely, 5%, 25%, 75% and 95% Pt. The potential energy variation with temperature for the same was studied. Fig. 3-15 shows that the melting point progressively increases with an increase in the concentration of Pt in the bimetallic. The melting temperatures based on potential energy jump (Fig. 3-16) for various compositions are summarized in Table 3-7.

Table 3-7. Variation of melting point with composition for the 456 and 1088 atom clusters respectively.

Composition	Melting point (K)	
	1088 atoms	456 atoms
5% Pt	1250±10	1120±10
25%Pt	1340±10	1200±10
50%Pt	1460±10	1280±10
75%Pt	1540±10	1370±10
95%Pt	1600±10	1430±10

The melting point could be related to the composition for 456 atom cluster by,

$$T_m = 3.4X + 1100 \qquad (3.27)$$

where, X is the percentage composition of Pt.

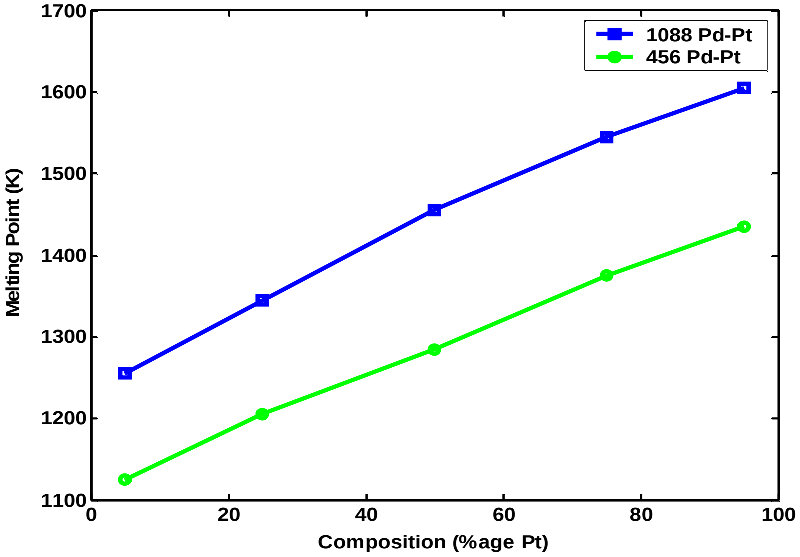

Figure 3-15. Melting point variations with composition for $(Pd_x\text{-}Pt_{(1-x)})_{456}$ (circles) and $(Pd_x\text{-}Pt_{(1-x)})_{1088}$ (squares).

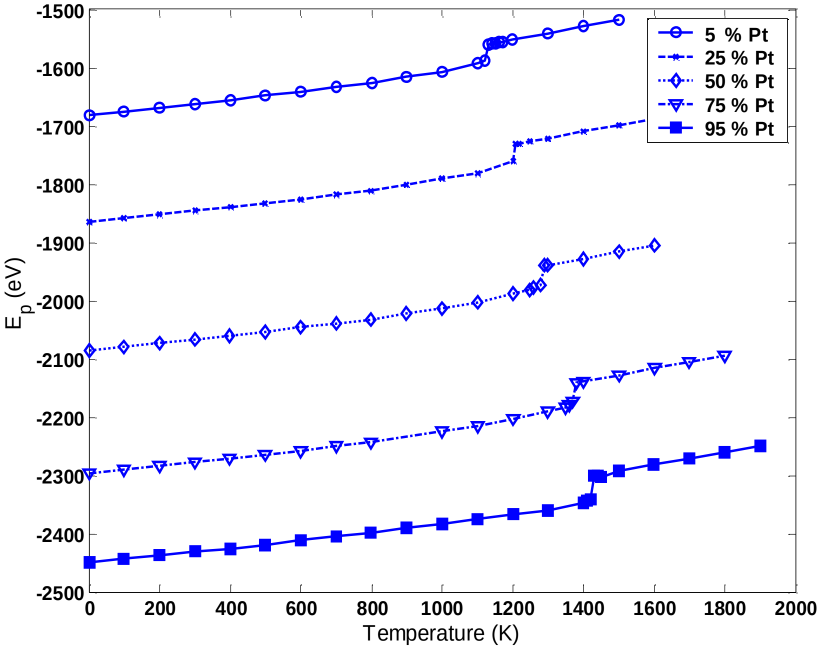

(a)

Figure 3-16. Potential energy variation with temperature for different compositions (x) for (a) $(Pd_x\text{-}Pt_{(1-x)})_{456}$ and (b) $(Pd_x\text{-}Pt_{(1-x)})_{1088}$ cluster.

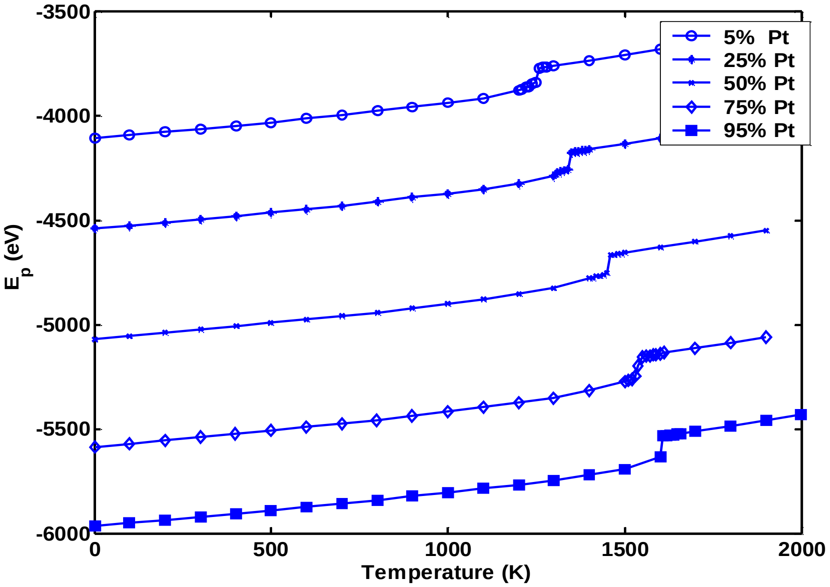

(b)

Figure 3-16: Continued

This nearly linear behavior is seen even for larger cluster sizes (1088 atoms) as seen in Fig. 3-15. In calculating the melting points for different compositions, we used the jump in potential energy corresponding to the melting of the Pt rich cluster core. The linear variation of melting point can be attributed to the proportional change in the radius of the solid Pt core with composition. In addition, we find that clusters which are rich in Pd show surface melting to a greater extent. This feature is characterized by increasing deviations of the potential energy curve from linearity with increasing Pd composition.

Metal nanoclusters used to carry out chemical reactions at high turnover and selectivity often operate in 400-1000 K range[100]. In sensor applications, the gas adsorption mechanism is primarily dependent on the surface morphology. DFT studies as well as experiments indicate certain sites such as Pd (111) are more preferred for O_2 adsorption than Pd (110)[101]. The selectivity, sensitivity and the speed of sensor response is then influenced by the relative densities of such sites. As temperature increases, the movement of surface atoms as a result of surface melting can have an important effect on the catalytic and sensing activity.

Understanding the variation of surface melting characteristics with compositions could help optimize the operating conditions required for catalysis and sensing.

3.5.5 Comparison with experiments

To justify the choice of the QSC potential with the listed parameters used in the MD simulations, bulk melting of Pd and Pt was carried out using the same models with periodic boundary conditions in a constant NPT system and the results are summarized in Table 3-8. The calculated melting points from the simulations agree well with the bulk experimental values of Pd and Pt. The slight differences could be attributed to the empirical nature of the potential function. The enthalpy of melting also compares well with the experimental values.

The heating process in our simulations is homogeneous. Experimentally however, it is difficult to maintain such homogeneity and the thermal conductivity of the material under study plays a role in determining the extent of homogeneity attained in the heating process. Available literature data point to a heterogeneous melting process in which temperature gradients exist between the outer surface and inner core[102]. The energy transfer mechanism as well as transfer of a part of thermal energy to latent heat of melting leads to temperature gradients or non-homogeneity in the heating process. Thus, the kinetics of the melting process is also important in understanding the melting mechanism.

Table 3-8. Comparison of bulk simulation results with experimental values.

	Melting Point (Pd)	Melting Point (Pt)	ΔH(Pd) KJ/mol	ΔH(Pt) KJ/mol
Experiments	1840 K	2040 K	16.7	20
Bulk Simulation	1760 K	2090 K	15.8	18.74

In recent experiments, homogeneous heating has been achieved by using pico-second and femto-second pulse laser irradiation thereby, attaining extremely high heating rates of 1014 K/s (ultrafast thermal melting)[103]. Additionally, homogeneous heating process can be carried out through proper choice of experimental parameters like large penetration depth of optical heating pulse, proper pulse duration as well as a detection technique with a sufficient probing depth. The numerical values of transition temperatures will likely differ from experimental measurement, if a heterogeneous process is approximated in the physical experiment. It is also likely that the transition will appear not as sharp as in the simulations.

3.6 Conclusions

The melting behavior of Pd-Pt nanoclusters having 456 and 1088 atoms is characterized by pre-melting of surface segregated Pd atoms followed by homogeneous melting of Pt core. The melting point of the nanoclusters is clearly identified by studying the variation in potential energy and specific heat capacity. The melting point of nanoclusters calculated from our simulations is much lower than the corresponding bulk Pd and Pt crystals. The bond order parameters indicate a change from an FCC type structure to an HCP one before transformation to a liquid phase. As melting proceeds, the Pd atoms tend to diffuse inside while the Pt atoms diffuse outside. The extent of diffusion is not the same, leading to a net increase in the number of surface atoms characterized by shape change from spherical to somewhat oval. This melting behavior is different from some of the bimetallics (for example, Cu-Ni) studied earlier. The difference in behavior can be explained on the basis of variation of surface energy difference with temperature. The surface melting phenomenon is indicated by the deviation of potential energy curve from linearity. Shell based self diffusion coefficients give better insights into the surface melting phenomenon. The melting phenomenon was studied for different compositions and a linear trend was observed for both 456 and 1088 atom cluster. The homogeneous heating process carried out in the present study is difficult to carry out experimentally. However, proper manipulation of the experimental variables can lead to conditions close to those used in simulations. On the whole, the description of the melting transition agrees qualitatively with previous simulation and experimental studies on nanoclusters.

Chapter Four

Molecular Dynamics Simulation Study of the Melting and Structural Evolution of Bimetallic Pd-Pt Nanowires

4.1 Abstract for chapter four

Thermal characteristics of Pd-Pt metal nanowires with diameters ranging from 2.3 to 3.5 nm and of several compositions were studied by molecular dynamics simulations utilizing the Quantum Sutton-Chen potential function. Monte-Carlo simulations employing bond order simulation model were used to generate the initial wire configurations that consisted of surface segregated structures. Melting temperatures were estimated based on variations in thermodynamic properties such as potential energy and specific heat capacity. We find that the melting transition temperatures for the nanowires are much lower than those of bulk alloys of the same composition and at least 100-200 K higher than those of nanoclusters of the same diameter. Density distributions along the nanowire cross-section and axis as well as components of shell-based diffusion coefficients and velocity auto-correlation functions were used to investigate the melting mechanism in these nanowires. Our findings indicate a surface-initiated melting process characterized by predominantly larger cross-sectional movement. This two-dimensional surface melting mechanism in nanowires differs from that in nanoclusters in which atomic movement is more isotropic in all three dimensions. Differences in the surface melting mechanism result in structural transformations from fcc-hcp type and lead to simulated phase boundaries for nanowires that are different from bulk alloys as well as from same-diameter nanoclusters. A composition and temperature dependent fcc-hcp transformation occurs prior to the melting transition in both nanowires and nanoclusters. Hcp phase occurs over a wider temperature range at Pd-rich compositions and a narrower range at low Pd compositions with the fcc-hcp and hcp-liquid transition temperatures showing a minimum at 25% Pt composition.

In contrast, the nanoclusters exhibit a near-linear dependence of melting temperature on Pd composition with the hcp phase existing over a much narrower range of temperatures, closer to the melting transition. Thermal stability of the solid phases of these nanowires was investigated by simulating two alternative starting configurations such as a hypothetical hcp and an annealed-solid structure for two compositions. The size and composition dependence of nanowire melting temperatures are consistent with those predicted by available melting theories.

4.2 Melting of Pd-Pt nanowires

Metal nanowires have attracted much attention in recent years due to their potential applications in nanoscale materials and devices[104]. These nanowires exhibit physical, chemical and electronic properties which are different from both bulk materials as well as single molecules[105-113]. One such structure is nanowires of Pd and its alloys which find extensive use in hydrogen sensing and in catalysis. The key to all potential applications of nanowires lies in their small size and structure. This makes knowledge and control over their size and shape distributions, surface compositions as well as crystal structure, critical to improved device designs. With increasing miniaturization of devices, it becomes important to develop a quantitative understanding of the thermodynamic and structural properties of these nanowires.

The numerous applications of metallic nanowires have prompted a lot of experimental effort being focused on the synthesis and preparation of single component as well as bimetallic nanowires. Recent experimental studies have revealed the formation of stable ultra-thin nanowires of gold having length to diameter ratios of over ten[114,115]. Nanowires of Ag-Pt with lengths up to 3.5 µm and diameters between 3 and 20 nm have been produced by irradiation of aqueous solutions of Ag-Pt ions with gamma rays[116]. In addition to the well known template synthesis, other electro-deposition methods, such as a combination of “slow growth” and “nanowire growth” to produce beaded bimetallic nanowires with high aspect ratios are also gaining interest[117]. One of the most challenging issues is the control over the size and morphology of these nanostructures. Knowledge of the thermal properties of these metallic nanowires and their associated effects on the size, shape, and composition would have a bearing on the method of synthesis, processing, and the performance of these nanowires in their various areas of applications.

The melting points of nanowires decrease with decreasing diameter and their values are much below the bulk melting points[118-125]. The large ratio of surface to bulk atoms is primarily responsible for this lowering effect. Experimentally, it is difficult to observe the microscopic processes associated with melting. Computer simulations offer an effective tool to study the properties of nanowires and complement experimental efforts[63].

Considerable experimental and theoretical research has been dedicated to understanding the thermodynamics and kinetics of nanowire growth and stabilization when subjected to thermal and other stresses[126-133]. For example, experimental investigations have revealed the growth of InAs to be limited by the melting temperature of As-In alloy[134]. A molecular dynamics study of the melting of one dimensional zirconium wire indicated melting of nanowires to initiate from the inner core shell atoms.[121] Similarly, diffusion of the central atoms along the nanowire axis in palladium nanowires (diameter < 2 nm) resulted in the onset of melting.[120] On the other hand, surface melting in Pd nanowires with 2.3 nm diameter results from predominantly cross-sectional movement of Pd atoms.[135] Studies on the melting of gold nanowires indicated that surface melting temperature is representative of the overall wire melting temperature[124]. This behavior is very much different from that of nanoclusters where the onset of melting results from enhanced movement of the less restrained surface atoms[60]. A coexistence of liquid and solid phases was also observed in the melting process of titanium nanowires[119]. Similarly, a study of ultra-thin titanium nanowires, with diameters less than 1.2 nm, indicated no clear characteristic first-order transition during the melting process[123]. Structural transformations from a helical multi-walled to a bulk-like rectangular structure have also been observed for 1.7 nm titanium wires[119].

Bimetallic nanomaterials are better suited for catalytic and sensing applications than their monometallic counterparts[50]. Complex phenomena such as surface segregation and micro-mixing occur in alloys of finite-sized structures such as nanowires. For a given composition of the bimetallics, the microstructure is dictated by surface energies and mixing energies of the constituent atoms[76,78]. Atoms with lower surface energies tend to segregate to low coordination number sites, the extent of which is determined by the interplay between surface energies, mixing energies and entropy. There is enough experimental evidence to indicate the occurrence of this phenomenon in nanowires of Pd-Ag and Pt-Ag[136]. In the present work, we study thermal characteristics, low temperature solid phases and melting transitions of Pd-Pt nanowires of different diameters and compositions using molecular dynamics (MD) simulations employing the quantum Sutton-Chen potential function.

4.3 Initial nanowires size, structure, and composition

All the transition elements including Pd and Pt exhibit an fcc structure in the bulk solid phase. A large block of fcc was formed from a fcc unit cell by replicating in ABC directions. Using various cutoff radii, cylindrical structures representing nanowires of different diameters (D) ranging approximately from 2.3 nm to 3.5 nm were created. By choosing different length/diameter ratios, it was ensured that the results were not influenced by the periodic boundary conditions for the simulated infinitely long nanowires. The range of nanowire diameters was selected to facilitate comparisons with nanoclusters of similar diameters used in our previous studies[137,138]. Alternative starting configurations comprising of hcp nanowires were also generated and utilized in simulations.

To identify the initial atomic distribution of the constituent atoms for a given composition of the bimetallic, these structures were subjected to a Metropolis Monte-Carlo simulation employing a bond order simulation (BOS) model[77,83], to generate the minimum energy initial configurations which were subsequently used for studying the melting phenomena. The BOS model was modified to include periodic boundary condition along the nanowire axis. The stable configurations generated in the above simulations consisted of surface segregated structures with lower surface energy atoms preferentially located at the surface. The extent of segregation depends on factors such as surface energy, mixing energy and entropy. For Pd-Pt nanostructures, lower surface energy Pd atoms occupy most of the surface sites, whereas the core is mainly composed of Pt atoms.

4.4 Computational details

4.4.1 Potential function

Molecular Dynamics (MD) simulations using DLPOLY[139] were performed to gain insights into the melting process and thermal properties at the atomistic level. All the thermodynamic and transport properties were obtained as time averages over the particle positions and velocities. The embedded atom potential[85] and other long range potentials like the Sutton-Chen potential[86] based on Finnis-Sinclair type of potentials have been used in the literature successfully to predict the properties of fcc based metals such as Pd and Pt. The local electronic density is included to account for the many body terms.

Based on the Sutton-Chen potential, the potential energy of the finite system having N atoms is given by,

$$U_{tot} = \varepsilon \left[\frac{1}{2} \sum_{i=1}^{N} \sum_{\substack{j=1 \\ j \neq i}}^{N} \left(\frac{a}{r_{ij}} \right)^{n} - c \sum_{i=1}^{N} \rho_i^{1/2} \right] \tag{4.1}$$

where the local density accounting for cohesion associated with any atom i is $\rho_i = \sum_{\substack{j=1 \\ j \neq i}}^{N} \left(\frac{a}{r_{ij}} \right)^{m}$. The Quantum Sutton-Chen potential[87] (hereafter referred to as QSC), includes quantum corrections and takes into account the zero point energy allowing better prediction of temperature dependent properties for both single component and alloy systems[67,75,88]. The QSC parameters for the Pd and Pt are listed in Table 4-1. The geometric mean was used to obtain the energy parameter ε and the arithmetic mean was used for the remaining parameters, to predict the nature of interaction between Pd and Pt.

4.4.2 MD simulation details

The MD simulations were carried out with a constant number of atoms N and temperature T with periodic boundary condition applied along the nanowire axis. A constant temperature Berendson thermostat[91] with a relaxation time of 0.4 ps was used. The equations of motion were integrated using Verlet leapfrog algorithm[63] with time step of 0.001 ps. The nanowires were initially subjected to mild annealing in the 0-

300 K interval which was followed by heating to 1800 K in increments of 100 K. Near the melting point, the temperature increments were reduced to 10 K to account for the large temperature fluctuations. The simulations were carried out for 400 ps of equilibration followed by production time of 200 ps for generating time-averaged properties. These simulations are essentially at zero pressure as the nanowire is able to expand freely in the radial direction.

Table 4-1. Potential parameters used in MD simulations for Pd-Pt nanowires.

Quantum Sutton-Chen	n	m	ε (eV)	c	a(Å)
Pd	12	6	3.2864e-3	148.205	3.8813
Pt	11	7	9.7894e-3	71.336	3.9163

4.5 Results and discussion

Structural and dynamic properties at different temperatures leading up to the phase transition and higher were calculated and analyzed to gain insights into the mechanism of nanowire melting. Simulated phase boundaries representing composition dependency of various transitions were generated and compared to those for nanoclusters of the same diameter, and the bulk alloy. The size dependency of melting point is also discussed for a nanowire of representative 50% Pd composition.

4.5.1 Melting and freezing point identification

The phase transition from solid to liquid and *vice versa* is usually identified by studying the variation in either the thermodynamic properties such as potential energy and specific heat capacity or some structural properties such as Bond Order Parameters[95] and Wigner values. The present study employs both these methods to identify melting points for different nanowire sizes and compositions.

4.5.1.1 Potential energy

The phase transition from solid to a liquid phase and *vice versa* can be identified by a jump in the total potential energy *vs*. temperature curve shown in Fig. 4-1 (a) and (b). This corresponds to a melting temperature of 1230 ±20K for $(Pd_{0\ 75}\text{-}Pt_{0\ 25})_{2\ 34nm}$ and 1470 ±10K for $(Pd_{0\ 5}\text{-}Pt_{0\ 5})_{2\ 34nm}$ nanowires. There is a greater deviation from linearity in the potential energy curve in case of $(Pd_{0\ 75}\text{-}Pt_{0\ 25})_{2\ 34nm}$ as compared to $(Pd_{0\ 5}\text{-}Pt_{0\ 5})_{2\ 34nm}$ nanowire. This might be attributed to the increased surface melting at higher Pd compositions.

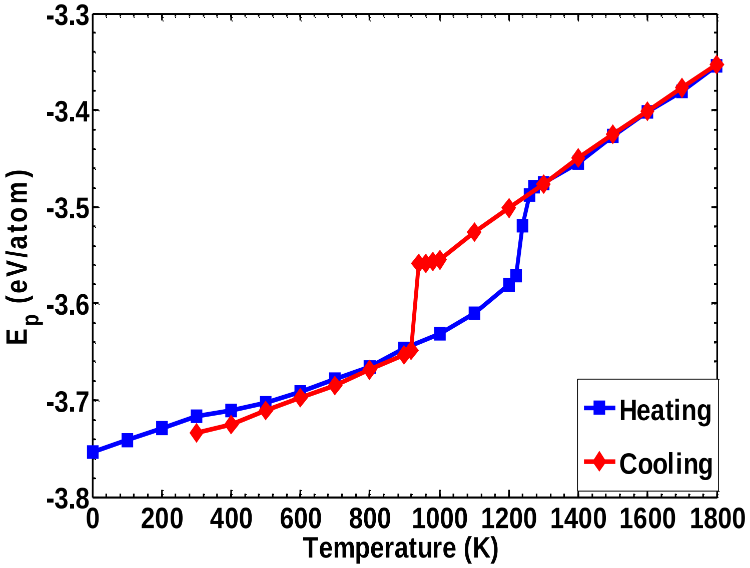

(a)

Figure 4-1. Variation of potential energy with temperature for 2.34 nm diameter nanowires (a) $(Pd_{0.75}\text{-}Pt_{0.25})$ and (b) $(Pd_{0.5}\text{-}Pt_{0.5})$ alloy having 672 atoms. The solid lines with solid squares correspond to the heating, and solid lines with diamonds represent cooling of 2.34 nm Pd-Pt alloy nanowires with an initial fcc structure.

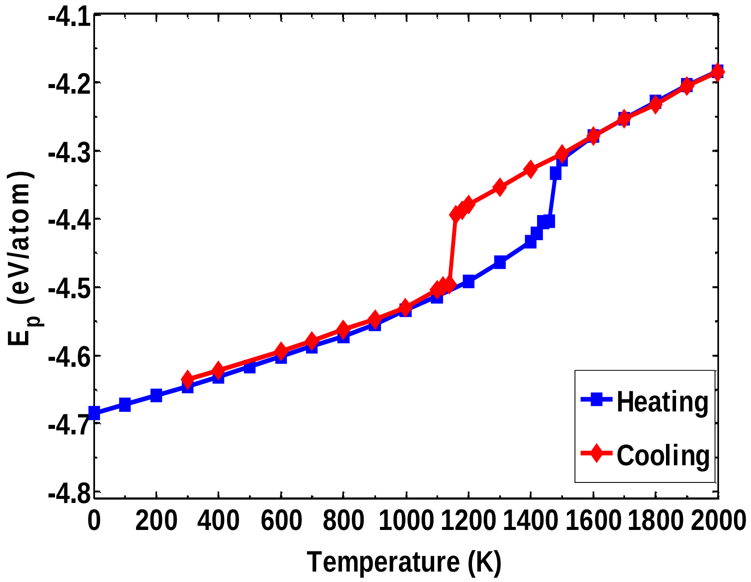

(b)

Figure 4-1: Continued

Upon cooling, the nanowires undergo a sharp liquid-solid transition and show a strong hysteresis which is a consequence of the need for super cooling in the transition from liquid to solid. The freezing points for $(Pd_{0\ 5}\text{-}Pt_{0\ 5})_{2\ 34nm}$ and $(Pd_{0\ 75}\text{-}Pt_{0\ 25})_{2\ 34nm}$ nanowires are 1150 ±10 and 930 ±10 K, respectively. Although the potential energy of the new solid phase is not very different from the initial one (fcc), structural differences prevail. It is interesting to note that the energy of the new solid phase (referred to as annealed-solid hereafter) in case of $(Pd_{0\ 5}\text{-}Pt_{0\ 5})_{2\ 34nm}$ nanowires is slightly higher than its initial fcc phase whereas it is lower than the initial fcc phase for $(Pd_{0\ 75}\text{-}Pt_{0\ 25})_{2\ 34nm}$ nanowires. This indicates that the annealed-solid structure is closer to the global minima for $(Pd_{0\ 75}\text{-}Pt_{0\ 25})_{2\ 34nm}$ whereas the fcc phase is a more suitable starting configuration for $(Pd_{0\ 5}\text{-}Pt_{0\ 5})_{2\ 34nm}$ nanowires. The thermal stability of different starting configurations is discussed in detail in subsequent sections.

4.5.1.2 Specific heat capacity

The specific heat capacity at constant pressure in a weak coupling ensemble such as that achieved with the Berendson thermostat can be written as a function of fluctuations in the instantaneous enthalpy $<\delta H^2>$.[94]

$$C_p = \frac{\left\langle \delta H^2 \right\rangle_{NPT}}{N k_B T^2} = \frac{\left\langle H^2 \right\rangle - \left\langle H \right\rangle^2}{N k_B T^2} \tag{4.2}$$

To identify the melting temperature, the specific heat capacity at constant pressure is plotted in Fig. 4-2. For $(\mathrm{Pd}_{0\ 75}\text{-}\mathrm{Pt}_{0\ 25})_{2\ 34\mathrm{nm}}$ and $(\mathrm{Pd}_{0\ 5}\text{-}\mathrm{Pt}_{0\ 5})_{2\ 34\mathrm{nm}}$ wires, the maximum in the specific heat capacity corresponds to the melting temperatures i.e. T_m=1230 K and 1470 K, respectively.

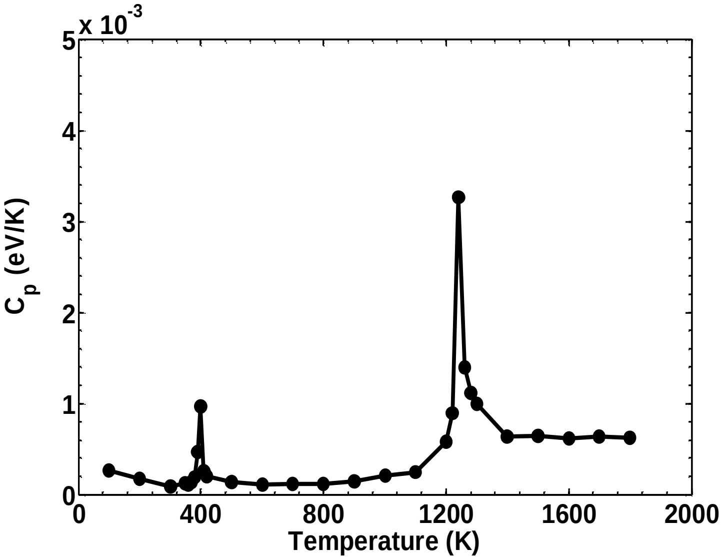

(a)

Figure 4-2. Variation of specific heat capacity with temperature during heating of 2.34 nm diameter nanowires (a) ($\mathrm{Pd}_{0.75}$-$\mathrm{Pt}_{0.25}$) and (b) ($\mathrm{Pd}_{0.5}$-$\mathrm{Pt}_{0.5}$) alloy with an initial fcc structure.

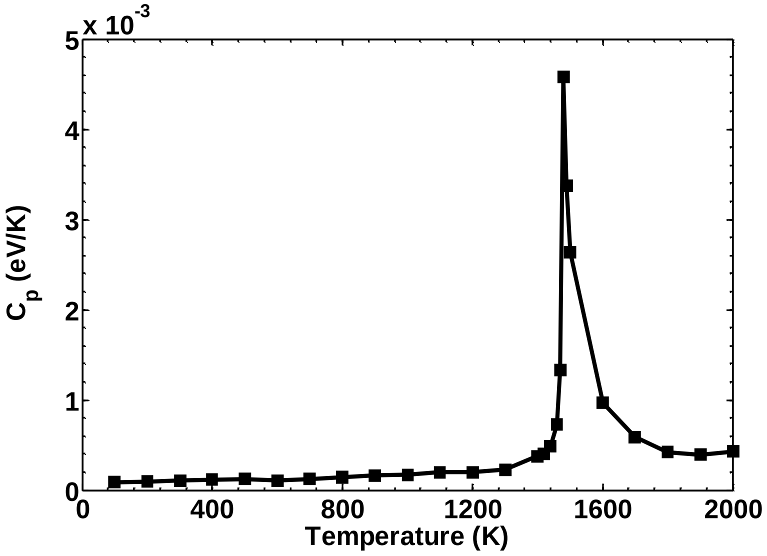

(b)

Figure 4-2: Continued

It is also observed that there is a sharp peak at 400 K for $(Pd_{0\ 75}\text{-}Pt_{0\ 25})_{2\ 34nm}$ This could be attributed to some isomerization or structural changes in the nanowire[96]. Although wires having Pt compositions lower than 15% and higher than 40% also exhibit such a transition, the onset in these composition ranges occurs at temperatures closer to the wire melting point. Similar solid-solid transition was also found in same-sized spherical bimetallic nanoclusters of Pd-Pt near the melting temperatures[140], however the early onset experienced over a limited composition range (approx. 15-40% Pt in this case) is unique to bimetallic nanowires. To gain insights into the nature of this solid-solid transition occurring in different composition ranges, we utilize bond orientational order parameters.

4.5.1.3 Bond orientational order parameters

Bond orientational order parameter method[95] can be used to analyze cluster structure as well as to distinguish between atoms in solid (close-packed) and liquid environments generated at the onset of melting. The value of the global bond orientational order parameter Q_l in a solid cluster depends on the relative bond orientations and has a unique value for each crystal structure as shown in Table 4-2.

Table 4-2. Bond orientational order parameter values for various geometries.

Geometry	Q_4	Q_6
Fcc	0.19094	0.57452
Hcp	0.09722	0.48476
Liquid	0	0

The temperature dependence of bond orientational order parameters Q_4 and Q_6 for $(\mathrm{Pd}_{0\ 75}\text{-}\mathrm{Pt}_{0\ 25})_{2\ 34\mathrm{nm}}$ and $(\mathrm{Pd}_{0\ 5}\text{-}\mathrm{Pt}_{0\ 5})_{2\ 34\mathrm{nm}}$ wires is shown in Fig. 4-3. Both the nanowires were started with an initial, annealed fcc structure at 300 K. As temperature increases, the atoms undergo vibrations about their equilibrium positions leading to a distortion of the crystal structure, characterized by Q_4 and Q_6 values. It can be seen from Fig. 4-3 (a), that there is a sharp transition in the nature of close-packing at 400 K for $(\mathrm{Pd}_{0\ 75}\text{-}\mathrm{Pt}_{0\ 25})_{2\ 34\mathrm{nm}}$ wire.

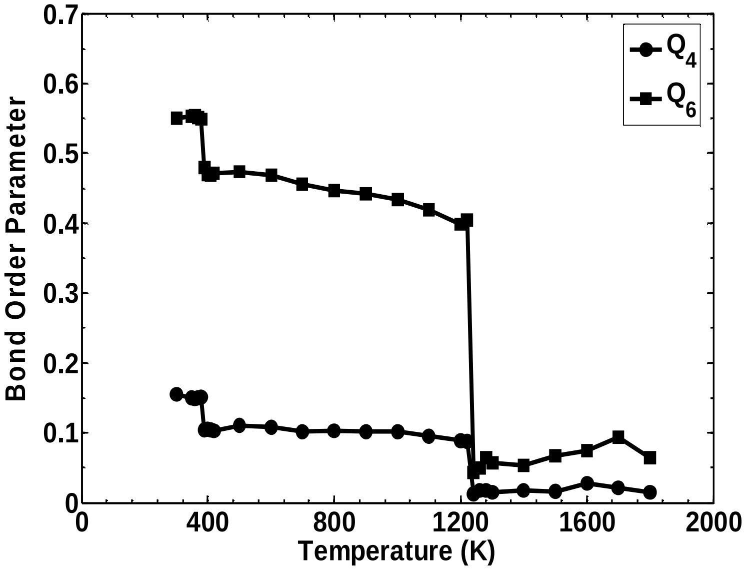

(a)

Figure 4-3. Temperature dependence of bond orientational order parameters (Q_4 (circles) and Q_6 (squares)) during heating of 2.34 nm diameter alloy nanowires (a) ($Pd_{0.75}$-$Pt_{0.25}$) and (b) ($Pd_{0.5}$-$Pt_{0.5}$).

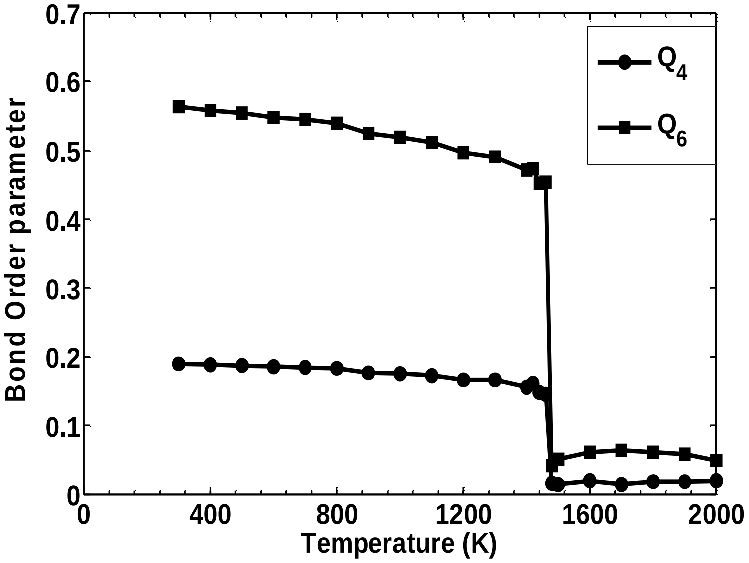

(b)

Figure 4-3: Continued

Comparison of the Q_4 and Q_6 values in Fig. 4-3 (a) with those in Table 4-3 reveals a rearrangement from an fcc to a metastable hcp structure in the temperature range (400-1200 K) for the $(Pd_{0\ 75}\text{-}Pt_{0\ 5})_{2\ 34nm}$ wires . Such an early transition does not occur for $(Pd_{0\ 5}\text{-}Pt_{0\ 5})_{2\ 34nm}$ wire, where the stable structure remains as fcc over the temperature range (300-1350 K) which then transforms to a near hcp type crystal structure (1350-1460 K). The onset of such solid-solid transition has been observed in theoretical investigations on gold nanoclusters[74] as well as experimental investigations on bimetallic Pt-Ru nanoclusters[141]. At the melting point, all the order parameters rapidly decrease to zero indicating a phase change to liquid. This happens at 1230±20 K and 1470±10 K, respectively, for $(Pd_{0\ 75}\text{-}Pt_{0\ 25})_{2\ 34nm}$ and $(Pd_{0\ 5}\text{-}Pt_{0\ 5})_{2\ 34nm}$ wires.

4.5.2 Understanding nanowire melting phenomenon

Insights into the nanowire melting phenomenon can be obtained by analyzing the density profiles, shell-based diffusion coefficients and velocity autocorrelation functions. Such results are presented in this section.

4.5.2.1 Density profiles

The nanowire melting process is associated with the redistribution of atoms owing to their increased motion, especially at high temperatures. Fig. 4-4 shows the atomic distribution of Pd atoms in $(Pd_{0.5}$-$Pt_{0.5})_{2.34nm}$ along the nanowire axis during the melting process. At lower temperatures, we find that the solid-like features are preserved as is indicated by the distinct peaks. In the temperature range 300-1300 K, the peaks remain distinct and the shift in the peak is less than 0.2 Å. This suggests relatively lesser movement of the atoms along the nanowire axis in the specified temperature range. With an increase in temperature, the peaks become broader, suggestive of the relatively larger movement of metal atoms. At the melting point, the atomic distribution becomes smooth indicative of the liquid phase. Similar conclusions can be drawn from Pt atomic density profile along the nanowire axis.

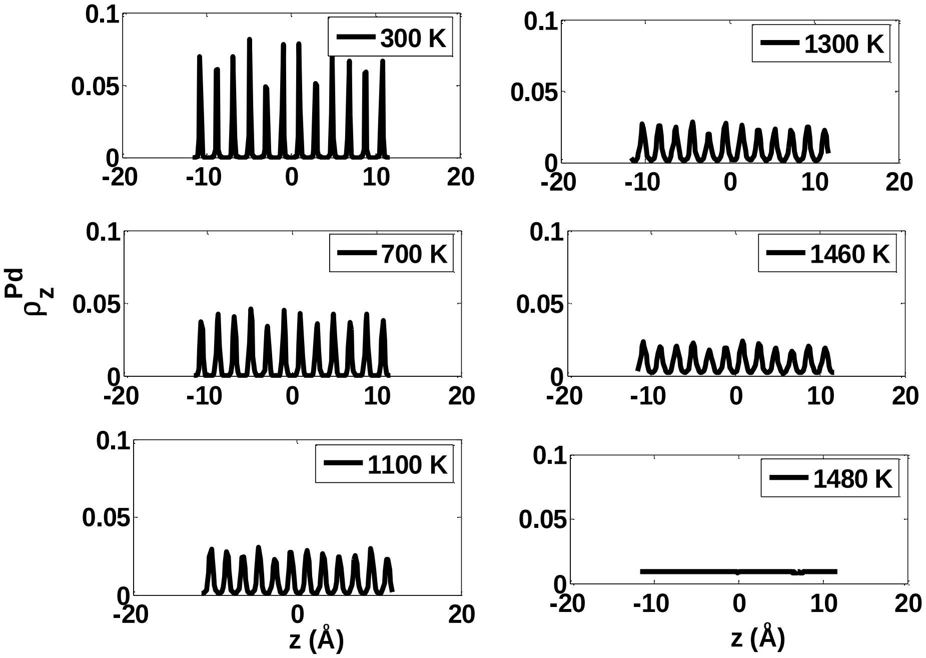

Figure 4-4. Atomic density profiles along the nanowire axis for Pd atoms in $(Pd_{0.5}$-$Pt_{0.5})_{2.34nm}$ at temperatures leading up to melting.

To understand the melting characteristics of the bimetallic nanowire further, we analyzed the radial density profiles of Pd (Fig. 4-5) and Pt (not shown) at different temperatures. Surface segregation of Pd atoms was evident from the initial radial density profiles at 300 K. With an increase in temperature from 300 to 1300 K, the peaks merge for both Pd and Pt profiles (radius>7.5 Å) and become broader, indicative of the much larger movement of these atoms along the nanowire cross-section (x-y plane). Although the peaks in the inner core (radius < 7.5 Å) of the nanowire (composed mainly of Pt) also become broader at 1300 K, they remain distinct and well defined suggestive of the solid phase. Above 1480 K, we find liquid like behavior for both atoms which correspond to the homogeneous melting temperature predicted for $(Pd_{0\ 5}\text{-}Pt_{0\ 5})_{2\ 34nm}$ nanowire.

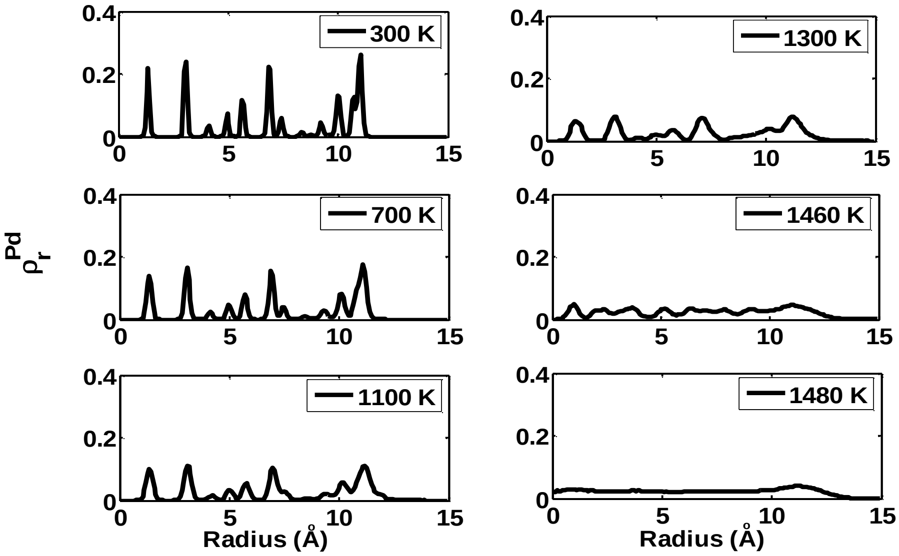

Figure 4-5. Atomic density profiles for Pd atoms along wire cross-section in $(Pd_{0.5}\text{-}Pt_{0.5})_{2.34nm}$ at temperatures leading up to melting.

It therefore appears from the atomic density profiles along the nanowire axis and radius that the onset of the melting process results from the radial movement of surface Pd atoms, with melting then proceeding inwards towards the Pt core. However, better insights into the diffusional movement of the constituent atoms in the bimetallic can be obtained by analyzing shell-based diffusion coefficients and velocity autocorrelation functions.

4.5.2.2 Shell-based diffusion coefficients

Our previous investigations of nanoclusters[140] revealed that better insights into surface melting behavior are obtained by calculating diffusion coefficients for the nanowire cross-section partitioned into radial shells of equal width, dR. The mean square displacement (MSD) calculated within each shell was used to calculate the self diffusion coefficients for atoms in that shell. The inter-atomic distance between atoms in the Pd-Pt bimetallic (2.75Å) was used as dR. The atoms were assigned to the bins based on their initial positions at the end of the equilibration period and MSD for each shell were then generated by averaging over a 200 ps trajectory with sampling done every 0.1 ps. In this work, the radial diffusion coefficient for each shell was obtained from the two dimensional (d=2) square displacement[98], for the five different shells cut across the wire cross-section:

$$D_i = \frac{1}{2d\Delta t}\left\langle \left| r_i(t+s) - r_i(s) \right|^2 \right\rangle \tag{4.3}$$

where $\mathbf{r}_i(t+s)$ is the vector position of the i^{th} atom on the x-y plane (cross-section), the average is over atoms of type i and over choices of time origin s. The diffusion coefficient calculated above reflects the mobility of the atoms along the wire cross-section and characterizes the in-plane or radial movement. Similarly, the axial or out-of-plane movement refers to mobility of the atoms in the radial shells along the wire axis (z direction) and is the one dimensional (d=1) diffusion coefficient calculated based on the axial position vector of atoms. To facilitate comparisons between the axial and radial diffusion coefficients for the same shells, their dependence on radial distance of the wire was plotted.

Fig. 4-6 shows components of the shell-based diffusion coefficients calculated in the radial and z-directions to depict the in-plane (radial) and out-of-plane (axial) movement of Pd atoms in $(Pd_{0\ 5}\text{-}Pt_{0\ 5})_{2\ 34nm}$ wire. In all the cases, we find the diffusivities of outer shells (shell 4 and 5) to be higher than those of the inner ones (shells 1-3) indicating a surface initiated melting process. Surface melting starts at ~900 K predominantly from the radial movement, as seen from the in-plane radial and axial diffusion coefficients of Pd for shells 4 and 5 (Fig 4-6 (a)). As the temperature increases to 1460 K, the atoms in shell 3 also begin to show higher diffusivities. At temperatures above the melting transition, atoms in all the shells have much higher diffusivities, which is indicative of a phase transition from solid to liquid. Similar behavior is also exhibited by Pt atoms.

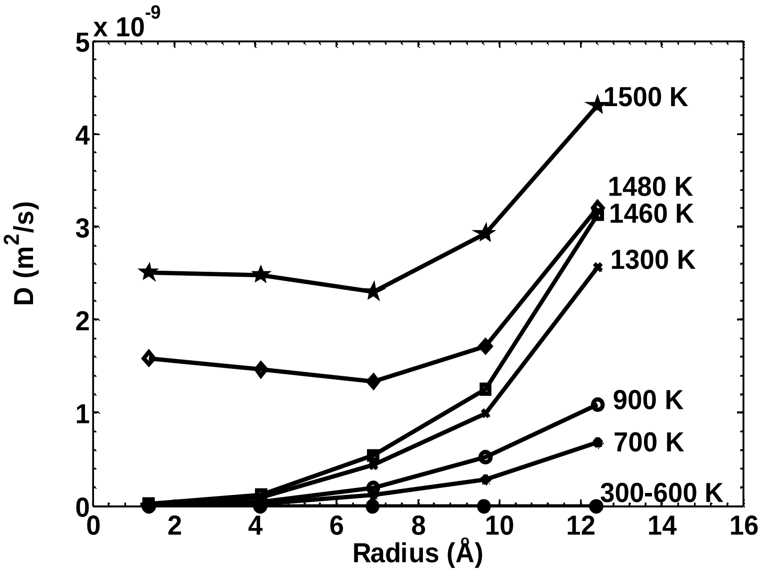

(a)

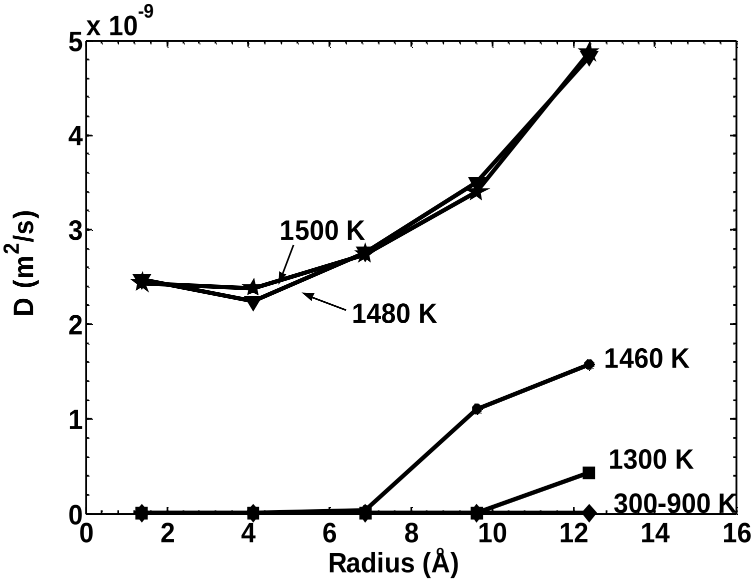

(b)

Figure 4-6. Shell based diffusion coefficients characterizing (a) radial (x-y plane) (b) axial (z direction) movement of Pd atoms in $(Pd_{0.5}\text{-}Pt_{0.5})_{2.34nm}$ nanowire.

Comparisons of Fig. 4-6 (a) with 4-6 (b) reveal that all the shells have higher radial diffusion coefficients as compared to axial below the melting point (1460 K). In the 300-600 K range, the atoms are mostly solid-like and only vibrate about their equilibrium positions. Hence, both the radial and axial components of the diffusion coefficients for Pd (Fig. 4-6) and Pt atoms (not shown) are very small. In the 700-900 K range, the radial components of the diffusion coefficients for both Pd and Pt are much larger than the corresponding axial components, especially for shells 4 and 5. Around 1300 K, shell 3 also begins to exhibit a similar characteristic. This indicates the increased tendency of the atoms to move in the wire cross-sectional directions (radial and/or tangential) than along the axis before the phase transition. At temperatures near and above the melting point, the atomic movements along both the radial and axial directions become comparable. Snapshots at different temperatures (Fig. 4-7 and 4-8) corroborate the arguments presented above and reveal the surface melting characteristics in nanowires.

Our analysis of normalized radial ($\Psi r = \langle Vr\ (t_k).Vr\ (t_k+t)\rangle$), tangential ($\Psi_\theta = \langle V_\theta\ (t_k).V_\theta\ (t_k+t)\rangle$) and axial ($\Psi z = \langle Vz\ (t_k).Vz\ (t_k+t)\rangle$) components of the velocity autocorrelation functions (Ψ) calculated for Pd and Pt atoms in $(Pd_{0\,5}\text{-}Pt_{0\,5})_{2\,34nm}$ wire for different cylindrical shells cut along wire radius at 900 K further confirm the above findings. Examination of Ψr and Ψ_θ with Ψz for both Pd and Pt atoms indicate shorter correlation time and much larger depth of minima for Ψ_θ signifying larger movement in the tangential and radial (to a lesser extent) directions than along the wire axis.

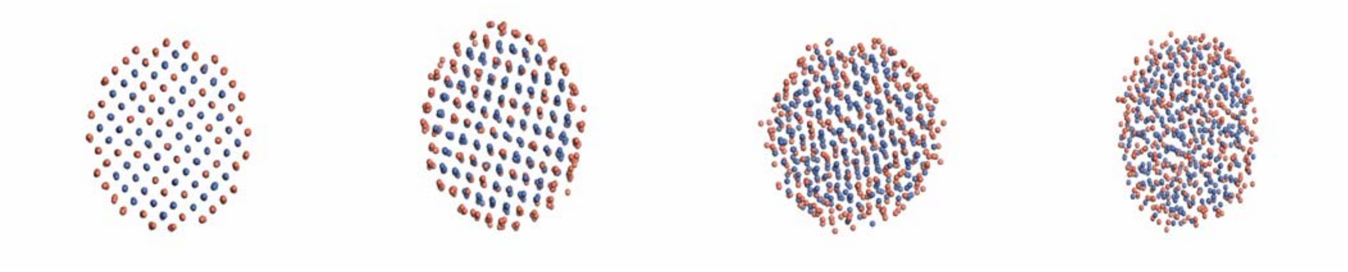

(a) **(b)** **(c)** **(d)**

Figure 4-7. Snapshots showing cross-sectional view of $(Pd_{0.5}\text{-}Pt_{0.5})_{2.34nm}$ nanowires at (a) 300 K (b) 900 K (c) 1400 K (d) 1470 K. Pd atoms are represented by light spheres (orange color), whereas dark spheres represent Pt atoms (blue color).

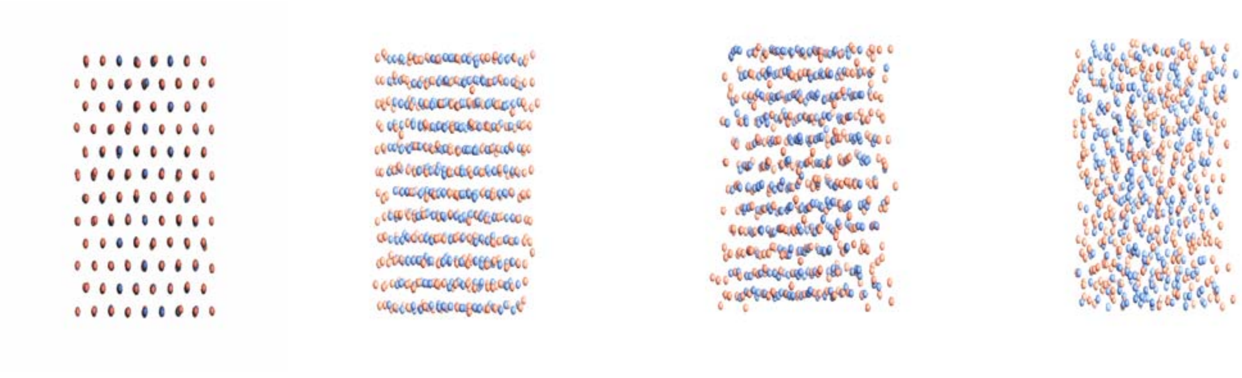

(a) **(b)** **(c)** **(d)**

Figure 4-8. Snapshots showing side (along the axis) view of $(Pd_{0.5}\text{-}Pt_{0.5})_{2.34nm}$ nanowires at (a) 300 K (b) 900 K (c) 1400 K (d) 1470 K. Pd atoms are represented by light spheres (orange color), whereas dark spheres represent Pt atoms (blue color).

4.5.3 Thermal stability of alternative starting configurations

Our simulation results indicate that the nanowires undergo structural transformation from fcc to hcp, with the transition temperature depending on the nanowire composition and diameter. To identify the most stable low-temperature solid-phase configurations for the bimetallic nanowires, alternative starting configurations have been utilized for $(Pd_{0.75}\text{-}Pt_{0.25})_{2.34nm}$ and $(Pd_{0.5}\text{-}Pt_{0.5})_{2.34nm}$ nanowires. These were hcp and fcp structures, and the annealed-solid structure obtained at the end of one heating-cooling cycle shown in Fig. 4-1. It is expected that a thermally stable starting configuration would yield a higher melting point for a given nanowire size and composition, when taken through the annealing and heating/cooling schedule described in an earlier section.

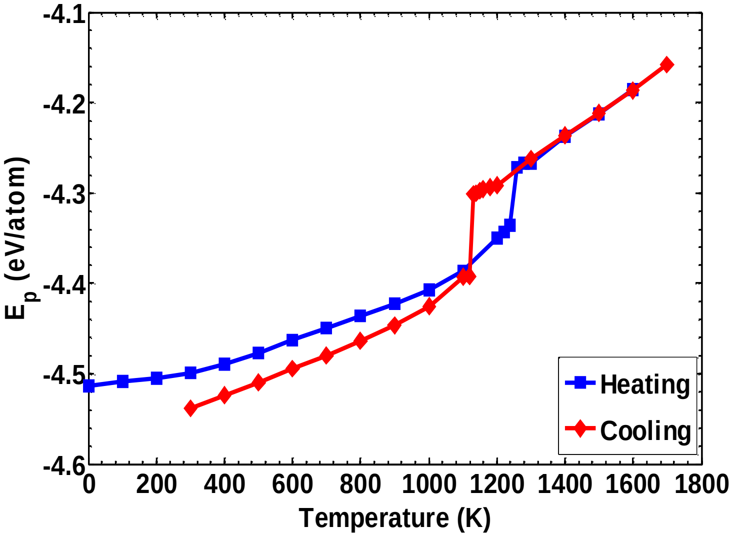

(a)

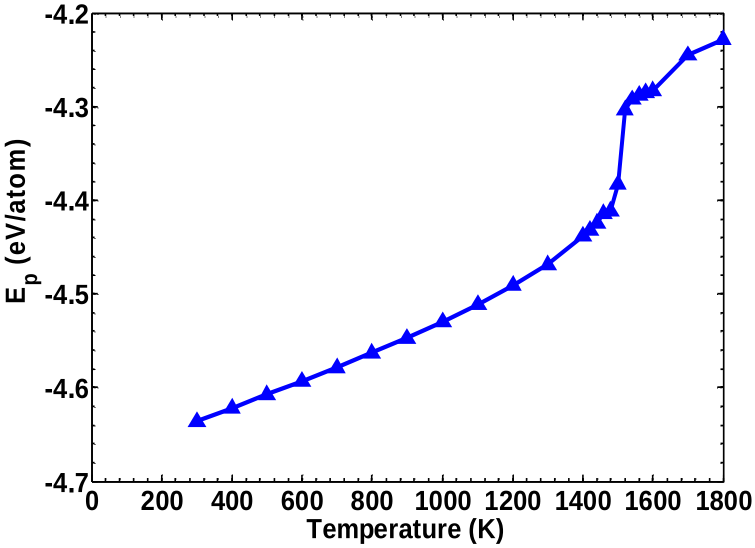

(b)

Figure 4-9. Variation of potential energy with temperature for different starting configurations of $(Pd_{0.5}\text{-}Pt_{0.5})_{2.34nm}$ nanowires (a) hcp having 712 atoms and (b) annealed-solid having 672 atoms. The solid lines with squares and diamonds represent heating and cooling of hcp wires, respectively. Solid line with triangles represents the heating of annealed-solid nanowire. The melting points for the two configurations are 1250 K and 1510 K, respectively.

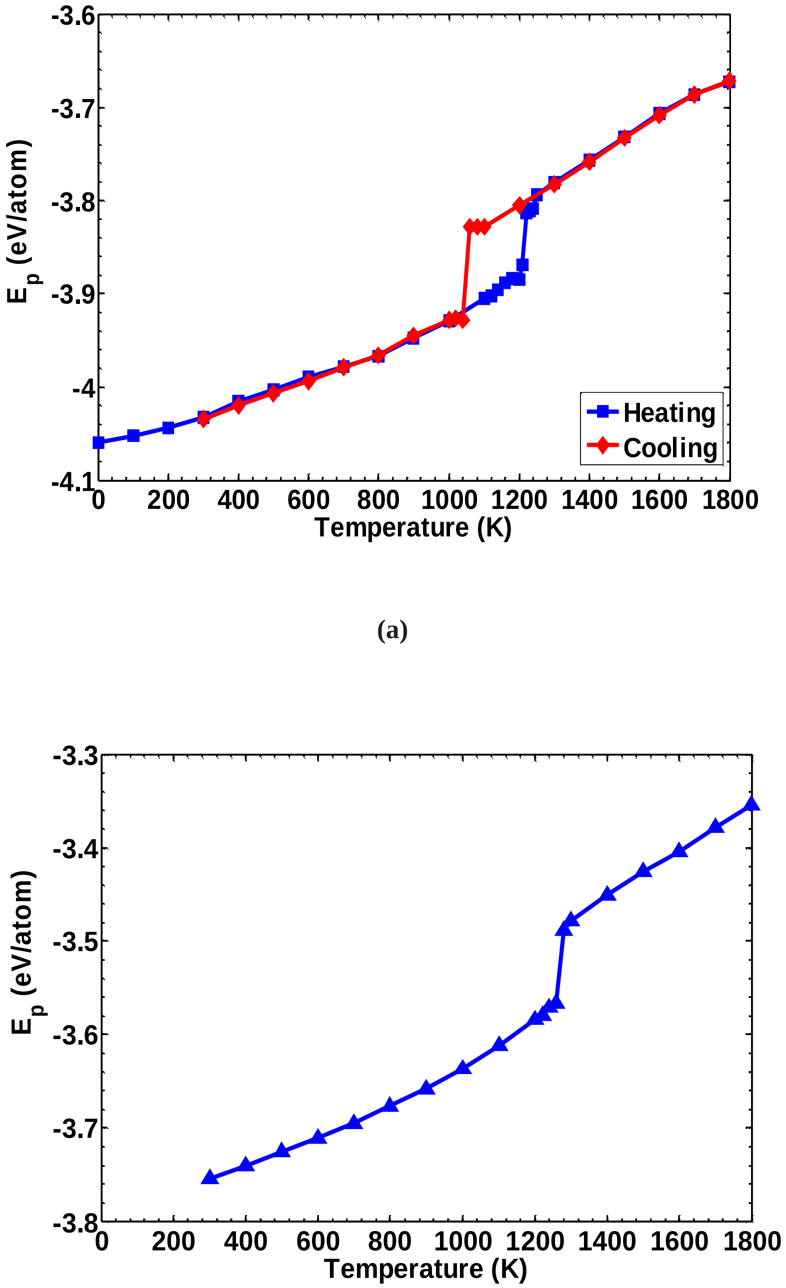

(a)

(b)

Figure 4-10. Variation of potential energy with temperature for different starting configurations of $(Pd_{0.75}\text{-}Pt_{0.25})_{2.34nm}$ nanowires (a) hcp having 712 atoms and (b) annealed-solid having 672 atoms. The solid lines with squares and diamonds represent heating and cooling of hcp wires, respectively. Solid line with triangles represents the heating of annealed-solid nanowire. The melting points for the two configurations are 1220 K and 1270 K, respectively.

Fig. 4-9 and 4-10 show the potential energy variation with temperature of the two alternative (hcp and annealed-solid) low temperature starting configurations for $(\mathrm{Pd}_{0\ 5}\text{-}\mathrm{Pt}_{0\ 5})_{2\ 34\mathrm{nm}}$ and $(\mathrm{Pd}_{0\ 75}\text{-}\mathrm{Pt}_{0\ 25})_{2\ 34\mathrm{nm}}$ nanowires. It is interesting to note the increased surface melting in case of hcp structures (Fig. 4-9 (a)) than in fcc (Fig. 4-1 (b)). For $(\mathrm{Pd}_{0\ 5}\text{-}\mathrm{Pt}_{0\ 5})_{2\ 34\mathrm{nm}}$ nanowire, the melting point of hcp configuration (1250 K) is much lower than that of fcc (1470 K) and that of the annealed-solid (1510 K). This indicates that the fcc starting configuration is more stable than the hcp for $(\mathrm{Pd}_{0\ 5}\text{-}\mathrm{Pt}_{0\ 5})_{2\ 34\mathrm{nm}}$ nanowire in the low temperature solid phase. As expected, the annealed-solid structure is closer to the global minimum, although the difference from the fcc melting point is not very large. Bond orientational order parameters of the annealed-solid structure indicate that it is closer to fcc than hcp thereby corroborating the fact that an fcc low-temperature configuration is more stable for this particular composition of nanowire.

On the other hand for the $(\mathrm{Pd}_{0\ 75}\text{-}\mathrm{Pt}_{0\ 25})_{2\ 34\mathrm{nm}}$ nanowire, there is not much difference between the melting points obtained using fcc (1230 K) and hcp (1220 K) starting configurations. The annealed-solid structure (1270 K) is only slightly more stable than the other two. Considering that the magnitude of the difference between the melting points for different configurations is less than 50 K and also the fact that the temperature fluctuations around the melting point are of the order of 20 K, it might appear that the starting configuration has no effect on the actual melting point for this nanowire composition. However, in case of fcc starting configuration, a solid-solid transition (fcc to hcp) takes place at 400 K. Bond orientational order parameters for the annealed-solid structure formed after the first round of heating-cooling cycle in Fig. 4-1 also indicate that the structure is closer to hcp type. These seem to suggest that a hcp starting configuration is more stable for $(\mathrm{Pd}_{0\ 75}\text{-}\mathrm{Pt}_{0\ 25})_{2\ 34\mathrm{nm}}$ nanowire. The low temperature fcc-started nanowire undergoes a structural transformation to hcp within the finite simulation time, indicating the possibility of a fcc-hcp phase transition at low temperatures at this composition. Combined, within the limitations of the MD techniques employed here, we conclude that the possibility of hcp structure formation in the higher Pd content alloy nanowire is higher. At least, such structures may exist over larger temperature ranges for these Pd-rich alloys. On the other hand, it is likely that the fcc structure is stable over larger temperature ranges for the Pt-rich alloys.

The cooling curves for the hcp starting configurations (Fig. 4-9 (a) and 4-10 (a)) further strengthen the arguments presented above. The energy of the cooled solid phase for $(\mathrm{Pd}_{0\ 75}\text{-}\mathrm{Pt}_{0\ 25})_{2\ 34\mathrm{nm}}$ nanowire (Fig. 4-10 (a)) is very close to the initial hcp phase whereas the same in case of $(\mathrm{Pd}_{0\ 5}\text{-}\mathrm{Pt}_{0\ 5})_{2\ 34\mathrm{nm}}$ nanowire is much lower. Analysis of the crystal structure using bond orientational order parameters for the cooled solid phase indicate a near hcp packing for $(\mathrm{Pd}_{0\ 75}\text{-}\mathrm{Pt}_{0\ 25})_{2\ 34\mathrm{nm}}$ and a near fcc structure for $(\mathrm{Pd}_{0\ 75}\text{-}\mathrm{Pt}_{0\ 25})_{2\ 34\mathrm{nm}}$ nanowires. Therefore, the possibility of hcp structure for the $(\mathrm{Pd}_{0\ 75}\text{-}\mathrm{Pt}_{0\ 25})_{2\ 34\mathrm{nm}}$ and fcc structure for the $(\mathrm{Pd}_{0\ 5}\text{-}\mathrm{Pt}_{0\ 5})_{2\ 34\mathrm{nm}}$ nanowires is indicated by these simulations. The existence of such composition dependent stability of fcc and hcp structures in nanostructures is not unusual and has been found in experimental investigations of bimetallic transition metal (Pt-Ru) alloys[141].

4.5.4 Compositional dependence of simulated phase transitions

The thermal stability of different starting configurations can be surmised from the data presented in Table 4-3. For 50% Pt composition, fcc clearly appears to be a better starting point than hcp, whereas for 25% Pt both fcc and hcp starting configurations result in approximately the same final melting temperatures. It is possible that the fcc configuration might indeed be more stable than hcp for 25% Pt at 300 K and that the limitations imposed by the finite simulation time might not have allowed the system to overcome the energy barrier for the hcp-fcc transition. Considering the fact that Pd-Pt alloys have an fcc structure in their bulk form, it is expected that an fcc starting configuration might provide reasonable insights into the simulated phase transitions in nanophase alloys. In this section, simulated phase diagram for nanowires and same-diameter nanoclusters are constructed and compared with each other as well as that of bulk Pd-Pt alloy. The starting configuration at the lowest temperature was taken as fcc for all these simulations.

Phase transitions in nanophase alloys are known to differ from those of bulk[141,142]. As discussed in the previous sections, the mechanism of surface melting in nanowires differs from that of nanoclusters and of bulk alloys[140]. The Pd-Pt nanowires of this work exhibit a two-dimensional surface melting mechanism characterized by greater cross-sectional atomic diffusion compared to that along the axis. Pd-Pt nanoclusters on the other hand, were found to undergo a three-dimensional surface melting mechanism characterized by atomic movement which is more isotropic. These differences in the thermal behavior of nanowires (Section 4.2) from nanoclusters and bulk, along with existence of fcc and hcp structures for a given composition in different low-temperature ranges (Section 4.3) might result in a simulated phase diagram which presents some features unique to nanowires.

Table 4-3. Stability of alternative starting configurations.

Starting configuration	T_m (K)		Crystal type of annealed structures at 300 K.	
	25% Pt	50% Pt	25 % Pt	50% Pt
Fcc	1230	1470	Hcp	Fcc
Hcp	1220	1250	Hcp	Fcc
Annealed-solid	1270	1510	-	-

Fig. 4-11 and 4-12 show the simulated composition dependence of transitions in 2.34 nm diameter Pd-Pt nanowires and nanoclusters, as well as in bulk Pd-Pt alloy obtained from FSnobl database[143]. An interesting feature in both the nanocluster and nanowire simulated phase transition diagrams is the existence of hcp structure at Pt compositions lower than 42% and 45%, respectively. At these compositions, the nanowires and nanoclusters undergo a solid-solid transformation from an initial fcc to a metastable hcp phase. The melting (liquidus) and the simulated fcc-hcp phase transition temperatures go through minima at a composition of 25% Pt for the nanowires. This behavior is different from that observed in same-diameter nanoclusters (Fig. 4-11 (b)) of these metals[140] as well as in bulk alloys (Fig. 4-12) which show a monotonic variation of melting (liquidus) temperature with Pt composition.

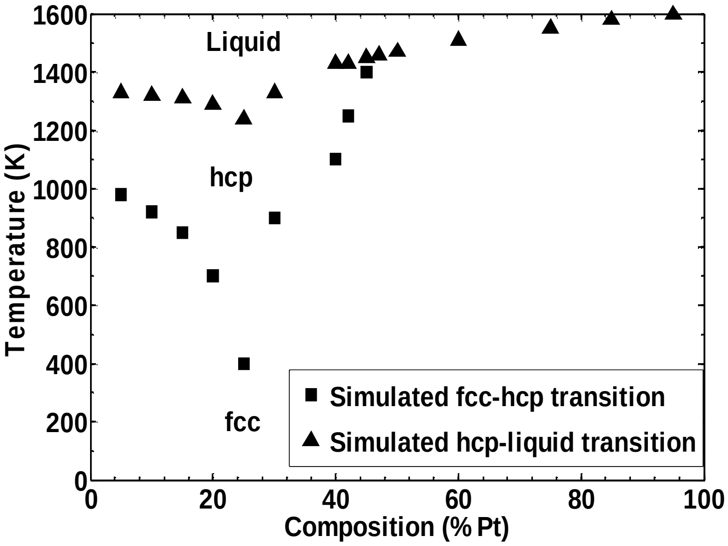

(a)

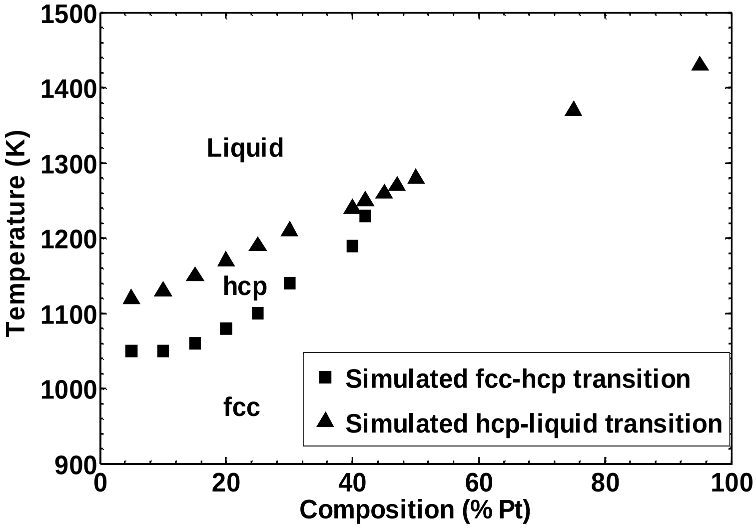

(b)

Figure 4-11. Simulated phase transition diagram for Pd-Pt alloy (a) nanowire and (b) nanocluster of 2.34 nm diameter. Squares represent simulated phase boundary for fcc-hcp transition in both wires and clusters. Triangles represent the simulated liquidus temperatures in wires and clusters, respectively. Simulations at all compositions for wires and clusters were started from an fcc structure.

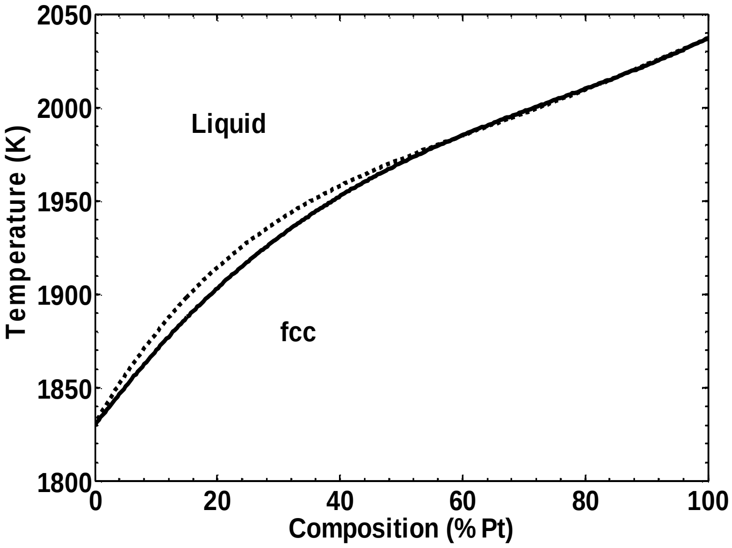

Figure 4-12. Phase diagram of bulk Pd-Pt alloy obtained from FSNOBL database. The region enclosed between the solidus (solid line) and the liquidus (dotted line) curve represents the two phase region.

Our simulation results (Fig. 4-11) indicate the absence of a sharp fcc-hcp transition for compositions greater than 45% Pt in nanowires and 42% Pt in nanoclusters. In this composition range, the fcc-hcp transformations are more continuous and hence produce no observable (sharp) change in the thermodynamic or structural properties. The nanocluster and nanowire melting process is associated with two competing processes i.e. solid-liquid (surface melting) and solid-solid transformation. The continuous transition from fcc-hcp is associated with a competing solid-liquid transition. For a given alloy composition, if the solid-liquid transition temperature is below that of fcc-hcp transition, then the melting point is reached before a complete transformation to an hcp structure might occur. The sharp fcc-hcp transition point for compositions greater than 45% Pt in nanowires and 42% Pt in nanoclusters might lie above the melting point and is therefore not seen in the simulated phase transition diagram.

There is sufficient experimental and theoretical evidence showing the existence of hcp structures in nanostructures of transition metals (Au[68], Pd[144]) as well as alloys[136,141] which otherwise have an fcc structure in bulk form. The atomic rearrangement associated with melting in finite-sized structures leads to changes in the nature of close-packing (fcc to hcp) resulting in the existence of hcp structures over temperature ranges whose widths vary with composition.

The differences in the temperature ranges over which hcp phases exist in the nanocluster and nanowire phase diagram might be attributed to the differences in the segregation characteristics arising from the different geometries (cylinder vs. sphere) as well as the differences in melting mechanisms. The proportion of surface to core sites in case of nanoclusters is greater than in same diameter nanowires. Therefore, for a given alloy composition, the extent of surface segregation of Pd atoms in case of clusters would be greater than in wires. Surface melting, which depends on the segregation profiles, would thus be affected. Additionally, the Pd-Pt nanowires exhibit a two-dimensional surface melting mechanism characterized by greater cross-sectional atomic diffusion as compared to that along the wire axis. Pd-Pt nanoclusters on the other hand, experience a three-dimensional surface melting mechanism characterized by atomic movement which is more isotropic. The differences in the segregation characteristics coupled with the differences in the surface melting mechanism appear to result in hcp phase being distributed over temperature ranges of varying widths in nanoclusters and nanowires.

We find that hcp structures for all compositions surface melt more in comparison to fcc. Therefore, the earlier the onset of the solid-solid transformation from fcc to hcp, the higher are the chances of surface melted structures being hcp and therefore, greater would be the extent of surface melting. This implies that compositions over which hcp phase exists over a broader temperature range are expected to surface melt more and have lower melting temperatures. At compositions higher and lower than 25% Pt, the wires show hcp existence over a narrower temperature range and therefore, experience reduced surface melting leading to higher melting temperatures. As a result, a non-monotonic variation of melting transition temperatures with minimum located at 25% Pt is observed in the nanowire simulated phase diagram.

4.5.5 Melting model for nanowires and nanoclusters

For nanoclusters of radius R, a melting temperature ($T_m(R)$) can be obtained phenomenologically by equating the Gibbs free energy of solid and liquid spherical clusters with the assumption of constant pressure conditions (Eq. 14 from Ref. (58)):

$$\frac{T_m^b - T_m(R)}{T_m^b} = \frac{2}{\rho_s L^b R}\left[\gamma_s - \left(\frac{\rho_s}{\rho_l}\right)^{2/3}\gamma_l\right] \tag{4.4}$$

where T_m refers to the melting temperatures for bulk (superscript b) and nanostructures (as a function of radius R), L is the molar latent heat of fusion, ρ_s and ρ_l are densities of solid and liquid phase, respectively, and γ_s and γ_l are the solid and liquid phase interfacial tensions, respectively. The melting theory developed for nanoclusters can be extended to nanowires and the depression in melting point from bulk value can be calculated using the following expression:

$$\frac{T_m^b - T_m(R)}{T_m^b} = \frac{1}{\rho_s L^b R}\left[\gamma_s - \left(\frac{\rho_s}{\rho_l}\right)^{1/2}\gamma_l\right] \tag{4.5}$$

The factor of two difference between the melting point depressions of cluster and wire arises because of the change in curvature and consequently Laplace pressure when going from a spherical cluster to a wire. Similarly geometrical considerations result in a change in the ratios of densities (2/3rd power in sphere *vs* 1/2 in wires). For small density changes between solid and liquid such as in Pd-Pt alloy, we get $(\Delta T)_{nc}/(\Delta T)_{nw}=2$ (subscript nc and nw refer to nanocluster and nanowire, respectively). For 50% Pt composition, the ratio of melting point depression of nanowires to nanoclusters from our simulations is approx. 1.4. Values for the other compositions are listed in Table 4-4. The differences between this phenomenological model and the simulated values can be attributed to the approximations made in deriving the model. The surface energy anisotropy of the solid is not taken into account and the possibility of the existence of inhomogeneous phases (liquid skin wetting the solid wire and cluster) is also neglected. Also, the segregation profiles of wires and clusters are different and may lead to varying interfacial tension values. Inclusion of the above in the phenomenological model might lead to closer agreements with the simulated values.

Table 4-4. Ratio of simulated melting point depression of wire and cluster.

Composition (% Pt)	5 %	25%	50%	75%	95%
Bulk m.p (K)	1860	1925	1970	2003	2030
Simulated $(\Delta T)_{nc}/(\Delta T)_{nw}$	1.3	1.2	1.4	1.4	1.4

4.5.6 Size dependence of melting point

The melting point of the bimetallic nanowires is known to increase with diameter. To explore the diameter-dependence of the nanowire melting temperature, simulated values are plotted against the reciprocal of diameter (1/D) for the ($Pd_{0\,5}$-$Pt_{0\,5}$) wires in Fig. 4-13.

The melting temperatures fit well to the linear dependence obtained by rearranging Eq. (4.4),

$$T_m(D) = T_m^b - \beta / D \tag{4.6}$$

where T_m^b = 2100 K represents the extrapolated melting temperature at infinite limit. The melting points calculated in the above expression correspond with the melting of the core composed mainly of Pt atoms and the extrapolated value agrees well with the bulk melting point (2090 K) of Pt calculated using Sutton-Chen potential[145]. The constant β = 1400 K nm characterizes the linear dependence of T_m on diameter (D).

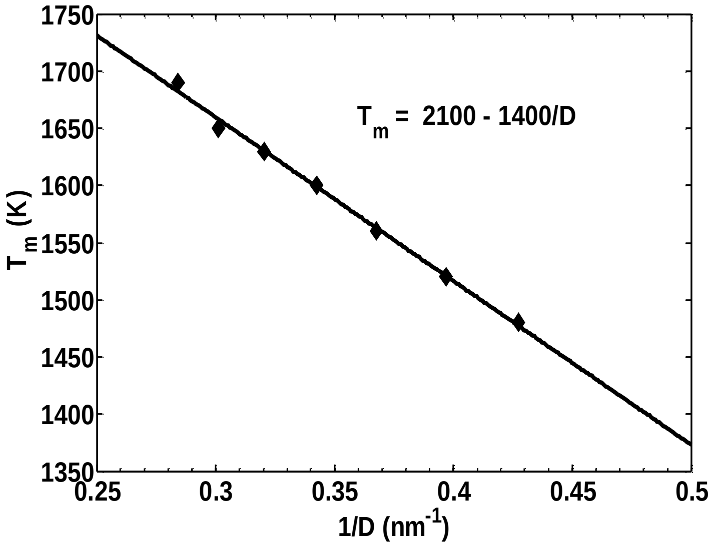

Figure 4-13. Diameter-dependence of melting temperature (T_m) for ($Pd_{0.5}$-$Pt_{0.5}$) nanowires. Solid diamonds represent the melting points of different sized ($Pd_{0.5}$-$Pt_{0.5}$) nanowires. The solid-line is a linear fit to the data showing size dependence of melting temperature in nanowires.

4.6 Conclusions

The thermal characteristics of Pd-Pt nanowires of different diameters and compositions have been investigated in the present study. The melting point is clearly identified by studying the variations in potential energy and specific heat capacity as well as structural parameter such as bond orientational order parameter. The melting points of nanowires are higher than those for nanoclusters of same diameter and composition and much lower than the bulk values. The melting behavior in nanowires is characterized by pre-melting of surface segregated Pd atoms followed by homogeneous melting of the mostly Pt core.

The melting mechanism in nanowires differs from that in same-diameter nanoclusters. Investigations into the diffusional characteristics of the constituent atoms in the bimetallic using atomic density profiles along nanowire axis and cross-section as well as shell-based diffusion coefficients and velocity autocorrelation functions suggest that the onset of surface melting of nanowires is characterized by higher in-plane or cross-sectional movement than along the axis. At higher temperatures close to the nanowire melting transition, both these movements become significant. This two dimensional melting mechanism is very different from the three dimensional one observed in same-diameter nanoclusters in which the atomic movement is more isotropic.

The simulated phase diagram of bimetallic nanowires is quite different from that of same-diameter nanoclusters as well as that of bulk Pd-Pt alloy. Nanowires undergo solid-solid transition from fcc to hcp resulting in the existence of metastable hcp phase over temperature ranges which vary with the wire composition. The observed differences in the surface melting mechanism of wires and clusters as well as the strength of the metal-metal interactions for a given segregation profile dictate the onset of solid-solid transition from fcc-hcp for a particular nanowire composition. Our simulation results indicate that phase boundaries (fcc-hcp and solid-liquid) dictated by two competing processes i.e. surface melting and solid-solid transformation are present in nanophase alloys. Although longer simulations times are necessary to establish the accuracy of the phase boundaries of various transitions, the existence of hcp structures is clearly established. The hcp phase acts as a precursor to nanowire melting. The variation of melting point with composition for alloy nanowires is non-monotonic. The extent of surface segregation as well as the type of crystal structure associated with the initiation and propagation of surface melting dictates the degree to which the surface melting occurs for a particular composition, which in turn affects the final phase transition temperature. This manifests itself in the form of non-monotonic variation of melting point with the alloy composition. The alloy phase diagram goes through a minimum at 25% Pt composition which also experiences the earliest onset of fcc-hcp transition.

On cooling, nanowires undergo a sharp liquid-solid transition and show a rather strong hysteresis leading to an annealed-solid structure. Our findings with detailed simulations of two compositions indicate that both hcp and fcc structure are suitable starting points for 25% Pt whereas fcc is a better starting configuration for 50% Pt. In both the cases, the annealed-solid structure was found to be more thermally stable than a pure fcc or hcp structure.

A melting theory developed for nanoclusters was extended to nanowires to facilitate comparisons with the same. The simulated nanowire and nanocluster melting temperatures over a range of alloy composition are in moderate agreement with the predictions of the phenomenological models. Sources of discrepancies have been discussed. A linear variation of melting point with reciprocal nanowire diameter was found. The size and composition dependence of nanowire melting temperatures are thus consistent with the available melting theories.

Chapter Five

Molecular Dynamics Simulations of the Structural and Dynamic Properties of Graphite Supported Bimetallic Transition Metal Clusters

5.1 Abstract for chapter five

Molecular dynamics simulations were carried out for Pd-Pt, Pd-Rh and Pd-Cu nanoclusters supported on a static graphite substrate using the Quantum Sutton-Chen potential for the metal-metal interactions. The graphite substrate was represented as layers of fixed carbons sites and modeled with the Lennard-Jones (LJ) potential model. Metal-graphite interaction potentials obtained by fitting experimental cohesive energies were utilized. Monte-Carlo simulations employing the bond order simulation model were used to generate initial configurations. The melting temperatures for bimetallic nanoclusters of varying composition were estimated based on variations in thermodynamic properties such as potential energy and heat capacity. Melting transition temperatures were found to decrease with increasing Cu (for Pd-Cu) and Pd (for Pd-Pt and Pd-Rh) concentrations and are at-least 100 to 200 K higher than those of the same-sized free clusters. Density distributions perpendicular to the surface and components of the velocity auto-correlation functions in the plane of the surface indicate that one of the metals in the bimetallic nanoclusters wets the graphite surface more, and that this weak graphite substrate is able to structure the melted fluid in the first few monolayers. The wetting characteristics are dictated by the delicate balance between metal-metal and metal-graphite interactions. Components of velocity-autocorrelation functions characterizing diffusion of constituent atoms in these bimetallics suggest greater out-of-plane movement, which increases with Cu (for Pd-Cu) and Pd (for Pd-Rh and Pd-Pt) concentrations. Deformation parameters showed that the core (Pd in Pd-Cu, Rh in Pd-Rh and Pt in Pd-Pt) atoms diffuse out and the surface-segregated (Cu in Pd-Cu, Pd in Pd-Rh and Pd-Pt) atoms diffuse into the nanoclusters upon melting. Near linear dependence of melting temperature on composition was found for unsupported clusters in our recent work, which results from the balance between the extent of surface melting and the radius of remaining solid core.

Non-linear dependence was found in these supported clusters, as a result of reduced surface melting at higher Pd concentrations, due to the substrate effect. Shell-based diffusion coefficients for layers perpendicular to the graphite substrate suggest surface melting to start from cluster-surface experiencing least influence of the graphite field. Surface melting was seen in all three nanoclusters with calculated bond orientational order parameters revealing the order of Pd-Cu>Pd-Pt>Pd-Rh, for onset of melting. Cluster snapshots on graphite substrate and calculated cluster diffusion coefficients indicate these nanoclusters to diffuse as single entities with very high diffusivities consistent with experimental observations.

5.2 Melting of supported nanoclusters

Metal nanoparticles exhibit physical, chemical and electrical properties that are different from those of bulk materials or single molecules.[146] The unique properties imparted to nanoparticles by the large fraction of surface atoms help them find applications in areas such as heterogeneous catalysis, sensors, and micro-electronics. The size, shape and composition of these nanoparticles are known to affect their physical and chemical properties. In sensing applications for instance, the increased surface area leads to improved sensitivity, selectivity and speed of response. As an example, Pd and its alloy nanoparticles have found use in hydrogen sensing[51,52]. Literature suggests that bimetallics exhibit superior properties in comparison to their single metal counterparts[50]. In catalysis and sensing applications, bimetallic nanoparticles supported on substrates such as alumina, ceria, carbon, quartz or lithium niobate are commonly used. The behavior of nanoclusters under the influence of a substrate is different from that of isolated nanoclusters[147-150]. The properties in these cases are not only dependent on the particle size and surface composition, but also on the surface morphology and nature of metal-substrate interaction. The key to all potential applications lies in a thorough understanding of thermal, structural and dynamic properties of these nanoparticles especially under the influence of a substrate. Recent advances in experimental techniques[151,152] as well as the insights gained by using first principles calculations such as DFT[65,153,154] have led to improved understanding of the same.

During the fabrication process, nanomaterials are subjected to chemical, thermal, and mechanical treatments which alter their surface morphology and hence their catalytic activity. A detailed study of the melting process of metal nanoclusters is useful in understanding their thermal stability[149]. The solid-liquid transition in nanoclusters differs significantly from that in bulk materials[53,59]. Both experimental and theoretical studies indicate that melting starts from the surface and propagates to the interior, with surface melting starting at temperatures significantly lower than the homogeneous transition temperature[66,155,156]. This phenomenon is a result of reduced coordination of surface sites compared to bulk atoms making them less constrained in their thermal motion. Melting at the nanoscale is known to proceed through an intermediate state at which solid and liquid state coexist (dynamic coexistence) and the structure fluctuates between solid and liquid[60]. Experimental studies and molecular simulations[151,157] give further insights into the dependence of the nanomaterial melting point on size, shape and composition. In most cases, the cluster melting point is lower than bulk melting value and is known to decrease with cluster size. The variation of melting point is not always a monotonically increasing function of cluster size, with quantum effects playing a role at smaller cluster sizes[61,69,158].

Previous studies in catalysis and sensing applications have indicated improved selectivity towards specific reactions obtained by controlling surface composition of alloys[159-161]. The alloying process leads to variations in structure and surface atomic distribution depending on nanocluster size, shape, and overall composition. At nanoscale, bimetallic nanoclusters exhibit a phenomenon known as surface segregation in which one of the metals preferentially segregates to the surface. The relative surface energy difference between the two metals dictates the extent to which segregation occurs[76,77]. Additional complexities are induced by micromixing. As a result, the melting behavior of alloys differs significantly from that of single component metal nanoclusters.

Supported bimetallic clusters are used extensively in catalysis and sensor applications, with the support used primarily to provide mechanical stability. The support also serves to spread out the metal cluster over more surface area. Recently, the bottom–up approach based on the concepts of self–organization and self–assembly of suitable nanostructures on a substrate is emerging as a viable alternative for low cost manufacturing of nanostructured materials[162]. However, substrate induced effects on nanoparticle properties are difficult to predict due to the lesser known nature of metal-substrate interactions[163].

Model catalysis studies involve deposition of transition metal clusters in sub-monolayer quantities on a substrate, with the morphology and reactivity studied by surface sensitive techniques such as STM, TDS and XPS[162]. It is expected that the substrate should mimic the properties of the support material used in real catalysis and sensing applications. However, the strong interaction of metal oxides such as TiO_2 and MgO with metal clusters makes it difficult to study experimentally[164]. An alternative is to use a relatively inert substrate such as graphite or gold so that the underlying properties of the cluster can be isolated from that of the substrate[163]. Graphite which represents the most stable allotropic form of carbon also has a relatively higher melting point compared to the nanoclusters under study. This makes it an excellent candidate for determining thermal characteristics of supported transition metal nanoclusters.

Highly oriented pyrolitic graphite substrates have been utilized to grow Pt nanoparticles using pulsed laser deposition techniques (PLD)[165]. Cluster atomic distributions characterized by STM have been used to gain insights into the growth kinetics. It is likely that the surface defects on the graphite substrate act as nucleation sites for the diffusing Pt species. Similarly, the properties of other metal clusters such as those of gold[150,152], platinum[166] and Cu-Ni[147] on a graphite substrate have been studied in the past and the metal-substrate interactions have been found to result in properties that are different from those of isolated clusters. Graphite supported cubic and tetrahedral platinum nanocrystals of 8 nm diameter were found to evolve to spherical shapes at temperatures higher than 500 ºC, with surface and total melting occurring at a slightly higher temperature[54]. Nanocluster diffusivity on surfaces plays a key role in cluster aggregation processes. Experimental studies suggest rapid diffusion of small antimony clusters on graphite substrates, a fact corroborated by molecular dynamics (MD) studies of Lennard-Jones clusters diffusing on non-epitaxial crystalline surfaces[167]. Similar MD studies conducted on 249-atom gold nanoclusters indicated high diffusivity on graphite surface[150]. The role played by substrate atoms on the thermal stability and melting behavior of nanoclusters has been studied only to a limited extent. A comprehensive understanding of the structure and dynamics of substrate supported metal nanoclusters and their effect on the melting behavior of bimetallics is desirable.

In most experimental studies, melting is characterized by changes in shape. However, shape changes are also observed when solid nanoparticles on a substrate jump from one local minimum to another making it difficult to calculate the precise transition temperature[56,149]. Experimental studies to understand the role played by a substrate on nanocluster properties are both cost intensive and sometimes difficult to perform. MD simulations offer a simple and comprehensive tool to understand the complex microscopic phenomena of segregation and micromixing, and provide insights into the role played by the substrate. In the present work, we employ MD simulations to study the properties of Pd-Cu, Pd-Rh and Pd-Pt nanoclusters of varying compositions and sizes, supported on a graphite substrate. The large available experimental data on graphite supported nanoclusters as well as the recent advances in experimental techniques[162] can help provide insights into the validity of the simulation results.

5.3 Initial configuration set-up

All the transition metals under study in this work (Cu, Pd, Pt and Rh) have an fcc structure. Hence, an fcc block/lattice of 500 atoms was constructed from an fcc unit cell by replication in the ABC direction with centre located at (0, 0, 0). The initial atomic positions of the bimetallic system were determined using Metropolis Monte Carlo (MC) simulations employing the bond order simulation (BOS) model.[76,77] The energy parameters and site energies needed for the BOS model were generated using density functional theory (DFT) by Yang[83] and the same values have been used in the present study. This approximately cubic nanocluster is supported on a graphite substrate, with the initial metal-substrate distance set to 2 Å. The graphite substrate containing 3600 atoms in two layers was built by AB type stacking to have 73.8 x 73.8 x 6.7 Å dimensions. The surface segregation phenomenon present in bimetallic nanoclusters results in lower surface energy atoms being located at low coordination number sites such as surfaces, edges, and corners. The extent of surface segregation depends on a number of factors such as difference in surface energy, mixing energy, and entropy. The final microstructure is a result of interplay among these factors[76,77]. In the present case, the segregation profile of Pd atoms is different in the three bimetallics (Pd-Cu, Pd-Pt and Pd-Rh). In case of Pd-Cu, Cu with much lower surface energy completely segregates to the surface with Pd atoms forming the cluster core. The reverse is true for Pd-Rh where Pd has much lower surface energy than Rh. Pd-Pt represents an intermediate case with more Pd atoms located at the surface than Pt, due to slightly lower surface energy of Pd than that of Pt.

5.4 Computational details

5.4.1 Pair potential function

MD simulations were performed using DL_POLY[139] to gain insights into the melting process at the atomistic level. The embedded atom potential[85] and other long range potentials like the Sutton-Chen potential[86] based on Finnis-Sinclair type of potentials have been used in the literature successfully to predict the properties of fcc-based metals such as Pd, Cu, Rh and Pt. The local electronic density is included to account for the many-body terms.

Based on the Sutton-Chen model, the potential energy of the finite system is given by,

$$U_{tot} = \sum_i U_i = \sum_i \varepsilon \left[\sum_{j \neq i} \frac{1}{2} V(r_{ij}) - c \rho_i^{1/2} \right] \tag{5.1}$$

Here, $V(r_{ij})$ is a pair potential to account for the repulsion resulting from Pauli's exclusion principle.

$$V(r_{ij}) = \left(\frac{a}{r_{ij}} \right)^n \tag{5.2}$$

The local electronic density accounting for cohesion associated with any atom *i* is given by,

$$\rho_i = \sum_{j \neq i} \phi(r_{ij}) = \sum_{j \neq i} \left(\frac{a}{r_{ij}} \right)^m \tag{5.3}$$

The Sutton-Chen potential predicts properties involving defects, surfaces and interfaces poorly. The Quantum Sutton-Chen potential[90] (hereafter referred to as QSC), includes quantum corrections and takes into account the zero point energy, allowing better prediction of temperature dependent properties. The QSC potential function was found to be better suited to melting and phase transformation studies of bulk Cu-Ni and Cu-Au alloys[67,75]. The QSC parameters for the metal atoms are listed in Table 5-1. The geometric mean was used to obtain the energy parameter ε and the arithmetic mean was used for the remaining parameters, to model the nature of interaction between metal atoms.

To represent the relatively weak interactions between the carbon atoms in the graphite substrate and an adsorbed metal atom, the LJ potential function has been used. Previous work on substrate supported metal nanoclusters indicates that the LJ potential for this interaction provides reasonable predictions of the thermal behavior of the clusters[147]. The LJ parameters (ε = 0.002413 eV, σ = 3.4 A) for graphite have already been determined in studies of small molecule physisorption, to quantitatively describe properties such as monolayer structure and phase transitions[168-171]. The LJ parameters for metal atoms were taken from Agrawal[172] and Lorentz-Berthelot mixing rules were employed to find well-depth and size parameters for metal-C interactions. These parameters are listed in Table 5-2. A static substrate with fixed positions for C atoms was used to reduce the computational load.

5.4.2 MD simulation details

The MD simulations were carried out in an ensemble approximating the canonical with a constant number of atoms N and volume V (much larger than the cluster size) without any periodic boundary conditions. A constant temperature Berendson thermostat with a relaxation time of 0.4 ps was used. The equations of motion were integrated using Verlet leapfrog algorithm[63] with a time step of 0.001 ps. The nanocluster was initially subjected to mild annealing in the 0-300 K interval. This was followed by heating to 1800 K in increments of 100 K. Near the melting point, the temperature increments were reduced to 10 K to account for the large temperature fluctuations. The simulations were carried out for 400 ps of equilibration followed by a production time of 200 ps for generating time-averaged properties.

Table 5-1. Potential parameters used in MD simulations for metal-metal interactions.

Quantum Sutton-Chen	n	m	ε (eV)	C	a(Å)
Pd	12	6	3.2864e-3	148.205	3.8813
Pt	11	7	9.7894e-3	71.336	3.9163
Rh	13	5	2.4612e-3	305.499	3.7981
Cu	10	5	5.7921e-3	84.843	3.603

Table 5-2. Potential parameters used in MD simulations for metal-graphite interactions.

LJ potentials	ε (eV)	σ(Å)
Pd-C	0.0335	2.926
Pt-C	0.04092	2.936
Rh-C	0.04072	2.898
Cu-C	0.03164	2.839

5.5 Results and discussion

The following subsections discuss identification of the nanocluster melting point and characterization of structural changes associated with the melting phenomenon for the three bimetallics at the 50% Pd representative composition. Particular emphasis is on Pd-Cu and Pd-Rh nanocluster which have contrasting segregation profiles for Pd. Dynamic properties through the nanocluster melting process and the effect of varying compositions of bimetallics on the thermal characteristics are studied and discussed. The effect of graphite support on the cluster diffusivity and melting properties is also investigated.

5.5.1 Melting point identification

The transition temperature from solid to liquid phase is usually identified from the variation in either the thermodynamic properties such as potential energy and specific heat capacity or structural properties such as bond orientational order parameters or Wigner values. The present study employs both these methods to identify melting points for different cluster sizes and compositions.

5.5.1.1 Potential energy

Fig. 5-1 shows the temperature dependence of the overall potential energy for the $(Pd_{0\ 5}\text{-}X_{0\ 5})_{500}$ atom clusters where X=Pt, Rh or Cu. The potential energy shown in Fig. 5-1 includes both the metal-substrate interactions as well as the metal-metal interaction. Our calculations indicate that the contribution of the metal-substrate interaction to the overall potential energy is at least two orders of magnitude less than that of metal-metal interaction for all the three clusters.

The transition from a solid to a liquid phase can be identified by a simple jump in the total potential energy curve. This corresponds to a melting temperature of 1390 ±10K for $(Pd_{0\ 5}\text{-}Pt_{0\ 5})_{500}$, 1590 K ±10K for $(Pd_{0\ 5}\text{-}Rh_{0\ 5})_{500}$ and 1020 ±10K for $(Pd_{0\ 5}\text{-}Cu_{0\ 5})_{500}$, as seen in Fig. 5-1. We find that at temperatures greater than 800 K for Pd-Pt, 900 K for Pd-Rh and 600 K for Pd-Cu, the metal-graphite energy decreases with temperature and undergoes a sudden decrease near the melting point. The small decrease could be attributed to the increased metal-substrate interaction resulting from the collapse of the solid structure at the melting point. The metal-metal interaction on the other hand increases with temperature. Positive deviations from linearity in the metal-metal potential energy curve indicate tendency of the clusters to surface melt. The metal-substrate energy profile follows an opposing trend in the temperature range where surface melting occurs. Therefore, the metal-substrate interaction tends to delay the onset as well as reduce the extent of surface melting in nanoclusters, thereby resulting in a delay in the final solid-liquid phase transition.

The variation of total potential energy with temperature for clusters of different compositions is discussed in subsequent sections. These melting temperatures are 100-200 K higher than those for isolated clusters of similar composition and size. Numerical comparison of the melting transition temperatures is provided later in this paper. The delay in the onset of the melting point is a result of the lesser degree of freedom for atoms close to the substrate. Influence of the graphite support on the dynamics of cluster melting will be discussed in subsequent sections.

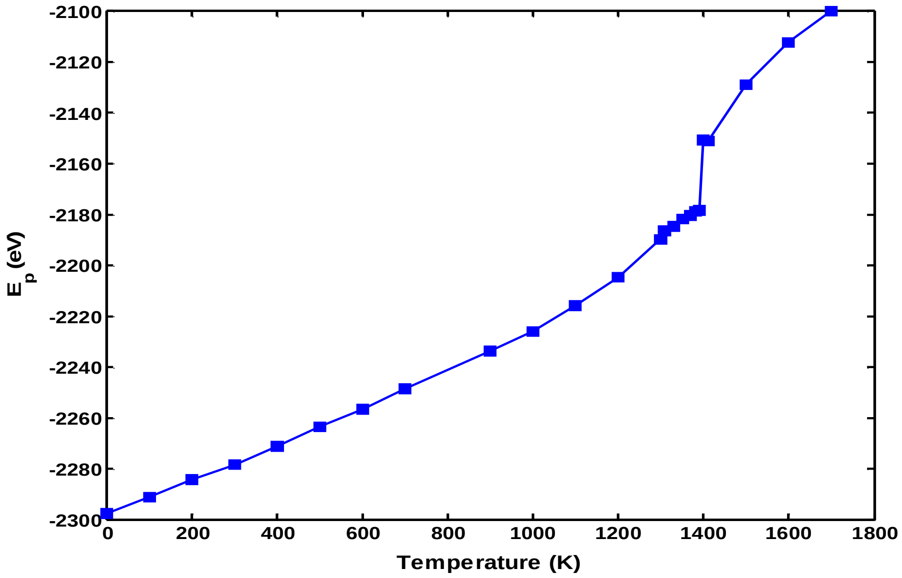

(a)

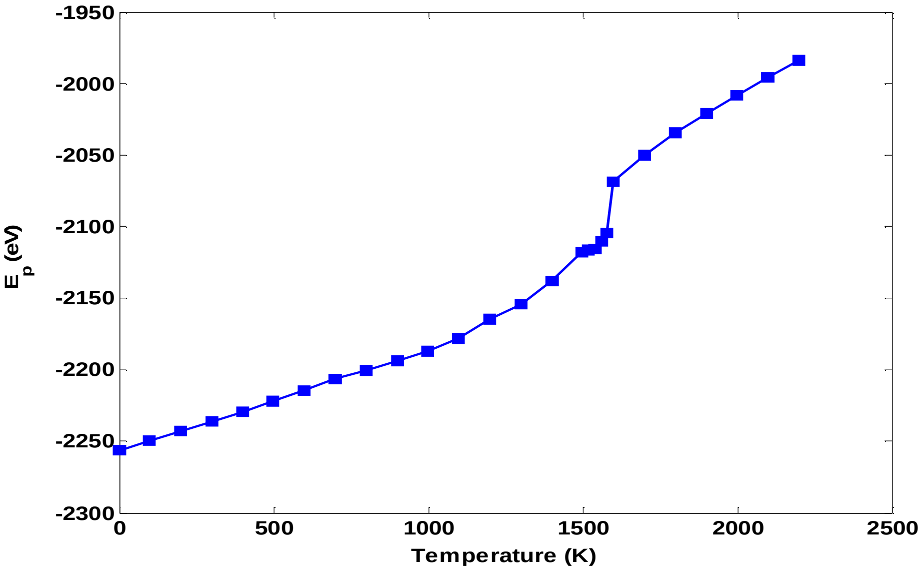

(b)

Figure 5-1. Potential energy variation with temperature for $(Pd_{0.5}\text{-}X_{0.5})_{500}$ clusters (a) X=Pt (b) X=Rh (c) X=Cu.

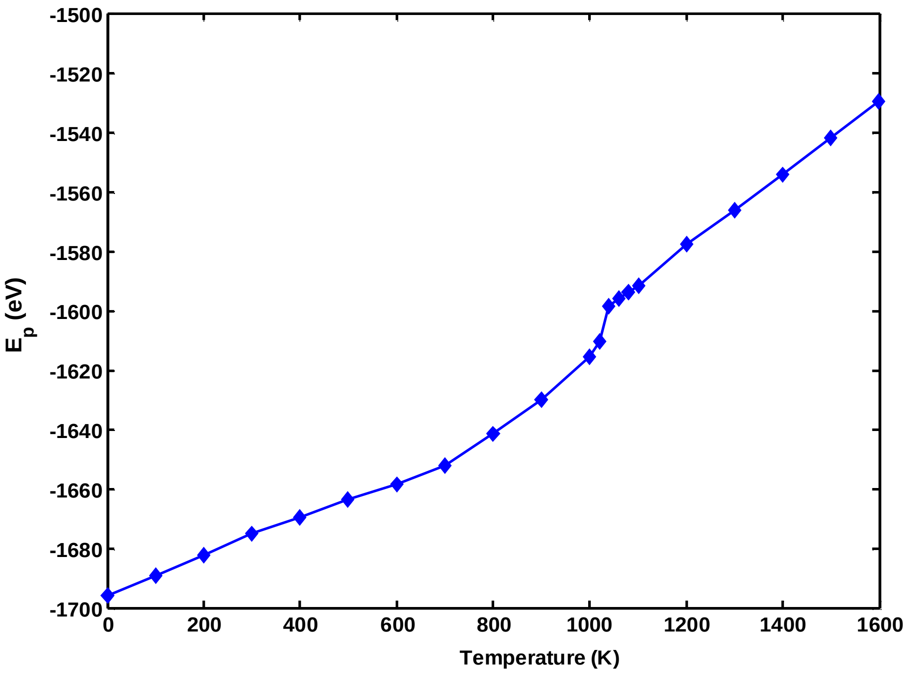

(c)

Figure 5-1: Continued

5.5.1.2 Specific heat capacity

The specific heat capacity (C_v) in a weak coupling ensemble such as achieved with the Berendson thermostat can be written as a function of fluctuations in the potential energy $<(\delta Ep)^2>$[94]. Strictly speaking, the specific heat capacity also includes the contribution arising from the ideal gas kinetic energy, which is however constant and hence has no effect on the change of C_v with temperature.

$$C_v = \frac{k<(\delta E_p)^2>}{(kT)^2 - 2\alpha <(\delta E_p)^2>/3N} \tag{5.4}$$

where $<(\delta E_p)^2> = <E_p^2> - <E_p>^2$ and α is the ratio of the standard deviations of kinetic and potential energies.

$$\alpha = \sqrt{<(\delta KE)^2 > / <(\delta Ep)^2 >} \tag{5.5}$$

Morishita has proved that a weak coupling ensemble approaches a canonical ensemble for very short relaxation times (α ≈ 0) and to a microcanonical ensemble for longer relaxation times (α ≈ 1). In the present case, the Berendson thermostat with a coupling parameter of 0.4 ps leads to $\alpha \approx 10^{-4}$, making the calculation for specific heat capacity similar to that of a canonical ensemble as given in Eq. (5.6)

$$C_v = \frac{k\left\langle (\delta E_p)^2 \right\rangle}{(kT)^2} \tag{5.6}$$

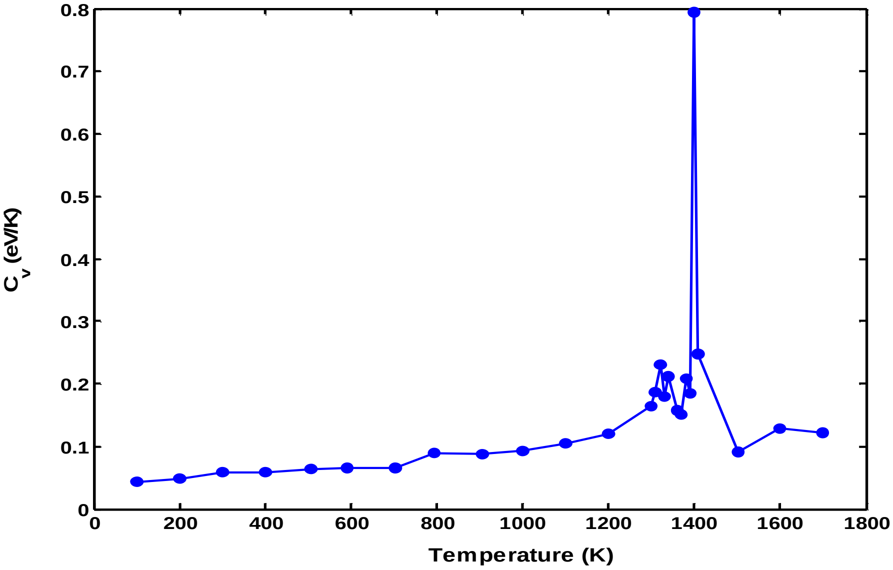

(a)

Figure 5-2. Variation of specific heat capacity with temperature for $(Pd_{0.5}\text{-}X_{0.5})_{500}$ clusters (a) X=Pt (b) X=Rh (c) X=Cu.

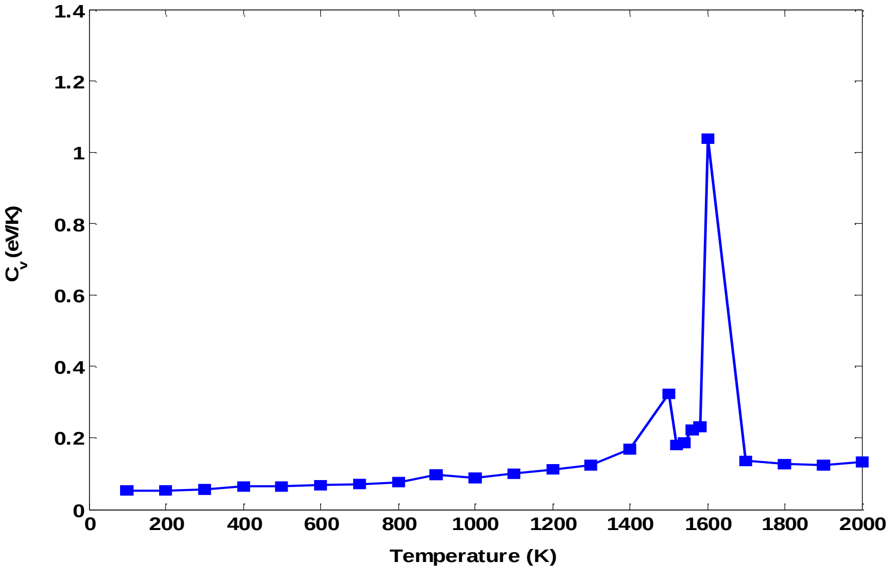

(b)

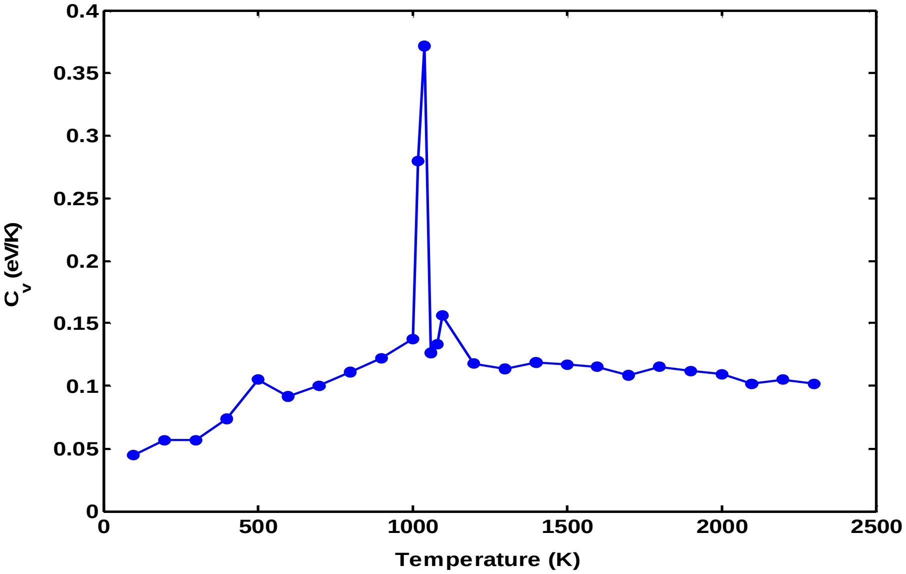

(c)

Figure 5-2: Continued

To identify the melting temperature, the specific heat capacity at constant volume is plotted in Fig. 5-2. For all three $(Pd_{0.5}\text{-}X_{0.5})_{500}$ clusters, the maximum in the specific heat capacity corresponds to the temperature where a jump in potential energy is observed. This leads to melting temperature estimates of T_m=1390 ± 10 K, 1590 K ±10K, and 1020 ±10K for $(Pd_{0\ 5}\text{-}Pt_{0\ 5})_{500}$, $(Pd_{0\ 5}\text{-}Rh_{0\ 5})_{500}$, and $(Pd_{0\ 5}\text{-}Cu_{0\ 5})_{500}$, respectively. Our calculations reveal that the metal-substrate part has little effect on the specific heat capacity of the clusters. The specific heat capacity calculated on the basis of the fluctuations in the metal-substrate energy identifies same transitions as those shown in Fig. 5-2. However, they are an order of magnitude smaller than those reported in Fig. 5-2.

The small peaks in the specific heat capacity curve at temperatures lower than the actual melting point indicate onset of surface melting. The early onset of surface melting at about 500 K in case of Pd-Cu would mean that the extent of surface melting is much more than in Pd-Pt and Pd-Rh. Indeed, experimentally based interfacial energies and crystallographic considerations suggest Cu and Pd nanoclusters to surface melt a lot more than Pt and Rh.[67,173]

5.5.1.3 Bond orientational order parameters

There are several criteria used to identify local and extended orientational symmetries. One such method is the bond orientational order parameter method[95], which is used to analyze cluster structure as well as to distinguish between atoms in solid (closed packed) and liquid environment generated at the onset of melting. The value of the global bond orientational order parameter Q_l in a solid cluster depends on the relative bond orientations and has a unique value for each crystal structure. Based on local solid symmetry, it was found that cubic and decahedral clusters have nonzero values of $q_l(i)$ for $l \geq 4$ and at $l = 6$ for those with icosahedral symmetry. All global order parameters vanish in isotropic liquids for $l > 0$. The global bond orientational order values for different types of symmetry are reported in Table 5-3.

The atoms in a solid undergo vibrations about their equilibrium positions leading to distortion of the crystal structure which is characterized by Q_4 and Q_6 values. The magnitude of the nonzero $\{Q_l\}$ values depends on the definition of nearest neighbors and can be changed by including surface bonds in the average. The cutoff distance (r_{cut}) for identifying the nearest neighbors was taken to be 3.6 Ǻ at 300 K. This corresponds to the position of the first minimum in the pair correlation function for fcc Pd-Pt. The cut-off distance (r_{cut}) at other temperatures and different clusters were similarly identified.

Table 5-3. Bond orientational order parameter values for various geometries.

Geometry	Q_4	Q_6
Fcc	0.19094	0.57452
hcp	0.09722	0.48476
bcc	0.03637	0.51069
Icosahedral	0	0.66332
sc	0.76376	0.35355
Liquid	0	0

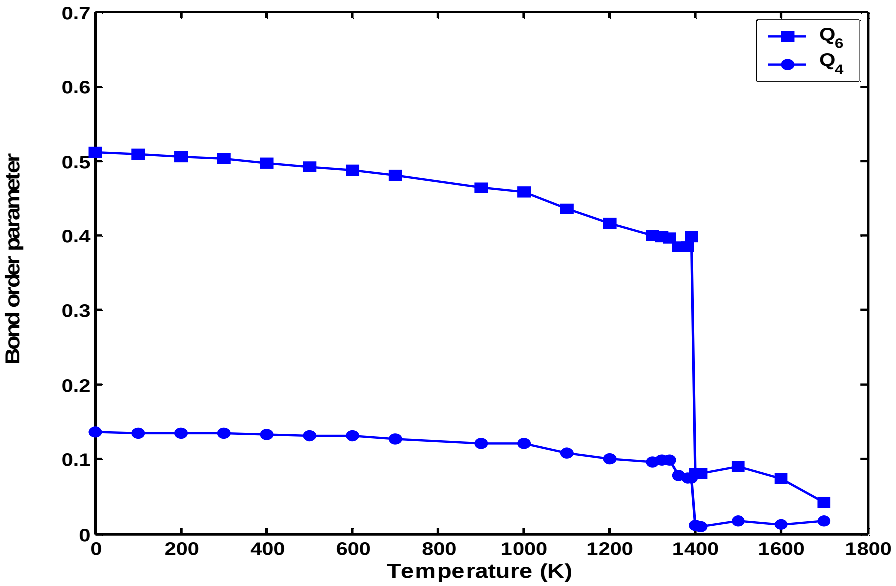

(a)

Figure 5-3. Variation of bond orientational order parameters with temperature for $(Pd_{0.5}$-$X_{0.5})_{500}$ clusters (a) X=Pt (b) X=Rh (c) X=Cu.

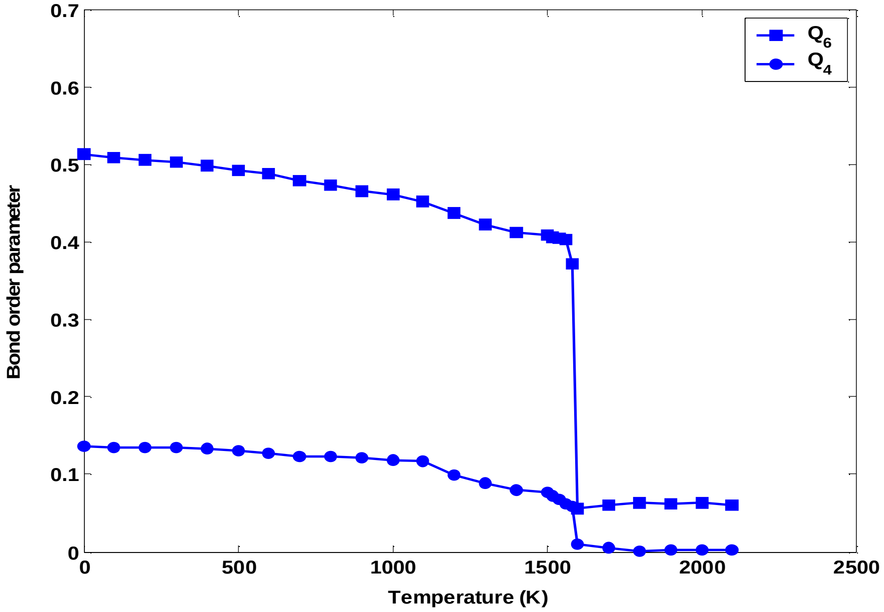

(b)

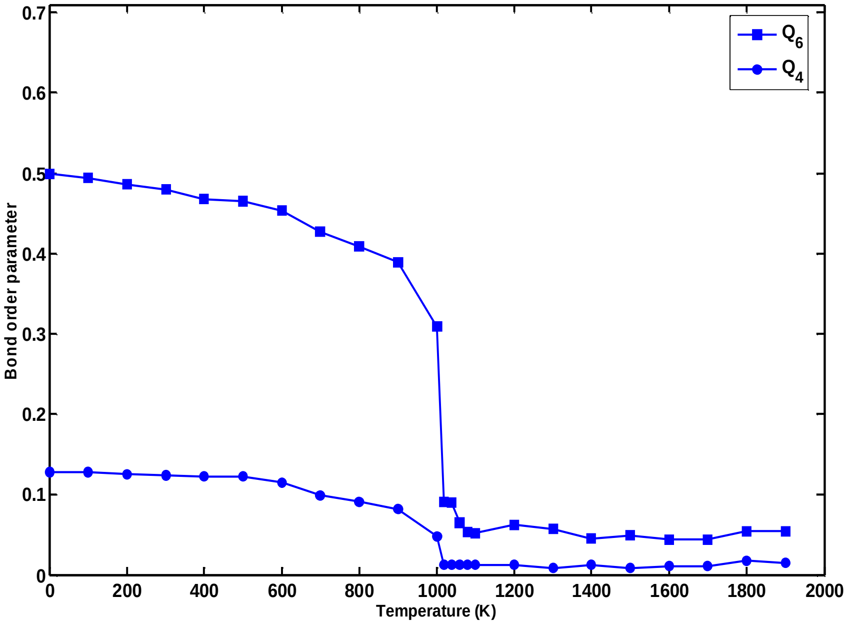

(c)

Figure 5-3: Continued

Fig. 5-3 shows the variation in bond orientational order parameter (BOP) with temperature for the three bimetallics. Comparison of Q_4 and Q_6 values for fcc with those in Fig. 5-3 indicates rapid structural rearrangement in all three bimetallic nanoclusters when subjected to annealing between 0-300K. The change in order parameters of Pd-Cu is more continuous than in the cases of Pd-Rh and Pd-Pt. The rapid structural changes in the Pd-Cu might be attributed to the early onset as well as greater extent of surface melting. Fig. 5-3 (a) and (b) indicate Pd-Rh to surface melt more in comparison to Pd-Pt. This effect is more pronounced with increasing compositions of Cu in Pd-Cu and Pd in Pd-Pt and Pd-Rh. These observations are in line with the experimental studies which suggest a surface melting order of Cu>Pt >Rh[56]. All the three nanoclusters show a transformation to a more or less hcp structure before the melting transition. At the melting point, the Q_4 order parameters of all the three nanoclusters show a sudden decrease to near zero indicating the transition from solid to liquid phase. The global order parameter Q_6 for the three clusters has non-zero values after the phase transition, which could be attributed to the layering effect of the substrate. The melting points found using these order parameters match those found using potential energy and specific heat capacity curves.

5.5.2 Structure and dynamics of cluster melting

The following subsections discuss the structural and dynamical changes associated with cluster melting. Influence of the graphite field on these properties is also discussed as is the effect of composition.

5.5.2.1 Analysis of density profiles

Fig. 5-4 shows the atomic distributions of Cu and Pd atoms, respectively, during the melting process for the $(Pd_{0\ 5}\text{-}Cu_{0\ 5})_{500}$ cluster along the z-axis, perpendicular to the surface. Sharp peaks in the density distributions of both Cu and Pd are evident below the melting transition temperature. The sharper peaks for Pd than for Cu at 900 K, a little below the melting temperature, are possibly indicative of higher mobility of Cu atoms. This conclusion is strengthened by other properties that indicate surface melting, and surface segregation of Cu atoms. The distributions for both Pd and Cu at 1020 K and 1030 K (slightly above the melting transition temperature) indicate that the weak graphite field is able to structure both Cu and Pd in the first few monolayers. This layered structuring in the first few monolayers is evident even at the much higher temperature of 2000 K, for both Cu and Pd. It appears that the bimetallic cluster can wet the graphite surface, and the observed layering effects from the graphite substrate (for clusters) are a result of the finite time of simulation. The effect of a change in the cluster composition is manifested in the form of structural changes as a function of temperature. There is higher Cu enrichment near the graphite substrate with increasing Cu composition in the bimetallic.

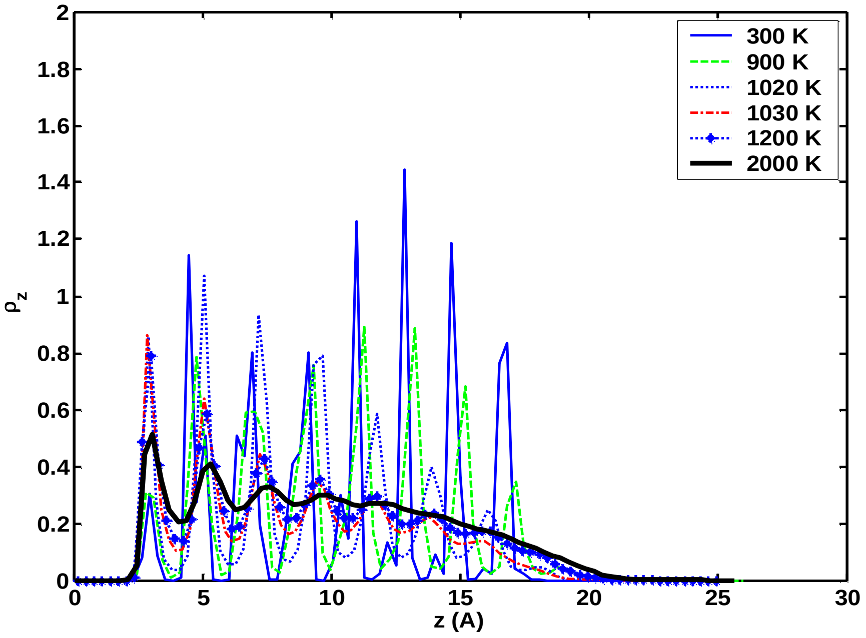

(a)

Figure 5-4. Density profile representing number density (number of atoms/volume) of atoms as a function of temperature for (a) Pd, (b) Cu from simulations of the $(Pd_{0.5}\text{-}Cu_{0.5})_{500}$ cluster.

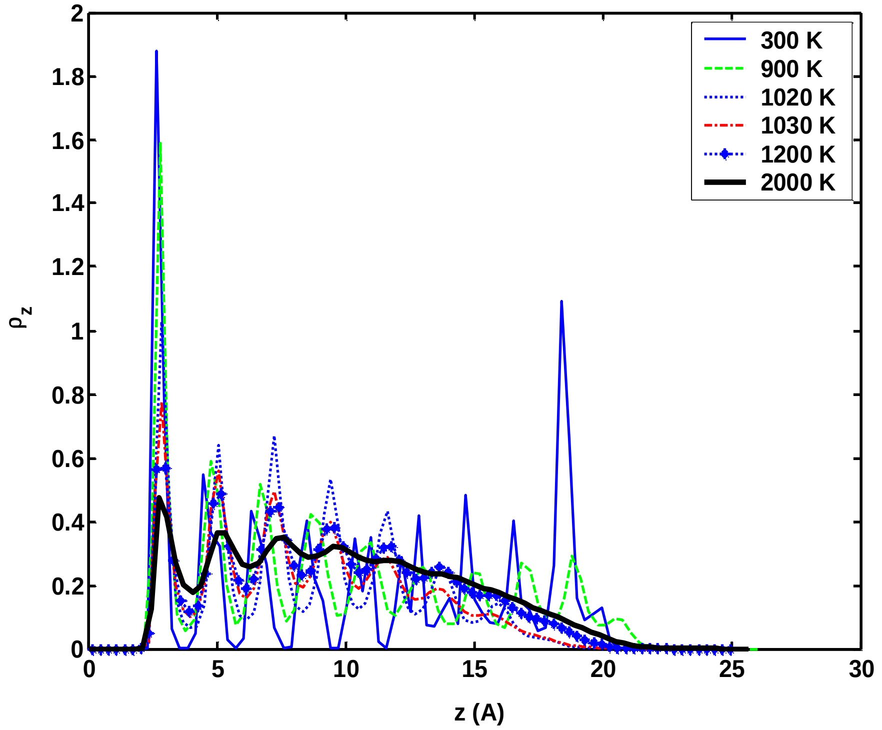

(b)

Figure 5-4: Continued

Similar wetting features are observed in the cases of $(\mathrm{Pd}_{0.5}\text{-}\mathrm{Rh}_{0.5})_{500}$ and $(\mathrm{Pd}_{0.5}\text{-}\mathrm{Pt}_{0.5})_{500}$. In both these cases, Pd with lower surface energy enriches the surface. In both cases of Pd-Pt and Pd-Rh clusters, Pd with smaller L-J well depth tends to wet the graphite substrate more. Even though C-Rh and C-Pt L-J well depth parameters are larger than that of C-Pd, leading one to expect Rh and Pt to be present at the surface more, it is the higher cohesive energy (higher melting point) resulting from a stronger Rh-Rh and Pt-Pt interactions which leads to Pd spreading on the graphite substrate and Rh and Pt retaining their hemispherical shape. This is shown for Pd-Rh in Fig. 5-5. As the percentage of Pd in the bimetallic increases, the Pd wetting phenomenon also increases. The delicate balance between the metal-metal and metal-graphite interactions determines these wetting characteristics.

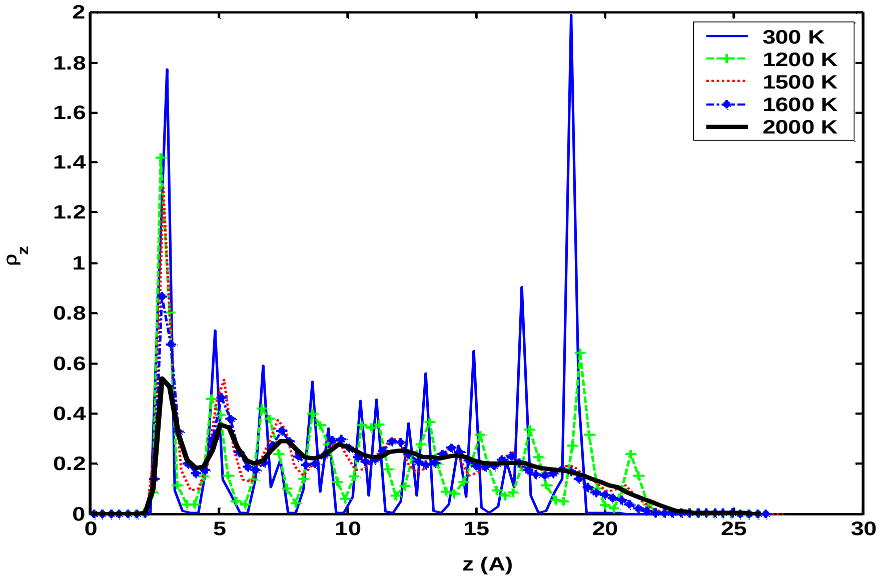

(a)

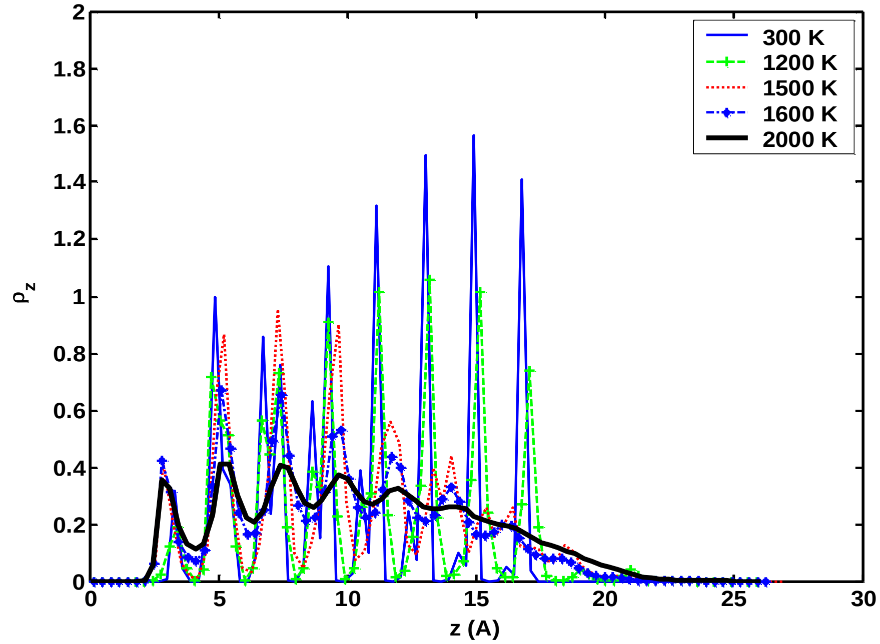

(b)

Figure 5-5. Density profile representing number density (number of atoms/volume) of atoms as a function of temperature for (a) Pd, (b) Rh from simulations of the ($Pd_{0.5}$-$Rh_{0.5}$)$_{500}$ cluster.

5.5.2.2 Deformation parameters

To explore the surface melting behavior and the associated shape changes, we use deformation parameters and shell-based self-diffusion coefficients.[140] The melting phenomenon is associated with changes in nanocluster size and shape resulting from the relative diffusion of Cu and Pd atoms. To characterize these transformations, we use deformation parameters given by,

$$\varepsilon_q = \frac{\sum_{i=1}^{N} | q_i - q_{cen} |}{N} \tag{5.7}$$

where, q_i refer to either the position coordinates of i^{th} atom in an N atom cluster along one of the three (x, y, z) directions, or the position vector **r** (x, y, z), and q_{cen} is the cluster center of mass.

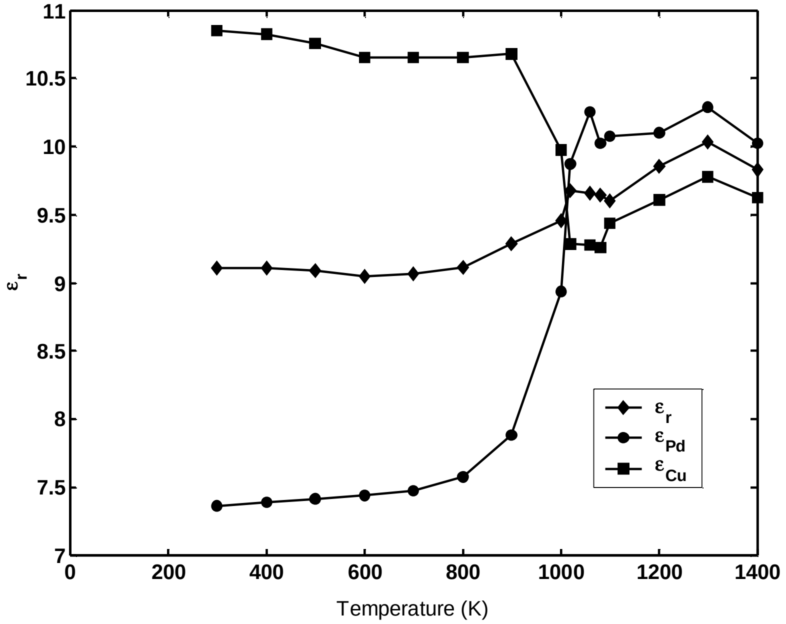

Figure 5-6. Deformation parameter for $(Pd_{0.5}\text{-}Cu_{0.5})_{500}$ at different temperatures.

Fig. 5-6 shows the deformation parameters for $(Pd_{0.5}\text{-}Cu_{0.5})_{500}$ plotted as functions of temperature. Eq. (5.8) indicates atoms with larger deformation parameter to be located farther from the cluster center of mass. As $\varepsilon_{Cu} > \varepsilon_{Pd}$ at low temperatures, the initial cluster structure is segregated with Cu atoms located at surface and cluster-core composed of Pd. Near the phase transition, ε_{Cu} decreases, whereas ε_{Pd} increases indicative of the inward diffusion of the Cu atoms and outward diffusion of Pd atoms, thereby leading to a change in the overall cluster structure. Also, the atomic composition at the metal-graphite interface changes thereby affecting the cluster diffusivity on the graphite substrate. Similar behavior is observed for Pd-Rh and Pd-Pt clusters where Pd atoms move to the interior and Rh (in Pd-Rh), Pt (in Pd-Pt) to the outside.

5.5.2.3 Diffusion coefficients

The cluster diffusion coefficient is given by

$$D = \frac{1}{6\Delta t}\left\langle \left| (r_i(t+k) - r_i(k)) \right|^2 \right\rangle \tag{5.8}$$

where $r_i(t)$ represents vector position of i^{th} atom at time t with averages taken over k time origins.

As indicated before, better insights into the surface melting process can be obtained by calculating shell-based diffusion coefficients. In the present case, insights into the effect of graphite field on the melting of different layers in nanocluster could be studied by partitioning the cluster into shells of equal width (dz) in a direction (z) perpendicular to the graphite substrate. Mean square displacements calculated within each shell were used to calculate the self-diffusion coefficients using Eq. 4.9 for atoms in that shell. The average inter-atomic distance between atoms in the bimetallic was used as dz. This corresponds to 2.66, 2.75 and 2.72 Å for Pd-Cu, Pd-Pt and Pd-Rh, respectively. The atoms were assigned to the bins (shells) based on their initial positions at the end of the equilibration period. The mean square displacements for each shell were then generated by averaging over a 200 ps trajectory with sampling done every 0.1 ps.

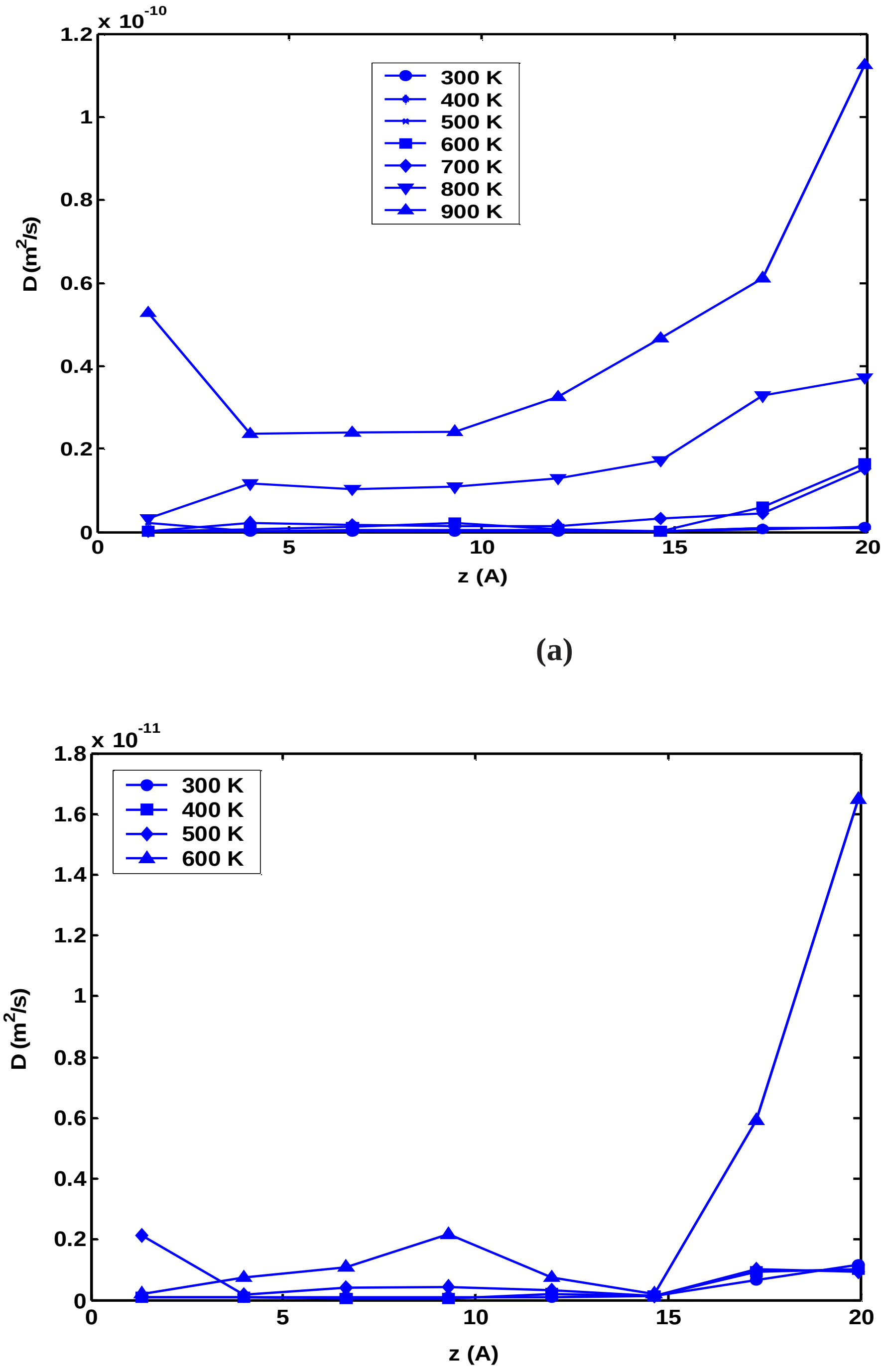

(a)

(b)

Figure 5-7. Shell based diffusion coefficients in z-direction for $(Pd_{0.5}\text{-}Cu_{0.5})_{500}$ at (a) Temperatures leading up to melting (300-900 K) (b) Low temperatures (300-600 K).

As seen in Fig. 5-7 (b), at low temperatures (300-500 K), the diffusion coefficients of different shells are nearly the same. However, as temperature increases to 600 K, the outermost shells (7th and 8th) with majority of atoms located far away from the graphite substrate, show relatively higher diffusivity. Melting clearly starts from the cluster surface. However, in case of supported clusters, it starts from the surface which experiences the least influence of the graphite field. This is evident from the much higher diffusivity of shell 8 located farthest (approx. 19.75 Å) from the graphite substrate. With further increase in temperature (800-900 K), the effect of the graphite substrate is confined to a few monolayers and more shells (5th-8th) exhibit the same behavior. Above the melting point, all the shells show relatively greater diffusivity indicative of phase transformation. Cluster snapshots taken at different temperatures corroborate the same (Fig. 5-8). Interestingly, the layer (shell 1) closest to the graphite substrate exhibits much higher diffusivity compared to 2nd, 3rd and 4th shells at 900K for this Pd-Cu cluster. This effect could be a result of increased number of Cu atoms having higher diffusivity than Pd, in shell 1 at elevated temperatures (Fig. 5-8 (e)), thereby signaling the onset of surface melting in this layer.

Similar surface melting features are observed in case $(Pd_{0.5}\text{-}Pt_{0.5})_{500}$ and $(Pd_{0.5}\text{-}Rh_{0.5})_{500}$, although the onset of surface melting takes place at slightly higher temperatures. Same size clusters richer in Pd (in case of Pd-Rh and Pd-Pt) and Cu (in case of Pd-Cu) compositions surface-melt more in comparison to others.

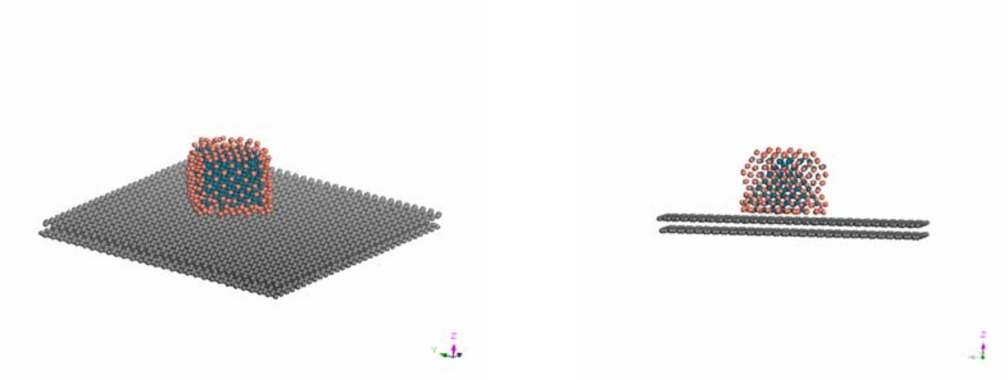

(a) **(b)**

Figure 5-8. Cluster snapshots taken at different temperatures for $(Pd_{0.5}\text{-}Cu_{0.5})_{500}$ at (a) 300K (b) 500 K (c) 600 K (d) 700 K (e) 900 K (f) 1000 K.

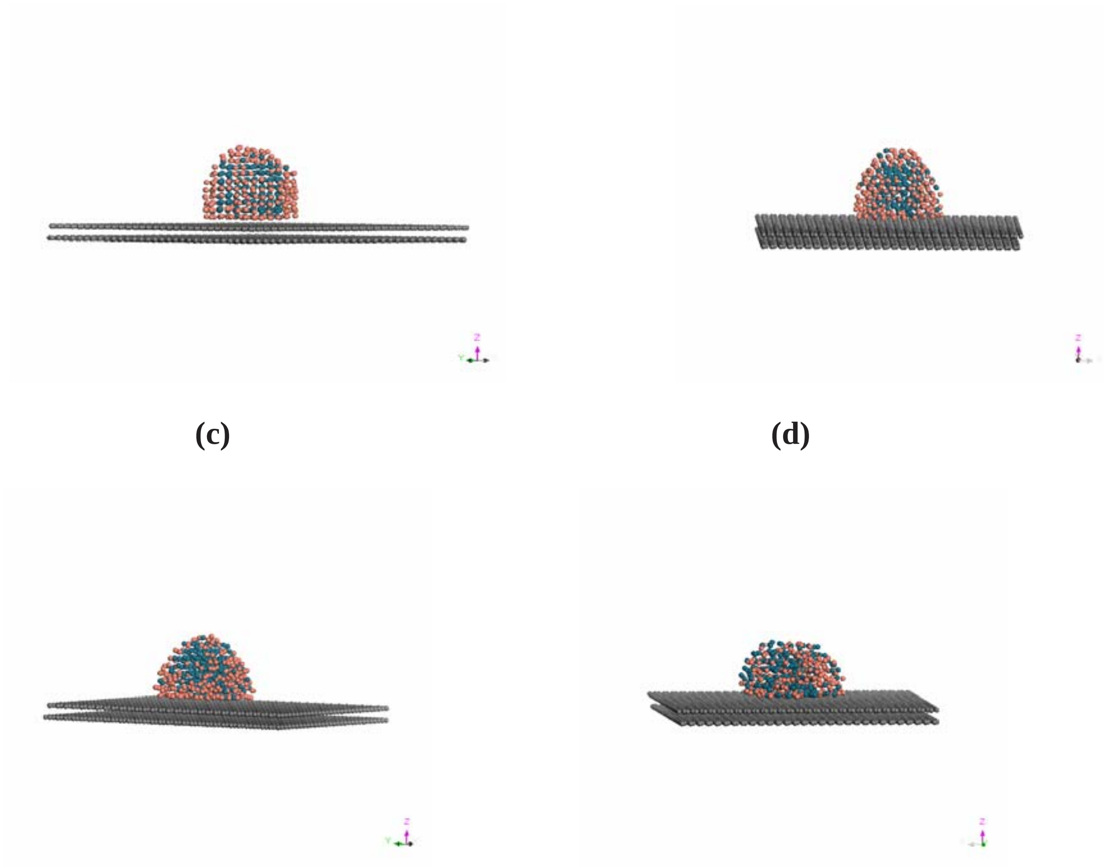

(c) **(d)**

(e) **(f)**

Figure 5-8: Continued

5.5.2.4 Velocity auto-correlation functions

Fig. 5-9 shows normalized in-plane ($\Psi r=<V_r(t_k).V_r(t_k+t)>$) and out-of-plane ($\Psi z =<V_z(t_k).V_z(t_k+t)>$) velocity autocorrelation functions (Ψ) calculated for Cu and Pd atoms for different shells along z-direction perpendicular to the graphite substrate at 900 K. The partitioning of shells has been discussed in the previous section and few shells are omitted in Fig. 5-9 for clarity. At high densities (solid phase), atoms are closely packed, causing rebounding oscillations to be more numerous than scattering collisions, and many rebounds cause Ψ to change sign. At lower densities within the cluster corresponding to the liquid phase, Ψ(t) becomes negative and passes through a minimum before approaching zero. The above arguments and Fig. 5-9 (a) and (b) suggest shells 1-3 (closer to graphite substrate) to exhibit solid like and those far away (shells 5-8) to exhibit liquid like characteristics for Cu atoms. Similarly, Pd atoms in shells 1-7 exhibit solid like characteristics and those in 8 show liquid like behavior. This suggests surface melting to start from the surface which experiences the least influence of the graphite field.

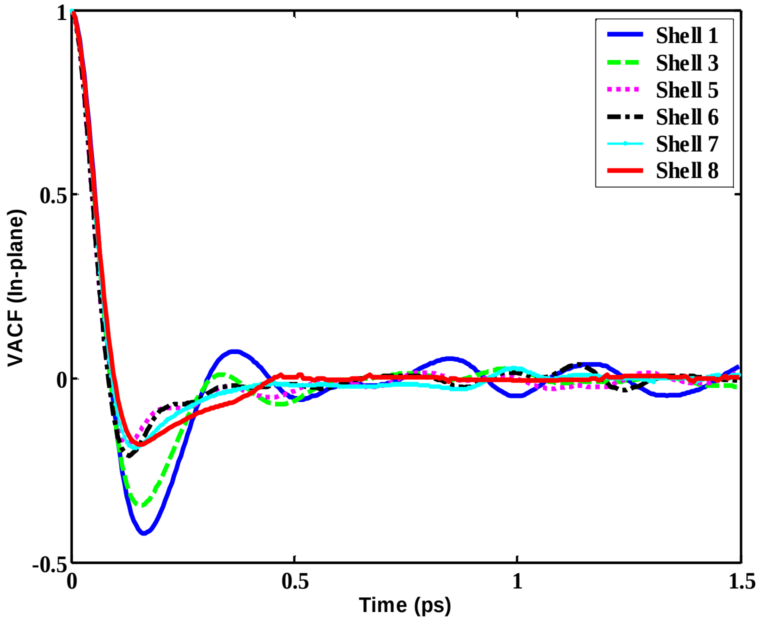

(a)

Figure 5-9. Shell based velocity autocorrelation function for Cu atoms in $(Pd_{0.5}\text{-}Cu_{0.5})_{500}$ at 900 K (a) In-plane (b) Out of plane.

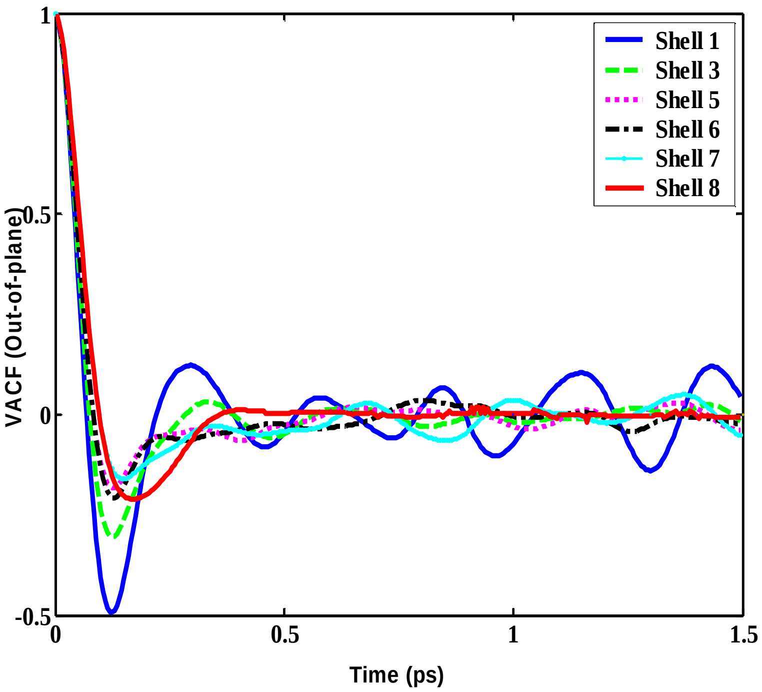

(b)

Figure 5-9: Continued

Components of velocity autocorrelation function (Ψr and Ψz) characterize the diffusion of Cu and Pd atoms at 900 K in x-y plane (In-plane) and z-direction (Out of plane) respectively. Comparison of Ψr (Fig. 5-9(a)) and Ψz (Fig. 5-9(b)) for Cu atoms, indicate shorter correlation time and much larger depth of minima for the latter signifying larger z-directional motion than in the x-y plane. The greater z-directional motion is attributed to the stronger attractive pull of the graphite field on the surface melted Cu atoms. Similar diffusion characteristics (larger z-directional motion) are also observed for Pd atoms in all shells, with most of the shells (1-7) exhibiting solid like characteristics as evident from the much higher rebounding oscillations. We find that Pd atoms in the outermost shell (Shell 8) experience less attractive pull from the graphite field than Cu atoms in the same shell. The above arguments not only corroborate the results presented in the earlier sections, but also suggest peeling off of the surface melted Cu atoms (as was evident from z-density profiles in Fig. 5-4, 5-5 and the snapshots in Fig. 5-8), thereby exposing the inner solid Pd atoms (1-7). This effect becomes more profound with increasing compositions of Cu in Pd-Cu.

The implications of such an exposure of Pd atoms on sensing applications would be discussed in subsequent sections. At still higher temperatures leading up to melting, even the shells closer to graphite substrate exhibit more scattering collisions than the rebounding oscillations suggesting a phase transformation to liquid.

In case of $(Pd_{0\,5}\text{-}Pt_{0\,5})_{500}$ and $(Pd_{0\,5}\text{-}Rh_{0\,5})_{500}$ nanoclusters, stronger metal-metal interaction results in similar behavior being observed at elevated temperatures i.e. 1300 K and 1450 K respectively. An increase in the composition of Pd in these nanoclusters results in a pronounced surface melting effect, leading to greater attractive pull on the surface melted atoms by the graphite field. The increased surface melting causes the otherwise weak graphite field to overcome the strong metal-metal interaction resulting in higher concentration of surface melted atoms (Cu in Pd-Cu, Pd in Pd-Pt and Pd-Rh) in shells closer to graphite substrate. Thus, the delicate balance between various metal-metal and metal-graphite interactions dictate the onset of surface melting as well as the diffusion characteristics (greater out of plane z-directional motion) of nanoclusters.

5.5.3 Effect of cluster composition on cluster melting point

Fig. 5-10 (a) shows the variation of melting point with composition for Pd-Pt clusters. The melting point of supported clusters is greater than unsupported clusters for all compositions. The reduced degrees of freedom of supported cluster atoms are responsible for the larger melting temperatures. While unsupported clusters exhibit a near-linear variation in melting point with composition, the supported clusters show a deviation from linearity for high Pd compositions. The near-linear variation for unsupported clusters results from the balance between the extent of surface melting and the radius of remaining solid core. At higher Pd compositions, reduced surface melting due to the effect of graphite field leads to nonlinear variation. In case of Pd-Cu and Pd-Rh nanoclusters (Fig. 5-10 (b)), increasing compositions of Pd lead to an increase and decrease in melting points, respectively. However, in both the cases, clusters rich in more surface melting metals (Cu in Pd-Cu and Pd in Pd-Rh) exhibit much higher deviation from an otherwise linear behavior.

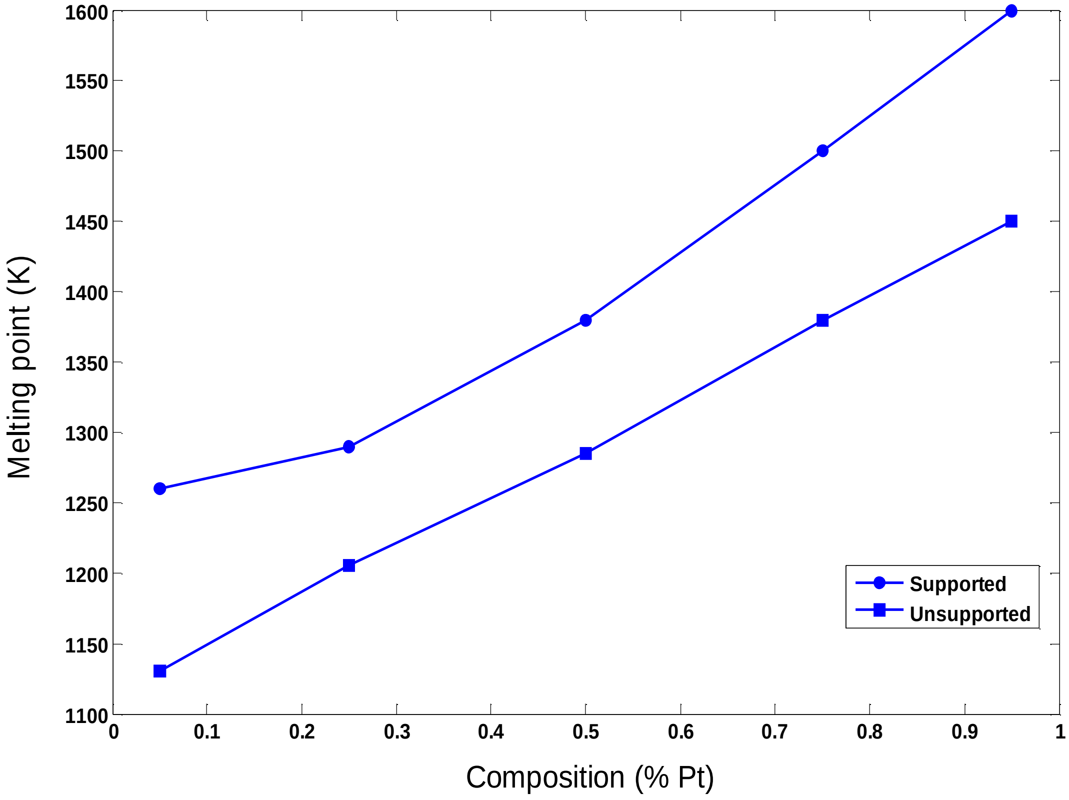

(a)

Figure 5-10. Variation of melting point with cluster composition for (a) supported and unsupported Pd-Pt clusters having 500 atoms (b) Supported Pd-Cu and Pd-Rh clusters having 500 atoms (c) Supported Pd-Pt cluster having 256 atoms.

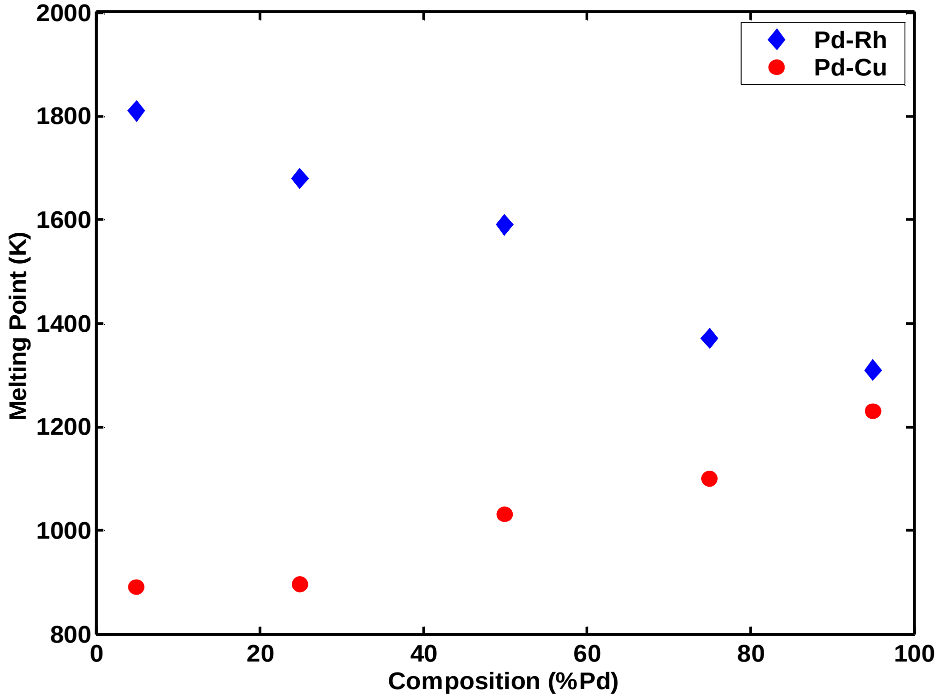

(b)

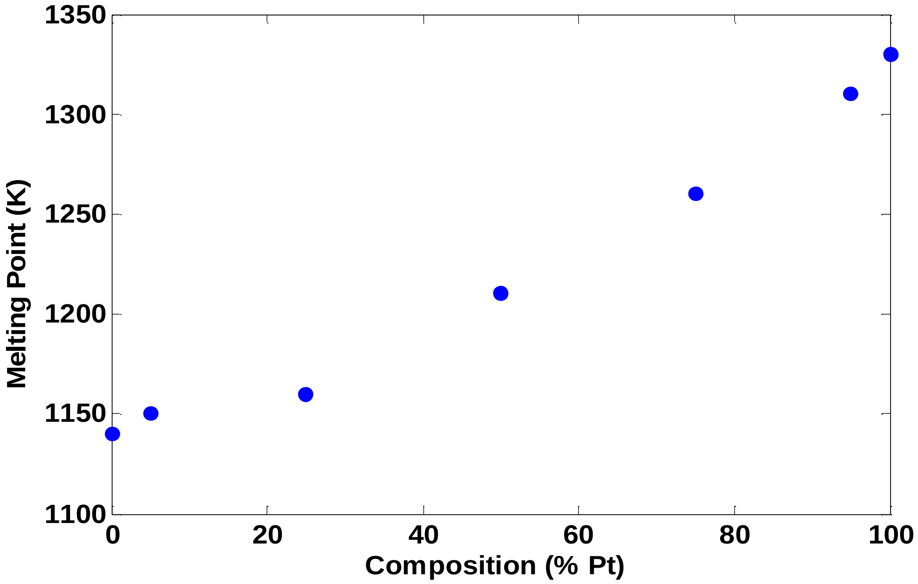

(c)

Figure 5-10: Continued

The finite size of nanocluster alloys leads to phenomenon such as surface segregation as well as surface melting which results in the phase diagram of nanocluster alloys being different from those of bulk alloys. It is interesting to note from Fig. 5-10 (a) that the difference between the melting points of pure Pd and Pt clusters correspond to 350 K and 310 K for supported and unsupported cases. This is very close to the difference between bulk melting points for Pd and Pt calculated using the same potential function (330 K)[174]. For small cluster systems, it is expected that the melting point difference should be lesser than the bulk, a fact corroborated by our simulations involving smaller sized clusters of Pd and Pt where the melting point difference is 190 K (Fig. 5-10 (c)).

5.5.4 Effect of graphite support

As indicated by the density profiles, one of the metals in the bimetallics wets the surface more, leading to enriched compositions of the same near the substrate surface. The substrate also delays the onset of surface melting, thereby, increasing the overall cluster melting temperature. When the cluster is in a surface melted state, the effect of the substrate is to pull the loosely bound surface melted atoms. The net effect is to peel off the surface layers of the bimetallic thus exposing the inner core. This effect is more pronounced at higher compositions of Cu in Cu-Pd and that of Pd in Pd-Pt and Pd-Rh clusters. Fig. 5-11 shows the time evolution of a Cu atom located at the top surface. Each interval of 200 ps corresponds to an increment of 100K starting at 300K. Thus, at temperatures much below melting (<800K), the atoms mostly vibrate about their equilibrium temperature, characteristic of solid phase. At slightly higher temperatures close to melting, larger fluctuations and movement are seen. Another striking feature is the reduction in the distance between the surface-segregated metal atom and substrate with an increase in temperature. This behavior is true for all the loosely bound surface atoms.

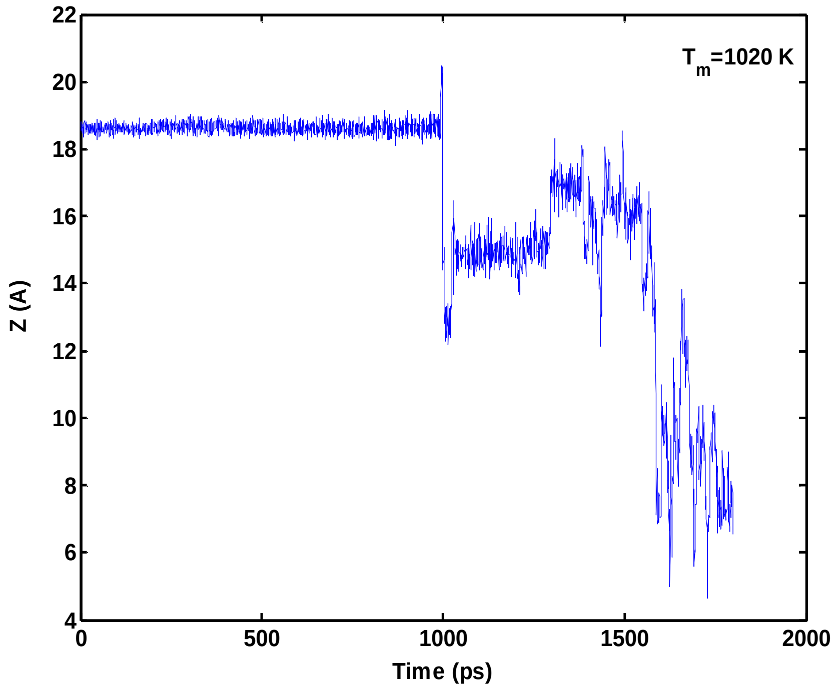

Figure 5-11. Trajectory of one such copper atom located at surface. The melting point (T_m) of the Pd-Cu cluster is 1020 K.

In case of sensor and catalytic applications, results of energetic studies using density functional theory (DFT) indicate the segregation profiles to be reversed on exposure to gases like CO[175,176], thereby reducing poisoning. However, the presence of substrate exposes the inner core of surface melted clusters. Under these conditions, poisoning gases like CO could have serious implications on effectiveness of sensors, especially at higher temperatures.

5.5.5 Cluster mobility on graphite substrate

The cluster mobility on the graphite substrate was studied by monitoring the motion of cluster center–of-mass at different temperatures over a time period of 600 ps. As seen from the cluster snapshots, the cluster diffuses as a single entity. At low temperatures, the cluster motion is restricted to less than 1 Å^2 typical of the atomic vibrations in solid phase. After phase transition, cluster movement is over a much larger area (approx. 90 Å^2). Our calculations indicate that the surface-diffusion coefficient remains low at cluster solid phase *i.e.* below 800 K and increases greatly near the cluster melting point. An increase in the composition of Cu in Pd-Cu and Pd in Pd-Rh leads to higher values of cluster diffusion coefficient, resulting in higher cluster mobility on the graphite substrate. This is attributed to the size mismatch between the metal and carbon atoms at the interface. The inward diffusion of Cu atoms into the cluster core near the melting point changes the interfacial concentration leading to changes in the cluster mobility (diffusion coefficient). The high mobility of the clusters is consistent with experimental results[167] and is likely a result of the size mismatch between the metal and carbon atoms.

5.6 Conclusions

The melting characteristics of graphite-supported bimetallic clusters have been studied using MD simulations. The melting points of bimetallic nanoclusters have been found by studying variations in thermodynamic and structural properties with temperature. In all the cases, the effect of the weak graphite support is to delay the onset of melting leading to higher transition temperatures compared with isolated nanoclusters, but still lower than bulk melting points. The delay results from the opposite trends observed in metal-graphite and metal-metal temperature-energy profiles. For all the three nanoclusters, most of the contribution to the total energy and specific heat capacity arises from metal-metal interactions. The melting temperature depends on nanocluster size and composition with the finite size of nanoclusters resulting in melting temperatures being different from bulk alloys. Our studies indicate that structural transformations occur at temperatures much below the phase transition. The graphite field causes a rapid rearrangement of atoms located close to the substrate. Bond orientational order parameters suggest a more rapid structural transformation with increasing temperatures in Pd-Cu clusters than Pd-Pt or Pd-Rh nanoclusters. This effect is more pronounced at higher compositions of Cu (Pd-Cu) and Pd (Pd-Pt and Pd-Rh clusters).

The dynamic properties associated with substrate-supported cluster melting were studied using deformation parameters, diffusion coefficients, velocity auto-correlation functions and analysis of density profiles. Components of velocity auto-correlation function characterizing diffusion of the constituent atoms in the bimetallic nanoclusters suggest greater out-of-plane movement in comparison to in-plane which increases with increasing composition of Cu in Pd-Cu and Pd in Pd-Rh and Pd-Pt. The effect of cluster composition on melting of graphite supported nanoclusters is a nonlinear variation for high Pd composition in case of Pd-Pt nanoclusters. Supported Pd-Cu and Pd-Rh clusters also exhibit similar characteristics at higher Cu and Pd compositions, respectively. The graphite support serves to reduce the extent of surface melting thereby introducing nonlinearity. The melting point differences between pure Pd and Pt supported nanoclusters decreases with cluster size. Simulated melting temperatures for bulk alloys agree well with experimental values.

Our studies indicate that wetting behavior is influenced by the weak metal-graphite, and the metal-metal interactions. Influence of the graphite field is restricted to a few monolayers of atoms and has a more prominent effect on surface melted atoms. Shell-based diffusion coefficients indicate greater surface melting in shells located farther away from the graphite substrate. We find the cluster to diffuse as a single entity on the graphite surface. All the three nanoclusters studied exhibit high diffusivities on the graphite substrate, consistent with experimental observations.

Chapter Six

Molecular Dynamics Simulation of Temperature and Strain Rate Effects on the Elastic Properties of Bimetallic Pd-Pt Nanowires

6.1 Abstract for chapter six

Molecular dynamics simulation is used to investigate the mechanical properties of infinitely long, cylindrical bimetallic Pd-Pt nanowires, with an approximate diameter of 1.4 nm and two different compositions (25 and 50% Pt). The nanowires are subjected to uniaxial tensile strain along the [001] axis. The quantum Sutton-Chen potential function is used to describe the inter-atomic potentials between the transition metal atoms. A loose-coupling thermostat (Berendson) is selected for temperature control of the simulated system, with a time constant of 25% of the total relaxation time during each strain increment. In the present simulation, these nanowires are subjected to varying strain rates of 0.05%, and 5.0% ps^{-1}, at simulation temperatures of 50 and 300 K, to study the effects of strain rates and thermal conditions on the deformation characteristics and mechanical properties of the nanowire. The rupture mechanism of these nanowires subjected to uniaxial tensile stress is explored in detail. Analyses of the changes in crystal structure associated with the wire deformation are carried out and are used to deduce mechanical properties. Comparisons to the behavior exhibited by pure Pd and Pt nanowires of similar diameter are also made.

The mechanism of stress-strain response is investigated under various loading conditions. It is found that yielding and fracture mechanisms depend on the applied strain rate as well as atomic arrangement, and temperature. At low temperature and strain rate, where crystal order and stability are highly preserved, the calculated stress-strain response of pure Pt and Pd as well as Pd-Pt alloy nanowires showed clear periodic, stepwise dislocation-relaxation behavior.

Crystalline to amorphous transformation takes place at high strain rates (5% ps^{-1}), with amorphous melting detected at 300 K. Due to higher entropy of the nanowire at higher temperature and strain rate, periodic stress-strain behavior is absent, and superplasticity behavior is observed. Deformation of nanowires at higher strain rates and low temperature, where the superplasticity characteristic is significantly enhanced, results in the development of a multishell helical structure. Mechanical properties of the alloy nanowires are significantly different from those of bulk phase and are dictated by the applied strain rate, temperature, alloy composition as well as the structural rearrangement associated with nanowire elongation. We find that the Young's modulus of both the single component as well as alloy nanowires depends on the applied strain rate and is about 70-75% of the bulk value. Ductility of the studied nanowires showed a non-monotonic variation with Pd composition at low strain rates and was significantly enhanced for wires developing and rearranging into a multishell helical structure which occurred at higher strain rates. The Poisson ratio of Pd rich alloys is 60-70% of its bulk value whereas that of Pt rich alloys is not significantly changed at the nanoscale. The calculated differences in the nanowire mechanical properties are shown to have significant effect on their applicability in areas such as sensing and catalysis.

6.2 Mechanical properties of Pd-Pt nanowires

Nanowires represent structures having multifunctional potential and have been the focus of intense research primarily due to their unusual mechanical[177], thermal[138,174,178], electrical[179] and optical[180] properties. The unique properties of nanowires result from their finite size and help them find applications in many different areas such as catalysis, sensing, microelectronics, etc. In particular, knowledge of mechanical properties of nanowires is extremely important for emerging applications in areas of nanocomposite strengtheners[181], nanoscale interconnects[182] and active components in nanoelectromechanical (NEMS) devices[183,184].

The search for nanomaterials having combinations of desirable properties such as high mechanical strength, reversible inelastic deformation, fatigue resistance and the ability to act as sensors and actuators has intensified in recent years.[185,186] Our interest lies in their application in sensing. Nanomaterial sensing layers such as Pd and its alloys are employed for chemical and biological species detection in surface acoustic wave (SAW) sensors.[52] The propagation of SAWs results in these nanowires being subjected to continual stresses. The elastic properties of these nanowires play a significant role in determining the device sensitivity and speed of response.

The Young's modulus as well as the Poisson's ratio of a material influences the speed of propagation and reflection of surface acoustic waves.[1] In sensing applications, the ratio of compressional to shear wave speed is important in inferring the device sensitivity and speed of response. This wave speed ratio depends on Poisson's ratio. Poisson's ratio also affects the decay of stress with distance, and the distribution of stress. Thus, the response of sensors utilizing nanomaterial sensing layers can be expected to be different from those utilizing thin films. Hence, knowledge of the mechanical properties of these nanowires is important to establish the stability and robustness of nanomaterial based SAW sensors.

Experimental work based on the scanning tunneling microscopy (STM) and atomic force microscopy (AFM) and related techniques have been used to study the stress-strain relationship in nanowires[187,188]. In these experiments, the tip of the STM or AFM is brought sufficiently close to the substrate at elevated temperatures and a whisker of material is drawn till it breaks. The force acting between the tip of the STM or AFM and the substrate can be measured and the resulting high resolution stress-strain plots can be analyzed to understand the mechanical behavior of these wires. It has been found that the properties strongly depend on the temperature, nature of the material involved as well as the dimensions of the sample. In one such study, the diameter dependence of mechanical properties such as Young's modulii of individual tungsten oxide (WO_3) nanowires, directly grown onto tungsten scanning tunneling microscopy tips, was carried out using a custom-built in situ transmission electron microscopy (TEM) measurement system.[189] Recently, the atomic aspects associated with Au-Ag alloy nanowire thinning during mechanical stretching have also been experimentally investigated using high resolution transmission electron microscopy by Bettini et al.[190]

Computer simulations such as molecular dynamics (MD) represent a form of numerical experiments which can be used to complement laboratory studies based on STM or AFM.[191-193] Atomistic simulations at the nanoscale have shown that surface stresses and crystallographic orientation play a dominant role in determining material properties[194,195]. The effects of intrinsic surface stresses have been found to endow nanowires with extremely high yield stresses and strain[196,197], as well as yield strength asymmetry in tension and compression. Similarly, crystallographic orientations have been shown to have a direct, first order effect on the deformation mode in fcc nanowires.[198]

Most of the MD simulations to calculate mechanical properties have focused on single component metals. In particular, analysis of tensile failure modes in metal nanowires under different orientations has received greater attention. Wen et al. studied the structure and properties of Ni nanowires.[199] Koh et al. studied temperature and strain rate effects on solid platinum nanowires subjected to uniaxial tension.[200] Several such studies on gold nanowires are also available[201-203]. These demonstrate the ability of gold nanowires to form single atomic chains under tensile loadings. Stress driven phase transformation from fcc to bct (body-centered tetragonal) in gold nanowires was observed by Diao et al.[177,204] Similarly, stress induced phase transformation in inter-metallic Ni-Al nanowires was reported by Park.[205] Shape memory and pseudo-plastic behavior were observed in single crystalline monatomic fcc nanowires.[206] Gonzalez et al. studied structural and quantum conductance properties of atomic size Cu nanowires generated by mechanical stretching.[207] Recently, Cao et al. have investigated the differences in the mechanical behavior of Cu fcc nanowires and those with five fold twinned structures.[208] Ikeda et al. used Finnis-Sinclair potentials to study strain induced amorphization in Ni and Ni-Cu alloys.[209]

Although many studies have focused on single component systems such as gold, nickel and copper nanowires, few studies have been dedicated to the study of mechanical properties of alloy nanowires. Complex phenomena such as surface segregation and micro-mixing occur in alloys of finite-sized structures such as nanowires.[76] For a given composition of the bimetallics, the microstructure is dictated by surface energies and mixing energies of the constituent atoms. Atoms with lower surface energies tend to segregate to low coordination number sites, the extent of which is determined by the interplay between surface energies, mixing energies and entropy. Our prior investigations of the thermal properties of these nanowires indicate a composition and temperature dependent solid-solid phase transformation from fcc to hcp structures. The preferential movement of atoms along the nanowire cross-section than along the wire axis led to the occurrence of these transformations. Such transformations can result in the failure modes of alloy nanowires that are different from single component wires. Further, in view of the available experimental and theoretical evidence suggesting the dependence of mechanical properties on alloy composition and nanostructure; we are motivated to study the elastic properties of bimetallic nanowires.

In the present work, we study the effect of strain rate and temperature on the mechanical properties of bimetallic Pd-Pt nanowires using MD simulations employing quantum Sutton-Chen potential function[87] for two representative Pd compositions *viz* 25% and 50% Pt.

6.3 Initial nanowire size and configuration

Transition elements such as Pd and Pt exhibit an fcc structure in the bulk solid phase. A large block of fcc was formed from a fcc unit cell by replicating it in ABC directions. Using various cutoff radii, cylindrical structures representing nanowires of different diameters (D) having approximately 1.4 nm were created. The nanowires were modeled as infinitely long wires by the application of periodic boundary condition along the wire axis. By choosing different length/diameter ratios, it was ensured that the results were not influenced by the periodic boundary conditions for the simulated infinitely long nanowires.

In order to identify the initial atomic positions of the constituent atoms for a given bimetallic composition, these structures were subjected to a Metropolis Monte-Carlo simulation employing a bond order simulation (BOS) model[76,77], to generate the minimum free energy initial configuration which was subsequently used for studying the stress-strain response. The BOS model has been tested over a range of bimetallics and comparisons with experimental data reveal close agreement with the microstructure predicted by the BOS model. Although Monte-Carlo simulations employing Sutton-Chen potential have also been used to predict the global minima of transition metal clusters, our calculations indicate that the equilibrium structures obtained using BOS model are more energetically stable compared to those obtained using Sutton-Chen potential model[140]. Although there are slight differences in the segregation profiles obtained using the BOS and Sutton-Chen potential model, we find that the initial stresses generated in the simulations under high and low strain rate conditions, using the minimum energy configuration obtained from Sutton-Chen potential, are not very different from those obtained using configurations generated utilizing BOS model.

The stable configurations or nanostructure generated in the above simulations consisted of surface segregated structures with lower surface energy Pd atoms occupying lower coordination number sites and therefore preferentially locating themselves at the surface. The core comprised mainly of high surface energy Pt atoms. These surface segregated nanowires were then subjected to uniaxial tensile stresses using molecular dynamics simulations for evaluating their mechanical properties (Fig. 6-1).

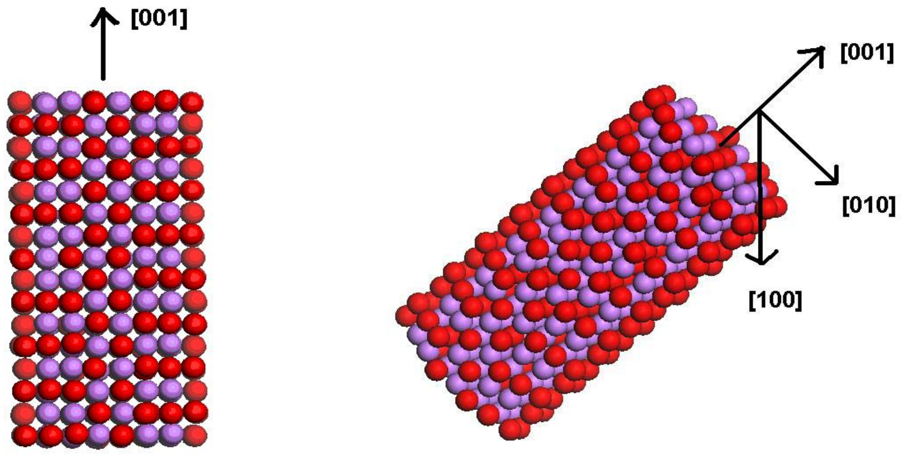

Figure 6-1. ($Pd_{0.5}$-$Pt_{0.5}$) nanowire having 16 atomic layers (416 atoms) in its initial unstressed state. Pd atoms are shown in red and Pt atoms in purple.

6.4 Computational details

Molecular Dynamics (MD) simulations using DLPOLY[139] were performed to gain insights into the mechanical properties at the atomistic level. All the properties were obtained as time averages over the particle positions and velocities. The embedded atom potential[85] and other long range potentials such as the Sutton-Chen potential[86] based on Finnis-Sinclair type of potentials have been used in the literature successfully to predict thermal and mechanical properties of fcc based metals such as Pd and Pt. The local electronic density is included to account for the many body terms in these potentials.

6.4.1 Potential function

Based on the Sutton-Chen potential, the potential energy of the finite system is given by,

$$U_{tot} = \sum_i U_i = \sum_i \varepsilon \left[\sum_{j \neq i} \frac{1}{2} V(r_{ij}) - c\rho_i^{1/2} \right] \tag{6.1}$$

Here, V (r_{ij}) is a pair potential to account for the repulsion resulting from Pauli's exclusion principle.

$$V(r_{ij}) = \left(\frac{a}{r_{ij}} \right)^n \tag{6.2}$$

The second term in Eq. (6.1) represents the metallic bonding energy associated with the local electron density (ρ_i) given by,

$$\rho_i = \sum_{\substack{j=1 \\ j \neq i}}^{N} \left(\frac{a}{r_{ij}} \right)^m \tag{6.3}$$

The Sutton-Chen potential poorly predicts properties involving defects, surfaces and interfaces. The quantum Sutton-Chen potential[87] (hereafter referred to as QSC), includes quantum corrections and takes into account the zero point energy allowing better prediction of temperature dependent properties. The QSC parameters for the Pd and Pt are listed in Table 6-1. The geometric mean was used to obtain the energy parameter ε and the arithmetic mean was used for the remaining parameters, to predict the nature of interaction between Pd and Pt.

Table 6-1. Potential parameters used in MD simulations of Pd-Pt nanowires.

Quantum Sutton-Chen	n	m	ε (eV)	c	a(Å)
Pd	12	6	3.2864e-3	148.205	3.8813
Pt	11	7	9.7894e-3	71.336	3.9163

Differentiating Eq. (6.1) with respect to r_{ij}, the total force of the system is given by:

$$F_{QSC} = -\frac{\varepsilon}{r_{ij}} \sum_{j \neq i} \left[n\left(\frac{a}{r_{ij}}\right)^{n} - \frac{mc}{2}\left(\rho_i^{-1/2} + \rho_j^{-1/2}\right)\left(\frac{a}{r_{ij}}\right)^{m} \right] \hat{r}_{ij} \tag{6.4}$$

In the above expression, $\hat{r}_{ij}$ is the unit vector representing inter-atomic distance between atoms *i* and *j*.

6.4.2 MD simulation details

The MD simulations were carried out in an ensemble approximating the canonical with a constant number of atoms N and volume V with periodic boundary condition applied along the nanowire axis. The equations of motion were integrated using the velocity-Verlet algorithm.[63] The atomic velocities were scaled to the simulation temperature using the Berendsen thermostat.[91] The simulated strain rate is given as:

$$\dot{\varepsilon} = \frac{\Delta\varepsilon_{zz}}{N_{step}\Delta t} \tag{6.5}$$

where, $\varepsilon_{zz} = \frac{L_z(N_{step}) - L_z(0)}{L_z(0)}$ represents the nominal strain of the nanowire at each time-step. The strain increment at each step was fixed at 0.5% per increment. The number of relaxation steps (N_{step}) was fixed at 10000. By varying the time-step of the simulation (Δt) from 0.01 fs to 1 fs, different strain rates ranging from 5% ps^{-1} to 0.05% ps^{-1} were simulated. For a 3 nm nanowire length, these strain rates correspond to approximate stretch velocities of 1.5 and 150 m/s, respectively. The Berendsen thermostat with a coupling constant of τ=0.025, 0.25 and 2.5 ps was used for the respective strain rates. These resulted in modest temperature fluctuations, which lead to correct canonical averages of the system properties. The system properties during each strain increment were computed by averaging over the final 2000 steps. The axial stress was computed as the arithmetic mean of the local stresses on all the atoms:

$$\sigma_{zz}(\varepsilon) = \frac{1}{N\Omega^i} \sum_{i=1}^{N} \sum_{\substack{j=i \\ j \neq i}}^{N} F_{ij}^z(\varepsilon) r_{ij}^z(\varepsilon) \tag{6.6}$$

In the above equation, F_{ij}^z represents (001) component of the pair-wise inter-atomic force between atoms *i* and *j*, obtained from Eq. (3.6). Ω^i refers to volume of atom *i* and $r_{ij}{}^z$ represents inter-atomic distance along the (001) direction between the *ij* pair. The stress-strain responses (Eq. (6.6)) as well as elastic properties such as Young's modulus and Poisson's ratio of nanowire obtained from the simulation statistics are analyzed in the subsequent sections.

6.5 Results and discussion

The simulated stress-strain response of Pd, Pt and their alloys under various loading conditions is presented in this section. The temperatures at which the response was studied were well below the surface melting temperatures of the nanowires[140]. This ensured that the starting configurations of nanowires were completely solid phase. In the present study, we have used various potential cutoff values (for generation of Verlet neighbor list) between 2-2.5*lattice constant for each temperature and strain rate and found that the results obtained are independent of the same.

6.5.1 Mechanism of stress-strain response in alloy nanowires under low strain rate conditions

The stress-strain response starting from an initial unstressed state to complete rupture for Pd, Pt as well as their alloy nanowires (25 and 50% Pt) simulated at 50 K and 0.05% ps^{-1} strain rate are shown in Fig. 6-2. Nanowires at these four compositions respond to the strain in qualitatively the same way. The initial nonzero stress arises from the capillary forces associated with the free surfaces[209]. The nanowire extension commences with an elastic deformation from its initial state (<A> of Fig. 6-3) to its threshold value defined as the first yield state <B>. At this low strain rate, stress is related to strain by Hooke's law. For 50% Pd alloy nanowires, the first yield strain (ε_{fy}) corresponds to 0.095 and the corresponding stress (σ_{fy}) is 15.03 GPa.

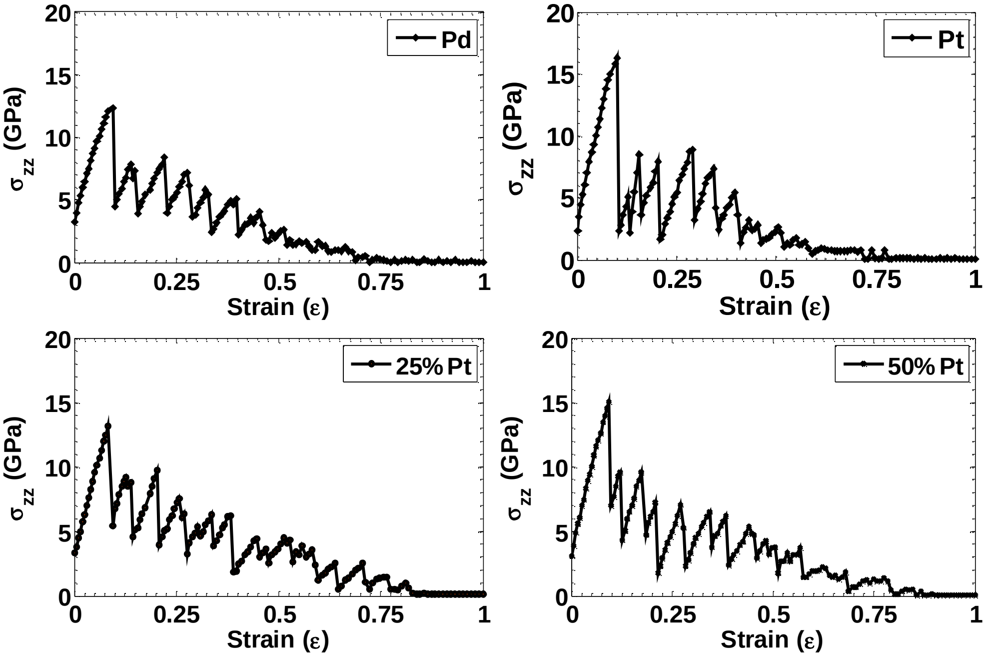

Figure 6-2. Stress-strain response of Pd, Pt and Pd-Pt alloy nanowires at T=50 K and strain rate=0.05% ps^{-1}.

Beyond the first yield state, the wire experiences an abrupt dislocation and undergoes an irreversible structural rearrangement to a reconstructed crystal configuration shown in <C> (Fig. 6-3). The nanowire at <B> undergoes slippage along the (111) plane which results in a nearly discontinuous drop in the stress value. For a closed pack structure such as fcc, the smallest Burgers vectors exist along the [110] direction, which makes it energetically favorable to reconstruct along the (111) slip planes. This dislocation mechanism has been discussed in detail by Finbow et al.[212] The number of atomic layers increases from 16 to 18 beyond the elastic limit. It can be seen from Fig. 6-2 that alloys having higher composition of Pt require higher stress to bring about slippage along (111) plane and experience this dislocation at higher strains.

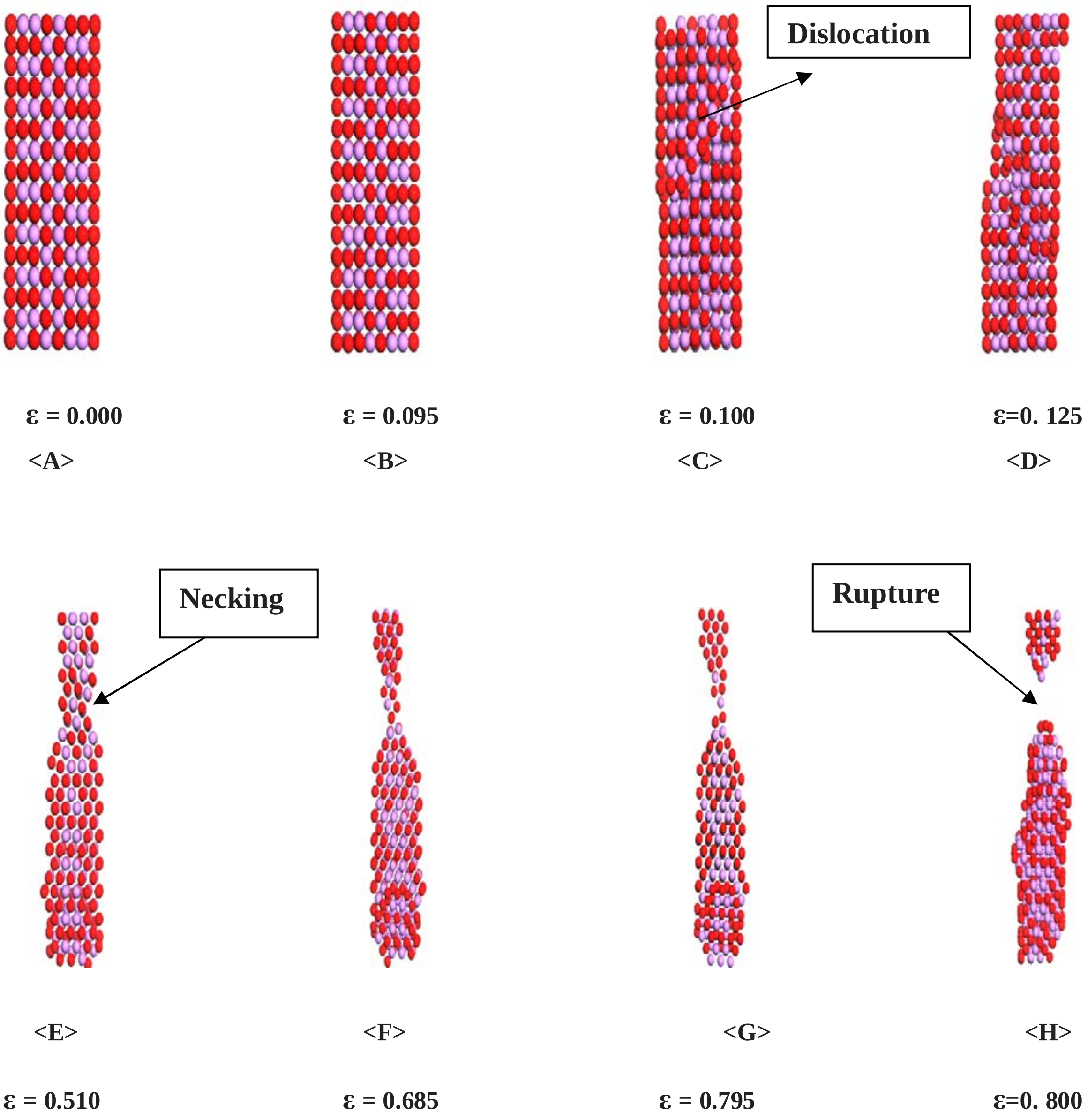

Figure 6-3. Snapshots showing atomic arrangement of ($Pd_{0.5}$-$Pt_{0.5}$) wires at different strain values for T=50 K and strain rate=0.05% ps^{-1}. Pd atoms are represented in red and Pt atoms in purple.

Extension of the reconstructed nanowires results in a second dislocation to state <D>. A smaller stress (approx. 9.6 GPa for 50% Pt) is required to bring the nanowires to the second dislocation point at ε=0.125.

In this regime, an out-of-plane rearrangement of atoms along the (111) plane occurs. The reconstructed lattice obtained after the first dislocation is not able to attain the minimum energy state and hence a smaller stress is sufficient to bring about further dislocations. Further increase in strain leads to repetition of the dual process *i.e.* an elastic stretch followed by a slip. Thus, a series of such dislocations and crystal rearrangement occurs for the subsequent strains. The amount of stress required to bring about subsequent dislocations decreases. During this process, the surface atoms are progressively displaced from their original positions and this leads to surface rupture which results in the neck formation at $\varepsilon=0.510$ as shown in <E>. The location of the neck depends on the point of greatest concentration of the multiple twinning planes for low applied strain rates[213]. The neck continues to become smaller from <E> to <G> where the two nanowire segments are joined by a mono-atomic strand. The nanowire radius continues to decrease with wire elongation. Once this is sufficiently narrow, *i.e.* approx. 2*lattice constant, breaking can take place. This complete rupture occurs at a strain value greater than 0.800 for 50% Pt wires as illustrated in <H>.

At this low temperature, the lattice order is highly preserved owing to the smaller atomic oscillations about their equilibrium positions. The crystal structure has a tendency to maintain its stable configuration which results in well defined periods of yielding. Therefore, the stress-strain response of nanowires at low strain rates and low temperatures follows a stepwise periodic behavior in which the nanowire undergoes slippage, relaxes and subsequently reconstructs. It was found that qualitatively there is no difference in the deformation and rupture mechanism of Pd-Pt nanowires of various compositions, which could mainly be attributed to the very small size mismatch between the constituent atoms. This is true for other loading conditions also and hence, nanowire having representative composition of 50% Pt would be discussed in the subsequent sections.

The stress-strain response of the four studied nanowires (Pd, Pt, Pd-Pt at 25% and 50% Pt) at 300 K and 0.05% ps^{-1} strain rate is shown in Fig. 6-4. With an increase in temperature (from 50 to 300 K), the entropy increases and the atoms vibrate about their equilibrium position with increased amplitudes. The increased oscillations in turn result in relatively larger lattice instability. As a result, the system favors disruption of lattice order and encourages lattice reconstruction. Therefore, compared to Fig. 6-2, the nanowires at this higher strain rate experience an early onset of slippage. For example, the 50% Pt nanowire has a 21% lower yield strain (ε_{fy}) and a corresponding 20% smaller yield stress (σ_{fy}).

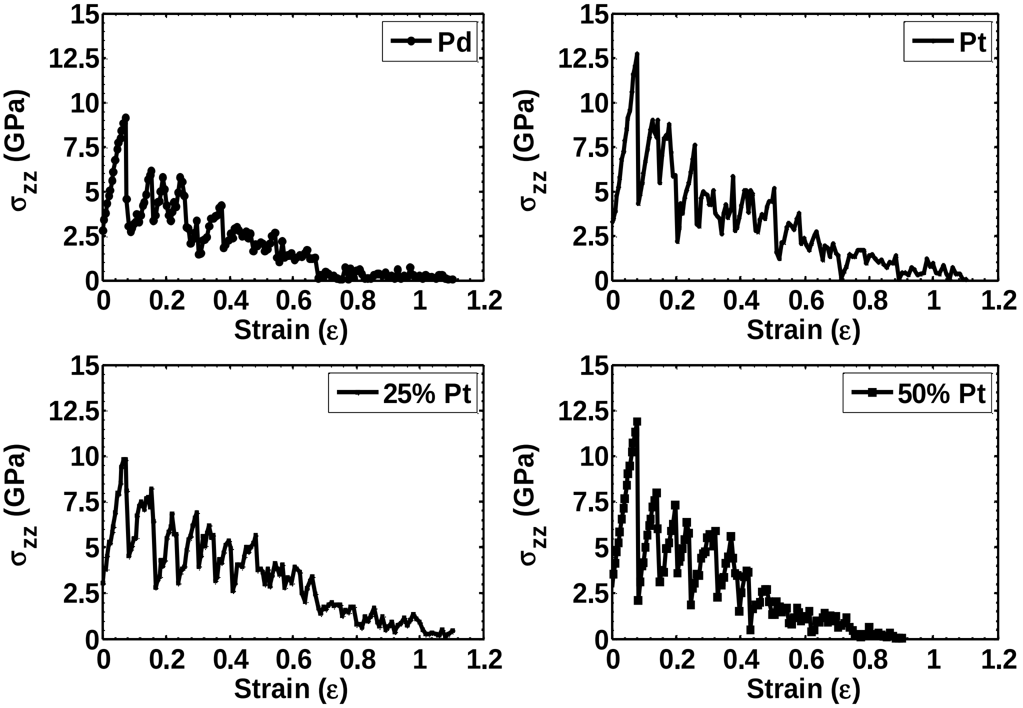

Figure 6-4. Stress-strain response of Pd, Pt and Pd-Pt alloy nanowires at T=300 K and strain rate=0.05% ps^{-1}.

The onset of out-of-plane slippage at 300 K in 50% Pt nanowires occurs earlier at $\varepsilon = 0.080$ (Fig. 6-5 <C>), compared to $\varepsilon = 0.100$ at 50 K. The periodic slippage and lattice rearrangement continues till surface rupture at $\varepsilon = 0.140$. Further increase in strain results in necking observed at $\varepsilon_{ne} = 0.255$. The neck continues to become narrower until complete rupture at $\varepsilon_{ru} = 0.770$.

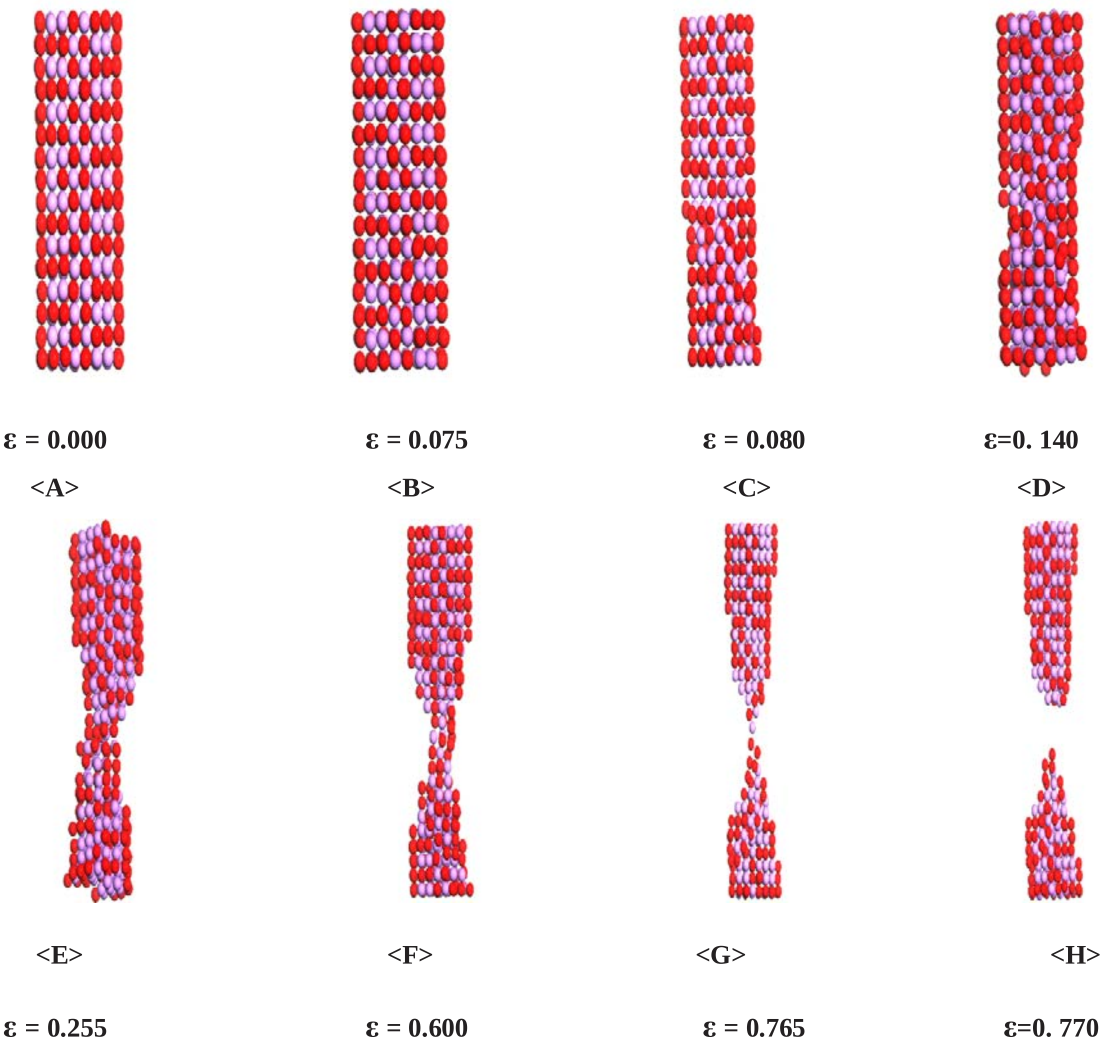

ε = 0.000 **ε = 0.075** **ε = 0.080** **ε=0. 140**

<A> **<B>** **<C>** **<D>**

<E> **<F>** **<G>** **<H>**

ε = 0.255 **ε = 0.600** **ε = 0.765** **ε=0. 770**

Figure 6-5. Snapshots showing atomic arrangement of ($Pd_{0.5}$-$Pt_{0.5}$) wires at different strain values for T=300 K and strain rate=0.05% ps^{-1}. Pd atoms are represented in red and Pt atoms in purple.

The ductility of the nanowire is typically defined as the percent elongation in its length before undergoing complete rupture. In the present study, a modified ductility parameter ($\Delta\varepsilon_D$) of a nanowire is defined as the strain interval between the onset of necking and complete rupture and used as a measure of its ductility. This parameter assumes special significance in characterizing the ability of the nanowires to form linear atomic chains. For 50% Pt alloy at 300 K and 0.05% ps^{-1}, $\Delta\varepsilon_D$=0.770-0.255=0.515 or 51.5% whereas the same at 50 K is (0.800-0.510=0.29) or 29%. Therefore, the 50% Pt alloy nanowire at 300 K is about 22% more ductile than at 50 K. The ductility of the studied nanowires is summarized in Table 6-2. It can be seen that the ductility of alloy nanowires shows a non-monotonic variation with composition and increases with temperature. At both the temperatures, nanowires of 75% Pd composition are more ductile than the 50% Pd alloy as well as mono-metallic wires.

As brought out earlier, the initial surface and core compositions of nanowires vary with the alloy composition and for a given alloy composition, depend on the surface energies of the constituent atoms. Upon stretching the nanowires, the slippage and dislocations leading up to the necking result in variations in the nanowire cross-sectional area along the wire axis. Depending on the alloy composition, the induced local variations in surface area might result in expelling or engulfing of constituent atoms. As a result, the strength of metal-metal interaction which dictates the onset of necking and final rupture also changes with wire elongation and affects the onset of necking and final rupture. Therefore, the strain interval between the onset of necking and rupture is strongly influenced by alloy composition and is dictated by the relative strength of the metal-metal interactions in the binary alloy nanowires. The influence of ductility on nanowire applications is discussed in a subsequent section.

Table 6-2. Ductility of nanowires at strain rate (0.05% ps^{-1}) and different temperatures.

Nanowire composition (% Pd)	50 K		Ductility ($\Delta\varepsilon_D$ %)	300 K		Ductility ($\Delta\varepsilon_D$ %)
	ε_{ne}	ε_{ru}		ε_{ne}	ε_{ru}	
0	0.315	0.610	29.5	0.350	0.910	56
50	0.510	0.800	29	0.255	0.770	51.5
75	0.290	0.775	48.5	0.430	1.050	62
100	0.330	0.670	34	0.250	0.690	44

6.5.2 Mechanism of stress-strain response in alloy nanowires under high strain rate conditions

Under high strain rate conditions ($\dot{\varepsilon} = 5\%$ ps^{-1}), the stress-strain response of nanowires exhibits a completely different behavior as shown in Fig. 6-6. The stress-strain response of the nanowires at $\dot{\varepsilon} = 5\%$ ps^{-1} and 50 K exhibits “mini-peaks” or “wavelets” during the yielding cycles, indicative of higher disorder in the crystal lattice. This behavior was observed by Koh et al.[200] in their simulations of Pt nanowires and by Ikeda et al.[209] for Ni and Cu-Ni alloy nanowires, when subjected to strain rates of up to 4% ps^{-1} and 5% ps^{-1}, respectively, by these two authors. This phenomenon is attributed to the onset of amorphous deformation at higher strain rates. Beyond the first yield strain, the system changes continuously from a crystalline fcc phase to an amorphous phase.

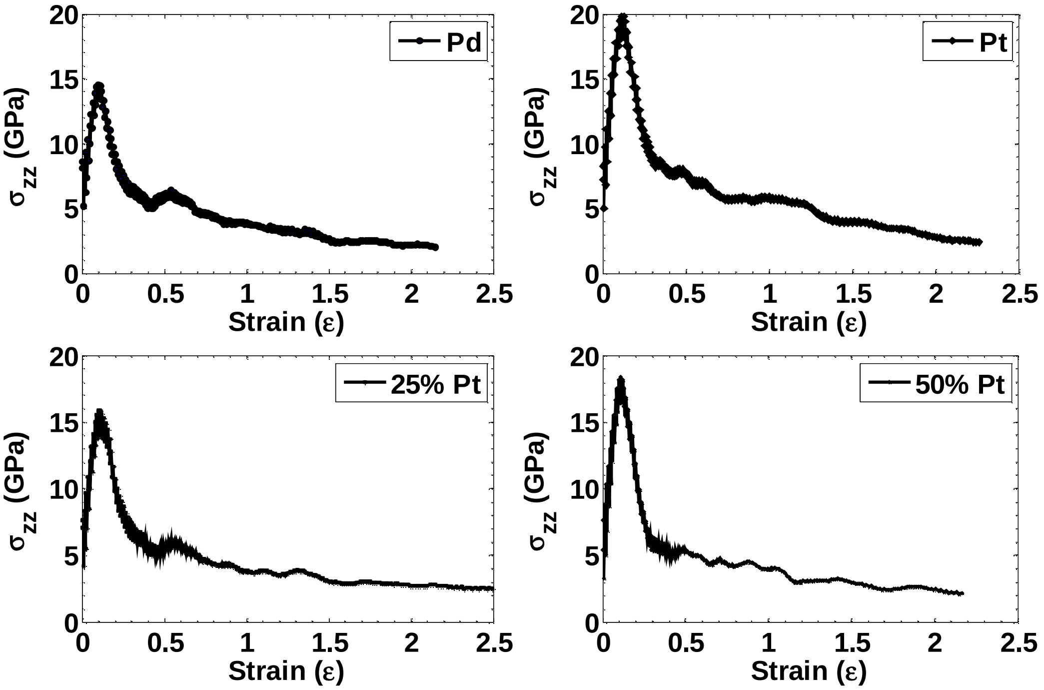

Figure 6-6. Stress-strain response of Pd, Pt and Pd-Pt alloy nanowires at T=50 K and strain rate=5% ps^{-1}.

The onset of amorphous phase at the higher strain rate and lower temperature is indicated by the snapshots shown in Fig. 6-7. The amorphization at high strain rates is attributed to the increased kinetic energy of the atoms. When the strain induced kinetic energy of the atoms exceeds the enthalpy of fusion, the onset of amorphization takes place[213]. Nanowires rich in Pt composition have higher enthalpy of fusion and hence experienced the onset of amorphization at higher strains. Our findings indicate that at high strain rates, the slippage allowing for reconstruction along the (111) plane is absent. Instead, the wires exhibit superplasticity behavior right after yielding. Owing to the high degree of lattice disorder, the nanowires yield at extremely high stresses. For 50% Pd nanowires, the yield stress (σ_{fy}) is 18.4 GPa and corresponding yield strain (ε_{fy}) i.e. 0.110 at 50 K. The stress required at 50 K is 22 % higher and the corresponding strain is 16% higher than that required at $\dot{\varepsilon}$ =0.05% ps^{-1}. Beyond this strain, deformation of the nanowire proceeds uniformly with no necking phenomenon observed for all the wires. The nanowires continue to extend and experience complete rupture at much higher strains. The rupture strain (ε_{ru}) is 2.10 for the 50 % Pd nanowire.

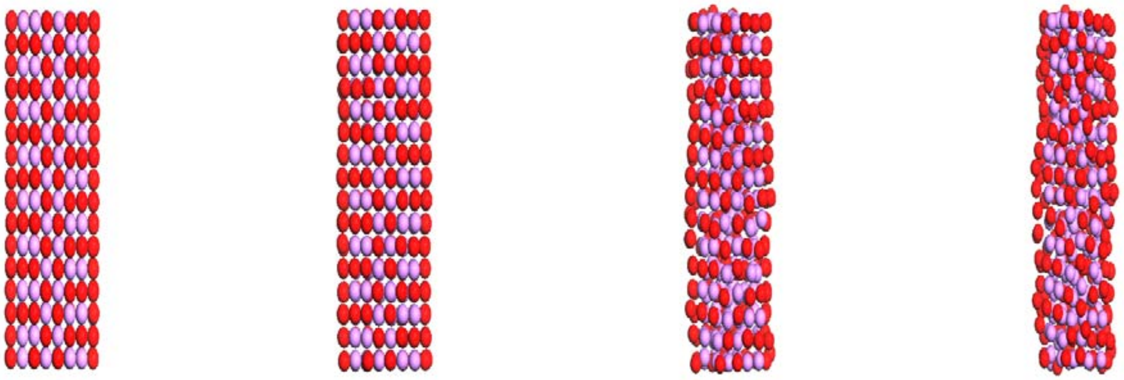

ε = 0.000 **<A>**

ε = 0.110 **<B>**

ε = 0.160 **<C>**

ε=0. 280 **<D>**

Figure 6-7. Snapshots showing atomic arrangement of ($Pd_{0.5}$-$Pt_{0.5}$) wires at different strain values for an applied strain rate=5% ps^{-1} and T=50 K. Pd atoms are represented in red and Pt atoms in purple.

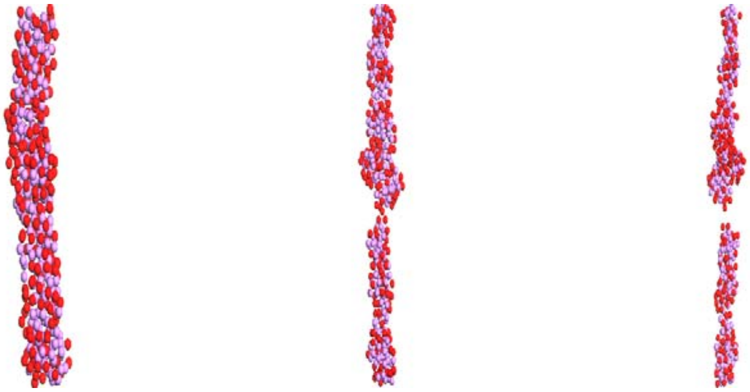

ε = 0.640 **ε = 1.75** **ε = 2.10**

<E> **<F>** **<G>**

Figure 6-7: Continued

Further extension of nanowires at higher strain rate appears to be associated with structural changes. From the snapshots shown in Fig. 6-7, the nanowires appear to evolving into a helical structure. The existence of helical structures in Pt nanowires was seen in the simulations of Koh et al.[200] However, at the strain rates simulated by these authors, the formation occurred at the junction of the two nanowire segments before complete rupture. In our case, the nanowire appears to be evolving into stable helical structures along its entire length. It appears that at the extremely high aspect ratios, the fcc structure might not represent the most stable phase and therefore the amorphous/melted material would transform into a multi-shelled helix. Indeed, such a structure has been reported to occur for Pt nanowires by Oshima et al.[214] who used electron beam thinning method at elevated temperatures to form 6-0 single walled platinum nanotube approximately 0.48 nm diameter. It is possible that the mechanical extension of fcc nanowires at 50 K and $\dot{\varepsilon} = 5\%$ ps^{-1} might have lead to the formation of similar helical structure observed by Oshima et al. Depending on the alloy composition, a residual stress of about 2.5-3 GPa was observed after the rupture of the nanowire into its fragments. This could be attributed to the presence of stable structures (possibly helical) within the broken fragments or else to an artifact of the long range nature of the potential, which would give rise to a detectable force between the separated portions of the wire. This would however require a separate investigation of its own.

The stress-strain response of 50% Pd nanowires subjected to high strain rate ($\dot{\varepsilon} = 5\%$ ps^{-1}) and 300 K is shown in Fig. 6-8. At the higher temperature (e.g. 300 K) and the higher applied strain rate ($\dot{\varepsilon} = 5\%$ ps^{-1}), the nanowires exhibit superplasticity behavior after yielding (ε_{fy} = 0.060) as can be seen from the snapshots of 50% Pd wires in Fig. 6-9. The nanowires, however, yield at lower stresses (σ_{fy} = 8.04 GPa for 50% Pd) and corresponding lower strain (ε_{fy} = 0.060) as seen from the stress-strain response in Fig. 6-8. The stress required at 300 K is 55% lower and the corresponding strain is 45% lower than that required at $\dot{\varepsilon}$ =0.05% ps^{-1} at 50 K. This might be attributed to the increased entropy of the system at higher temperatures. The rupture mechanism as well as the response characteristics of the nanowires (Pt, 50% Pt, 25% Pt and Pd) under varying loading conditions are in qualitative agreement with those of Koh et al.[200] and Finbow et al[212], who studied the mechanical behavior of Pt nanowires subjected to uniaxial tension.

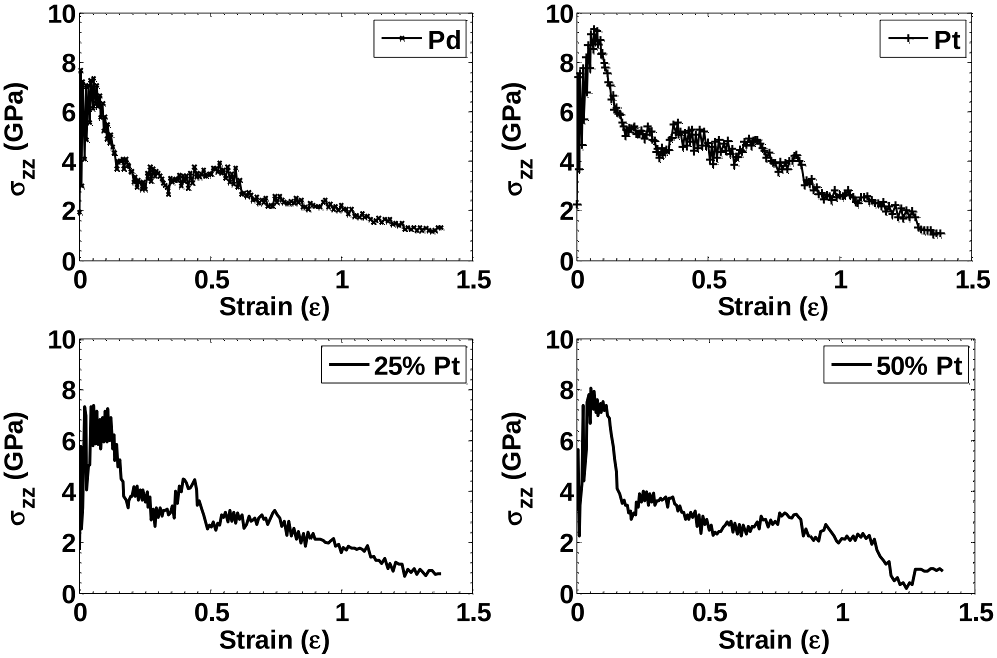

Figure 6-8. Stress-strain response of Pd, Pt and Pd-Pt alloy nanowires at T=300 K and strain rate=5% ps^{-1}.

The nanowires continue to deform after yielding and finally ruptured at much lower strains (ε_{ru} = 1.10 for 50% Pd). The multishell helical structure similar to that observed at 50 K appears to evolve at 300 K also.

However, at higher temperatures and strain rates, there was insufficient time for these structures to further relax and develop to a longer length. As a result, the rupture strains (and hence the ductility) are much lower than those observed at low strain rates and lower temperatures.

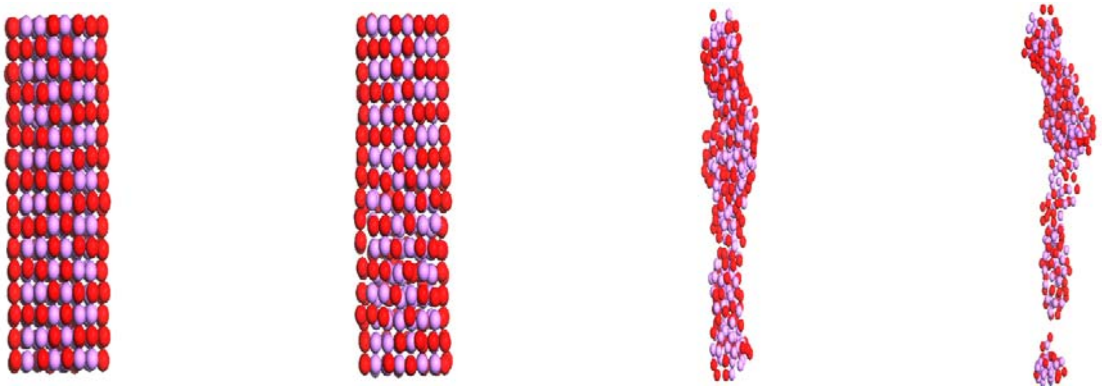

ε = 0.000 **ε = 0.060** **ε = 0.640** **ε=1. 100**

<A> **<B>** **<C>** **<D>**

Figure 6-9. Snapshots showing atomic arrangement of ($Pd_{0.5}$-$Pt_{0.5}$) wires at different strain values for an applied strain rate=5% ps^{-1} and T=300 K. Pd atoms are represented in red and Pt atoms in purple.

6.5.3 Structural analysis

Radial distribution function[98] (RDF) can be used to analyze the structural changes associated with the different strain rates. RDF of ($Pd_{0\,5}$-$Pt_{0\,5}$) nanowire strained along the [001] direction at 50 K and at the lower strain rate as shown in Fig. 6-10. The crystalline fcc structure is clearly evident from the RDF of nanowires at ε=0. With an increase in strain, the peak value of the nearest neighbor distance is reduced. Further a split in the peaks is also observed. The phenomenon responsible for splitting of the peaks is illustrated in Fig. 6-11. Upon elongation to ε=0.09, the nearest neighbor distance along the (001) plane is reduced whereas the nearest distance along the (100) plane increases leading to a face centered orthorhombic structure as shown in Fig. 6-11. The corresponding distributions of the first neighbor distances are therefore split into the two peaks, each peak representative of the nearest neighbor distance along the (100) and (001) planes, respectively. Further stretching of the nanowires beyond the first yield

(ε_{fy}) results in a crystal rearrangement back to an fcc structure as shown in Fig. 6-10. The number of atomic layers increases from 16 to 18 to compensate for the increase in length while maintaining the inter-atomic distance of 2.75 Å.

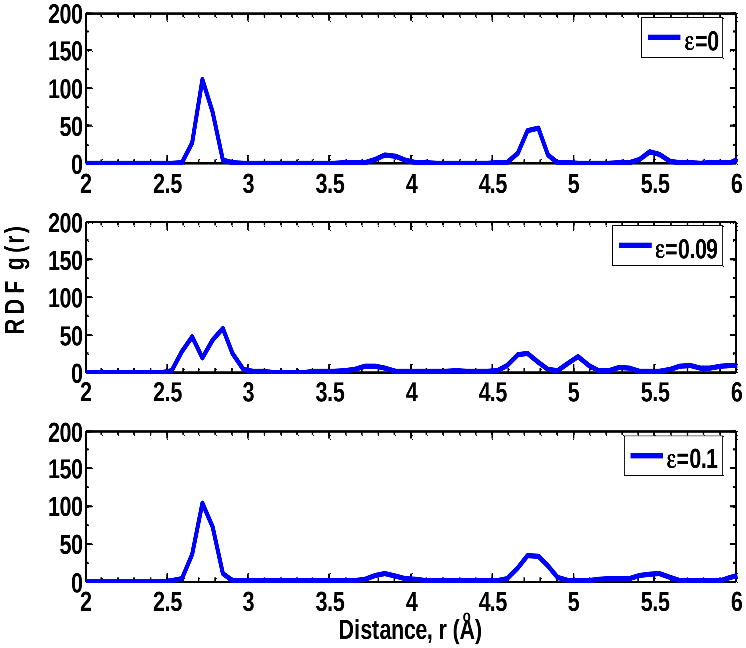

Figure 6-10. Radial distribution function of ($Pd_{0.5}$-$Pt_{0.5}$) nanowire strained along the [001] direction at 50 K and 0.05% ps^{-1}.

When subjected to the higher strain rate (5% ps^{-1}), the first peak in the nanowire RDF broadens whereas the second peak, located at ~ 0.38 nm and representing the octahedral sites, gradually disappears as the strain increases beyond ε=0.11 (shown in Fig. 6-12). The nanowire structure transforms homogeneously from an original crystalline fcc structure to the amorphous state with no evidence of strain hardening or necking that is observed in metal nanowires at lower strain rates. At higher strain rates, the atoms do not have sufficient time to diffuse and form a stable crystalline configuration corresponding to the physical configuration with lower energy. Similar behavior is also exhibited by Ni[192] , Au[215] and NiCu[209] nanowire when subjected to high strain rates (5-15% ps^{-1}).

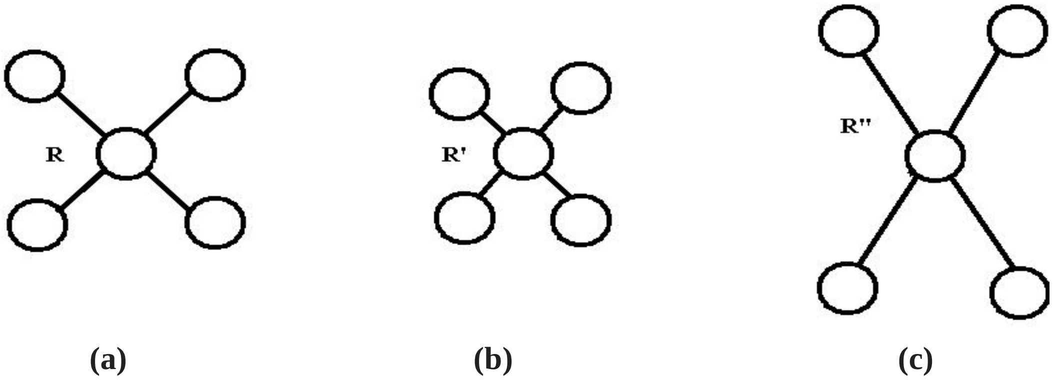

Figure 6-11. During elastic deformation, fcc evolves into a fco (face centered orthorhombic) structure. The initial fcc structure with radius R at zero strain is shown in (a). When subjected to a tensile strain along the [001] direction, the nearest neighbor distances change as R''>R>R'. Along the (001) plane, the inter-atomic distance in nanowires reduces as shown in (b), whereas it increases along the (100) plane as shown in (c).

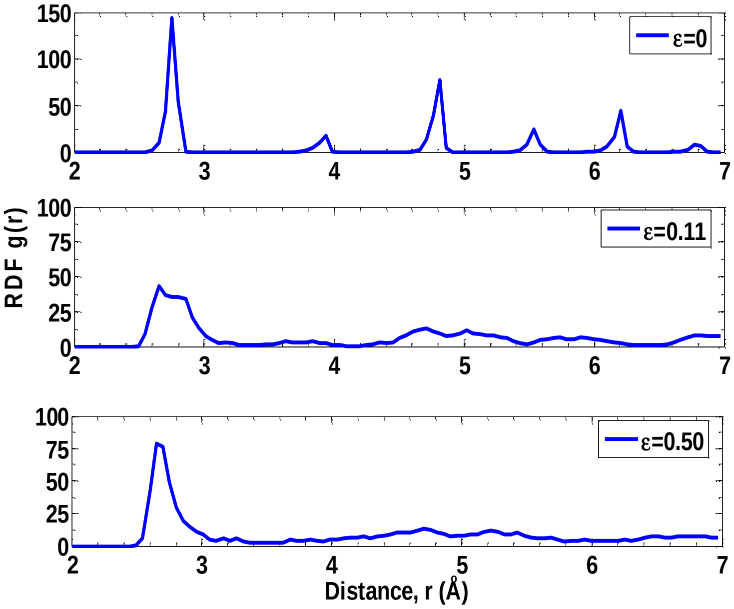

Figure 6-12. Radial distribution function of ($Pd_{0.5}$-$Pt_{0.5}$) nanowire strained along the [001] direction at 50 K and 5% ps^{-1}.

6.5.4 Elastic properties of alloy nanowires

The Young's modulus and Poisson ratio are computed for the different nanowires prior to the first yield strain at the two studied temperatures and strain rates. A linear regression analysis of the stress-strain data was used to obtain the least squares best fit straight line through the sample points. The slope of the line gave the Young's modulus under various loading conditions. A correlation coefficient (***r***) was used to quantify the degree of linearity between the stress and strain data points. Physically, it is indicative of the stability of the lattice when subjected to axial deformation. The higher the value of the correlation coefficient, the more stable is the crystal lattice. At ***r***=100%, the constituent atoms do not vibrate about their equilibrium positions (e.g. lattice structure at T=0 K) whereas at ***r***=0% the system is in a state of maximum entropy and is indicative of a completely random cluster with the atoms exhibiting Brownian motion (e.g. dilute gases). The Young's modulii and the associated correlation coefficients are summarized in Table 6-3.

Table 6-3. Young's modulus (GPa) of various nanowires under different loading conditions.

Nanowire	Property	$\dot{\varepsilon}$ =0.05% ps^{-1}		$\dot{\varepsilon}$ =5% ps^{-1}	
		50 K	300 K	50 K	300 K
Pd	E (GPa)	105	89.8	82.1	80.1
	r (%)	99.75	99.73	83.29	84.01
$\mathrm{Pd}_{0\ 75}$-$\mathrm{Pt}_{0\ 25}$	E (GPa)	120	97.7	104	88.9
	r (%)	99.97	99.35	84.32	82.86
$\mathrm{Pd}_{0\ 5}$-$\mathrm{Pt}_{0\ 5}$	E (GPa)	130	117	134	98.8
	r(%)	99.78	99.74	85.64	85.17
Pt	E (GPa)	152	126	135	100
	r(%)	99.96	99.72	89.94	88.24

The bulk value of Young's modulus for Pd and Pt are 121 and 168 GPa, respectively. Our findings in Table 6-3 indicate that the Young's modulus shows a near linear increase with composition of Pt in the Pd-Pt alloy nanowires for the various strain rates. The extent of deviation from bulk value depends on the alloy composition. Our results indicate that the alloy nanowires rich in Pt are stiffer and show lesser deviation from bulk value than Pd rich alloys.

At low strain rates, the Young's modulus for the nanowires is 13% (for Pd) and 25% (for Pt) lower than the bulk values at 300 K whereas it is 10% (for Pd) - 14% (for Pt) lower at 50 K. Similar behavior is exhibited by the alloy nanowires. At the higher strain rate and at 50 K, the elastic modulus is 32% (for Pd) and 20% (for Pt) lower than the respective bulk values. Increase in temperature at high strain rates leads to a significant drop in the Young's modulus for both single component as well as alloy nanowires. The correlation between the stress and the strain values is above 99% and is therefore very strong at lower strain rates. At high strain rates, the nanowire experiences higher degree of disorder. The onset of amorphous phase results in significant lowering of the correlation coefficients (85-90%), even at temperatures as low as 50 K as shown in Table 6-3. Therefore, nanowires when subjected to higher strain rates are significantly softened as also indicated by the Young's modulus. The implications of a lesser stiff nanowire on their applicability in MEMS and other areas are discussed in a subsequent paragraph. The effect of alloying on the mechanical properties of Pd nanowires is clearly evident from Table 6-3. Young's modulus increases with Pt composition for the various simulated loading conditions. It appears that alloys having 50% or more Pt would have mechanical properties closer to that of pure Pt.

The Poisson ratio was calculated following a similar procedure by carrying out a regression analysis on a scatter plot of radial (ε_{rr}) *vs*. axial strain (ε_{zz}). The radial strain of the nanowire is defined as $\varepsilon_{rr} = \dfrac{R - R_i}{R_i}$, where R is the radius of the wire at strain state ε_{zz}, and R_i is the initial radius of the nanowire in its unstressed state. The mean distance of the surface atoms from the centroid of nanowire was used to obtain the average radius R at each strain state. Fig. 6-13 shows the determination of Poisson ratio from a plot of axial *vs*. lateral strain for one particular case. The results for different loadings are summarized in Table 6-4.

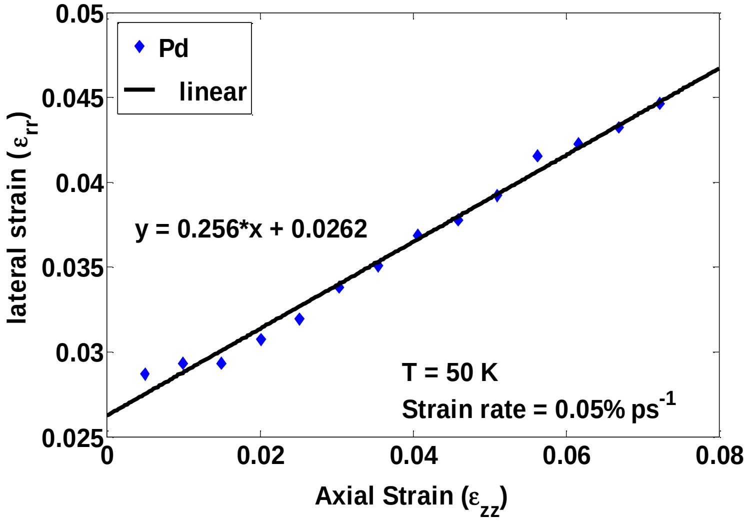

Figure 6-13. Determination of Poisson ratio for Pd nanowire at T=50 K and $\dot{\varepsilon} = 5\%$ ps^{-1}.

The Poisson ratio for bulk Pd and Pt are 0.38 and 0.39, respectively. The Poisson ratios of Pd-Pt alloys also have values between 0.38 and 0.39. At the nanoscale, the Poisson ratios of Pd and Pd rich alloys differ significantly from bulk values. The Poisson ratio of Pd and 25% Pt alloy nanowires are 32% and 21% lower than bulk values, respectively. Our results in Table 6-4 indicate that the Poisson ratio of Pd rich nanowires shows a stronger deviation from the bulk behavior. This suggests that the deformations in the radial and axial directions are less strongly correlated for Pd rich nanowires than for Pt rich alloy nanowires. The Poisson ratio of most materials lies between 0 and 0.5. Materials with Poisson ratio ≈ 0.5 (e.g. rubber) are considered incompressible. The lower value of Poisson ratio suggests that the material is more compressible. This indicates that Pd and Pd rich alloys are therefore more compressible and malleable than Pt and Pt rich alloys.

Table 6-4. Poisson ratio (ν) of nanowires for different loading conditions.

Nanowire	Property	$\dot{\varepsilon}$ =0.05% ps^{-1}		$\dot{\varepsilon}$ =5% ps^{-1}	
		50 K	300 K	50 K	300 K
Pd	N	0.26	0.23	0.27	0.26
	r (%)	99.46	95.21	88.17	88.61
$\text{Pd}_{0\ 75}$-$\text{Pt}_{0\ 25}$	N	0.30	0.28	0.28	0.27
	r (%)	99.24	98.07	89.34	89.69
$\text{Pd}_{0\ 5}$-$\text{Pt}_{0\ 5}$	N	0.32	0.30	0.29	0.30
	r (%)	99.66	97.75	91.38	90.12
Pt	N	0.35	0.34	0.34	0.31
	r(%)	99.79	98.02	97.16	95.61

At low strain rates and high temperatures such as 300 K, the Poisson ratio of nanowires is 3-13% lower than at a lower temperature such as the simulated 50 K, depending on the alloy composition. The slightly higher compressibility is attributed to the increased kinetic energy at higher temperature. With increase in strain rates, onset of amorphous transformation takes place and there is a further reduction in the Poisson ratio of nanowires. The higher malleability is attributed to increased lattice disorder. The increase in crystal ductility as well as malleability and compressibility, results from the development of short ranged order of the crystal structure at higher strain rates. The Poisson ratio and other mechanical properties of ($\text{Pd}_{0\ 5}$-$\text{Pt}_{0\ 5}$) nanowires are summarized in Table 6-5.

The influence of the various derived mechanical properties on the applicability of nanowires in sensing and other applications is discussed herewith. Comparisons of finite element simulations of a typical SAW gas sensor (100 MHz) utilizing a Pd nanomaterial sensing layer with properties derived from the present study and a thin Pd film have shown significant differences in the wave propagation velocities. Our simulations (ignoring any mass loading effect) indicate a time delay of 1 ns in the acoustic wave propagation between the two cases which is attributed to changes in elastic modulus.[211] Experiments by Srinivasan et al.[216] have also shown significant differences in the sensitivity and speed of response of SAW sensor devices utilizing nanomaterials which cannot be solely explained on the basis of increased surface area. Although the mechanical properties of nanowires in gaseous and liquid environment are required to quantitatively establish the sensor characteristics, the present results do indicate that significant differences between the nanoscale and bulk elastic properties prevail which are likely to have a bearing on the applications of nanowires as sensing layers in some types of gas and biological sensors.

Table 6-5. Summary of mechanical properties of ($Pd_{0.5}$-$Pt_{0.5}$) nanowires.

Nanowire property		$\dot{\varepsilon}$ =0.05% ps^{-1}		$\dot{\varepsilon}$ =5% ps^{-1}	
		50 K	300 K	50 K	300 K
First Yield	Strain	0.095	0.075	0.110	0.060
	Stress (GPa)	15.03	11.90	18.38	8.04
Rupture		0.800	0.770	2.10	1.10
Ductility		29	51.5	146	46
Young’s Modulus (GPa)		130	117	134	98.8
Poisson ratio (v)		0.32	0.30	0.29	0.30

Apart from sensor applications, the nano-mechanical properties also influence the electronic properties *i.e.* conductance quantization.[217,218] We find that the deformation behavior of nanowires subjected to high train rates is very different from those subjected to low strain rates. The slips, necking, and atomic rearrangements might be responsible for the sudden reduction of area, and, subsequently, the quantized conductance, that has been observed both numerically and experimentally for nanowires, especially at low strain-rate[219]. Consequently, it is reasonable to predict that the conductance of nanowires under high strain-rate deformation will be quite different from low strain-rate cases. It is expected that the conductance at high strain-rate deformation would be a continuous function of elongation instead of a quantized change due to the smooth reduction of area.

Several experimental and theoretical studies have tried to establish the correlation between the conductance quantization and nanowire mechanical properties[218,220]. The mechanical instability is reflected as a jump in the conductance and force plots. The conductance slope between jumps was found to be influenced by the Poisson ratio. Simplified models developed by Torres and Saenz[221] predict the normalized conductance to decrease with Poisson ratio and wire elongation for transition metals such as Au and Pt. Therefore, the data in Table 6-4 implies that wires rich in Pt composition would be a better choice than Pd rich wires as nano-contacts in NEMS applications.

6.6 Conclusions

Molecular dynamics simulations, of Pd, Pt and Pd-Pt alloy nanowires subjected to uniaxial tensile strain along the [001] direction, were carried out. The changes in the crystal structure and mechanical properties of nanowires under various loading conditions were analyzed. It was observed that the crystalline order is preserved at low strain rates and lower temperature. Under these conditions, the nanowire elongation is accompanied with periodic elastic yielding cycles, with planar dislocation and slippage occurring along the (111) plane. The deformation behavior at low temperatures such as 50 K is characterized by slips and rupture with low ductility. On elongation within the first yielding, the analysis of RDF reveals that the initial fcc crystal structure changes into face centered orthorhombic (fco) type. Alloys richer in Pt composition required higher applied stresses before yielding and yield at higher strains than alloys having lower Pt. With an increase in temperature for the same applied strain rate, the system entropy increases and periodic response of the nanowires becomes less defined. The ductility of nanowires increases with temperature over the entire range of Pd composition.

The stress-strain response at high strain rates is less strongly correlated. An increase in strain rate at 50 K results in a continuous change from crystalline to amorphous type for all the nanowires, thereby displaying superplasticity behavior. The amorphous nanowire appears to transform into a relative stable multishell helical structure. The helical structure significantly increases the ductility of the nanowires. Complete rupture occurs when the wire length is approximately three times its original length. The helical structure is also observed at higher temperatures. However, the increased entropy results in reduced stability of these nanowires. Although the stress-strain response of the alloy nanowires is qualitatively similar to that of single component nanowires, significant quantitative differences exist. These differences manifest themselves in the form of unexpected variations in the nanowire mechanical properties with alloy composition.

Mechanical properties of the alloy nanowires are found to be significantly different from those of bulk phase and are dictated by the applied strain rate, temperature, alloy composition as well as the structural rearrangement associated with nanowire elongation. The initial surface and core compositions of nanowires vary with the alloy composition and were also found to significantly influence their mechanical properties. The ductility of alloy nanowires at low strain rates was found to exhibit a non-monotonic variation with Pd composition. At the nanoscale, the calculated Young’s modulus and Poisson ratio depend on the applied strain rate. It was found that the Young’s modulus of alloy nanowires varies approximately linearly with Pd composition for the various applied strain rates and is about 70-85% of the bulk value with the exact lowering dependant on the alloy composition, temperature and the applied strain rate. Similarly, the Poisson ratio of Pd rich alloys is 60-70% of its bulk value whereas that of Pt rich alloys is not significantly changed at the nanoscale. The differences in elastic properties are attributed to the finite size effect. The effect of the differences in mechanical properties of nanowires on their applicability in sensing and other areas is discussed.

The results from the present study might be used as input for linear continuum and macro-scale modeling of catalysis and sensing related applications which typically involve nanostructures of Pd, Pt and their alloys. Although, in view of the observed variations of mechanical properties with alloy composition and its dependence on the wire microstructure, the variations of elastic properties with alloy nanowire diameter can be expected to be very different from those of single component wires. This is primarily because for a given composition, the nanowire segregation profile or microstructure undergoes significant variations with size/diameter of alloy wires. The current findings have laid the groundwork for further investigations into the size effect of mechanical properties for alloy nanowires as well as other aspects of mechanical properties such as axial compression and bending for transition metal alloy nanowires.

Chapter Seven

Applications to Gas Sensing: Response of a SAW Hydrogen Sensor

7.1 Abstract for chapter seven

Surface acoustic wave (SAW) devices coated with a thin layer of chemo-selective material provide highly sensitive chemical sensors for the detection and monitoring of vapors and gases. The species detection is carried out by monitoring the shifts in frequency of the surface waves generated on piezoelectric substrates. These devices are conveniently small, relatively inexpensive and quite sensitive. The design of efficient sensors necessitates the development of response models which can lead to improved understanding of the wave propagation characteristics in SAW devices. The analytical models used to simulate the mechanical and electrical behavior of piezoelectric devices generally introduce simplifying assumptions that are often invalid for actual designs. Numerical techniques such as finite element method have proven to be a viable option to model wave propagation in SAW devices operating in the MHz-GHz range.

In this work, 3-D finite element models (FEM) based on a ~100 MHz YZ-$LiNbO_3$ piezoelectric substrate coated with a thin Pd sensing layer was simulated to gain insights into the H_2 sensor response. Literature suggests that structural and morphological changes due to gas absorption occurring at the molecular scale affect the material properties of the sensing layer which in turn affects the wave propagation at macro-scale. The changes in the material properties of the sensing layer on gas exposure were used to simulate the behavior of a SAW sensor. Frequency responses of the displacement and voltage waveforms generated at the output IDT nodes were used to quantify the effects of gas interaction. This study demonstrates the effectiveness of finite element models in understanding gas sensor response.

7.2 Gas sensing

Considerable attention has been dedicated to the development of analytical and computer modeling techniques to understand the characteristics of surface acoustic waves generated in SAW devices[36,37]. Recent advances in sensors and wireless communication systems indicate the need for high performance SAW devices often operating in high frequency (GHz) range. Most of the analytical techniques require simplification of second order effects such as backscattering, charge distribution, diffraction and mechanical loading.[222,223] However, these effects become significant for SAW devices operating in the high frequency range.

The models commonly used to simulate the mechanical and electrical behavior of piezoelectric transducers generally introduce simplifying assumptions that are often invalid for actual designs[224]. The geometries of practical transducers are often two (2-D) or three dimensional (3-D)[225,226]. Simulations of piezoelectric media require the complete set of fundamental equations relating mechanical and electrical quantities to be solved. Finite difference or finite element scheme are sufficient to handle the differential equations[227-231]. The finite element method has been preferred because it allows handling of complex geometries.

Finite element was applied by Lerch[226] (1990) to calculate the natural frequencies with related eigen modes of the piezoelectric sensors and actuators as well as their responses to various dependent mechanical and electrical perturbations. A direct finite element analysis was carried out by Xu to study the electromechanical phenomena in SAW devices[228]. The influence of the number electrodes on the frequency response was analyzed. These finite element calculations were able to evaluate the influence of the bulk waves at higher frequencies. Ippolito et al. have investigated the effect of electromagnetic feed through as wave propagation in layered SAW devices[229,230]. The same model was extended to study electrical interactions occurring during gas sensing[231]. Recently, a 3-D finite element model was developed for a SAW palladium thin film hydrogen sensor based on a XY-$LiNbO_3$ substrate[232]. An AC analysis was carried out to study the effect of the palladium thin film on the propagation characteristics of the SAW was studied in the absence and presence of hydrogen. Variations in mass loadings, elastic constants and conductivity were the factors used in evaluating the velocity change of the wave. All the above demonstrate the feasibility of finite element methods to adequately model SAW sensor response under varying conditions. In the present work, the variations in the Pd film properties placed on YZ-$LiNbO_3$ substrate, commonly used in gas sensing applications, are used to model H_2 sensor response. Instead of an AC analysis, an impulse voltage is applied on the IDT fingers and the frequency response based on the voltage waveform generated at the receiving IDT fingers is used to characterize the sensor response. The calculated displacement waveforms in the three directions are compared for the two cases (with and without H_2 absorbed). The design parameters (Substrate and IDT dimension) are different and closer to that used experimentally in our group. Preliminary results showing effect of gratings on transmission losses are also reported.

7.3 Finite element model

The propagation of acoustic waves in piezoelectric materials is governed by the mechanical equations of motion and Maxwell's equations for electrical behavior[1,36,37]. The constitutive equations of piezoelectric media in linear range coupling the two are given by:

$$T_{ij} = c_{ijkl}{}^{E} S - e_{kij}{}^{t} E \tag{7.1}$$

$$D_i = e_{ikl} S_{kl} + \varepsilon_{ik}{}^{S} E_k \tag{7.2}$$

The quasi-static assumptions help reduce Maxwell's equation to $\frac{\partial D_i}{\partial x_i} = 0$ and $E_i = -\frac{\partial \phi}{\partial x_i}$. The components of strain are defined by $S_{ij} = \frac{1}{2}\left(\frac{\partial u_i}{\partial x_j} + \frac{\partial u_j}{\partial x_i}\right)$.

The above equations give a system of four coupled wave equations for the electric potential and the three component of displacement in piezoelectric materials.

$$-\rho \frac{\partial^2 u_i}{\partial t^2} + c^{E}_{ijkl} \frac{\partial^2 u_k}{\partial x_j \partial x_l} + e_{kij} \frac{\partial^2 \phi}{\partial x_k \partial x_j} = 0 \tag{7.3}$$

$$e_{ikl}\frac{\partial^2 u_k}{\partial x_i \partial x_l} - \varepsilon_{ik}^S \frac{\partial^2 \phi}{\partial x_i \partial x_j} = 0 \tag{7.4}$$

These coupled wave equations can be discretized and solved for generating displacement profiles and voltages at each element/nodes. We use the commercially available FEM code ANSYS. The main advantage of using ANSYS lies in the flexibility in modeling different physical phenomena and also the pre- and post-processing capabilities.

7.4 Simulation details

A 3-D finite element model based on a piezoelectric (lithium niobate) substrate with dimensions (400μm width x 1600μm propagation length x 500μm depth) was simulated to gain insights into the sensor response. Two IDT finger pairs in each port were defined at the surface of Y-cut, Z-propagating $LiNbO_3$ substrate. The fingers were defined with periodicity of 40 μm and aperture width of 200 μm. The width of the IDT fingers (*d*) was taken as 10 μm. Thus, the wavelength of the wave generated ~ 40 μm ($\lambda=4d$). The velocity of the acoustic wave (v) on YZ-$LiNbO_3$ substrate is 3487 m/s. Hence the device frequency is expected ~ 87 MHz ($f = v/\lambda$). Sensors operating in such high frequency range (MHz-GHz) allow for higher sensitivity.

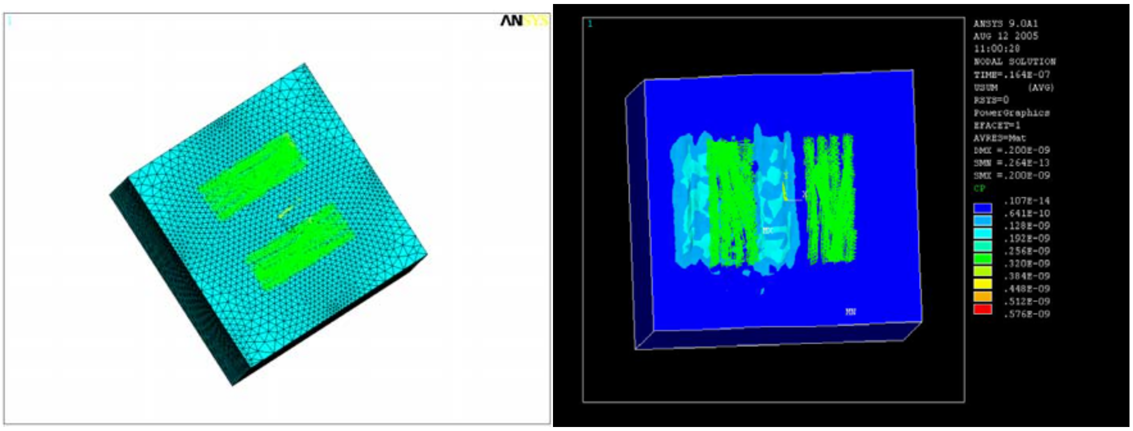

(a) **(b)**

Figure 7-1. Finite element model of wave propagation in YZ-$LiNbO_3$ (a) Patterned IDT fingers represented by coupled sets of nodes on the meshed substrate are shown (b) The application of impulse voltage at the transmitting generates Rayleigh waves which propagate in both the directions. The coupled IDT finger pairs are shown in green.

The IDT fingers were modeled as mass-less conductors and were represented by a set of nodes coupled by voltage degrees of freedom (DOF). A total of approximately 80,000 elements (more than 100000 nodes) were generated. The model was created to ensure higher node density at the surface and throughout the middle of the device to study the different modes of surface acoustic waves and the use of tetragonal elements with 4 DOF ensured the same. Three DOF's provided the displacements in the longitudinal (x), normal (y), and the shear horizontal (z) directions and a fourth for the voltage.

The structure (with and without sensing layer) was simulated for a total of 100 nanoseconds (ns), with a time step of 1 ns. The excitation of the structure was provided by applying an impulse function on the transmitter IDT fingers.

$$V_i = \begin{cases} \dfrac{1}{T_s}, 0 < t \le T_s \\ \\ 0, t > T_s \end{cases} \tag{7.5}$$

7.5 Sensing layers

The simulations of SAW gas sensor device were carried out for two different material properties of the sensing layer. The first part of the simulation involved calculating response at the output IDT for material property of the sensing layer without any gas adsorbed. In the second part, the material property of the film was varied in accordance with the changes expected for 3% hydrogen gas absorption. This would require the sensing film volume to be increased by 10% to compensate for the expansion due to mass change. The structure density was decreased by 2% and Young's modulus of elasticity changed from 128 GPa to 110 GPa[233,234].

Thin palladium films known to have high affinity for hydrogen were utilized as sensing layers in the present study. A 500 nm thick palladium film was defined between the two IDT ports. The film width and length were taken as 100 and 88 microns respectively. Interaction with H_2 gas results in changes in the palladium film properties which in turn affects the wave propagation velocity. For a known change in propagation velocity, the concentration of hydrogen gas could be calculated. The key factors contributing to the velocity change are variations in mass loadings, elastic constants and conductivity. Absorption of H_2 leads to a decrease in density and Young's modulus of elasticity.

7.6 Results and discussion

The voltage and displacement waveforms with and without hydrogen absorbed into a thin Pd film are shown in the Fig. 7-2 (a) and (b). The changes in material properties in accordance with hydrogen sorption results in a time delay of around 3 ns in these waveforms at the nodes representing the output IDT's. The substrate is anisotropic and hence the displacement profiles along the different directions independent of each other. The maximum time shift occurs in the surface normal displacement component (U_z) which is the closest to the Rayleigh mode.

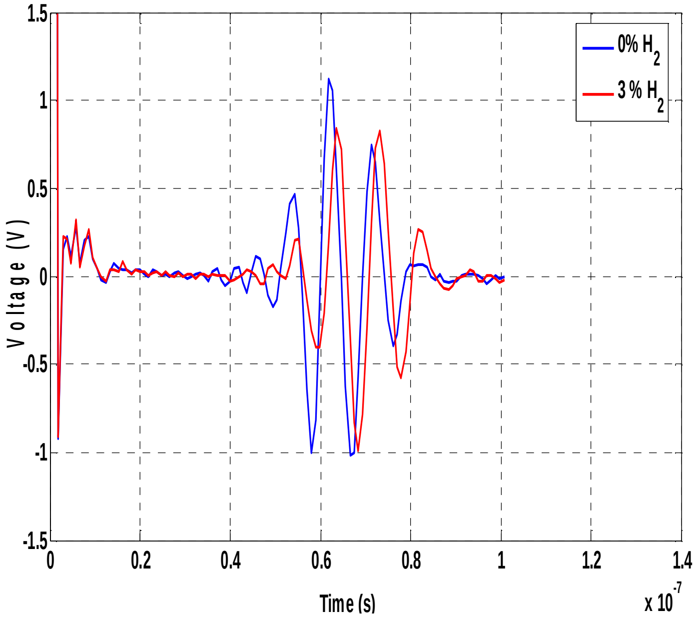

(a)

Figure 7-2. Voltage and surface normal displacement (U_z) profile at the output IDT, with and without hydrogen absorbed.

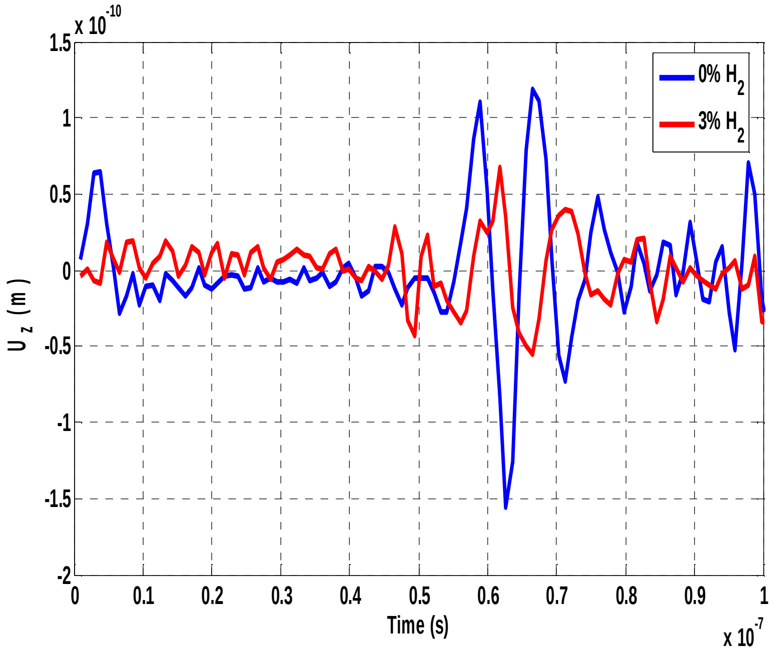

(b)

Figure 7-2: Continued

Also, the sorption of H_2 results in wave attenuation of the voltage and displacement waveforms. The least attenuation and time delay is experienced in the x-direction which represents the shear horizontal component (Fig. 7-3 (a)) of the generated wave. A 3D representation of the wave propagation in the YZ substrate is shown in Fig. 7-1. The input and the output IDT's are placed on the right and left side of the substrate. The wave travels from the input IDT to the output. The generated wave also travels outside the aperture of the IDT along the x-axis thereby dispersing part of the energy in the shear horizontal direction.

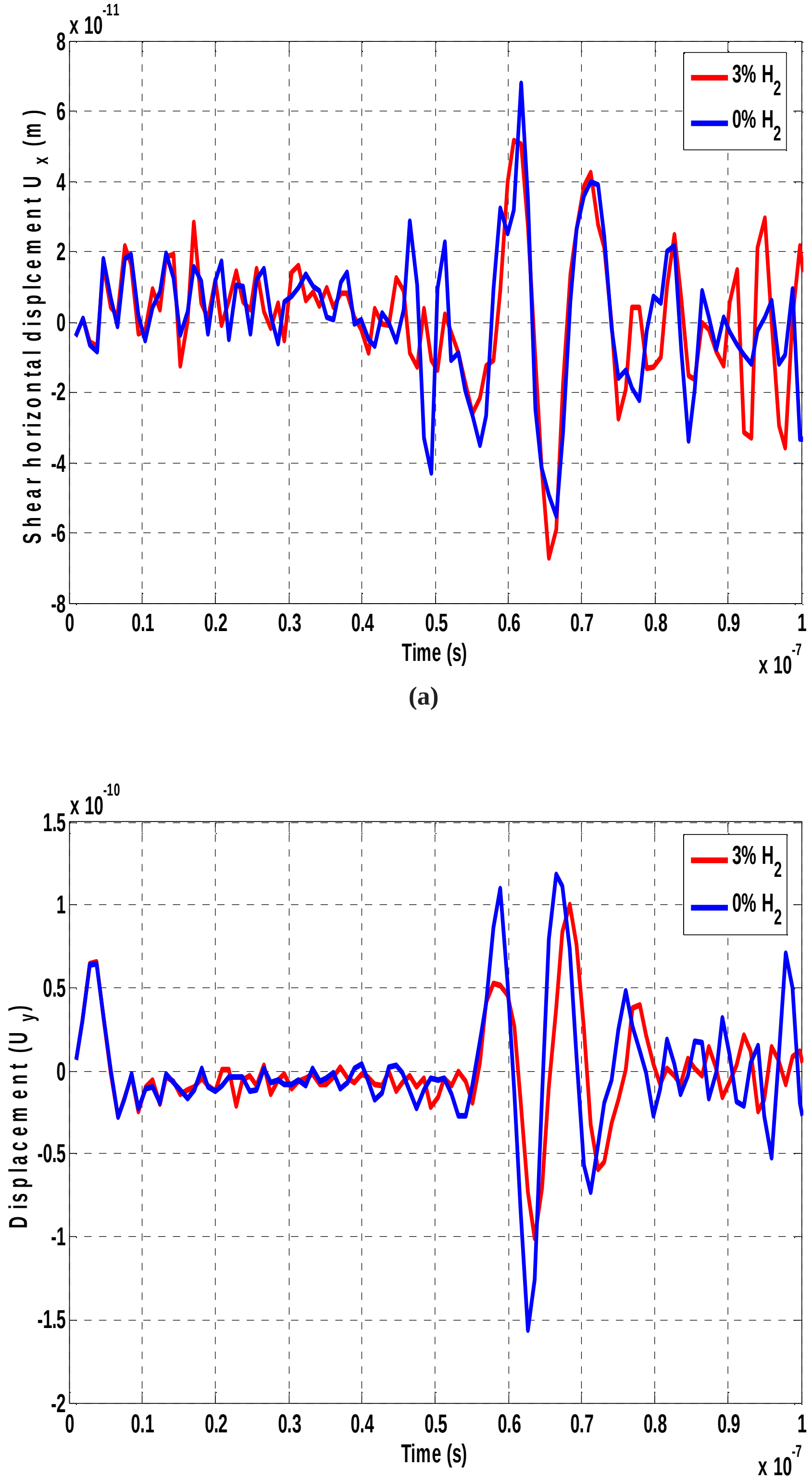

(a)

(b)

Figure 7-3. Displacement along the x (shear horizontal) and y-direction at the output IDT with and without hydrogen absorbed.

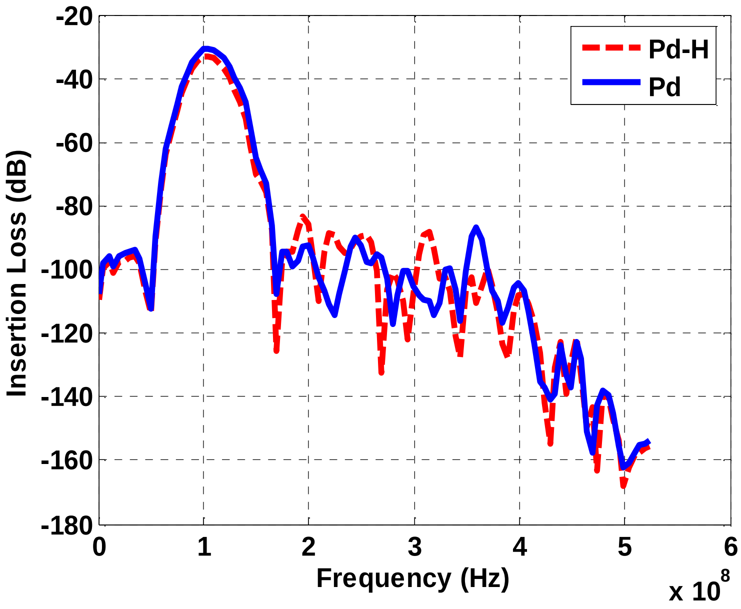

Figure 7-4. Frequency response of the SAW device with and without absorbed hydrogen.

Fig. 7-4 shows the frequency response at the output IDT. The sorption of hydrogen results in approximately 1.8 dB insertion loss for a ~100 MHz device. This result is comparable to typically observed experimental values.

7.7 Limitations of finite element simulations

A fine mesh generation is required for accurate modeling of a SAW gas sensor. The incorporation of a nanomaterial sensing layer would result in significant differences in the length scales of substrate and sensing layer, thereby requiring much higher node densities. Also, the simulations are time consuming. Simulation time will increase with increasing mesh size. Another major setback arises from acoustic wave reflection from the edges if the simulations are carried out for sufficiently longer times. One of the ways to overcome this limitation would be employment of damping elements at the ends of the substrate. While longer simulation times are necessary to attain a stable state, too long a simulation time results in wave reflections causing instabilities to set in. A simulation time of 100 ns was found to be optimum for the substrate dimensions considered in the present study.

7.8 Conclusions

3-D finite element models of SAW sensor with and without a sensing layer were developed to gain insights into the mechanism of sensor response. The gas absorption was modeled by changing the material properties of the sensing layer. Changes in the Young's modulus of elasticity and density of the palladium film were introduced into the simulations. Displacement and voltage profiles were calculated at the output nodes of the receiving IDTs. The finite element model reveals that the Rayleigh mode (z-direction displacement) is the most suitable for gas sensing. A time shift of approximately 3 ns and an insertion loss of 1.8 dB were observed when the gas sensor with thin Pd film was exposed to 3% H_2. The finite element modeling and simulation provides a powerful means to study surface acoustic wave propagation characteristics.

7.9 Nomenclature

T – Vector of mechanical stresses

S – Vector of mechanical strains

E – Vector of electric field

D – Vector of dielectric displacement

$\mathbf{c}^{\mathbf{E}}$ – Mechanical stiffness matrix for constant electric field E.

$\boldsymbol{\varepsilon}^{s}$– Permittivity matrix for constant mechanical strain

e – Piezoelectric matrix

φ –Electric potential function

u - Displacement

ρ – Substrate density

t – Time

Chapter Eight

Applications in Biosensing: Elimination of Biofouling

8.1 Abstract for chapter eight

All transducer devices used in biological species detection suffer from fouling resulting from the binding of non-specific protein molecules to the device surface. Acoustic streaming phenomenon, which results from the fluid motion induced by high intensity sound waves, can be used to remove these non-specifically bound proteins to allow more accurate determinations and reuse of these devices. In this paper, we present a computational and experimental study of the acoustic streaming phenomenon induced by surface acoustic waves (SAWs).

A coupled field fluid-structure interaction (FSI) model was developed to study surface acoustic wave interaction with fluid loading. Specifically, finite element models of a SAW device based on a micron sized piezoelectric substrate (YZ-$LiNbO_3$) in contact with a liquid loading were developed and solved to gain insights into the acoustic streaming phenomenon in SAW devices. The interdigitated transducer (IDT) fingers on the $LiNBO_3$ surface were modeled as mass-less conductors and used to simulate MHz frequency devices. Fluid domain was modeled using the Navier Stokes' equation; the arbitrary Lagrangian Eulerian approach was employed to handle the mesh distortions arising from the motion of the solid substrate. The fluid was modeled as incompressible, viscous, and Newtonian. The fluid-solid coupling was established by maintaining stress and displacement continuity at the fluid-structure interface. The fluid mesh was continuously updated as the piezoelectric substrate undergoes deformation. A transient analysis was carried out by applying a time varying voltage to the transmitter IDT fingers. Simulation results predict strong coupling of ultrasonic surface waves on the piezoelectric substrate with the thin liquid layer causing wave mode conversion from Rayleigh to leaky SAW which leads to acoustic streaming.

The above models were utilized to investigate methods for increasing induced acoustic streaming velocity while minimizing the effect on the antibody sensing layer in immuno-sensors. The transient solutions generated from the model were utilized to predict trends in acoustic streaming velocity for varying design parameters such as voltage intensity, device frequency, fluid viscosity and density. The extent of SAW induced streaming was found to be influenced by the device operating conditions as well as fluid properties. These results agree well with the analytical solution formulated in this study, on the basis of successive approximation method applied to Navier Stokes equation (Nyborg's theory) and perturbational techniques such as the Campbell-Jones method. Additionally, the model predictions were utilized to compute the various interaction forces involved and thereby identify the possible mechanisms for removal of non-specifically bound proteins. The streaming velocity fields computed using the finite element models in conjunction with the proposed mechanism were used to identify the conditions leading to improved removal efficiency. Predictions of the model are in good agreement with the experimentally observed trends of non-specific protein removal in typical SAW biosensing operation.

8.2 Biosensing

Fluid motion induced from high intensity sound waves is called acoustic streaming[235]. Surface acoustic waves propagating on the surface of a piezoelectric device can be used to induce acoustic streaming within the fluid[236-238]. The streaming phenomenon finds applications in various processes ranging from micro-mixing[239-241], surface reactions[242], sonic cleaning[243] to biological detection[244] amongst several others[245-247].

SAW and other transducer devices used in biological species detection suffer from fouling that results from binding of non-specific protein molecules[248-250] to the device surface. The acoustic streaming phenomenon can be used to remove these non-specifically bound proteins to allow more accurate determinations and reuse of these devices[251]. The generated sound fields cause tangential fluid motion along the inter-phase boundaries. These motions exert steady viscous stress on the boundary layer leading to liquid circulation near the boundaries. Although these stresses are not large, they are still significant enough to remove loosely bound material on the surface of the device. Understanding the fluid dynamics in such a system is useful for efficient removal of non-specifically bound proteins[252]. Towards this end, we focus on how acoustic streaming transforms into a velocity field profile near the interface region of the piezoelectric substrate and the fluid loading.

Surface acoustic waves are generated by the application of an alternating voltage signal to interdigital transducers patterned on a piezoelectric substrate[253-255]. The IDT geometry dictates the wavelength of the excited wave. The amplitudes of the SAWs depend on the applied voltage input, and are typically in the nanometer range. SAWs such as Rayleigh waves have a displacement component normal to the propagation direction. When in contact with a liquid, they tend to couple strongly with the liquid and leak ultrasonic power into the fluid in the form of acoustic waves called leaky SAWs. The leaky SAWs decay exponentially with distance from the source. The SAW interaction creates a net pressure gradient in the direction of sound propagation in the fluid which leads to an internal, acoustically induced streaming phenomenon. Experimentally, the resulting flow profiles can be captured using various techniques. Flow visualization employing a dye solution and a fluorescence video microscope has been utilized by Kondoh and Shiokawa[236,245,256,257]. On the other hand, Guttenberg et al. used fluorescent correlation microscopy (FCS) where movement of fluorescent particles are evaluated at the focal point of a confocal microscope using time autocorrelation of the intensity fluctuations[237]. A velocity map can be generated by successive measurements at different positions inside the fluidic device.

Computational techniques such as finite element (FE) present an alternative to the experiments and can be used for more precise calculation of the flow field and velocity. Most of the previous theoretical investigations were based on methods such as that of Campbell-Jones, which involves obtaining numerical solutions to the complex characteristic equations for leaky wave velocity or perturbational techniques, which treats leaky wave as a first-order perturbation on the non-leaky wave associated with surface-wave propagation, when the mechanical properties of the fluid are neglected. These techniques include many simplifying approximations[222,223,258-262] and are typically used to study acoustic streaming in simplified geometries. FE models developed so far have been mostly limited to solving for the fluid domain where the solid motion is superimposed as a boundary condition.[240,258] To capture the dynamics of fluid-solid interaction, the equations of motion for the fluid elements must be solved in conjunction with the acousto-electric equations for the motion of the solid. FE models involving coupling of fluid and solid domains have been constructed using acoustic elements for modeling the fluid region. However, these models solve only the simplified Navier-Stokes equation for the pressure field in the fluid and ignore viscous dissipation.[263] Uniform mean density and mean pressures are assumed, with the pressure solution being the deviation from the mean pressure, not the absolute pressure. The application of these models is limited to the study of wave damping.

A coupled field analysis is required to analyze the interactions between the solid motion and the induced fluid flow. In the present case, the problem of interest requires us to model fluid motion which can be accomplished using fluid elements which solves the generalized Navier-Stokes equation. To the best of our knowledge, no FE model involving coupled field analysis of fluid-piezoelectric solid devices has been presented in the literature so far. In the present work, FE models involving fluid-piezoelectric interaction are developed to study flow profiles in the interface region of a SAW biosensor device. The coupled field models are utilized to investigate methods for increasing induced acoustic streaming velocity while minimizing the effect on the antibody sensing layer in immuno-SAW sensors. Parameters studied in this model include voltage intensity, frequency, fluid density, and viscosity. The transient solutions generated from the model are used to predict trends in acoustic streaming velocity. Comparisons of model predicted trends with experimental data on the removal of non-specifically bound proteins from the sensing layers are also presented.

8.3 Computational details

The sequential coupling algorithm in ANSYS[264] was utilized to simulate the fluid-structure interactions. In this iterative coupling procedure, each domain (solid piezoelectric and fluid) is solved sequentially and the governing matrix equations for the two are solved separately. The solver iterates between each physics field (piezoelectric and fluid) until loads transferred across the interfaces converge. The nonlinear transient fluid-solid interaction analysis involves the following set of equations:

8.3.1 Solid domain

The propagation of acoustic waves in piezoelectric materials is governed by the mechanical equations of motion and Maxwell's equations for electrical behavior[253,265]. The constitutive equations of piezoelectric media in linear range coupling the two are given by:

$$T_{ij} = c_{ijkl}^{E} S_{kl} - e_{kij}^{t} E_k \tag{8.1}$$

$$D_i = e_{ikl} S_{kl} + \varepsilon_{ik}^{S} E_k \tag{8.2}$$

In the above equations, T_{ij} represent the components of stress, c_{ijkl}^{E} the elastic constant for constant electric field, S_{kl} the strain, E_k the electric field intensity, D_i the electric displacement, e_{kij}^{t} the piezoelectric constant, and ε_{ik}^{S} the permittivity for constant strain. The acoustic wave propagation velocity is five orders of magnitude smaller than that of electromagnetic waves. Therefore, the quasistatic assumptions help reduce Maxwell's equation to $\frac{\partial D_i}{\partial x_i} = 0$ and $E_i = -\frac{\partial \phi}{\partial x_i}$, where φ represents the electric potential.

The components of strain are defined by

$$S_{ij} = \frac{1}{2}\left(\frac{\partial u_i}{\partial x_j} + \frac{\partial u_j}{\partial x_i}\right). \tag{8.3}$$

The equation of motion in the absence of internal body forces is given as

$$\frac{\partial T_{ij}}{\partial x_j} - \rho \frac{\partial^2 u_i}{\partial t^2} = 0 \tag{8.4}$$

where ρ is the density and u_i represent the components of displacement. Substituting and rearranging the above set of equations leads to a system of four coupled wave equations for the electric potential and the three component of displacement in piezoelectric materials which are solved for the piezoelectric substrate or the solid domain:

$$-\rho \frac{\partial^2 u_i}{\partial t^2} + c_{ijkl}^{E} \frac{\partial^2 u_k}{\partial x_j \partial x_l} + e_{kij} \frac{\partial^2 \phi}{\partial x_k \partial x_j} = 0 \tag{8.5}$$

$$e_{ikl} \frac{\partial^2 u_k}{\partial x_i \partial x_l} - \varepsilon_{ik}^{S} \frac{\partial^2 \phi}{\partial x_i \partial x_j} = 0 \tag{8.6}$$

These coupled wave equations can be discretized and solved for generating displacement profiles and voltages at each element/node. The piezoelectric material displacements obtained from the above equations are applied to the fluid domain at each time step.

8.3.2 Fluid domain

Fluid is modeled as an incompressible, viscous, Newtonian fluid using the Navier-Stokes and continuity equation in the Eulerian frame of reference given below:

$$\rho\left(\frac{\partial v_f}{\partial t}\right) + v_f \cdot \nabla v_f + \nabla P - 2\eta \nabla \cdot D = 0 \tag{8.7}$$

$$\nabla \cdot v_f = 0 \tag{8.8}$$

Here, v_f, P, ρ and η denote the fluid velocity, pressure, density, and viscosity, respectively. D is the rate of deformation tensor given by

$$D = \frac{1}{2}\left(\nabla v_f + (\nabla v_f)^t\right) \tag{8.9}$$

8.3.3 Fluid-solid interaction

Discretization of the fluid and solid regions in the finite element domain requires the use of either the Lagrangian or Eulerian frame of reference. The equation of motion for the structural phase (piezoelectric substrate) is described by Lagrangian frame. The fluid domain can be described by either the Lagrangian or Eulerian frame of reference. In the former, the mesh embedded in the fluid domain moves with the velocity of the fluid while in the latter, the mesh, through which the fluid moves, is fixed. A purely Lagrangian frame is incapable of dealing with strong distortions of the fluid mesh. A purely Eulerian frame for the fluid domain introduces complexity in fluid-solid coupling. Therefore, mixed Lagrangian-Eulerian or Arbitrary Lagrangian Eulerian (ALE) methods are used for kinematical description of the fluid domain. The theory for ALE has been developed by Hughes et al. for viscous, incompressible flows.[266] In ALE, the Lagrangian description is used for 'almost contained' flows and Eulerian description is used for regions where the mesh would be highly distorted if required to follow fluid motion. In the ALE framework, the fluid equation of motion can be written as[267]:

$$\rho\left(\frac{\partial v_f}{\partial t}\right)+(v_f-w)\cdot\nabla v_f+\nabla P-2\eta\nabla\cdot D=0\,; \tag{8.10}$$

where w is the grid velocity such that $w \neq v_f \neq 0$.

To account for the fluid-solid interaction, an interface is defined across which displacements are transferred from solid to fluid and pressure from fluid to solid. The fluid mesh is continuously updated as the piezoelectric substrate undergoes deformation. The coupling conditions for the interface between the fluid and the solid region are the kinematics and equilibrium condition. The kinematic equation is the no-slip condition, *i.e.* the continuity of velocity:

$$v_f = v_s = \frac{\partial u}{\partial t} \tag{8.11}$$

and the equilibrium condition is the interface continuity in tractions replaced by continuity of stresses:

$$\sigma_{ij}^S n_j^S + \sigma_{ij}^f n_j^f = 0 \tag{8.12}$$

where n_j^S is the outward normal to the solid at the solid-liquid interface in the deformed configuration, so that $n_j^S = -n_j^f$ (indices *i* and *j* define directions of components according to axes of the applied 2-D coordinate system). The above equations are represented in terms of partial differential equations which are discretized using the finite element technique[268,269]

8.4 Model parameters

A fluid-solid interaction model of acoustic streaming phenomenon using finite element technique is presented in this work. Rayleigh wave propagation on a SAW device represents a plane wave problem.[257] Hence, 2-D FE models of SAW device based on YZ-$LiNbO_3$ with a liquid loading were developed.

8.4.1 Solid domain

A micron-sized piezoelectric substrate with dimensions (800μm propagation length x 500μm depth) was simulated to gain insights into the acoustic streaming in SAW devices. Three IDT finger pairs for the input port were defined at the surface of Y-cut, Z-propagating $LiNbO_3$ substrate. The fingers were defined with periodicity of 34.87 μm. 8-node quadrilateral coupled field solid elements were used to model the solid piezoelectric domain. The IDT fingers were modeled as mass-less conductors and represented by a set of nodes coupled by voltage degrees of freedom (DOF). A total of approx. 80,000 elements (more than 100,000 nodes) were generated. The model was created to ensure higher node density at the surface and throughout the middle of the device to study the different modes of surface acoustic waves and the use of 8-node coupled field (solid) elements with 3 DOF ensured the same. Two DOF's provided the displacements in the longitudinal (x), and the normal (y) directions and a third for the voltage.

8.4.2 Fluid domain

4-node quadrilateral fluid elements were used to model the transient system involving fluid region. The fluid properties of water were used in the simulations. The velocities are obtained from the conservation of momentum principle, and the pressure is obtained from the mass conservation principle. The fluid region with dimensions (800μm length x 100μm height) was modeled as an infinite reservoir by applying pressure P=0 on the upper fluid surface in Fig. 8-1. The standard k-ε model is used to study flow in the turbulent regime.

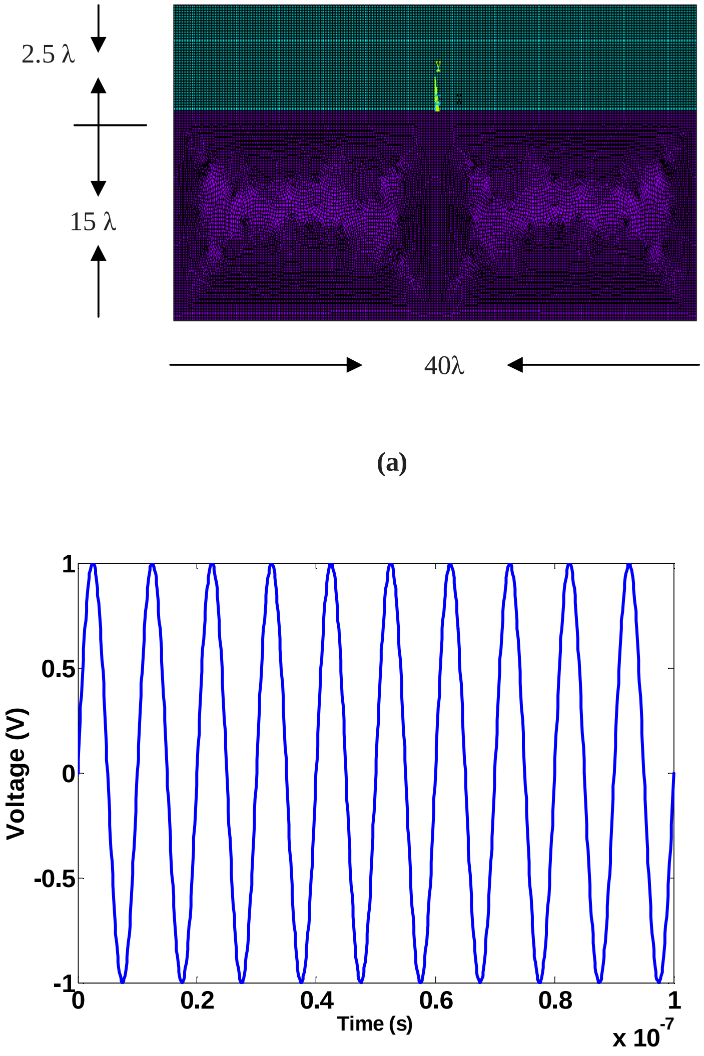

(a)

(b)

Figure 8-1. (a) Finite element model of liquid loading on a SAW device. Fluid domain is shown in green and the solid piezoelectric domain is shown in purple. The IDT fingers (not shown) are located at the center of the device on the fluid-piezoelectric interface (b) Applied input voltage profile for a 100 MHz SAW device.

8.4.3 Structure excitation

The center frequency of SAW devices simulated in this work is in the range of MHz. Hence, the structure was simulated for a total of 100 nanoseconds (ns), with a time step of 0.5 ns. The excitation of the piezoelectric solid was provided by applying an AC voltage (with varying peak values and frequency of 100 MHz) on the transmitter IDT fingers as shown in Fig. 8-1 (b).

8.5 Results

The following sections discuss the wave mode conversions that results from the imposed fluid loading as well as the flow profiles of the induced fluid motion. The effect of various design parameters on the streaming velocity profiles is also presented.

8.5.1 Rayleigh wave mode conversion

When the surface acoustic wave propagation surface comes in contact with a liquid medium, mode conversion from Rayleigh to leaky SAWs occurs. These leaky SAWs propagate along the boundary and excite longitudinal waves into the fluid at Rayleigh angle (θ) given by[260,261]:

$$\theta = Sin^{-1}\left(\frac{v_w}{v_R}\right)$$

v_w and v_R are the wave velocities in the liquid and piezoelectric medium. This ultrasonic radiation mechanism is shown in Fig. 8-2.

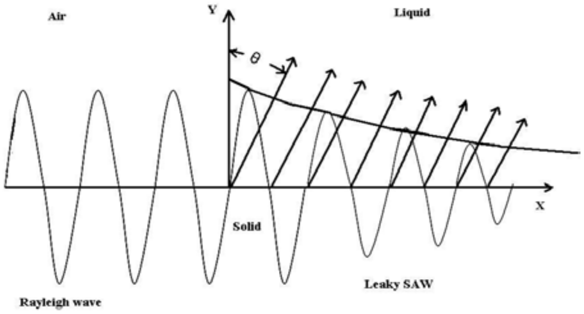

Figure 8-2. Ultrasonic radiation into the fluid medium.

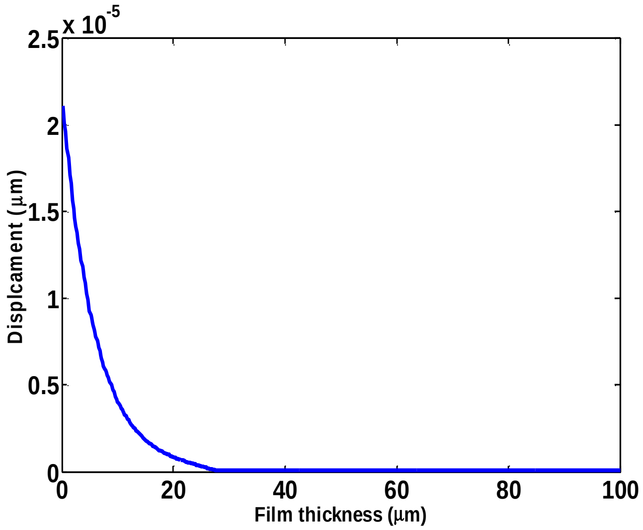

Figure 8-3. Displacement profile along the film thickness induced as a result of leakage of ultrasonic SAW power into the fluid. The exponential decay with distance from the source is similar to that of leaky SAW. The applied voltage was 0.1 V for a SAW device operating at 100 MHz.

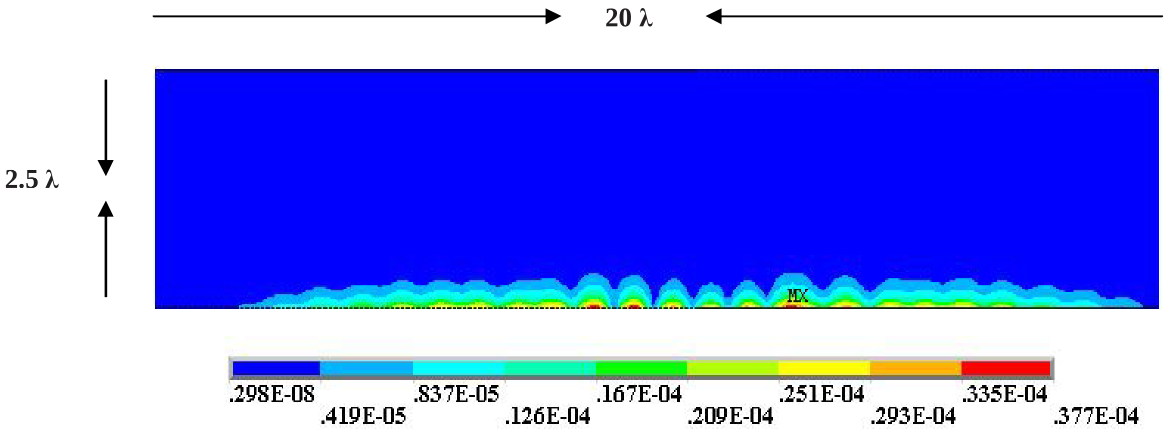

Figure 8-4. Contours showing particle displacement profile (microns) in fluid region for an applied AC peak voltage of 1 V. The wave decays with distance from the IDT fingers located at the center of the device. The displacements in the solid have been suppressed for clarity.

The generated longitudinal sound waves in the fluid medium are attenuated by the viscosity along their transmission through the medium. The displacement profile along the fluid film thickness for an applied voltage of 0.1 V is shown in Fig. 8-3. It can be seen that the mode conversion from Rayleigh to leaky SAW leads to an exponential decay in the fluid. The extent of the decay is dictated by the applied input voltage as well as the viscous dissipation encountered by the longitudinal wave in the fluid medium. The leaky surface wave also decays along the propagation length as shown by the displacement contours in Fig. 8-4.

8.5.2 Structural motion

The application of AC voltage on the IDT fingers located at the surface of the piezoelectric substrate results in mechanical deformations which causes acoustic wave propagation through the solid medium. The displacement waveforms along the depth of the piezoelectric substrate at two different locations along the SAW delay path are shown in Fig. 8-5. As can be seen from the depth profiles, most of the acoustic energy is confined to within a depth of 1-1.5 wavelengths into the substrate. As the acoustic wave propagates along the delay path, dissipation of acoustic energy occurs due to Rayleigh mode conversion into leaky SAW. As a result, the solid displacement is dampened with distance along the delay path. The displacement amplitudes of surface particles located at 10 micron distance from the IDT's is approx. 30 Å and reduces to 5 Å at 60 microns along the delay path for an applied input voltage of 1 V for a SAW device operating at 100 MHz.

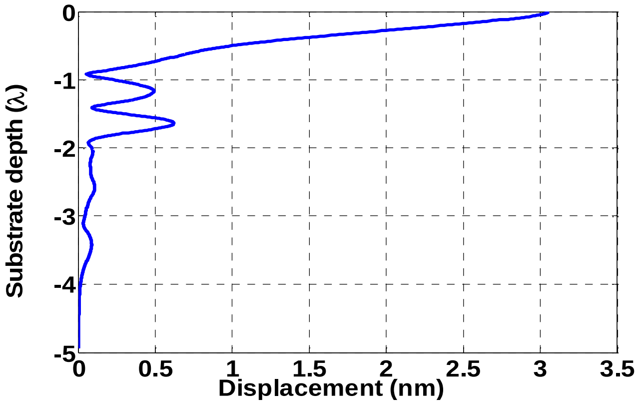

(a)

Figure 8-5. Normalized displacement profiles along the depth of the piezoelectric substrate. (a) and (b) represent the displacement profiles at two different locations (10 and 60 microns, respectively) along the SAW delay path.

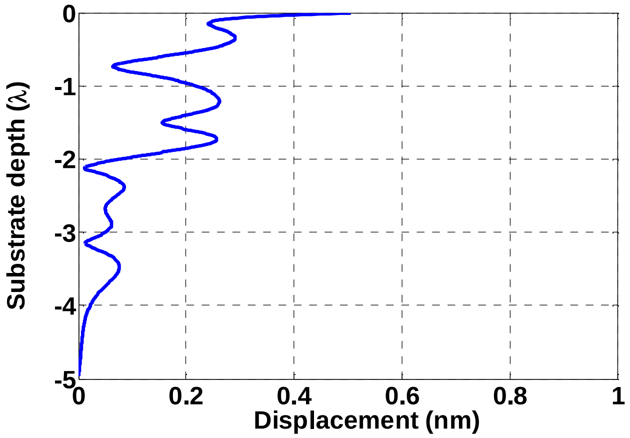

(b)

Figure 8-5: Continued

8.5.3 Fluid motion

As brought out in the earlier sections, the mode conversion from Rayleigh to leaky SAW results in longitudinal wave propagation into the fluid medium. If the intensity of the longitudinal waves propagating through the fluid is high enough, then the attenuation results in a net pressure gradient along the propagation direction of the wave. The induced gradient causes a flow in the fluid. This conversion of attenuated sound wave into a steady flow represents a nonlinear effect termed as acoustic streaming. The streaming effect that results from mode conversion is much stronger than that induced from a spatially constant amplitude plane wave.[236]

The fluid motion induced by the IDTs at a time instant (i.e. t=5 ns) is shown in Fig. 8-6. The fluid is expelled by the transducers to the top and flows back to the IDT regions from the bottom and top. Depending on the extent of the viscous damping, the flow velocity decays rapidly with distance from the IDT.

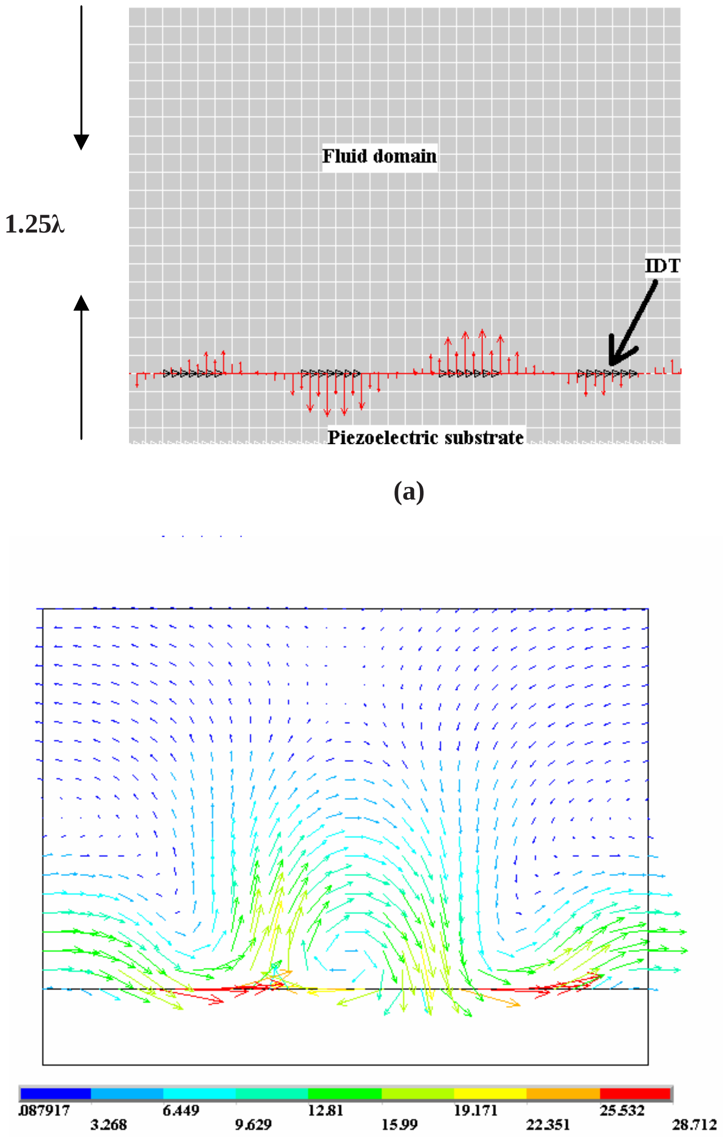

(a)

(b)

Figure 8-6. (a) Displacement of IDT fingers as indicated by arrows (b) Velocity vector plot at a given time instant (*t=5ns)* showing fluid recirculation over the IDT region shown in (a). The observed velocities are in µm/s.

It can be seen that the induced velocities are typically in microns/sec. The maximum velocity occurs at the layer closest to the piezoelectric surface. The recirculation patterns resulting from the wave motion gives rise to eddy formation. With increasing time, these eddies rise through the fluid and break into smaller ones, thereby dissipating their energy while new ones are created at the interface. Thus, the generated sound fields cause tangential motion along the inter-phase boundaries. These motions exert steady viscous stress on boundaries where the circulation occurs as shown in Fig. 8-6. Although these stresses are not large, they are still significant enough to remove loosely bound material on the surface of the device. Our simulation results indicate that the extent of recirculation decreases with increasing distance from the IDTs. It can therefore be seen from Fig. 8-7 that the generated shear stresses at the device surface also decay rapidly with distance from the IDT fingers. Optimization of design parameters such as fluid density, viscosity and applied voltage amplitude and frequency which could help generate sufficient shear stresses along the entire delay path (typically 100λ) thereby facilitating removal of nonspecifically bound proteins. The subsequent sections discuss the effect of some of the above mentioned parameters on the induced streaming velocity.

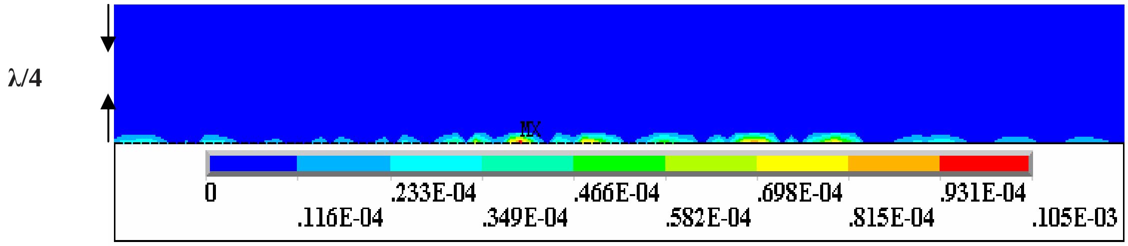

Figure 8-7. Shear stresses (MPa) generated as a result of the recirculation at the surface of the SAW device. The applied input voltage was 0.1 V and the fluid viscosity was 10 cP.

A series of simulations were performed to observe the effect of changing voltage intensity, excitation frequency, and fluid properties such as viscosity and density on the streaming velocity and its patterns. It is observed that the flow patterns described above are not influenced by the simulation conditions, but the magnitude of the acoustic streaming velocity is strongly influenced. Therefore, for the following analyses, only the variations of the streaming velocity magnitude along vortex centers located at various positions along the delay path are compared and discussed in the subsequent sections.

8.5.4 Acoustic streaming theory

The governing equations for acoustic streaming were derived by Nyborg (1958)[235] and are given by:

$$\mu\nabla^2 v_2 - \nabla p_2 = F\,, \tag{8.13}$$

$$F = \rho_0 \langle v_1 . \nabla v_1 + v_1 \nabla . v_1 \rangle \tag{8.14}$$

In the above equations, μ is shear viscosity, ρ_0 is the constant equilibrium density, v_1 is the oscillatory particle velocity, v_2 is the acoustic streaming velocity, p_2 is the steady state "dc" pressure, F is the nonlinear driving force term, and the angular brackets denote the time average over sufficiently large number of cycles.[270,271]

The leaky SAW propagates along the boundary and excites longitudinal wave into the liquid. The propagation constant (k_L) for leaky SAW is a complex number, with the imaginary part accounting for the extent of energy dissipation into the fluid medium. The particle displacements in the normal (u_x) and tangential (u_z) direction in the liquid can be put in the following form:

$$u_x = A \exp(j\omega t) . \exp(-jk_L x) \exp(-\alpha k_L z) \tag{8.15}$$

$$u_z = -jA\alpha \exp(j\omega t) . \exp(-jk_L x) \exp(-\alpha k_L z) \text{, where } \alpha = 1 - (v_L / v_w)^2 \tag{8.16}$$

A refers to the amplitude of SAW displacement, $\omega=2\pi f$ is the angular frequency; v_L and v_w represent the leaky and longitudinal wave velocities, respectively. The wave number (k_L) and velocity (v_L) of the leaky SAW can be computed by extending the method of Campbell-Jones to solid-liquid structures assuming displacement and stress continuity at the interface.[222,223] The oscillatory particle velocity v_1 can be found using $v = \frac{\partial u}{\partial t}$. The first order velocity comprises of two terms. The first varies with z as exp ($-\alpha z$) and represents the mass loading response of the fluid.[238,272,273] The second term (ignored in the solution) varies with z as exp ($-(1+j)\beta z$), where $\beta = \omega/\sqrt{2\nu}$, and represents the viscous response of the fluid. For the case of water loading at typical operational frequency of 100 MHz, $1/\beta$ which represents the viscous boundary layer was found to be less than 0.02 microns. Hence $\beta z >> 1$ and the second term can be ignored. Substituting the first order velocity into Eq. (8.14), we obtain the following components of force **F**:

$$F_x = -\rho_0 (1+\alpha_1^2) A^2 \omega^2 k_i \exp 2(k_i x + \alpha_1 k_i z) \tag{8.17}$$

$$F_z = -\rho_0 (1+\alpha_1^2) A^2 \omega^2 \alpha_1 k_i \exp 2(k_i x + \alpha_1 k_i z) \tag{8.18}$$

where, $\alpha=j\alpha_1$, $k_L=k_r+jk_i$ The force calculated above acts as a body force near the SAW-fluid interface. The decaying exponential factors in v_1 limit the extent of force into the fluid. This force which varies as the square of the first order velocity, in turn produces the second-order velocity v_2 Substitution of the above Eq. (8.17) and (8.18) into (8.13) would allow for predicting the acoustic streaming velocity induced as a result of SAW streaming. The leaky SAW velocities, wave numbers, attenuation factors as well as the SAW streaming force calculated based on the above formulation for two different crystal orientations are summarized in Table 8-1.

Table 8-1. Leaky SAW velocity and streaming force calculated using Nyborg streaming equations with parameters derived from the Campbell-Jones method. SAW streaming force is calculated at x=y=0 for a 100 MHz device frequency and applied input voltage of 1 V.

Crystal Orientation	Rayleigh wave velocity (m/s)	Water loaded leaky SAW velocity	Leaky SAW wave-number	Attenuation coefficient	SAW streaming force (N/m^2)
128° Y-X $LiNbO_3$	3994	3931+j68.1	2768	2.47	3.22×10^7
Y-Z $LiNbO_3$	3487	3194+j268.3	16409	1.92	4.05×10^8

The first order streaming velocity can be used to calculate the second order streaming velocity. Longuet-Higgins have given the general expression for calculating the limiting value of the second order streaming velocity (v_2) from the solution of the first order velocity[274],

$$U = \frac{-jv_m}{4\omega}\frac{\partial v_m^*}{\partial x}[8(1-\exp(-(1+j)\beta z)) + 3(1+j)(\exp(-2\beta z)-1)] \tag{8.19}$$

In the above equation, only the real part is of physical significance. U represents the tangential streaming velocity just outside the viscous boundary layer. v_m is equal to $v_{1x} - v_0$, where v_{1x} is the x-directed first order velocity and v_0 is the x-directed boundary condition on the first order velocity field at the SAW interface. For $\beta z >> 1$, the amplitude of the second order velocity obtained by substituting Eq. (8.18) into Eq. (8.19) is given by

$$U \approx \frac{5}{4}\alpha A^2 \omega k_i \tag{8.20}$$

The streaming velocity calculated above depends primarily on the wave amplitude and the excitation frequency. The viscous effects have been neglected and the density effects are implicitly accounted for through the leaky wave number k_i.

8.5.5 Streaming velocity

The finite element model of SAW streaming presented here is utilized for determining steady state streaming velocity profiles associated with a given transducer geometry and input acoustic pulse. The velocity $\boldsymbol{v}$ calculated from Eq. (8.7) and (8.8) contain harmonically varying terms and a "dc" term. The latter induces acoustic streaming. When averaged over a relatively longer time, the effect of the harmonically varying terms disappears and only the contributions from the dc part appear in the solution. The acoustic streaming velocity ($\bar{v}_{a,i}$, i=x, y, and z) is therefore obtained by averaging $\boldsymbol{v}$ over a time period as follows:

$$\bar{v}_{a,i} = \frac{1}{T}\int_0^T v_i dt \text{ , i}=x, y \text{ and } z$$

where T is the time period of the wave propagation.

The time averaging was applied during the various vibration cycles (for e.g. 5th cycle comprises of simulation steps #81 and #100 and gives the streaming velocity values for t=40-50 ns). The streaming velocities calculated based on the time averaging during 100-120th (t=50-60 ns) and at higher intervals do not differ significantly from the values computed at t=40-50 ns. Hence, the average streaming velocities were assumed to be cycle independent by this time (t=40 ns). The maximum streaming velocity value is found to be approximately 0.220 mm/s while the maximum instantaneous velocities reach 20 mm/s in the regions close to the IDT's for applied voltages up to 1 V and excitation frequencies up to 100 MHz. Experimentally, the observed streaming velocities are also much smaller than 20 mm/s for the loading conditions simulated in the present work and, hence for a fluid film thickness of 100 microns, the flow is characterized by Reynolds number smaller than 1. Hence the flow is completely laminar.

8.5.5.1 Effect of voltage intensity

The effect of varying input voltage intensity on the time averaged streaming velocities is shown in Fig. 8-8. The components of acoustic streaming velocities tangential and normal to the SAW device substrate along a fictitious vertical line passing through the device center are shown in Fig. 8-8. The fluid velocities are thus obtained at different positions along the fluid film thickness normal to the piezoelectric substrate.

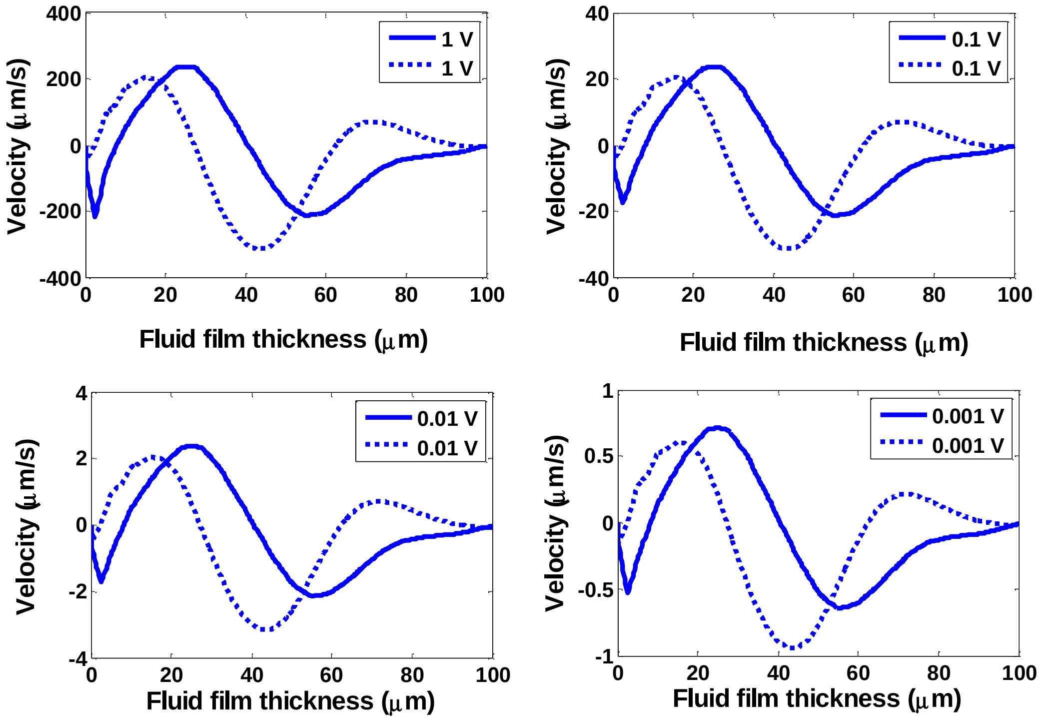

Figure 8-8. Simulated normal (solid lines) and tangential (dashed lines) streaming velocity profiles along the thickness of the fluid film. The applied input voltage shown here varies from 1 mV to 1 V. The streaming velocity profiles indicate reversal in flow direction and confirm the recirculation pattern observed in Fig. 8-6 (b).

The velocity profiles shown in Fig. 8-8 are indicative of reversal in flow direction at regions close to the SAW surface and at the center of the fluid region, thereby confirming fluid circulation patterns shown in Fig. 8-6 (b). At very short distances (<15 microns) close to the SAW surface, the tangential and normal velocity components attain a maximum before undergoing a flow reversal. This corresponds to approx. 48 and 220 µm/s in the normal and tangential directions for the typical applied input voltage of 1 V. The predicted streaming patterns are in good agreement with the experimental observations of Guttenberg et al.[237]

The tangential component of velocity has a larger magnitude than the normal for all the input voltages (Fig. 8-8). The maximum tangential flow velocity varies approximately from 0.5 µm/s to 50 cm/s, for the range of 0.001 to 100 V of input voltages. The velocities decrease rapidly with increasing distance from the IDT region as can be seen in the contour plot presented in Fig. 8-4. As the distance increases along the propagation direction, the extent of induced fluid motion and consequently the fluid velocity decrease. Most of the fluid motion is confined to within the first few layers (approx. 40 microns), especially for higher applied voltages. The extent of damping is dictated by the shear viscosity of the fluid as well as the applied wave frequency. The streaming patterns near the device substrate are directly influenced by the motion of the piezoelectric substrate, whereas those further along the fluid film are induced by streaming flows from the lower surface. It can be observed that the liquid flow is attenuated in the process of inducing streaming motions near the top liquid surface (> 80 microns). As a result, the larger streaming velocities are observed at regions near the surface of the substrate (i.e. < 20 microns). The simulated data at any particular fluid location can be fitted to a quadratic relationship of the velocity on the applied voltage.

The variation of SAW amplitude and the maximum streaming velocity with applied input voltage are shown in Fig. 8-9 (a) and (b), respectively. The maximum streaming velocity is taken at regions close to the SAW surface, before the fluid undergoes a reversal in flow direction. An increase in the applied input voltage results in a near linear increase in the amplitude of SAW motion for applied voltages higher than 0.1 V as shown in Fig. 8-9 (a). As a result, the induced streaming velocities which typically vary as square of the SAW displacement amplitudes (Eq. 4.8) show a near quadratic behavior for input voltages higher than 0.1 V.[240] The simulated maximum streaming velocity shown in Fig. 8-9 (b) agrees fairly well with the analytical solution formulated based on Nyborg’s theory, at these higher applied voltages. At low voltages

(≤ 0.1 V), the analytical solution slightly deviates from the simulated streaming velocities which could be attributed to the various approximations involved in deriving the streaming equations (section IV).

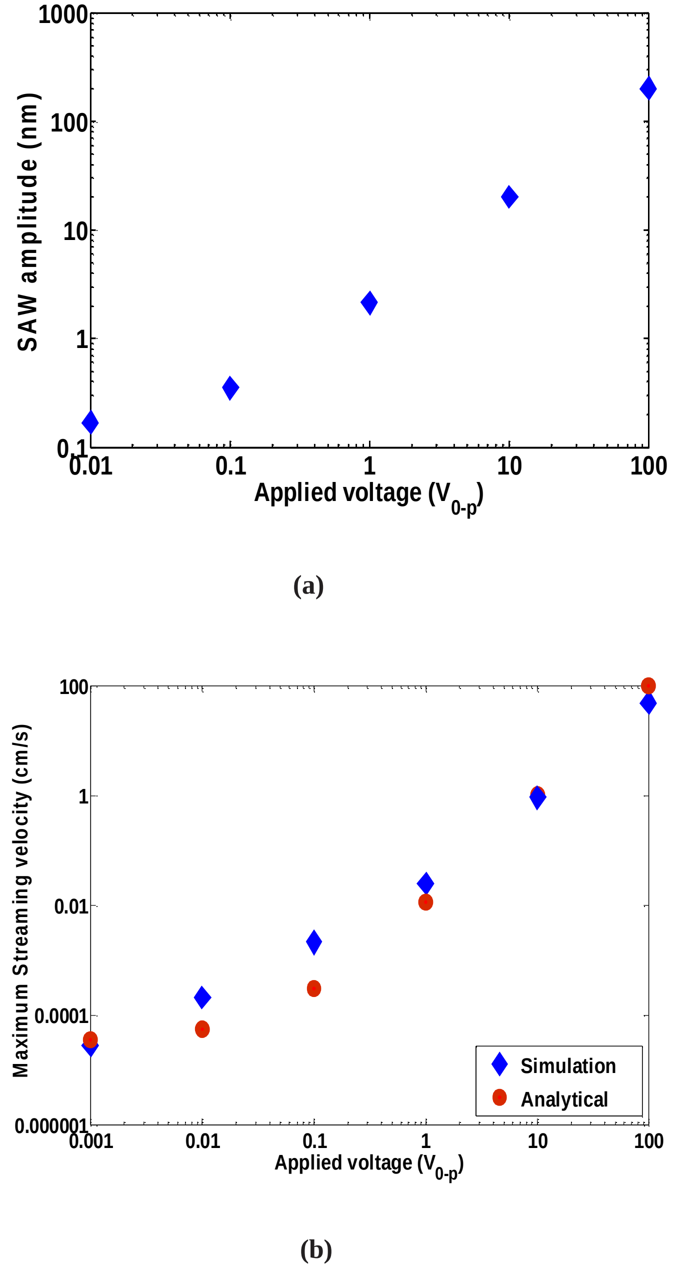

Figure 8-9. Variation of (a) SAW amplitude (b) Maximum streaming velocity with applied voltage. The simulated maximum streaming velocity varies quadratically for applied input voltages greater than 0.1 V and linearly for lower applied voltages.

8.5.5.2 Effect of input excitation frequency

The effect of the excitation frequency on the acoustic streaming velocity is presented in this section. Smallest attenuation in SAW devices is attained when the input excitation frequency matches the device frequency. SAW device operational frequency is given by $v/4f$, where v is the velocity of the acoustic wave in YZ $LiNbO_3$ and f is the finger spacing. The spacing between electrodes was modified to simulate SAW devices operating in different frequency range. Various input excitation frequencies with 1V peak amplitude and matching the device frequency were applied. The streaming velocities along the fluid film thickness obtained at distance 2.5 λ (where λ is the wavelength) along the delay path for input excitation frequencies of 100, 50, 10, and 1 MHz are shown in Fig. 8-10.

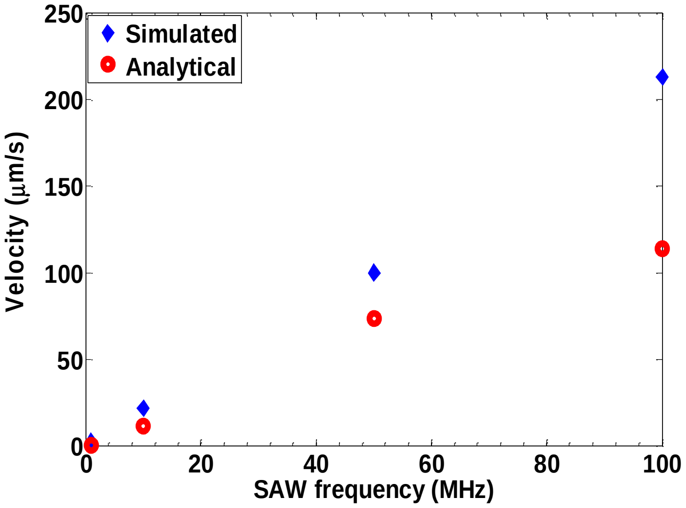

(a)

Figure 8-10. Effect of SAW device frequency on (a) tangential and (b) normal streaming velocities. The applied input voltage frequency was varied from 100 MHz to 0.1 MHz.

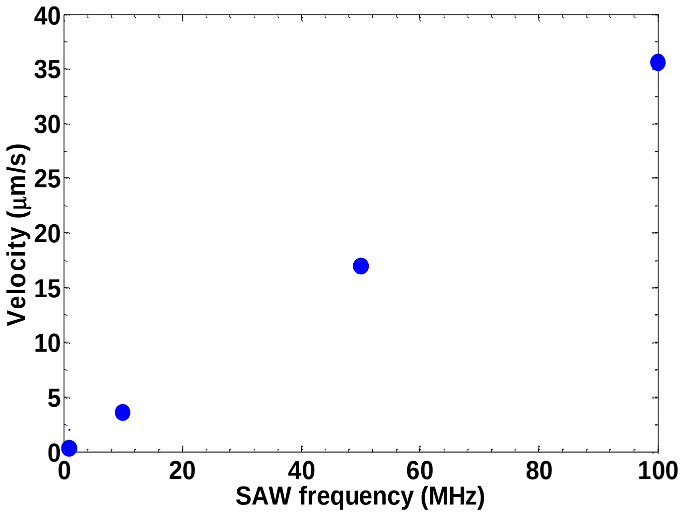

(b)

Figure 8-10: Continued

It is observed that the simulated streaming velocities increase with the device excitation frequency. We find that the tangential and normal components of the time averaged streaming velocities near the SAW surface vary from approx. 220 and 48 µm/s, respectively for a 100 MHz device to approx. 2.5 and 0.40 µm/s for a 100 KHz device with an applied peak voltage of 1 V. The simulated streaming velocities obtained in the µm/s range for devices operating in the MHz frequencies are in quantitative agreement with the experimental observations available in literature for streaming flows induced by SAW devices.[236,262,272] These experiments involved flow visualization of tracer particles, with their motion recorded using a high speed video (shutter speed, 1/500 second) and Ar ion laser light sheet. Subsequent image processing of tracer particle movements between the pictures was used to deduce the induced streaming velocities.

As the frequency of the surface acoustic wave device increases, it would lead to an increase in the irrotational velocity. This in turn results in an increase in the acoustic streaming velocity which is proportional to the square of the irrotational velocity[235]. As shown in Eq. (4.8), the streaming velocity depends on the input excitation frequency as well as the leaky SAW wavenumber which itself is a (linear) function of the SAW frequency. The tangential and normal velocity profiles are therefore expected to vary as square of the excitation frequency. However, the simulated streaming velocities in Fig. 8-10 show a near linear variation with the input excitation frequency. As brought out in Eq. (4.8), the acoustic streaming velocity is also proportional to the square of the amplitude of SAW displacement. The simulated SAW amplitudes tend to increase with decreasing device frequency as shown in Table 8-2. This has also been observed in the experimental studies of Sano et al.[236,275] Therefore, the increase in SAW amplitude somewhat offsets the corresponding decrease in the device frequency. As a result, the simulated and analytical SAW streaming velocities shown in Fig. 8-10 exhibit a near linear variation. It is interesting to note that the streaming velocities predicted analytically using Nyborg's theory are smaller than those from simulation. The analytical solution neglects the viscous effects and does not include attenuation of the flow, resulting in uniform streaming velocities across the fluid thickness.

Table 8-2. Variation of simulated SAW amplitudes for different device frequencies and input voltage of 1 V.

SAW device frequency (MHz)	SAW amplitude (nm)
100	2.15
50	3.45
10	6.84
1	10.53

The normal component of the velocity is significantly lower than the tangential for the range of device frequencies simulated in this work. This indicates that the surface normal component of the force exerted by the SAW is smaller than the tangential. Therefore, the lift-off forces would be smaller than the drag forces generated by acoustic streaming. This SAW streaming induced drag force results in the advection of particles along the surfaces and appears to be an important step in the mechanism of particle removal using surface acoustic waves. The details of the various interaction forces involved and their influence on the particle removal mechanism is discussed in a subsequent section.

8.5.5.3 Effect of fluid properties (viscosity and density)

To investigate the effect of fluid properties such as dynamic viscosity and density on the streaming velocity profiles, the FSI simulations were carried out under constant input conditions with only the fluid properties being varied. The effect of viscosity was investigated by simulating fluid loading with 1 cP and 10 cP viscosities, respectively. Amongst the various applied input voltages simulated in this study, the input voltage of 100 V represents conditions of maximum induced streaming velocities and hence the effect of fluid viscosity is discussed at this applied input voltage. The results presented here represent the upper bound on the streaming velocity variations under varying fluid viscosities. For lower applied input voltages (<1 V), we find that the variation in the magnitude of the streaming velocities with fluid viscosity is not very significant at the MHz device frequencies.

The streaming velocities obtained for the two simulations at different locations along the SAW delay path are shown in Fig. 8-11. It can be seen that at the MHz frequencies, fluid viscosity variations have a significant effect on the streaming velocities, especially near the IDT region. As the wave propagates along the delay path, it undergoes significant attenuation as is evident from the reduction in the magnitude of the streaming velocity from approx. 50 to 15 cm/sec near the fluid-solid interface for a propagation distance of approx. 2λ in a fluid having 1 cP viscosity. The effect of viscosity can be seen more prominently at distances further away from the IDT region when the wave has lost considerable energy. For locations further along the delay path (4λ), the streaming velocities rapidly decay to much smaller values (maximum of approx. 2 cm/sec for 1 cP fluid along the fluid film thickness). The rapid decrease in the streaming velocities along the fluid film thickness is attributed to wave conversion into longitudinal mode (section 3). This decay length calculated from the instantaneous velocity at t=60 ns is approx. 40 microns at 10 micron delay and approx. 30 microns at 100 micron delay.

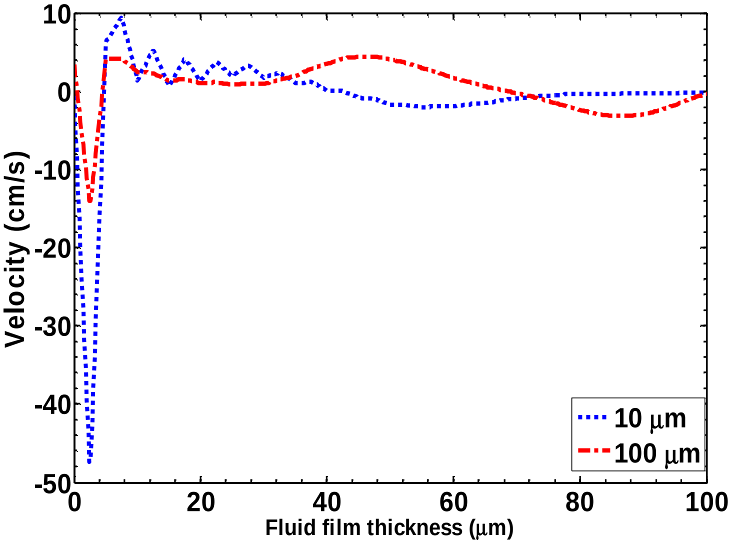

(a)

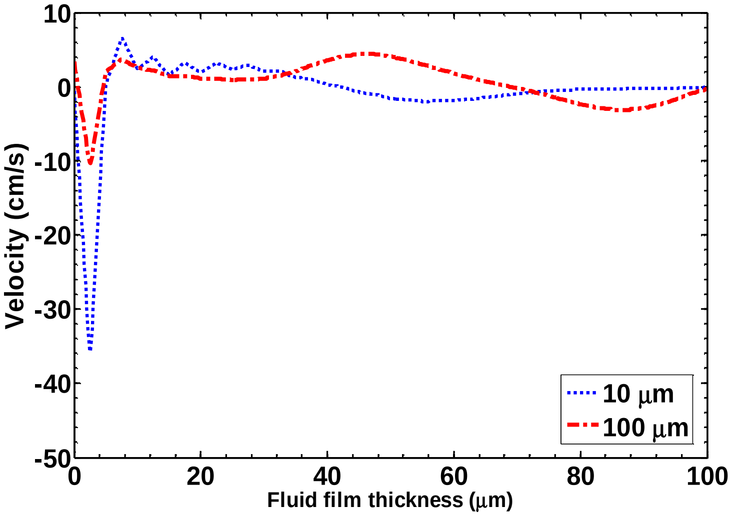

(b)

Figure 8-11. Streaming velocity profiles along the fluid film thickness for an input AC voltage of 100 V at 100 MHz and two different fluid viscosities. (a) and (b) represent two different locations on the SAW device delay path for two different fluid viscosity i.e. 1 and 10 cP, respectively.

Fig. 8-12 demonstrates the relationship between the fluid viscosity and maximum streaming velocity as determined from our simulations. We find that an increase in the fluid viscosity leads to a decrease in the streaming velocities. The decrease in the streaming velocities is attributed to the increased viscous losses. The more viscous the fluid, the lesser would be the SAW induced streaming force[244] for a given power input and hence lower would be the extent of cleaning. This is in agreement with our experimental observations reported by Cular et al. in which a reduced removal of non-specifically bound proteins from the surface of a SAW biosensor device was reported for more viscous fluids[276].

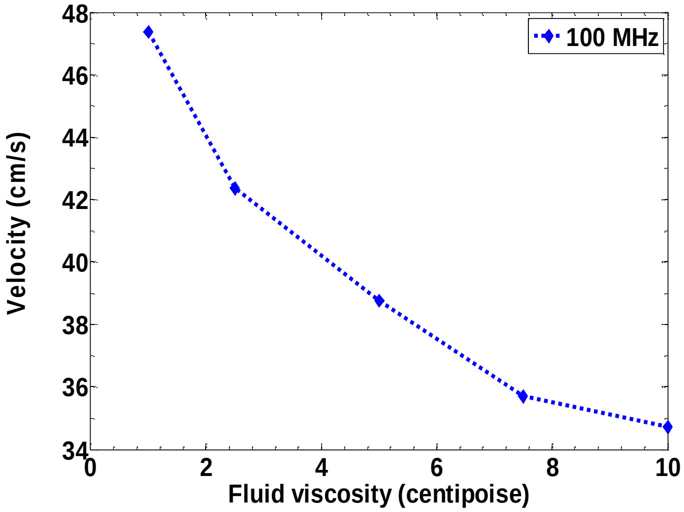

Figure 8-12. Variation in maximum streaming velocity for fluids of different viscosities. The applied input voltage was 100 V and the SAW device frequency was 100 MHz. The higher the fluid viscosity, the larger would be the force required to induce the SAW streaming.

Although viscosity variations in simulations at ultrasonic frequencies (typically in the kHz range) have not been performed, experimental findings[243] indicate that at those frequencies the wave damping due to viscous dissipation would be higher. The viscous boundary layer involved in the acoustic streaming phenomenon is defined as $\delta=\sqrt{2\nu/\omega}$, where δ is the thickness of the viscous boundary layer, ν is the kinematic viscosity and $\omega = 2\pi f$ is the angular frequency of the wave. For the range of viscosities employed in this study, the thickness of the viscous boundary layer would be tens of micrometers at ultrasonic frequencies. Inside the boundary layer, there is eddy formation resulting from the circular flow as the medium has to confirm to the no slip condition at the fluid-solid interface. The medium outside the boundary layer vibrates irrotationally in accordance with the sound field. Therefore, the extent of viscous dissipation resulting from the vortex formation near the SAW-fluid interface would be higher at ultrasonic frequencies than under megasonic frequencies and fluid viscosity would have a critical role to play.

The effect of density on the streaming phenomenon was evaluated by simulating fluids with properties similar to that of air (1 Kg/m^3) and water (1000 Kg/m^3). Although the viscosity of air (1.78x10^{-5} Kg/m.s) is significantly different from water (10^{-3} Kg/m.s), as brought out earlier, at the MHz frequencies the viscous effects are not significant. Hence the differences in the streaming profiles would result mainly from density difference between the two fluids. The simulation results for the two fluids for a SAW device operating at 100 MHz is shown in Fig. 8-13. The bulk compressibility factor (β) which is equal to the square of the sonic velocities was also varied in the simulations under study. The sonic velocity for air and water were taken as 340 and 1480 m/s, respectively. By specifying pressure P=0 at the top surface, an infinite reservoir of fluid was modeled.

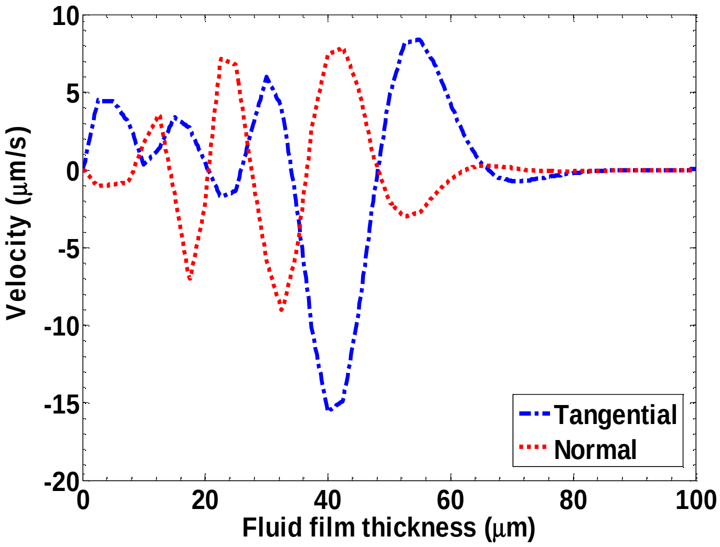

(a)

Figure 8-13. Streaming velocity profiles along the fluid film thickness for an input AC voltage of 0.001 V at 100 MHz and two different fluid densities (a) Air (b) Water. It can be seen that even at very low applied input voltages, significant differences in the streaming velocity profiles and magnitudes exist for the two simulated fluid densities.

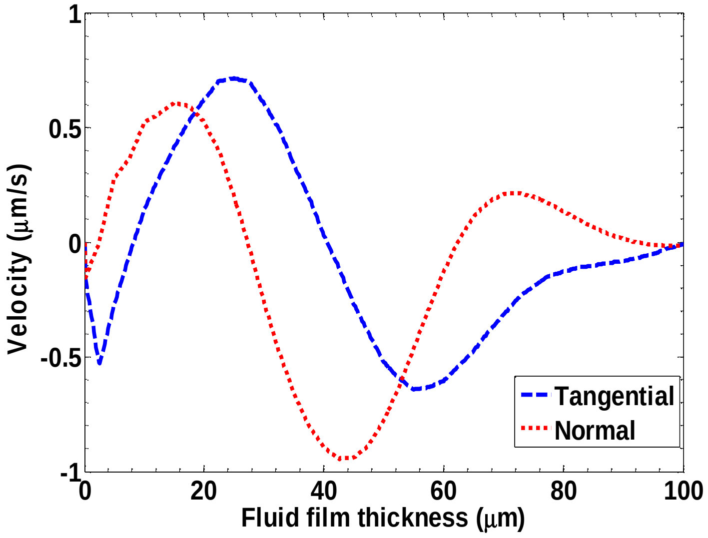

(b)

Figure 8-13: Continued

The streaming velocity profiles as well as contours for the two fluids are shown in Fig. 8-13 and 8-14. It can be seen that significant qualitative and quantitative differences exist between the velocity profiles for the two fluids. The extent of wave attenuation in case of air loading is much lower than that of water. Hence, the magnitude of streaming velocities obtained for air is an order of magnitude higher than for water loading. For lower density fluids such as air, the velocities closer to the substrate are much lower than those in the center of the fluid region. The maxima in SAW streaming velocity for both tangential (15 μm/s) and normal (8 μm/s) components, occur at a distance of approx. 40 microns from the substrate. The increase in fluid density dampens the fluid motion. The magnitude of fluid motion close to the fluid interface is comparable to that away from the interface. These findings are in qualitative agreement with the experimental streaming velocity profiles, resulting from ultrasonic vibrations, obtained by Loh et al. using particle imaging velocimetry (PIV).[277]

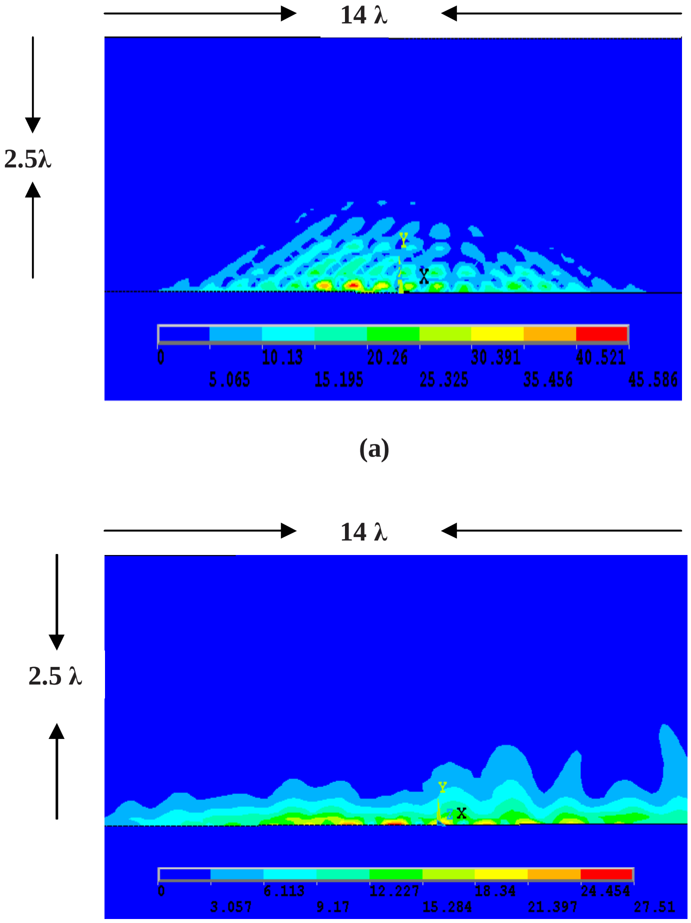

(a)

(b)

Figure 8-14. Contours showing the transient velocity field at t=40ns for an input AC voltage of 0.001 V at 100 MHz and two different fluid densities (a) Air (b) Water.

8.6 Application to surface cleaning i.e. biofouling elimination

Experimental results of the removal of non-specifically bound proteins using acoustic streaming induced by a SAW device are described in sub-section A. These experimental observations demonstrate the concept of streaming induced removal of non-specifically bound proteins and confirm the findings of the FEM simulations that SAW induced acoustic streaming phenomenon is an excellent method for surface stimulation in liquid environments. In sub-section B, useful insights into the dominant mechanism responsible for efficient removal of non-specifically bound proteins are sought from the estimates of various forces predicted on the basis of the FEM generated streaming velocity fields.

8.6.1 Experimental use of acoustic streaming to clean surfaces

A 108 MHz YZ $LiNbO_3$ SAW device was fabricated and its surface was coated with an anti-body layer (anti-mouse IgG) in a 40 µm array pattern. The pattern mask was removed and the non-anti-body coated regions were subsequently coated with Bovine Serum Albumin (BSA) as a blocking agent. An Alexa-488 fluorescently labeled 20 µl sample of BSA in phosphate buffered saline (PBS) pH 7.4 was applied to the entire (anti-body regions and BSA blocked regions) microarray surface and allowed to incubate undisturbed for 1 hour. After incubation excess Alexa-488 labeled BSA was removed with a thorough 5 ml of PBS rinsing. The prepared device was placed in a microfluidic probing fixture, connected to the necessary equipment and placed on a fluorescent microscope for intensity measurements. Full details of the complete experimental study are presented elsewhere in Cular et al.[276]

The percent intensity of regional area of the microarray was recorded as a function of RF power dose, as shown in Fig. 8-15. During the acoustic streaming, a flow rate of 150 µl / min 18 MΩ cm water was maintained except when acquiring images. Unwanted effects, such as photo bleaching, have been corrected for through the use of a control experiment that exposed an identical SAW device to all of the same conditions minus the acoustic streaming. The sum total of these unwanted effects was less than 3% of the recorded signal.

The first region in the data starts shortly after the acoustic streaming begins and ends at 1,600 mW sec. The 20% increase in intensity is thought to be from an increase in the number of light exposed fluorophores as shown by the greater distribution of Alexa-488 BSA in Fig. 8-15 (c) from the initial conditions, Fig. 8-15 (b). The second data region is a sharp decrease in intensity followed by a plateau (1,600 – 8,000 mW sec). This region has the largest decrease of intensity which correlates with the removal of the majority of loosely bound material. The third region, in the graph, is a transition region that removes the more strongly bound proteins. This is indicated from the scatter of the data in the dosage range of 8,000 to 12,000 mW sec. The data overall shows a significant reduction of the non-specifically bound BSA as shown by the reduction of intensity across the microarray in Fig. 8-15 (d).

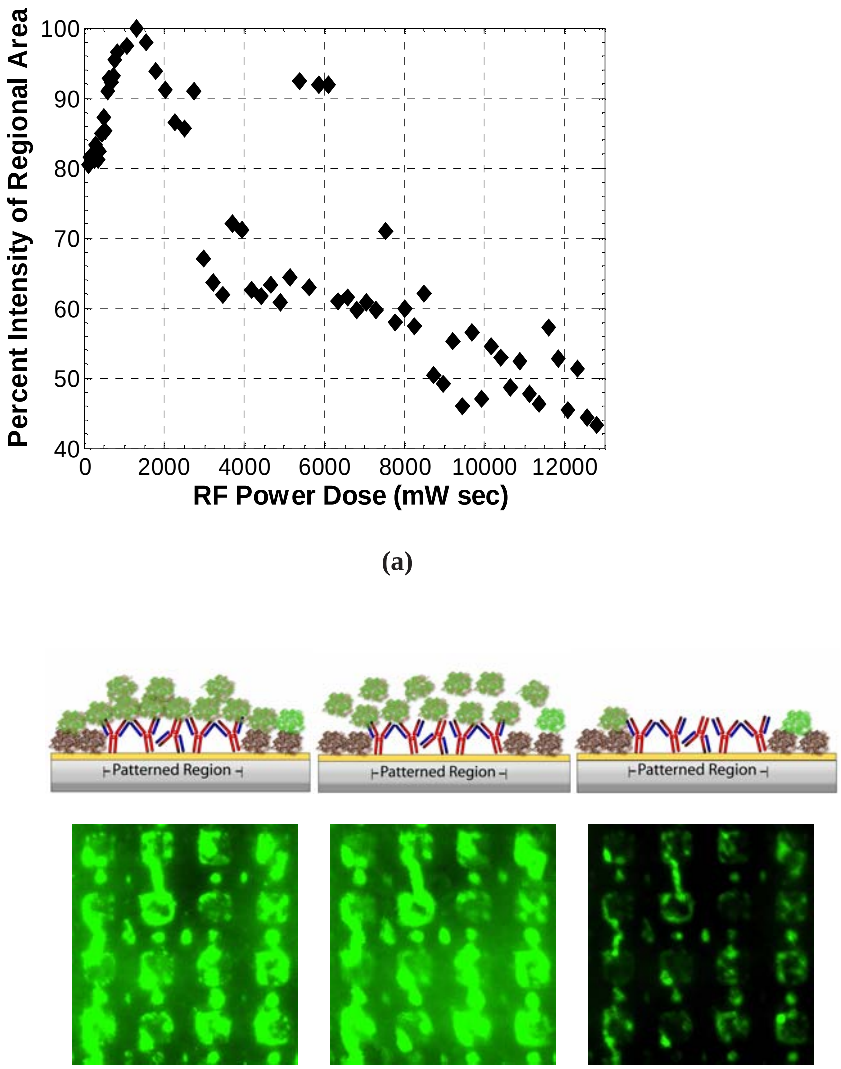

(a)

(b) (c) (d)

Figure 8-15. (a) Fluorescent intensity of Alexa-488 labeled BSA nonspecifically bound to the surface of a $LiNbO_3$ biosensor that was exposed to acoustic streaming. (b) Initial (RF Power Dose = 0 mW sec) fluorescent image (pseudo-colored) of SAW device surface with illustration above. (c) First region (RF Power Dose = 1,600 mW sec) fluorescent image (pseudo-colored) of SAW device surface shortly after turning on the acoustic streaming with illustration above. (d) Non-specifically bound BSA fluorescent image (pseudo-colored) with illustration above of SAW device surface at end of experiment (RF Power Dose = 12,500 mW sec).

8.6.2 Predicted mechanism of removal

As mentioned in the previous section, SAW sensors used for detection of biological species suffer from fouling which results from binding of non-specific protein molecules to the device surface. Fouling significantly lowers the sensitivity, selectivity as well as the sensor response speed. Removal of these non-specifically bound proteins would alleviate these problems and allow reuse of SAW devices. The finite element analysis of SAW induced acoustic streaming phenomenon presented in this work indicates that the shear forces generated from the fluid motion can be high enough to ensure the removal of non-specific proteins. The forces calculated analytically using the Campbell-Jones method[222,223] and Nyborg's theory[235] also corroborate this argument. Although an exact estimate of the principal adhesive forces such as van der Waals and electrical double layer involved in the binding of specific and non-specific proteins to the SAW surface are required to identify the conditions which allow for higher removal efficiency, the streaming velocity fields and trends predicted in the current work can be utilized to understand the mechanism which is responsible for efficient removal of non-specific proteins.

Typically, the cleaning forces on particles are hydrodynamic forces which could arise from linear as well as non-linear interactions between the ultrasonic field and the particles in fluid.[278] Linear interaction forces include added mass, drag, lift and Basset forces, whereas nonlinear ones include the drag forces that results from acoustic streaming. As mentioned in a previous section, the linear forces are time dependent and with mean value of zero whereas the streaming induced forces are time independent and on averaging, have nonzero values. The magnitude of the linear interactions is larger than the non-linear ones at moderate frequencies (kHz) whereas the non-linear forces also assume significance at higher frequencies in the MHz range. The combined effect of the various interaction forces (adhesive and removal) is required to gain insights into the actual removal mechanisms. This, however, is beyond the scope of this study. Instead, useful insights into the dominant mechanism responsible for efficient removal of non-specifically bound proteins can be obtained from the estimates of various forces predicted from the trends in the streaming velocity fields.

The dominant adhesive force for particle immersed in a liquid are the van der Waals and double layer forces[279]. For the sake of simplicity, we assume that the non-specifically bound proteins can be modeled as spherical particles of radius R. The van der Waals attraction force for a spherical particle near a flat surface is given by $F_{vdW} \sim \frac{AR}{6z^2}$ where A is the Hamaker constant for the non-retarded force and z is the distance of maximum force of adhesion. Typical values of A in a liquid environment ~ 10^{-20} J. With increasing distance z, the van der Waals force becomes insignificant. Typical values of z are in the range of 0.2-0.4 nm. The van der Waals adhesion force for different particle radii are given in Table 8-3. Electrical double layer forces result from the electrostatic attraction and are associated with particle having effective diameters less than 5 microns. A surface contact potential created between two different materials based on the local energy state of each material results in the surface charge build up. As a result, a double layer charged region forms around the particle to preserve charge neutrality leading to electrostatic attraction. For adhesion of sub-micron sized particles, it was found that the electrical double layer forces are of the same order of magnitude as van der Waals forces and can be neglected in favor of the van der Waals force.[280] For the order of magnitude analyses of adhesion forces, it is usually sufficient to consider only the van der Waals force. [278]

There are mainly three different mechanisms for particle removal namely sliding, rolling and lift-off. The dominant mechanism can be established by comparing the relative magnitudes of the various removal forces. The forces responsible for removal of particles are mainly characterized as the direct SAW forces, the lift and the drag forces that result from the mean velocity field in the fluid. The direct SAW forces results from the wave propagation on the boundary of SAW-fluid surface and was discussed in detail in subsection iv of Section 4. The magnitude of the direct force is given by $F_{SAW} \sim \sqrt{F_x^2 + F_z^2} R^2$. The components of forces F_x and F_z are given by Eq. (4.3) and (4.4). The fluid circulation around a particle results in inviscid lift forces, whose surface normal components act to remove the particle.[281] The lift forces can be estimated based on the Bernoulli's equation by utilizing the pressure difference that exists between the bottom and top of the particle and is given by $F_L \sim \rho(u_x R)^2$. u_x and R refer to the surface normal component of velocity and the particle radius, respectively. The acoustic streaming motion generated by SAW leads to a drag force, caused by the interaction between the mean flow and the particles. The drag force which results from the boundary layer-generated acoustic streaming is given by $F_{ST} \sim \mu R u_z$. Here,

u_z and μ refer to the tangential component of velocity and the fluid viscosity, respectively. Streaming is essentially parallel to the device surface and can potentially advect the particles along the surface. Thus, the relative magnitudes of the normal and tangential components of forces exerted by the SAWs on the fluid would dictate which of the three mechanisms is dominant. The SAW direct force as well as the lift and drag forces based on the velocity field generated in a 100 MHz SAW device for an applied input voltage of 10 V are given in Table 8-3. The calculated forces are for particles that are located closer to the IDT region. The relative magnitude of the removal forces *i.e.* lift, drag and the SAW direct forces would change with increasing distance along the delay path. The fluid density and viscosity were taken as 1000 Kg/m^3 and 10^{-3} Kg/m.s, respectively.

Table 8-3. Forces (in Newton) versus particle radius R (radius in microns) for a 100 MHz SAW device.

R	0.1	1	10
F_{vdW}	2×10^{-9}	2×10^{-8}	2×10^{-7}
F_{SAW}	4×10^{-6}	4×10^{-4}	4×10^{-2}
F_L	2×10^{-16}	2×10^{-14}	2×10^{-12}
F_{ST}	1×10^{-12}	1×10^{-11}	2×10^{-10}

Based on the order of magnitude analysis of the various forces listed in Table 8-3, an approximate removal mechanism can be proposed. For micron and sub-micron sized protein agglomerates, the results in Table 8-3 illustrate that the fluid induced removal forces are not significant enough to overcome the van der Waals forces at megahertz frequencies. The F_{SAW} is several orders of magnitude greater than the adhesion forces for the range of particle diameters considered in Table 8-3. It therefore appears that the SAW direct force causes the removal or detachment of the non-specific proteins from the SAW surface and moves the particle away from the region of influence of the adhesive forces. As mentioned earlier, the van der Waals adhesion forces decrease rapidly with distance from the SAW surface. However, the SAW direct forces also decay rapidly with distance into the fluid. Hence a steady force is required to cause the removal of the detached non-specific proteins. The horizontal streaming induced drag force (F_{ST}) helps to push the non-specific proteins away from the fouled area. The vertical streaming force or the lift force (F_L) helps to prevent the re-adhesion of the proteins to the surface. Thus, the fluid induced drag and lift forces result in a net displacement of the detached proteins.

Typically, the size of non-specifically bound proteins is in the range of 50-100 nm. For a given megahertz (MHz) frequency device, the results in Table 8-3 illustrate the increasing difficulty in removing proteins (or agglomerates) of decreasing sizes. In accordance with the mechanism predicted above and the trends in the streaming velocity fields, it appears that the detachment of proteins would be higher for devices operating at higher frequencies and for higher applied input voltages. Also, the tangential as well as the normal streaming velocities increase for these operating conditions. Therefore, the drag and the lift forces generated would increase and facilitate the removal of the detached proteins. With increasing fluid viscosity and density, we observe that the tangential and normal streaming velocities decrease. Hence although the detachment of proteins might not be severely affected, the removal efficiency would decrease as a result of reduced drag and lift forces. Thus, removal of non-specific proteins becomes increasingly difficult for fluids with higher viscosity and density. These observations are in line with our experimental results reported in Cular et al.[276]

8.7 Conclusions

An analysis of acoustic streaming induced in a piezoelectric SAW device has been carried out. The flow induced by the Rayleigh wave generated on the SAW device surface with the liquid boundary layer was investigated. The SAW interaction with fluid leads to an internal acoustically induced streaming and results in a mode conversion to the longitudinal leaky SAW which decays exponentially with distance in the fluid. The velocity vector field shows recirculation patterns in the fluid region resulting from the out of phase motion of the IDT fingers. The fluid recirculation exerts steady viscous stresses on the inter-phase boundaries which can be used for the removal of non-specifically bound proteins. The extent of recirculation and therefore the induced stresses were found to decrease with distance from the IDT fingers.

Optimization of parameters which can maximize the streaming and cause removal of unwanted proteins along the entire delay path is required. Towards this end, the effects of several design parameters such input voltage amplitude and frequency as well as fluid properties such as density and viscosity were studied. It was found that the variation in induced streaming velocity was nearly linear for low amplitude of applied voltage and quadratic with the higher input voltage. Therefore, the higher the applied voltage the greater would be the extent of acoustically induced streaming. For devices operating at higher frequency, the simulations predict increased streaming velocities. In all the cases, the tangential component of streaming velocity was higher than the normal. The effect of fluid properties such as viscosity and density on the SAW induced streaming was also investigated. The simulations predict a decrease in streaming velocity with increasing fluid viscosity and density. Therefore, for more viscous and dense fluids, the extent of streaming induced by SAW under a given operating condition would be lower. The model predictions are in fairly good agreement with the analytical solution formulated on the basis of Nyborg's theory and Campbell-Jones method.

The predicted streaming velocity fields as well as the trends in their variation for a range of operating conditions were utilized to compute the various forces generated in a typical SAW cleaning operation. An order of magnitude comparison of the various forces involved in the SAW cleaning operation was further used to predict the mechanism involved in the removal of non-specifically bound proteins. It appears that the removal of these proteins can be viewed as a combined process which involves overcoming adhesion forces, lifting them from the SAW surface and convecting them away. Based on the predicted cleaning mechanism and the velocity fields computed using finite element model, we find that the removal efficiency is higher for devices operating at higher frequencies and for higher applied input voltages. Also, the particles which are smaller in size are difficult to remove. The increase in fluid viscosity and density reduces the efficiency of removal of non-specifically bound proteins for a device operating at a given frequency and applied input voltage. This agrees well with the experimental observations. It is expected that the model generated trends in conjunction with the proposed mechanism would serve as guidelines for subsequent experimental investigation.

Chapter Nine

Finite Element Modeling of Hexagonal Surface Acoustic Wave Device in $LiNbO_3$

9.1 Abstract for chapter nine

We present a 3-D coupled field finite element model of a novel hexagonal surface acoustic wave (SAW) device which finds applications in materials characterization as well as chemical and biological sensing. Prior to the actual device fabrication on any piezoelectric substrate, it is important to establish the types of waves that are generated along the various delay paths. The choice of a delay path for any specific application depends on the propagation characteristics of the wave generated along the crystal cut and orientation corresponding to that delay path. The calculated frequency response as well as wave propagation characteristics along the three different delay paths corresponding to crystal orientation with Euler angles (0, 90, 90), (0, 90, 30) and (0, 90, 150) for a $LiNbO_3$ substrate is analyzed using the developed coupled field finite element structural model. The transient response of the hexagonal SAW device upon application of an impulse electrical input at transmitting interdigital transducer fingers is used to deduce its frequency response. The amplitude fields as well as displacement contours, generated in an AC analysis, along the SAW delay-line and substrate depth are analyzed and utilized to evaluate the wave propagation characteristics along the three propagation directions in a hexagonal SAW device. Our findings indicate that the acoustic waves generated in the three Euler directions are very different in character. The (0, 90, 30) and (0, 90, 150) directions have mixed modes with a prominent SH component whereas the (0, 90, 90) direction generates a Rayleigh wave. This would allow the hexagonal device based on $LiNbO_3$ to be used for rapid and simultaneous extraction of multiple film parameters (film material density, Lame and Shear modulii, sheet conductivity) of a thin film material and achieve a more complete characterization in comparison to a conventional SAW device.

Comparison of the simulation results with those obtained using perturbational models and experiments shows good agreement. This validation enables the consideration of more complicated configurations and allows for extending the developed models to analyze propagation characteristics in hexagonal SAW device fabricated on other bare and multi-layered piezoelectric substrates.

9.2 Hexagonal SAW device

Surface acoustic wave (SAW) devices used both individually as well as in arrays find applications in chemical and biological sensing as well as in materials characterization [232,234,282-285]. The conventional SAW devices typically comprise of dual delay line configurations with one delay line used as a reference to compensate for environmental variations[43,286,287]. Recent experimental efforts have focused on the design and fabrication of acoustic wave devices which can allow for better sensor characteristics as well as materials characterization possibilities [21,255,288]. One such novel device with a complicated transducer design is the hexagonal surface acoustic wave (SAW) sensor as shown in Fig. 9-1 [289]. It comprises of three different delay paths aligned in a manner such that it allows for generation of acoustic waves which are different in character. It is possible to exploit the generated multiple wave modes to develop SAW devices that can serve as better chemical and biosensor elements.

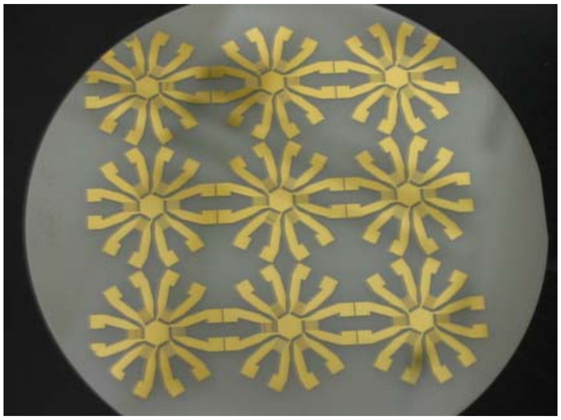

Figure 9-1. Hexagonal SAW device used for chemical and bio-sensing applications as well as materials characterization.

There are several advantages to the fabricated hexagonal SAW device. The three different delay paths could be used for simultaneous detection and the data collected across the three delay paths allows for better characterization of the sensing (thin film) material. This design allows for the simultaneous extraction of multiple properties (film material density or thickness, Lamé and shear modulii, sheet conductivity) of a thin film material to achieve a more complete characterization than when a single SAW device is utilized. Thus, these devices can serve as better *in-situ* characterization tools in thin film physical and chemical deposition equipment and are expected to perform better than the quartz crystal microbalance which yields only the thickness information.[290,291]

In sensor applications, this capability translates to better discrimination of the analyte and possibly more accurate determination of the concentration. Preliminary experimental results have shown increased sensitivity for these devices when used as a chemical sensor [289]. Other application of the hexagonal SAW in biosensing involves the ease of detection as well as removal of non-specifically bound proteins (acoustic streaming) enabling the repeated use of sensor device [292,293]. One of the delay paths is used for detection utilizing the shear horizontal SAW waves whereas the other delay paths with a dominant Rayleigh mode are used to simultaneously remove the non-specifically bound proteins using acoustic streaming phenomenon. The fabrication of a hexagonal SAW device can be carried out on any piezoelectric substrate such as lithium tantalate and lithium niobate. However, prior to the device fabrication, it is important to establish the type of waves that are generated along the various delay paths. The choice of a delay path for any specific application depends on the propagation characteristics of the wave generated along the crystal cut and orientation corresponding to that delay path. If it were possible to identify crystallographic directions, on a given piezoelectric substrate, which would enable fabrication of a hexagonal SAW device that can be functional in both gas and liquid phases, the same device could be used for chemical and biosensing applications. In the present work, we explore the feasibility of using finite element coupled field models to identify and evaluate acoustic wave propagation characteristics along the three delay line configurations in a hexagonal SAW device based on $LiNbO_3$

Simulations of piezoelectric media require the complete set of fundamental equations relating mechanical and electrical quantities to be solved [36,37]. To identify the wave propagation modes along the different crystallographic orientations in a surface acoustic wave device, it is necessary to obtain solutions to the coupled wave equations derived from the mechanical equations of motion and the Maxwell's equation for electrical behavior. The coupling between the electrical and mechanical parameters is achieved by means of the piezoelectric constitutive equations. There are several methods which can be used to solve the coupled wave equations and identify wave propagation characteristics.[33,45,226,294,295]

The models commonly used to simulate the mechanical and electrical behavior of piezoelectric transducers are based on perturbational theories or methods such as Campbell-Jones in which numerical solution to the complex characteristic equations for wave velocity are sought [294,295]. These generally introduce simplifying assumptions that are often invalid for actual designs [225]. The geometries of practical transducers are often two (2-D) or three dimensional (3-D) [226]. Finite element technique has been a preferred method for modeling acoustic wave propagation in piezoelectric devices such as SAW [296,297]. The main advantage lies in its ability to handle complicated transducer geometries[229,230]. A 3-dimensional finite element model is able to concurrently consider second order effects such as back scattering, bulk wave interference, harmonic responses as well as electromagnetic feed-through.

Finite element method was applied by Lerch (1990) [226] to calculate the natural frequencies with related eigen modes of the piezoelectric sensors and actuators as well as their responses to various dependent mechanical and electrical perturbations. A direct finite element analysis was carried out by Xu to study the electromechanical phenomena in SAW devices [227]. The influence of the number electrodes on the frequency response was analyzed. The finite element calculations were able to evaluate the influence of the bulk waves at higher frequencies. Ippolito et al. have investigated the effect of electromagnetic feed through as wave propagation in layered SAW devices [229]. The same model was extended to study electrical interactions occurring during gas sensing [231]. Recently, a 3-D finite element model was developed for a SAW palladium thin film hydrogen sensor [232]. The effect of the palladium thin film on the propagation characteristics of the SAW was studied in the absence and presence of Hydrogen. The variations in mass loadings, elastic constants and conductivity were the factors used in evaluating the velocity change of the wave. All the above demonstrate the feasibility of finite element models to adequately model acoustic wave propagation in SAW devices.

In the present work, a hexagonal SAW device based on $LiNbO_3$ substrate is modeled using FE technique. The wave propagation characteristics along the three different delay paths corresponding to crystal orientation with Euler angles (0, 90, 90), (0, 90, 30) and (0, 90, 150), respectively are evaluated. The developed FE model utilizes anisotropic material properties in a three dimensional description of $LiNbO_3$ substrate. In this paper, the particle displacement as well as voltage profiles obtained at the output IDT port as well as along the depth of the piezoelectric substrates along various locations across the three delay paths are analyzed and used to interpret the acoustic wave modes and velocity. Additionally, the response of each of the three delay lines to an applied voltage impulse is utilized to calculate its frequency response. The calculated frequency response as well as acoustic wave velocities are compared to those obtained experimentally and through perturbational theory based approach. The details are discussed in the subsequent sections.

9.3 Theory

The propagation of acoustic waves in piezoelectric materials is governed by the mechanical equations of motion and Maxwell's equations for electrical behavior. The constitutive equations of piezoelectric media in linear range coupling the two are given by:

$$T_{ij} = c_{ijkl}^{E} S_{kl} - e_{kij}^{t} E_k \tag{9.1}$$

$$D_i = e_{ikl} S_{kl} + \varepsilon_{ik}^{S} E_k \tag{9.2}$$

In the above equations, T_{ij} represent the components of stress, c_{ijkl}^{E} the elastic constant for constant electric field, S_{kl} the strain, E_k the electric field intensity, D_i the electric displacement, e_{kij}^{t} the piezoelectric constant, and ε_{ik}^{S} the permittivity for constant strain.

The acoustic wave propagation velocity is five orders of magnitude smaller than that of electromagnetic waves. Therefore, the quasistatic assumptions help reduce Maxwell's equation to $\frac{\partial D_i}{\partial x_i} = 0$ and $E_i = -\frac{\partial \phi}{\partial x_i}$, where φ represents the electric potential. The components of strain are defined by

$$S_{ij} = \frac{1}{2}\left(\frac{\partial u_i}{\partial x_j} + \frac{\partial u_j}{\partial x_i}\right) \tag{9.3}$$

The equation of motion in the absence of internal body forces is given as

$$\frac{\partial T_{ij}}{\partial x_j} - \rho \frac{\partial^2 u_i}{\partial t^2} = 0 \tag{9.4}$$

where ρ is the density and u_i represent the components of displacement. Substituting and rearranging the above set of equations leads to a system of four coupled wave equations for the electric potential and the three component of displacement in piezoelectric materials which are solved for the piezoelectric substrate or the solid domain:

$$-\rho \frac{\partial^2 u_i}{\partial t^2} + c^E_{ijkl} \frac{\partial^2 u_k}{\partial x_j \partial x_l} + e_{kij} \frac{\partial^2 \phi}{\partial x_k \partial x_j} = 0 \tag{9.5}$$

$$e_{ikl} \frac{\partial^2 u_k}{\partial x_i \partial x_l} - \varepsilon^S_{ik} \frac{\partial^2 \phi}{\partial x_i \partial x_j} = 0 \tag{9.6}$$

These coupled wave equations can be discretized and solved for generating displacement profiles and voltages at each element/node using the finite element method. The details of the computational model developed in this study are presented in the next section.

9.4 Computational details

The generation and propagation properties of transient Rayleigh and leaky waves are characterized by a three-dimensional finite element model. A transient analysis of the different delay-line configurations in a hexagonal SAW device was carried out for a total of 100 nanoseconds (ns) with 0.5 ns time step increments. The development of the finite element model for the analysis of the frequency response and wave propagation characteristics in hexagonal SAW devices as well as the applied electrical boundary conditions are described in detail in this section.

9.4.1 Model parameters

The 3-D FE model describes three two-port delay line structures along each of the Euler direction and consists of three finger pairs in each port. The inter-digital transducer (IDT) fingers are defined on the surface of a lithium niobate substrate and the fingers are considered as mass-less electrodes to ignore the second-order effects arising from electrode mass, thereby simplifying computation. The periodicity of the finger pairs is approximately 40 microns and the aperture width is 200 microns. The transmitting and receiving IDT's are spaced 130 microns or 3.25λ apart. The substrate for (0, 90, 90) or YZ-LiNbO3 was defined as 800 microns in propagation length, 300 microns wide and 150 microns deep. For simulating the other two directions, the geometry of substrate is kept the same, whereas the crystal coordinates are rotated. To achieve this, the material properties i.e. stiffness, piezoelectric and permittivity matrices are rotated by 60° and -60° along the x-z plane to model Euler directions (0, 90, 150) and (0, 90, 30), respectively. The simulated models have a total of approx. 250000 nodes and are solved for four degrees of freedom (three displacements and voltage). The model was created to have the highest densities throughout the surface and middle of the substrate. The 3-D meshed structure of the finite element model used for simulating the three different propagation direction is illustrated in Fig. 9-2.

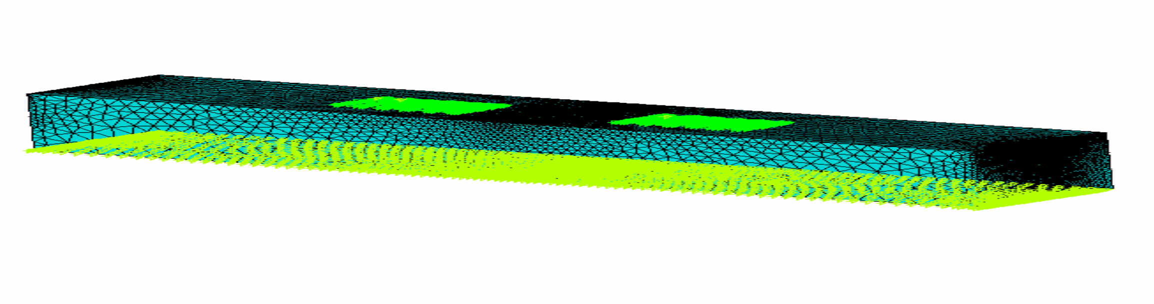

Figure 9-2. Three dimensional (3-D) meshed structure of the simulated finite element model of surface acoustic wave device. The transmitter and receiver IDT fingers are shown in green and represent coupled set of nodes. The bottom of the substrate is grounded to reduce the electromagnetic feed-through effect.

9.4.2 Structure excitation

The center frequency of SAW devices simulated in this work is in the range of 100 MHz. Hence, the structure was simulated for a total of 200 ns, with a time step of 0.5 ns. The excitation of the piezoelectric solid was provided by applying a time varying voltage signal (with varying peak values and frequencies equivalent to the device center frequency) on the transmitter IDT fingers of the SAW devices as shown in Fig. 9-2.

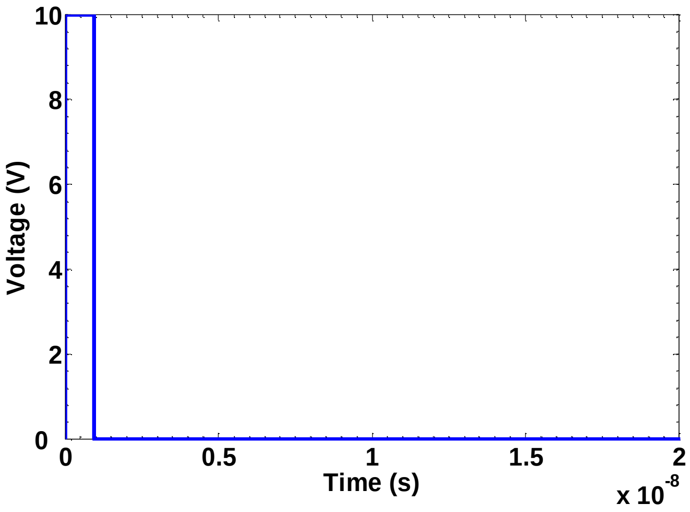

(a)

Figure 9-3. Applied input voltages at the transmitter IDT fingers (a) Impulse (b) AC voltage.

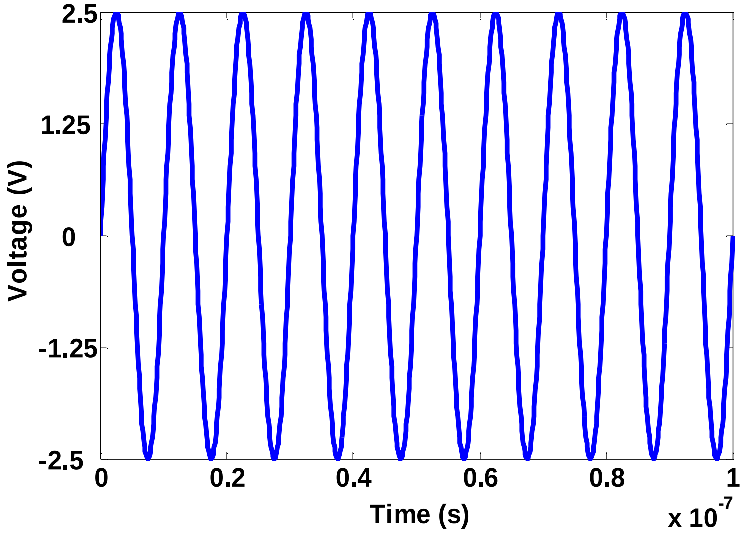

(b)

Figure 9-3: Continued

Two kinds of analysis are carried out along each of the three delay lines: 1) An impulse input of 10 V over 1 ns is applied to study the frequency response of the device and 2) AC analysis with a 5 V peak-peak input and 100 MHz frequency to study the wave propagation characteristics.

9.5 Results and discussion

The results of the transient analysis of acoustic wave propagation along the three delay paths in a hexagonal SAW device based on $LiNbO_3$ are presented in this section. The simulated displacement and voltage waveforms are analyzed for the different applied electrical inputs to the transmitter IDTs and used to identify the dominant wave modes along the three propagation directions. The frequency response of the hexagonal SAW device to an applied voltage impulse is calculated and compared to the experimental data. The details are presented below:

9.5.1 Response to applied AC voltage

In order to gain insights into the types of wave that are generated and propagating along the three directions, an AC analysis was carried out. This was done by applying a 5V peak-peak signal input for 200 ns at a frequency of 100 MHz as shown in Fig. 9-3. The application of electrical signal on the input transducer fingers results in generation of mechanical wave which then propagates towards the output transducer fingers. The coupled field finite element model developed in the present study is able to capture the generation and propagation of surface acoustic waves on a piezoelectric substrate such as $LiNbO_3$ as shown in Fig. 9-4.

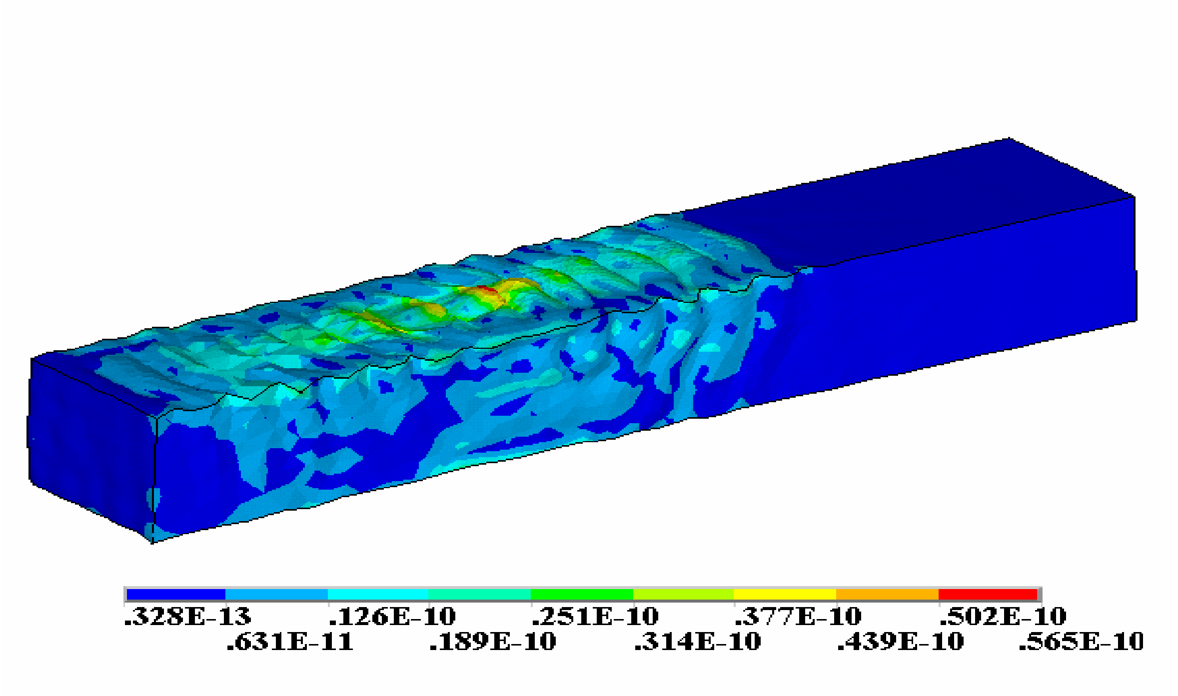

Figure 9-4. Surface acoustic wave propagation along the (0, 90, 30) Euler direction. The displacements shown on the scale bar are in meters. It can be seen that there is sufficient penetration of acoustic energy into the depth of the piezoelectric substrate.

When the array of IDT fingers are excited, the contributions from the odd (and evenly) located fingers constructively add up and a coherence of in-phase waves results leading to a maximum displacement in the fingers located at the end of the array [1]. The displacement amplitudes of the SAW are typically in the Å range as shown in Fig. 9-4. The wave travels outside of the aperture of the IDTs located on the $LiNbO_3$ surface, which indicates that part of the energy is being dissipated. The generated wave also propagates in the transverse direction opposite to the receiving transducer fingers and reaches the edge of the substrate at the end of 72 ns. Wave reflections from the substrate edge at longer simulation times are also observed from the 3-D representation of the simulated contours (not shown). The generated voltage and displacement waveforms for each of the delay line configurations are shown in Fig. 9-5 to 9-7. The response to an applied electrical input was obtained at the output IDT node located 210 microns away from the input IDT fingers.

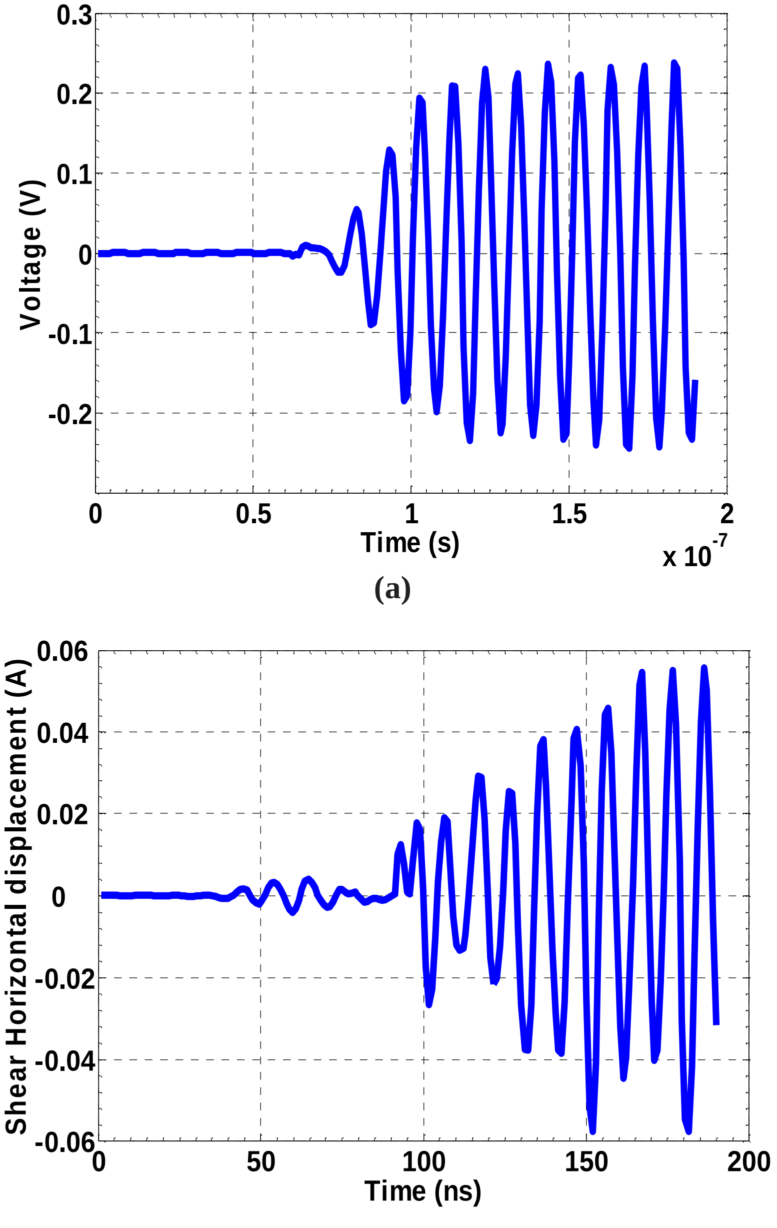

(a)

(b)

Figure 9-5. Displacement and voltage waveforms at the output IDT node along (0, 90, 90) Euler direction.

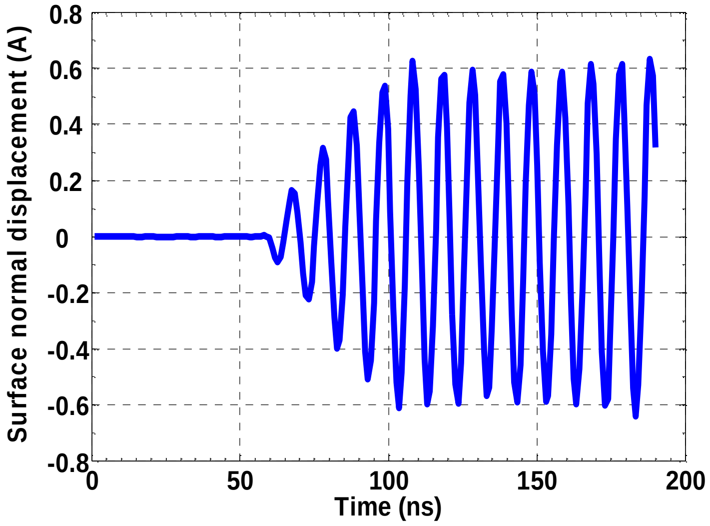

(c)

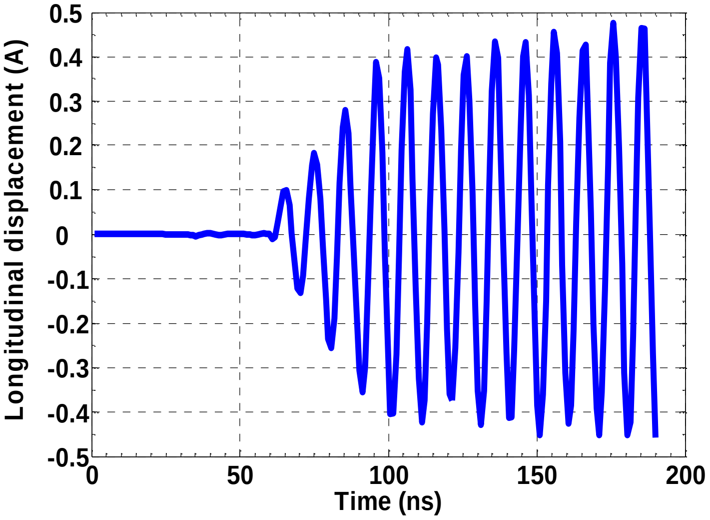

(d)

Figure 9-5: Continued

Figs. 9-5 through 9-7 (a) depict the generated voltage at the output node of the Hexagonal SAW device in response to a signal with 5V amplitude (peak-peak) at a frequency of 100 MHz. Voltage profiles obtained for the three Euler directions from the AC analysis indicate that the extent of wave attenuation is different for each of the simulated crystal orientation. The differences are attributed to the anisotropic nature of the piezoelectric substrate. It can be seen from the voltage profiles that the system stabilizes after a simulation time of approximately 110 ns. The stabilized value of the voltage obtained at the output IDT fingers show higher peak value for (0, 90, 90) direction followed by (0, 90, 30) and (0, 90, 150). This indicates lesser attenuation along (0, 90, 90) direction when compared to the other two.

The surface acoustic wave generated at the input transducer fingers takes approximately 60 ns to travel a distance of 210 microns along the (0, 90, 90) direction (Fig. 9-3). This leads to an approximate wave velocity of 3500 m/s. The simulated wave velocity compares well with the experimentally observed velocities of 3487 m/s as well as those calculated using perturbational approaches such as the Campbell-Jones method. A comparison of the simulated wave velocities with those obtained experimentally as well as calculated using Campbell-Jones method, along the three Euler directions is shown in Table 9-1. We find that the simulated wave velocities agree well with those obtained experimentally. This served as a validation of out simulation results shown in the present study.

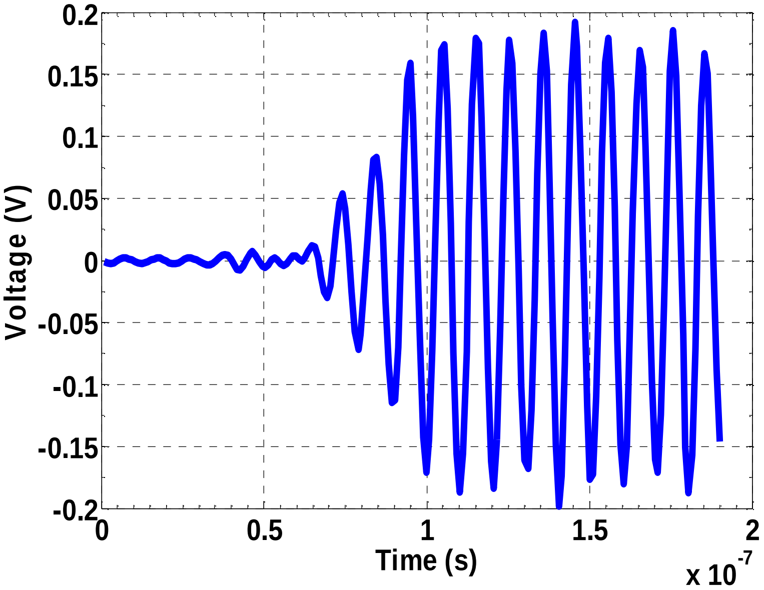

(a)

Figure 9-6. Displacement and voltage waveforms at the output IDT node along (0, 90, 30) Euler direction.

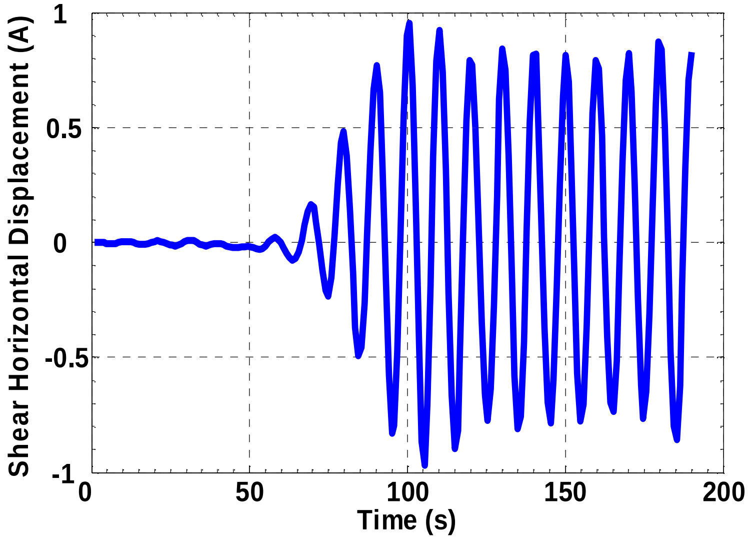

(b)

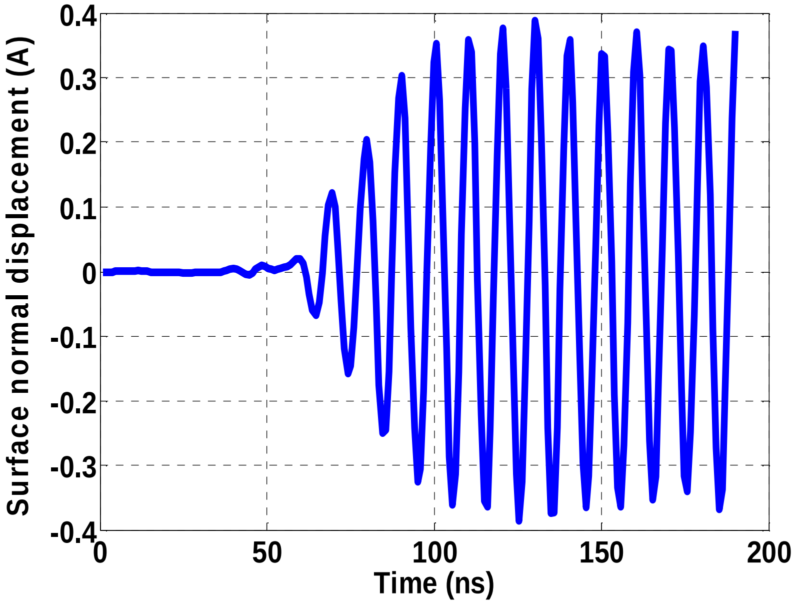

(c)

Figure 9-6: Continued

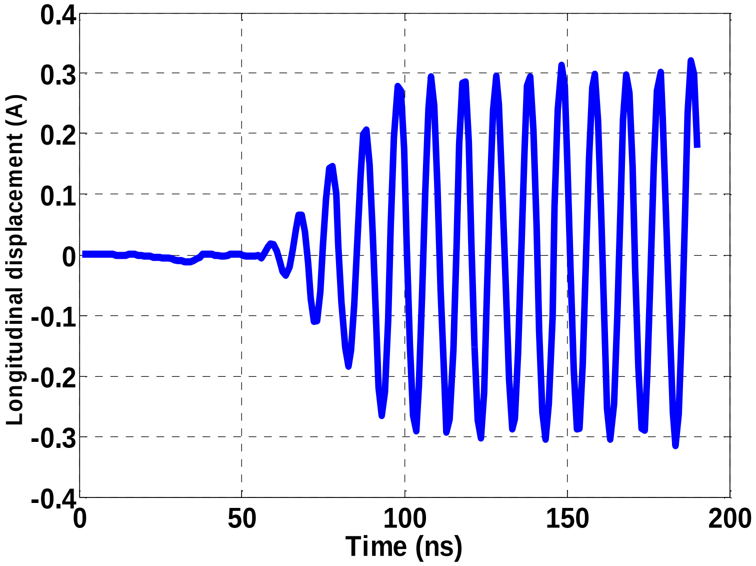

(d)

Figure 9-6: Continued

The particle displacement profiles along the three Euler directions are shown in Figs. 9-5 through 9-7. The anisotropic nature of the $LiNbO_3$ substrate results in varying amplitude values for the displacement profile, obtained at the output transducer fingers, along the shear horizontal direction (Figs. 9-5 through 9-7 (b)), surface normal (Figs. 9-5 through 9-7 (c)) and longitudinal (Figs. 9-5 through 9-7 (d)). These are used to characterize the nature of the generated surface acoustic waves. For the (0, 90, 90) direction, the surface normal and longitudinal components are an order of magnitude higher than the shear horizontal component indicative of wave motion which is more or less ellipsoidal. This type of wave motion corresponds to that of the Rayleigh mode.

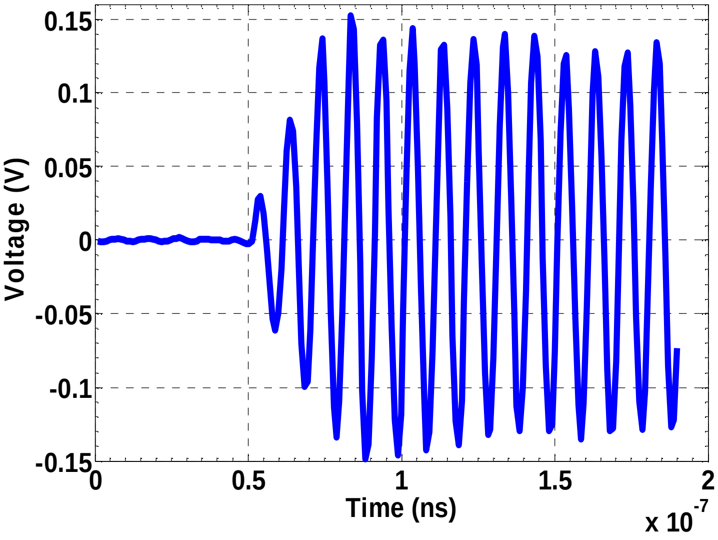

(a)

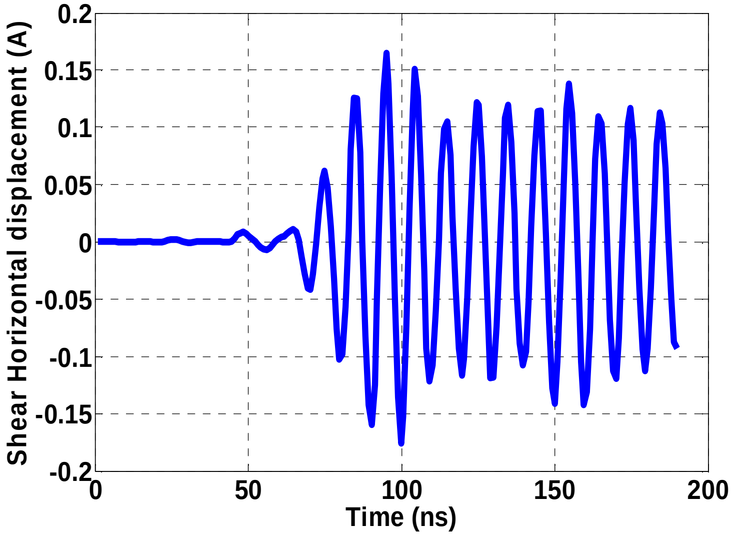

(b)

Figure 9-7. Displacement and voltage waveforms at the output IDT node along (0, 90, 150) Euler direction.

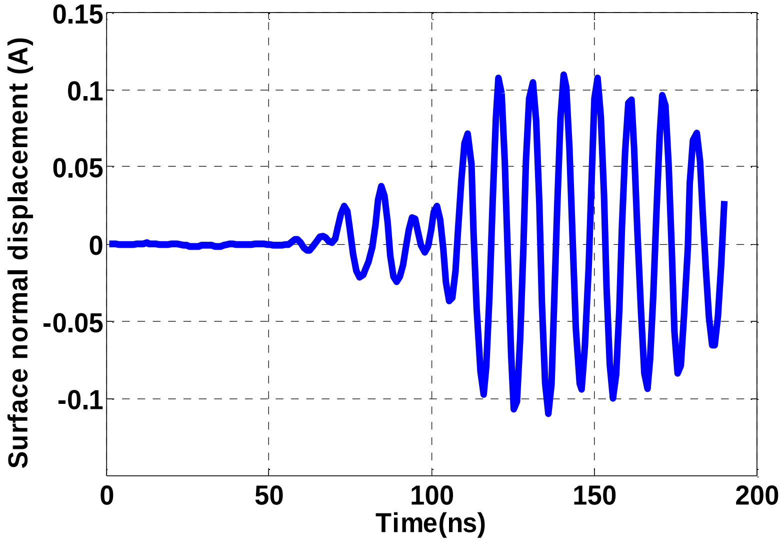

(c)

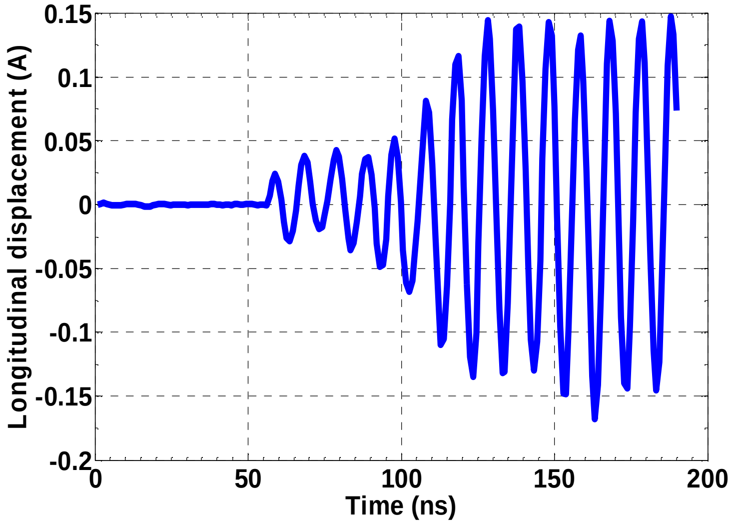

(d)

Figure 9-7: Continued

The displacement profiles of the off-axis components signified by (0, 90, 30) and (0, 90, 150) directions show lesser amplitude variations amongst the three directions indicative of mixed wave modes which are a combination of more than one wave type such as pure Rayleigh or Shear Horizontal modes. A pure

Rayleigh wave is a wave which concentrates its energy on the surface and propagates with no or little propagation loss. To verify the wave type obtained for the (0, 90, 90) Euler direction, we utilized the Campbell-Jones method. In this technique, the calculated four attenuation constants (α) have a positive real part for (0, 90, 90) direction. As a result, the depth displacement of the wave undergoes attenuation and the wave is confined to the piezoelectric substrate. The calculated four attenuation constants for the off-axis directions *i.e.* (0, 90, 150) and (0, 90, 30) also have real part, however, the magnitude of the same are much smaller. The acoustic energy along the off-axis directions would not be confined to within one wavelength from the substrate surface. This is indicative of wave propagation into the depth of the substrate which would result in propagation additional losses. The same is reflected in the simulated voltage profiles obtained at the output transducer fingers which indicate greater attenuation for the off-axis directions (~ 0.15 V) than the on-axis direction (~ 0.23 V). Further insights into the wave propagation along the piezoelectric substrate depth can be obtained by analyzing the displacement profiles into the substrate depth. The details are discussed in the next section.

Table 9-1. Simulated, theoretical and experimentally measured wave velocities along the different shorted delay paths of the hexagonal SAW device on lithium niobate.

Orientation *Euler angle* *(φ, θ, ψ)*	Theoretical [294,295] *(m/s)*	Experimental *(m/s)*	FEM Simulation (*m/s*)
(0,90,90)	3487	3593	3510
(0,90,150)	3646	3721	3710
(0,90,30)	3622	3620	3660

9.5.2 Analysis of wave displacement-substrate depth profiles

The mechanical stresses due to particle displacement arising from the acoustic wave propagation along or near the surface of the device, results in generation of an associated electric field in the piezoelectric material. This field may extend beyond the surface of the structure and result in energy dissipation into the bulk of the structure. For sensing applications, it is especially necessary to have acoustic confinement near the surface of the device to realize higher sensitivity. Amongst the three propagation directions in a hexagonal SAW device, it is necessary to establish the acoustic energy concentration as a function of substrate depth to determine their utility for potential sensing applications. Analysis of displacement *vs.* depth profiles as shown in Fig. 9-8 can also be carried out to yield more insights into the propagation characteristics of the waves along the three directions.

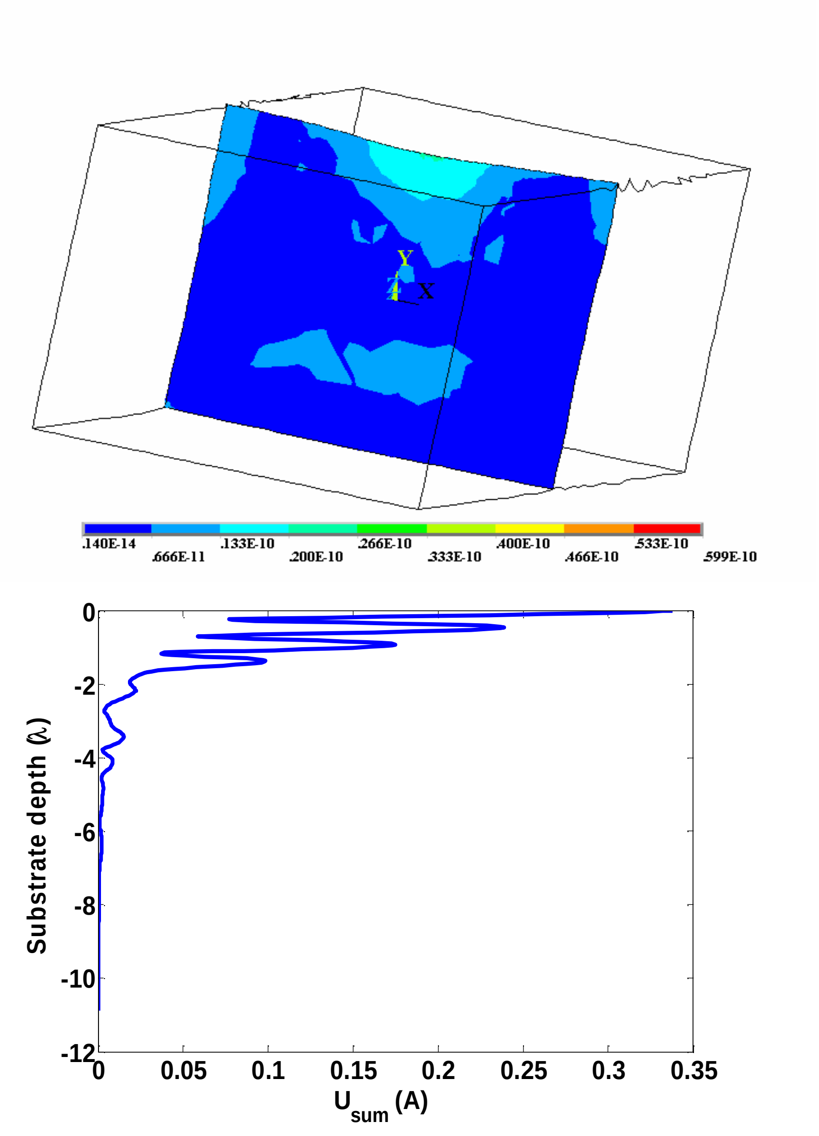

(a)

Figure 9-8. Displacement profile along the depth of the substrate for a section cut through the center of the delay path and normal to the propagation direction. The displacement contours shown on the left are obtained after the wave has stabilized. The displacement-depth plots shown on the right correspond to a path chosen along the center of the section displayed on the left. (a), (b) and (c) correspond to Euler directions (0, 90, 90), (0, 90, 30) and (0, 90, 150), respectively.

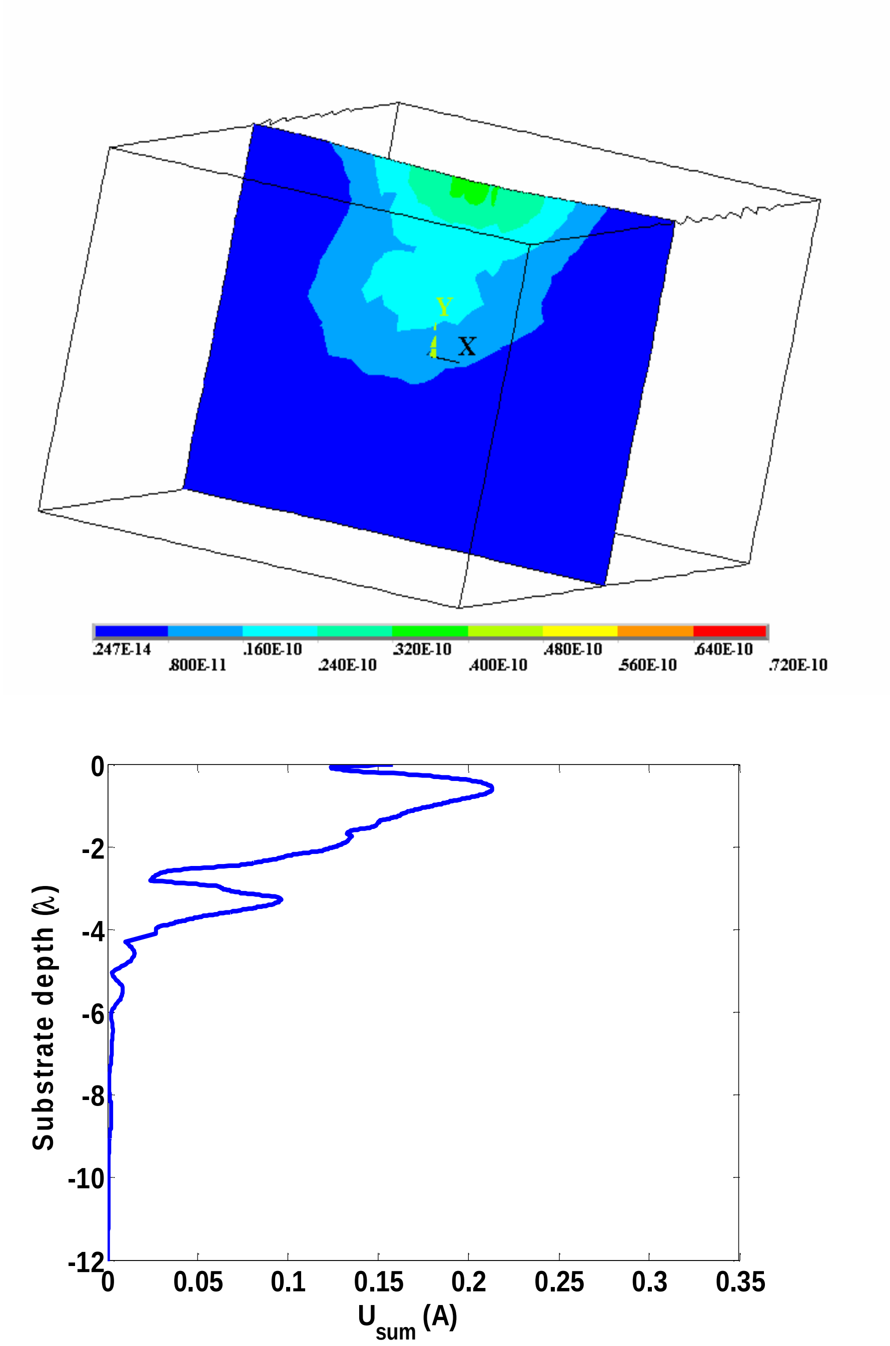

(b)

Figure 9-8: Continued

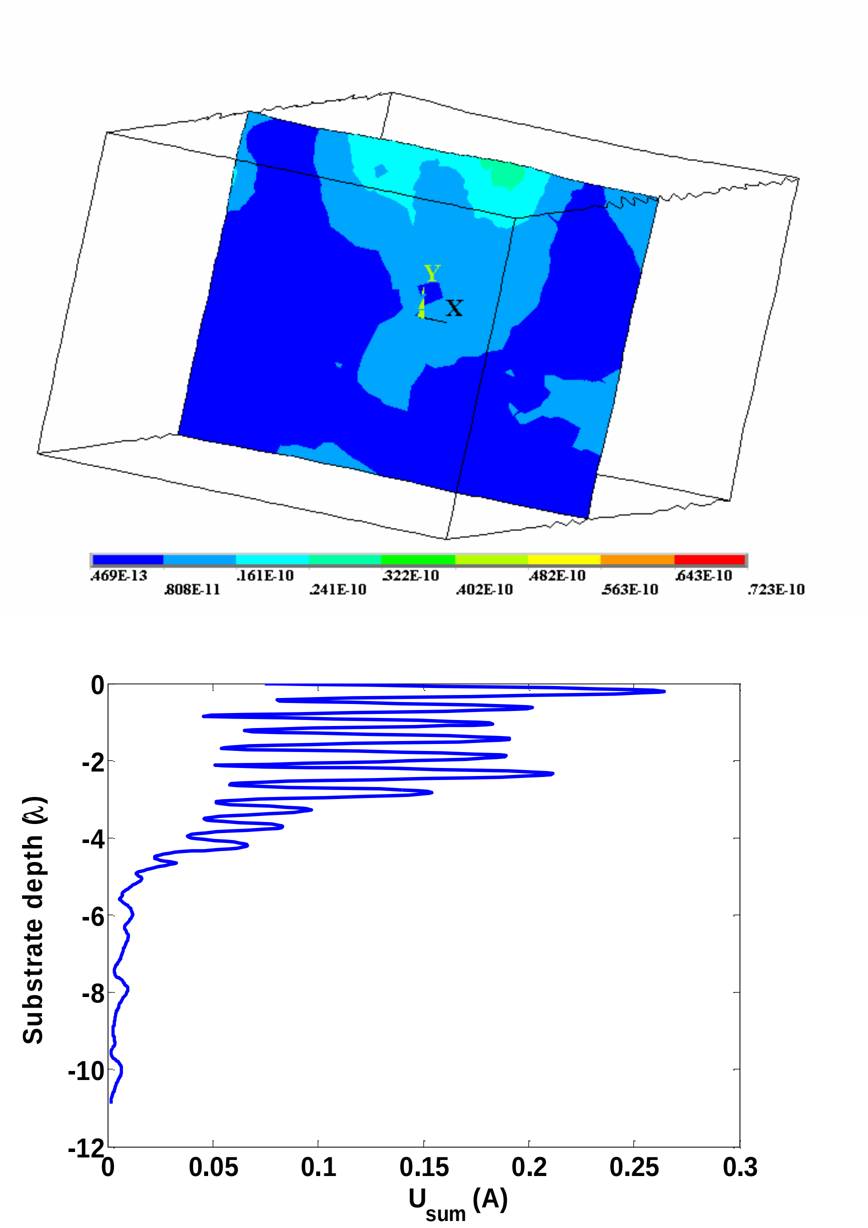

(c)

Figure 9-8: Continued

The analysis shown in Fig. 9-8 was done to determine the displacement variation along the substrate depth for a section cut normal to the propagation direction. The contours shown in Fig. 9-8 were taken after 60 ns of propagation time. As can be seen from the depth profiles shown in Fig. 9-8 (a), the (0, 90, 90) direction has most of the acoustic energy confined within one wavelength from the device surface. As discussed in the previous section, the waves propagating in (0, 90, 90) direction are Rayleigh waves which have a significant surface normal and longitudinal component. The wave, therefore, appears to be confined to the IDT aperture width and hence energy losses are minimal (Fig. 9-8 (a)). The surface displacements shown on RHS in Fig. 9-8 (a) for the (0, 90, 90) are higher than those for (0, 90, 30) and (0, 90, 150) (shown on the RHS of Fig. 9-8(b) and (c), respectively). Additionally from LHS of Fig. 9-8 (a) through (c), it can be seen that the depth penetration of the wave for (0, 90, 30) is higher than that for (0, 90, 90) direction, but lower than (0, 90, 150). The presence of a shear horizontal component in the (0, 90, 30) and (0, 90, 150) waves result in it traveling outside the aperture width of the IDTs and leads to higher losses.

Furthermore, the acoustic energy for the (0, 90, 30) dissipates to three-four wavelengths from the device substrate whereas for the (0, 90, 150) direction, the acoustic energy penetrates up to six wavelengths from the substrate surface (Fig. 9-8 (b)-(c)). The higher dissipation into the device substrate results in lesser magnitude of surface displacement for the (0, 90, 30) (~ 2.2 Å) and (0, 90, 150) (~ 2.5 Å) direction when compared to (0, 90, 90) (~ 3.5 Å). These results corroborate the findings obtained from the voltage profiles in Fig. 9-5 through 9-7 (a), which show that wave attenuation for (0, 90, 150) > (0, 90, 30) > (0, 90, 90). More insights into the wave attenuation can be obtained by looking at the frequency response of the hexagonal SAW device.

9.5.3 Impulse response

The impulse response detected by the output transducer is obtained directly from the finite element simulation in the form of voltage potential and particle displacements at the output IDT fingers of the receiving port. The frequency response of a SAW device H(f) can be obtained from its impulse response h(t) by taking the Fourier transform.

$$H(f) = \int_{-\infty}^{\infty} h(t) e^{-2\pi f t} dt \tag{9.7}$$

To obtain the impulse response, a signal of the following form is input at the transmitting electrodes [227]:

$$V_i = \begin{cases} \dfrac{1}{T_S} & 0 < t \leq T_S \\ \\ 0 & t > T_S \end{cases} \tag{9.8}$$

In the above equation, T_s is the sampling time used in the simulations, t is the time and V_i is the applied voltage at the input transducer fingers. Three IDT fingers at each port were defined with the nodes coupled to zero volts, whilst the three output IDT fingers were coupled separately. The impulse function represented above is applied to the remaining two input IDT fingers, and the average voltage profiles calculated at the output IDT fingers were used to derive the frequency response of the hexagonal SAW device along each of the three propagation directions. Thus, by applying an impulse function as an input, the frequency response can be calculated.

The velocities corresponding to wave propagation along the three Euler angles are given in Table 9-1. Since frequency is directly proportional to velocity, it is expected that the frequency response would follow the order (0, 90, 90) < (0, 90, 30) < (0, 90, 150). The calculated frequency response for an input impulse (1 ns) of 10 V is shown in Fig. 9-9. The calculated device frequency along the three directions follows (0, 90, 90) < (0, 90, 30) < (0, 90, 150). The least attenuation occurs along the (0, 90, 90) direction whereas the maximum is observed for (0, 90, 150). The calculated insertion loss for (0, 90, 90) direction is ~ 31 dB whereas the (0, 90, 150) propagation direction was found to have 3 dB higher insertion loss than (0, 90, 90). Also, we find that when the frequency is higher than 150 MHz for (0, 90, 90) direction, a high frequency signal appears. This might be the BAW signal or the electromagnetic feed-through effect. Considering that the BAW velocity in YZ $LiNbO_3$ or (0, 90, 90) direction is 7200 m/s, it appears likely that the high frequency signal might have resulted from BAW signal interference.[298]

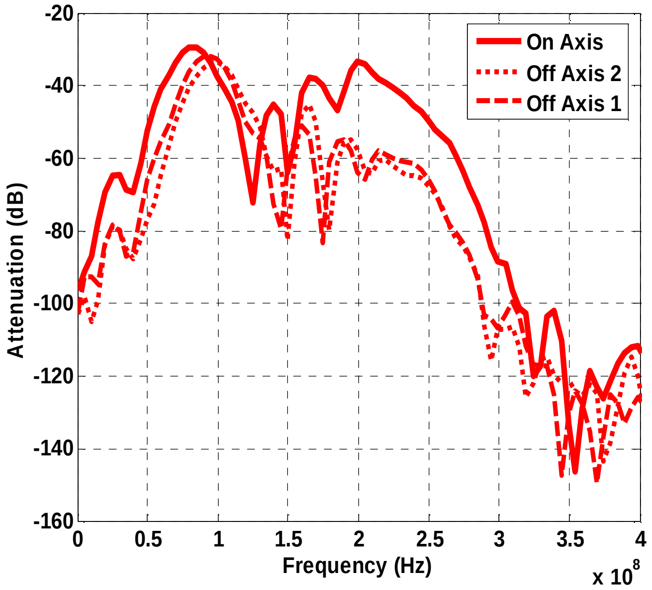

Figure 9-9. Frequency response calculated using simulated voltage profiles at output IDTs along the three Euler directions. On axis, Off Axis 1 and Off Axis 2 corresponds to (0, 90, 90), (0, 90, 30) and (0, 90, 150), respectively.

In the present simulations, we find that the pass-band width is broader and the insertion losses are higher than that observed experimentally. This is primarily attributed to the reduced number of IDT finger pairs. Our simulation results with increased number of finger pairs indicate that the pass-band width and the insertion loss become smaller with the increase in the number of pairs. If the number of IDT finger pairs is large enough, then the insertion loss would not decrease any further. However, in that case, the scale of the device would increase and so would the number of variables that require to be solved. These and other limitations are discussed in a subsequent section. However, despite the small quantitative differences, the trends predicted by our simulations qualitatively agree with the experimental results of Cular et al.[289]

9.6 Applications to material characterization and sensing

The finite element model of the hexagonal SAW device developed in this work indicates that the propagation characteristics of the acoustic wave generated along the three Euler directions is different owing to the anisotropic nature of the piezoelectric crystal. The wave propagating along the (0, 90, 90) direction are Rayleigh type waves with a dominant surface normal component whereas those propagating along the (0, 90, 30) and (0, 90, 150) direction comprised of mixed wave modes with a prominent shear horizontal component. The differing wave propagation characteristics along the three Euler directions in a hexagonal SAW based on $LiNbO_3$ can be utilized in materials characterization for non-destructive testing of thin films of different materials used in solid state devices. As seen from the impulse response analysis, the responses of the three delay lines are significantly different and can be effectively used to extract multiple film parameters that probe a common region.

Based on perturbational approach, the SAW gas response obtained for a given gas adsorption onto a thin isotropic sensing film on a semi-infinite anisotropic substrate, is given by:

$$\frac{\Delta v}{v} = \left(\frac{\pi h}{2\lambda}\right)\left[-\frac{\Delta\rho}{\rho}A + \frac{\Delta C_{44}}{C_{44}}B + \left(\frac{\left(1-\frac{\Delta C_{44}}{C_{44}}\right)^2}{1-\frac{\Delta C_{11}}{C_{11}}} - 1\right)C\right] \tag{9.9}$$

where h is the film thickness, λ is the SAW wavelength, ρ is the film density, C_{11} & C_{44} are the elastic constants, and A, B & C are propagation coefficients that depend on the normalized SAW displacements in the piezoelectric substrate. The values of A, B & C are available in literature. By applying Eq. (9.9) using the measured $\Delta v/v$ along the three different propagation directions in a hexagonal SAW device, we would get a system of three equations in three unknowns $\Delta\rho/\rho$, $\Delta C/C_{11}$ and $\Delta C_{44}/C_{44}$. Both the steady state and the time variations in film density and elastic constants can then be calculated from the steady state and dynamic values of $\Delta v/v$ to gain insights into the kinetics of gas adsorption. Thus nondestructive real time characterization of sensing layers upon gas adsorption is possible through the use of hexagonal SAW device.

In terms of sensor applications, the multiple parameters extracted from the film using the hexagonal SAW device can serve as multiple calibration curves and allow for a more unique and precise characterization of the concentration and type of analyte being sensed. Combined with the array concept, significantly more information can be obtained to better characterize the analyte. Additionally, the hexagonal SAW device can also be employed for chemical and biological sensing. It is well known that the conventional acoustic wave devices are specific to the phase in which they operate; for example, the Rayleigh wave device which are suitable for vapor sensing cannot operate in the liquid environment owing to excessive attenuation[12]. Our analysis indicates that the multiple directions in which the waves are launched in the hexagonal device of $LiNbO_3$ are different in character, and might allow for a common device to be functional in both gas and liquid phases. In the present work, we have shown that Rayleigh waves propagate along the (0, 90, 90) direction and mixed mode waves with prominent SH component propagate along the other two directions. Furthermore, the depth profile analysis indicates that the (0, 90, 90) direction has acoustic energy confined to the surface of the LiNbO3 substrate, whereas the acoustic wave penetration into the substrate for (0, 90, 30) and (0, 90, 150) direction have a higher penetration into the substrate. High sensitivity to surface perturbations is achieved for devices with minimal propagation energy losses and which have acoustic energy confined to the device surface. Therefore, the (0, 90, 90) or the on-axis direction is more suitable for chemical and vapor sensing applications. On the other hand, the off-axis directions can be used in conjunction with the on-axis direction to simultaneously and continually monitor the changes in the material properties of the sensing layer film due to gas-film interaction.

Additionally, in a separate investigation we have shown that the Rayleigh wave devices can be utilized in acoustic cleaning of nonspecifically bound proteins in biosensor applications[299]. The possibility of launching shear horizontal SAW waves in one direction and Rayleigh waves in another, the hexagonal device may well serve as a better biosensor element for liquid phase applications and help to simultaneously eliminate the problems associated with biofouling which render the conventional biosensors ineffective. Experimental and theoretical investigations to identify the best candidates for potential biosensing applications are underway in our laboratory, with the designs implemented in more suitable piezoelectric materials such as lithium tantalate and langasite.

9.7 Limitations of the finite element simulations

A fine mesh generation is required for accurate modeling of a SAW device. It is critical that the nodal densities for the substrate simulated are at least in the order of 20 nodes per wavelength for the highest device frequency. Therefore, the number of nodes required to simulate a 3-D SAW device is extremely large. The incorporation of a waveguide or a sensing layer (typically a few hundred nanometers) to simulate a hexagonal SAW sensor would result in significant differences in the length scales of substrate and sensing layer, thereby requiring much higher node densities. Additionally, the simulations are computationally intensive and time consuming, with the required CPU time increasing considerably with mesh size. Another major setback arises from acoustic wave reflection from the edges if the simulations are carried for sufficiently longer times. One of the ways to overcome this limitation would be employment of damping elements at the ends of the substrate. While longer simulation times are necessary to attain stable state, too long a simulation time results in wave reflections causing instabilities to set in. A simulation time of 200 ns was found to be optimum for the substrate dimensions considered in the present study.

9.8 Conclusions

A 3-D finite element coupled field model of a hexagonal SAW device based on a $LiNbO_3$ substrate is developed in this work. Insights into the acoustic wave generation and propagation along the three Euler directions corresponding to the multiple propagation directions in a hexagonal transducer configuration on a piezoelectric substrate is obtained using the developed model. The center frequency of the simulated devices obtained from the impulse response analysis was found to be around 100 MHz. The voltage and displacement profiles at the output transducer configurations for an AC analysis with input voltage of 5 V peak-peak and 100 MHz frequency at transmitter IDT fingers was used to identify the acoustic wave propagation characteristics along the three Euler direction. Our simulation results indicate that the waves propagating along the (0, 90, 90) direction are of pure Rayleigh type with a dominant surface normal component whereas those propagating along the (0, 90, 30) and (0, 90, 150) directions involve combination of multiple wave modes with a prominent shear horizontal displacement component.

Analysis of the particle displacements along the depth of the piezoelectric substrate was used to gain insights into the acoustic energy confinement and wave penetration into the SAW device. Our findings indicate that the higher propagation losses along the off-axis directions *i.e.* (0, 90, 30) and (0, 90, 150) are attributed to the presence of the shear horizontal displacement component as well as higher acoustic wave penetration into the depth of the piezoelectric substrate. These manifest themselves in the form of attenuated voltage response at the output transducer fingers for the (0, 90, 150) and (0, 90, 30) directions in comparison to the (0, 90, 90) direction. The calculated insertion losses for an impulse voltage input along the three propagation directions indicated the waves along the (0, 90, 90) direction are less attenuated than those along the (0, 90, 30) and (0, 90, 150) directions. The results of the finite element simulations are consistent with those obtained using perturbational technique based methods such as Campbell-Jones as well as those observed experimentally.

Based on the results of the finite element analysis, the utility of the multiple wave characteristics along the different delay line configurations in a hexagonal SAW device is also discussed. We find that the hexagonal SAW devices based on $LiNbO_3$ are more suitable for material characterization than the conventional SAW or QCM devices. Efforts are underway to identify more suitable transducer designs, geometry as well as piezoelectric substrates which might serve as better biosensor elements. The findings of this work have laid the groundwork for further investigations towards modeling SAW devices with more complicated transducer configurations and allows for extending the developed models to analyze propagation characteristics in hexagonal SAW device fabricated on other bare and multi-layered piezoelectric substrates.

Chapter Ten

Design of Efficient Focused Surface Acoustic Wave Devices

10.1 Abstract for chapter ten

Focused interdigital transducers (F-IDTs) patterned on surfaces of piezoelectric substrates can be used to generate surface acoustic waves (SAW) with high intensity and high beam-width compression ratio. A three dimensional coupled field finite element model of a focused SAW (F-SAW) device with interdigital transducers shaped as concentric circular arcs based on a YZ $LiNbO_3$ substrate is developed in this study. This model was utilized to investigate the effect of geometric shape of transducers on the focusing properties of F-IDTs to identify the optimal design for potential microfluidic applications. The transducer design parameters investigated in the current study include number of finger pairs, degree of arc, geometric focal length, and wavelength of F-SAW. The transient response of the device on application of impulse and AC electrical inputs at the transmitting FIDT fingers was utilized to deduce the device frequency response, and propagation characteristics of F-SAWs, respectively. The influence of applied input voltage on the propagation characteristics is also investigated. The insertion loss calculated for the various F-IDT designs was used to identify the optimal transducer configuration for sensing and microfluidic applications. The focusing properties as well as the wave propagation characteristics for the various F-IDT designs were evaluated in terms of the amplitude field and displacement contours generated in regions close to and at the focal point. Comparison with a conventional SAW device operating at MHz frequency range and uniform IDT design is also made. Our study indicates that the focusing property of the device is significantly influenced by the geometric shape of the F-IDTs.

Based on the simulation results of this study, we provide guidelines for designing various F-IDTs to suite desired applications. F-SAW devices operating with higher applied input voltages and at higher frequencies, with optimal geometric length and larger degree of arc are best suited for actuation and fluid micro-transport whereas those with smaller degree of arc are better suited for sensing applications.

10.2 Focused SAW device

In the present chapter, we evaluate the design and performance of a surface acoustic wave device, based on concentric circular arc fabricated in a $LiNbO_3$ substrate, by analyzing the wave generation and propagation characteristics for various focused interdigital transducer configurations in devices operating at MHz frequencies. We develop coupled field finite element structural models to investigate the dependence of acoustic wave generation and propagation characteristics on the various transducer configurations in F-SAW devices. The transient response of the model to various electrical inputs is used to identify the F-IDT configuration that would allow for enhanced streaming and increased micro-transport. The generated displacement profiles obtained at the receiving transducer port as well as other locations are used in conjunction with wave propagation parameters derived from perturbational models to calculate streaming forces and velocities based on successive approximation theory applied to Navier Stokes equation. The findings are used to identify the optimum transducer configuration for potential biosensing and microfluidic applications.

10.3 Surface acoustic wave device design

Surface acoustic waves are generated by the application of an alternating voltage signal to interdigital transducers (IDT) patterned on a piezoelectric substrate[1]. The phase velocity of the generated wave depends on the material properties of the waveguide, the piezoelectric and electrodes as well as on the geometric shape of the electrode. The IDT geometry dictates the wavelength of the excited wave and therefore the center frequency of the device (Fig. 10-1(a)). Modifications to the transducer geometry can result in significant changes in the acoustic wave propagation characteristics. In this work, we model the acoustic wave generation and propagation resulting from the use of concentrically oriented inter-digital transducer fingers on the surface of a piezoelectric substrate.

An illustration of a F-SAW device constructed using pairs of FIDTs based on concentric circular arcs is shown in Fig. 10-1(b). The FIDTs are characterized by design parameters such as degree of arc (D_a), geometric focal length (f_L) and the wavelength (λ). The effect of variation of these parameters on the acoustic wave propagation characteristics is presented in this work. The wave modes that are generated for each of the transducer designs are evaluated using 3-D finite element transient analysis for various applied electrical input conditions at the transmitter IDT fingers. The simulated displacement and voltage waveforms obtained at the output transducer and at different locations along the delay path are analyzed to deduce the dependence of the acoustic wave propagation characteristics on the device design parameters.

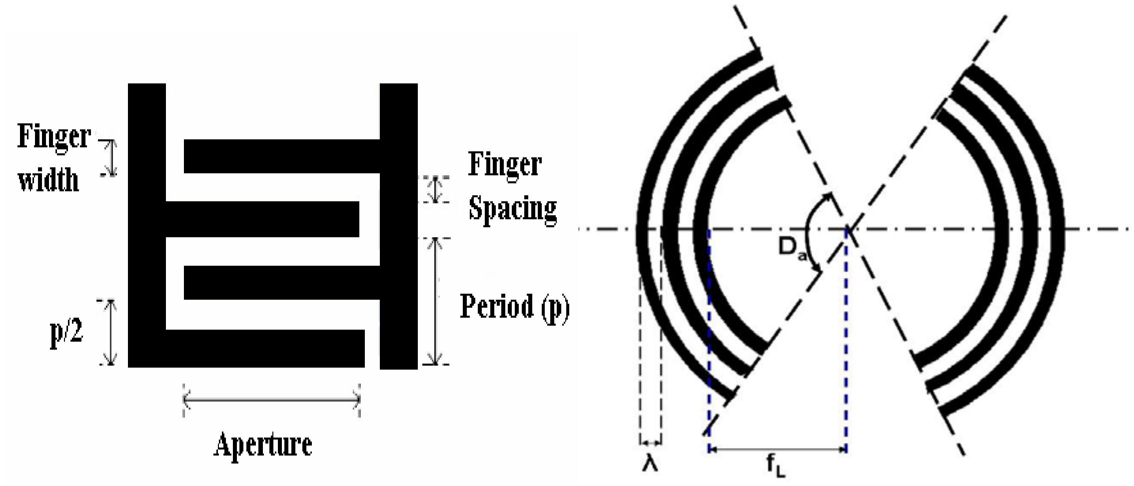

(a) (b)

Figure 10-1. Schematic diagram of (a) transducer design for a conventional SAW device (b) focused inter-digitated transducer (FIDT) design for a F-SAW device.

The amplitudes of the SAWs depend on the applied voltage input and frequency as well as device design characteristics and are typically in the nanometer range[1]. SAWs such as Rayleigh waves are generated in piezoelectric devices based on $LiNbO_3$ with a conventional IDT design and have a displacement component normal to the propagation direction. When in contact with a liquid, they tend to couple strongly with the liquid and leak ultrasonic power into the fluid in the form of acoustic waves called leaky SAWs. The leaky SAWs decay exponentially with distance from the source. The SAW interaction with the fluid creates a net pressure gradient in the direction of sound propagation in the fluid which leads to an internal, acoustically induced streaming phenomenon. SAW induced streaming finds applications in various processes ranging from micro-mixing, surface reactions, sonic cleaning to biological detection amongst several others. Altering the transducer electrode design from linear to circular causes the acoustic energy of the SAW device to be focused. This results in larger amplitude waves and, correspondingly larger streaming velocities are generated. Attempts to identify transducer designs which would increase the acoustic wave coupling with the fluid media and maximize the induced streaming phenomenon are made using structural 3-D finite element models. In particular, the transducer designs listed in Table 10-1 are simulated in the present work and used to identify the effect of the transducer design parameters on the focusing property of F-SAW device. These details are discussed in subsequent sections.

Table 10-1. Design parameters of different focused SAW transducers simulated in this work.

F-SAW design parameters	Number of finger pairs (N_p)	Degree of arc (D_a)	Geometric focal length (f_L) in µm	Wavelength (λ) in µm
Design-1	3	120°	45	40
Design-2	3	120°	45	*60*
Design-3	3	120°	45	*80*
Design-4	3	120°	*85*	40
Design-5	3	120°	*125*	40
Design-6	3	*90°*	45	40
Design-7	3	*60°*	45	40
Design-8	*4*	60°	45	40
Design-9	*5*	60°	45	40

10.4 Computational details

The propagation of acoustic waves in piezoelectric materials is governed by the mechanical equations of motion and Maxwell's equations for electrical behavior [1,265]. The constitutive equations of piezoelectric media in linear range coupling the two are given by [226]:

$$T_{ij} = c^{E}_{ijkl} S_{kl} - e^{t}_{kij} E_{k} \tag{10.1}$$

$$D_{i} = e_{ikl} S_{kl} + \varepsilon^{S}_{ik} E_{k} \tag{10.2}$$

In the above equations, T_{ij} represent the components of stress, c^{E}_{ijkl} the elastic constant for constant electric field, S_{kl} the strain, E_k the electric field intensity, D_i the electric displacement, e^{t}_{kij} the piezoelectric constant, and ε^{S}_{ik} the permittivity for constant strain. The acoustic wave propagation velocity is five orders of magnitude smaller than that of electromagnetic waves. Therefore, the quasistatic assumptions help reduce Maxwell's equation to $\frac{\partial D_i}{\partial x_i} = 0$ and $E_i = -\frac{\partial \phi}{\partial x_i}$, where φ represents the electric potential.

The components of strain are defined by

$$S_{ij} = \frac{1}{2}\left(\frac{\partial u_i}{\partial x_j} + \frac{\partial u_j}{\partial x_i}\right). \tag{10.3}$$

The equation of motion in the absence of internal body forces is given as

$$\frac{\partial T_{ij}}{\partial x_j} - \rho \frac{\partial^2 u_i}{\partial t^2} = 0 \tag{10.4}$$

where ρ is the density and u_i represent the components of displacement. Substituting and rearranging the above set of equations leads to a system of four coupled wave equations for the electric potential and the three component of displacement in piezoelectric materials which are solved for the piezoelectric substrate or the solid domain:

$$-\rho \frac{\partial^2 u_i}{\partial t^2} + c^E_{ijkl} \frac{\partial^2 u_k}{\partial x_j \partial x_l} + e_{kij} \frac{\partial^2 \phi}{\partial x_k \partial x_j} = 0 \qquad (10.5)$$

$$e_{ikl} \frac{\partial^2 u_k}{\partial x_i \partial x_l} - \varepsilon^S_{ik} \frac{\partial^2 \phi}{\partial x_i \partial x_j} = 0 \qquad (10.6)$$

These coupled wave equations can be discretized and solved for generating displacement profiles and voltages at each element/node using the finite element method.

10.5 Model parameters

A three dimensional finite element model was developed in the present study. A micron-sized piezoelectric substrate with dimensions (800μm propagation length x 500μm depth x 400 μm width) was simulated to gain insights into the wave propagation characteristics in F-SAW as well as conventional SAW devices. In most designs, three IDT finger pairs for the input port were defined at the surface of Y-cut, Z-propagating $LiNbO_3$ substrate. The fingers were defined with periodicity of 40, 60, and 80 μm for simulating F-SAW devices with varying wavelengths. 8-node quadrilateral coupled field solid elements were used to model the solid piezoelectric domain. The IDT fingers were modeled as mass-less conductors and represented by a set of nodes coupled by voltage degrees of freedom (DOF). A total of approx. 150,000 elements (more than 250,000 nodes) were generated. The model was created to ensure higher node density at the surface and throughout the middle of the device to study the different modes of surface acoustic waves and the use of 8-node coupled field (solid) elements with 3 DOF ensured the same. Three DOF's provided the displacements in the longitudinal (z), normal (y) and the shear horizontal (z) directions and a fourth for the voltage. The transient response of the F-SAW devices was simulated and used to identify conditions which would allow for enhanced ultrasonic microtransport.

10.5.1 Structure excitation

The center frequency of SAW devices simulated in this work is in the range of 50-100 MHz. Hence, the structure was simulated for a total of 200 nanoseconds (ns), with a time step of 0.5 ns. This enabled precise determination of the device frequency operating in the MHz range. The excitation of the piezoelectric solid was provided by applying a time varying voltage signal (with varying peak values and frequencies equivalent to the device center frequency) on the transmitter IDT fingers of the F-SAW devices as shown in Fig. 10-1. Two kinds of analysis were carried out for each of the F-SAW designs: (1) An impulse input of 100 V over 1 ns is applied to study the frequency response of the device and (2) AC analysis with a 5 V peak-peak input and 100 MHz frequency to study the wave propagation characteristics. A high input voltage impulse ensured that the amplitude of the acoustic wave impulse sampled at the output transducer fingers was sufficiently large enabling clear distinction from any possible interference arising from edge reflections. The applied voltage values chosen for AC analysis correspond to those used in typical experimental investigations[300].

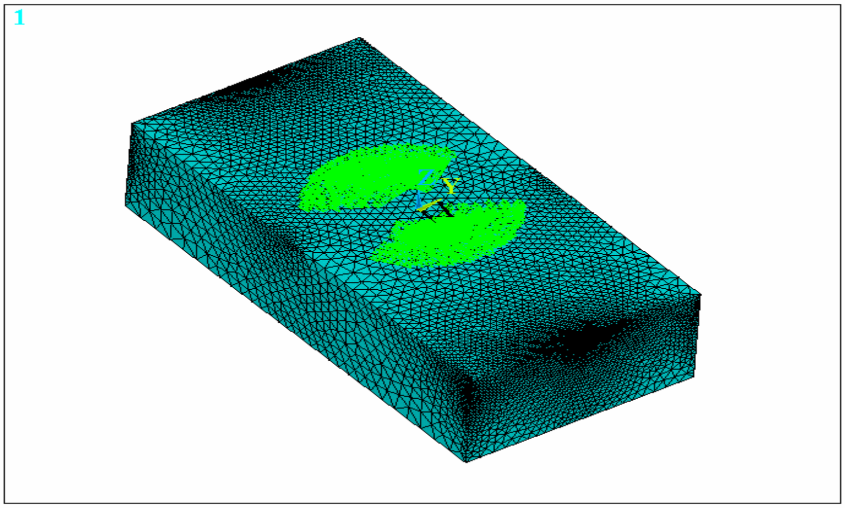

(a)

Figure 10-2. F-SAW device (a) Meshed structure (b) Applied input voltage profile for a 100 MHz SAW device.

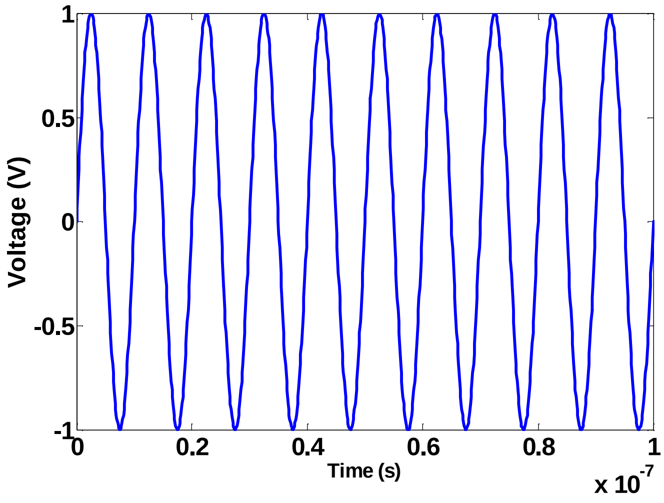

(b)

Figure 10-2: Continued

10.6 Results and discussion

Using a 3-D transient coupled field finite element model, the effect of transducer design parameters such as degree of arc (D_a), geometric focal length (f_L), wavelength (λ) as well as number of F-IDT finger pairs (as listed in Table 10-1) on the propagation characteristics (voltage and surface normal, longitudinal and shear horizontal displacement profiles) of F-SAW devices was investigated in the present work. Additionally, the effect of applied input voltages on the displacement waveforms along the F-SAW delay path was simulated. The transient response to an applied voltage impulse was used to calculate the center frequency of the F-SAW device and identify the propagation losses associated with each of the F-IDT designs. Analysis of particle displacements into the substrate depth was utilized to determine the acoustic energy confinement for the various F-IDT designs. The simulated frequency response as well as wave propagation characteristics obtained for an F-SAW are also compared with a conventional SAW device with similar design parameters. The details are presented in the following sections.

10.6.1 Frequency response analysis

The frequency response of the F-SAW device is necessary in most of their applications, such as filters, sensors, actuators, detectors, etc [1]. Although SAW devices with focused interdigital transducers have been studied for several years, the models required to calculate the frequency response are very limited [301-303]. In case of F-SAW devices, second order effects of SAW propagation such as SAW diffraction, refraction, and beam steering are much stronger than in the conventional SAW device and deeply influence the obtained frequency response [298,304]. Most of the simpler models are based on perturbational approach and are unable to account for such effects. Therefore, a simulation model such as the finite element technique which considers these second order effects is needed to accurately calculate the frequency response of a F-SAW device.

The frequency response of an F-SAW device H(f) can be obtained from its impulse response h(t) by taking the Fourier transform [228].

$$H(f) = \int_{-\infty}^{\infty} h(t) e^{-2\pi ft} dt \qquad (10.7)$$

To obtain the impulse response, a signal of the following form is input at the transmitting electrodes [227]:

$$V_i = \begin{cases} \dfrac{1}{T_S} & 0 < t \leq T_S \\ 0 & t > T_S \end{cases} \qquad (10.8)$$

In the above equation, T_s is the sampling time used in the simulations, t is the time and V_i is the applied voltage at the input transducer fingers. Three to five IDT fingers at each port were defined with the nodes coupled to zero volts, whilst the same number of output IDT fingers was coupled separately. The impulse function represented above is applied to the remaining input IDT fingers, and the average voltage profiles calculated at the output IDT fingers were used to derive the frequency response of the F-SAW device. The insertion losses associated with each of the transducer designs listed in Table 10-1 are calculated and used to identify the applicability of the various designs in the areas of microfluidics and sensing.

10.6.1.1 Effect of wavelength (λ)

To investigate the effect of acoustic wavelength on the propagation characteristics of F-SAWs, we simulated F-SAW devices with varying IDT finger spacing *i.e.* 10, 15 and 20 microns. Typically, the SAW device operational frequency is given by $v/4f$, where v is the velocity of the acoustic wave traveling along any particular crystallographic direction in the $LiNbO_3$ substrate and f is the finger spacing. Therefore, the spacing between electrodes was modified to simulate F-SAW devices operating in different frequency ranges and generating focused acoustic waves with varying wavelengths. The smallest attenuation is attained when the input excitation frequency matches the center frequency of the device. To identify the center frequency for subsequent AC analysis, an impulse input of 100 V was applied to the transmitter fingers. The frequency response obtained for the three designs with varying IDT finger spacing is shown in Fig. 10-3. The calculated center frequencies for the three cases are listed in Table 10-2. It can be seen that the center frequencies for 10, 15 and 20 micron F-IDT finger spacings correspond to 100, 75 and 55 MHz, respectively.

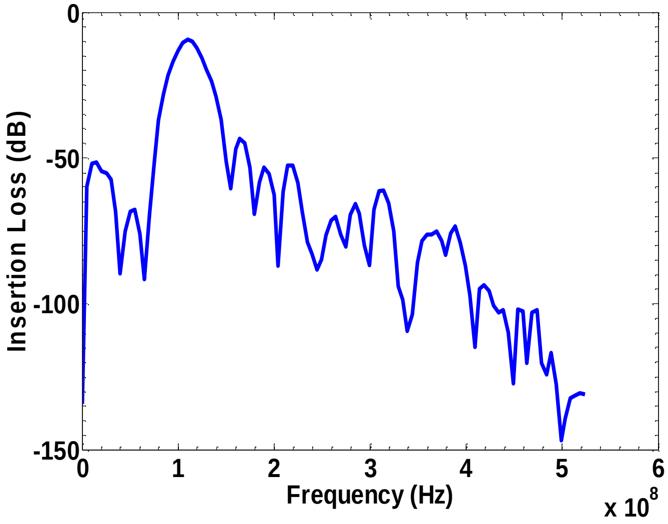

(a)

Figure 10-3. Simulated frequency responses of F-SAW devices (a) Design-1 (b) Design-2 (c) Design-3.

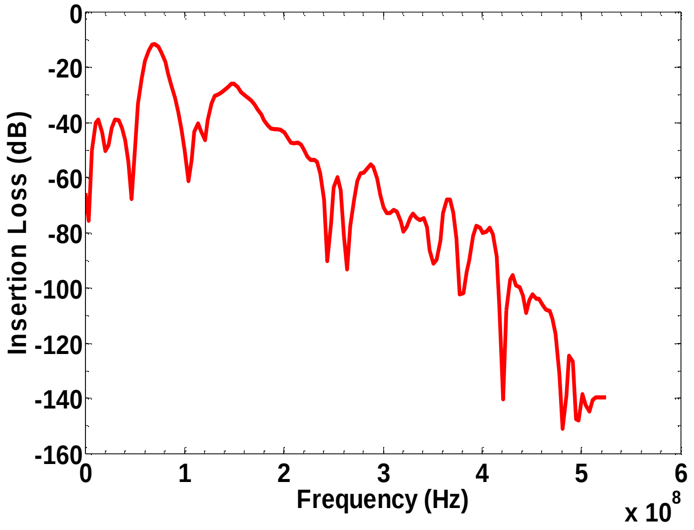

(b)

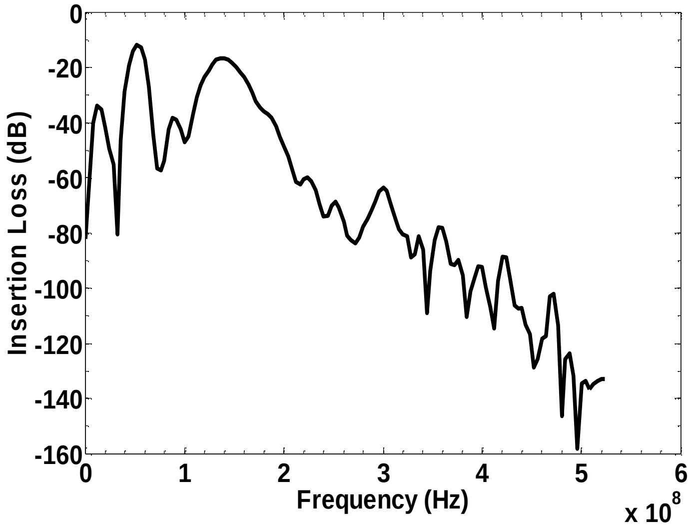

(c)

Figure 10-3: Continued

The insertion losses corresponding to the three designs are also listed in Table 10-2. We find that F-SAW devices operating at lower frequencies show higher propagation losses as compared to those operating at higher frequencies. This behavior is different from that seen in conventional SAW devices, in which the higher frequency devices have higher propagation losses. It is also worth noting that in the F-SAW devices operating at ~ 55 and 75, the frequency response appears to show significant bulk acoustic wave (BAW) interference at the high frequency end of the device passband. It is however also possible that the high frequency signal obtained at ~ 150 MHz is a result of electromagnetic feed-through effect. The BAW velocity in YZ LiNbO3 is 7220 m/s and hence it takes approximately 12 ns for the wave to travel the delay line distance of 45 microns between the input and output electrodes. The electromagnetic feed-through on the other hand is attributed to the initial signal which occurs mostly within the first few nanoseconds. Our analysis of the frequency response obtained without the electromagnetic feedthrough effect, *i.e.*, time domain signal picked up beyond 12 ns, indicated that the high intensity signal still existed and is therefore a result of BAW interference. Although the disappearance of the BAW signal in the 100 MHz F-SAW device is unclear, it is evident that the higher propagation losses associated with the 55 and 70 MHz devices as shown in Table 10-2 are due to BAW interference.

Table 10-2. Calculated center frequencies and insertion losses for three designs with varying finger spacing.

F-SAW transducer design	Wavelength (λ)	Center Frequency (MHz)	Insertion Loss (dB)
Design-1	40	100	-9.5
Design-2	60	70	-11.6
Design-3	80	55	-11.9

Based on these simulation findings, it appears that the 100 MHz frequency F-SAW device with lesser insertion loss is more suitable for applications involving microfluidics and sensing. Therefore, in the subsequent subsections, we compare the variations of geometric focal length and the degree of arc of F-IDT for the device operating at 100 MHz.

10.6.1.2 Effect of geometric focal length (f_L)

To investigate the effect of geometric focal length on the frequency response of the F-SAW device, we simulated devices with same degree of arc of 120° and finger spacing of 10 microns, but different focal lengths of 45, 85 and 125 microns. The simulated frequency response for the different device designs is shown in Fig. 10-4. It can be seen that the center frequency of the devices is unaffected by changes in the focal length and depends primarily on the F-IDT finger spacing. The calculated insertion losses corresponding to the various geometric lengths are summarized in Table 10-3. As expected, the F-SAW devices with higher focal length show increased insertion loss.

Table 10-3. Calculated insertion loss for F-IDTs with varying focal length.

F-SAW transducer design	Geometric focal length (f_L) in μm	Insertion Loss (dB)
Design-1	45	-9.5
Design-4	85	-9.2
Design-5	125	-13.9

The higher propagation losses are attributed to second order effects arising from substrate anisotropy such as SAW diffraction, refraction and beam steering which are stronger in F-SAW devices in comparison to conventional SAW ones, as has been shown in one of our investigations [304]. The calculated insertion loss shows little change for focal length variation from 45 to 85 microns. However, it increases significantly from approximately 9.2 dB to 13.9 dB when the focal length changes from 85 to 125 microns. It is likely that the insertion loss shows a non-linear dependence on geometric focal length, although more simulations are needed to confirm the same. This implies that beyond a certain optimal focal length, the propagation losses are significantly higher. F-SAW devices, beyond the optimal focal length, with higher insertion losses are unsuitable for sensing applications and might find applications primarily in actuation, whereas those within the optimal focal length might be suitable for both sensing and actuation. The localized amplitude variations in the focal region for each of the three designs are required to substantiate the above arguments. This and other details of the propagation characteristics for the three designs are discussed in the AC analysis in a subsequent subsection.

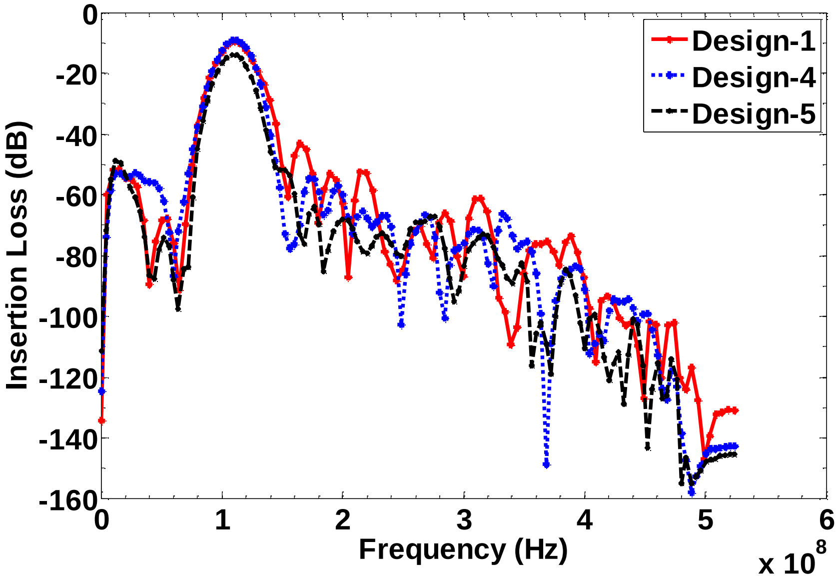

Figure 10-4. Simulated frequency response of F-SAW devices with transducer configurations having varying geometric focal length.

10.6.1.3 Effect of degree of arc

The effect of degree of arc of the F-IDTs on the frequency response of the F-SAW device is shown in Fig. 10-5. The simulated devices shown in Fig. 10-5 have the degree of arc varying from 120 for Design-1 to 60°for Design-7. The increase in the degree of arc of an F-IDT does not change the pass-band width of the device. However, there exist significant differences in the insertion loss of the device shown in Table 10-4. For smaller degree of arc such as 60°, the insertion losses are significantly reduced (3.8 dB). However, if the degree of arc is excessively large, then the insertion loss becomes larger, for example, it is 9.5 dB for a 120° arc. An increase in the degree of arc of F-IDTs results in an increase in SAW diffraction which results from the high anisotropy of the piezoelectric substrate. This typically occurs when the propagation direction is not along one of the pure-mode axes of the crystal, but at an angle θ with respect to it. In such cases, as in an F-SAW device with the transducers based on concentric circular arcs, the acoustic group velocity will propagate off at angle φ with respect to the phase velocity. The higher the degree of arc, the higher would be the SAW diffraction effect and hence greater would be the insertion loss as seen in Fig. 10-5.

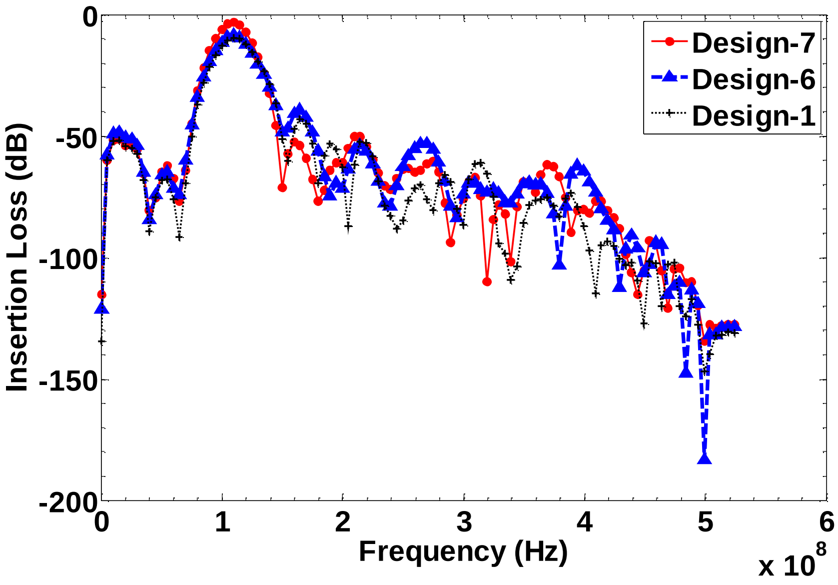

Figure 10-5. Simulated frequency response of F-SAW devices with transducer configurations having varying degrees of arc.

It is expected that an increase in the degree of arc of the FIDTs might lead to better focusing property with the amplitude field possibly reaching a focal point. This can be useful to build devices that are more suitable as actuators in microfluidic applications. However, as brought out earlier, F-SAW devices with higher propagation losses are not best suited for sensing applications. Hence, it is likely that F-SAW device with smaller degree of arc and lower insertion losses are more qualified to be applied as sensors or filters. A detailed AC analysis of the propagation characteristics of F-SAW devices with varying degrees of arc is presented in a subsequent section.

Table 10-4. Calculated insertion loss for F-IDTs with varying degrees of arc.

F-SAW transducer design	Degree of arc	Insertion Loss (dB)
Design-1	120°	-9.5
Design-6	90°	-8.6
Design-7	60°	-3.8

10.6.1.4 Effect of number of finger pairs

To simulate the effect of number of F-IDT finger pairs on the frequency response of the F-SAW device, we utilized Design-7 with three F-IDT finger pairs as the base case. The number of F-IDT fingers was subsequently increased to four and five and the results are shown in Fig. 10-6. We find that the pass-band width becomes narrower with an increase in the number of finger pairs while the insertion loss of the devices becomes smaller. It has been reported by Wu et al. that for large enough number of finger pairs (~ 120), the insertion loss of the F-SAW device does not decrease any further with increase of this number. However, the increase in finger pairs also increases the size of the device. As a result, it is necessary to optimize the number of F-IDT finger pairs in an F-SAW device according to the required pass-band and insertion loss.

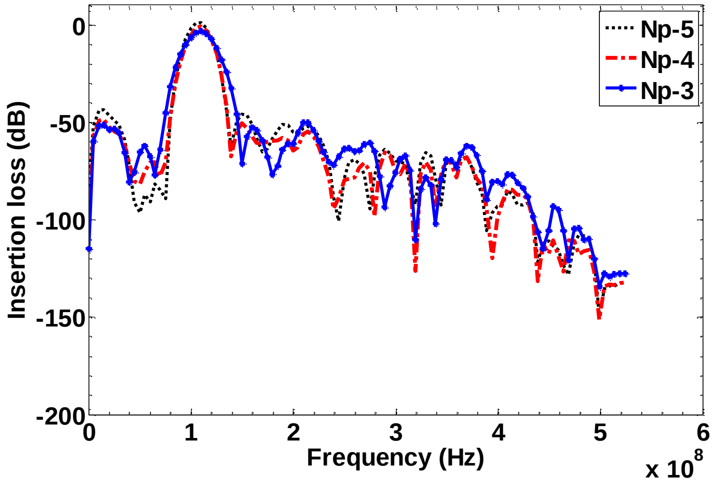

Figure 10-6. Simulated frequency response of F-SAW devices with transducer configurations having varying number of F-IDT fingers.

The simulation model developed by Wu et al. [298] was based on effective permittivity approach and perturbation theory. In the present case, although more robust, the finite element simulations involving larger number of finger pairs led to a considerable increase in the number of elements to model the F-SAW device and leading to a significant increase in the simulation time. The computationally intensive nature of the FE model makes it difficult to simulate F-SAW having increased number of finger pairs.

10.6.2 AC response analysis

AC analysis for the various F-IDT designs considered in the above section was carried out to investigate the focusing property as well as understand the propagation characteristics of F-SAWs. The simulated displacement contours showing F-SAW propagation along the substrate surface for a typical AC analysis of Design-4 are shown in Fig. 10-7. The focusing effect, which is clearly evident from Fig. 10-7, is analyzed for the various designs listed in Table 10-1.

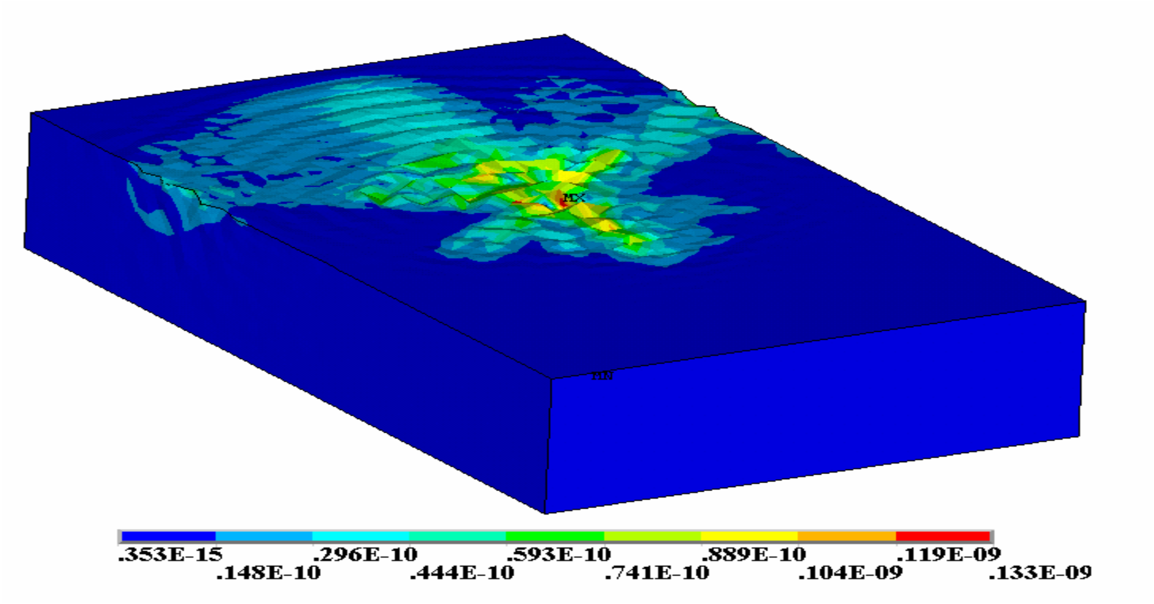

Figure 10-7. Simulated acoustic wave propagation in an F-SAW device. The parameters correspond to those of Design-4.

The propagation of acoustic waves in the F-SAW device is evaluated in terms of the displacement waveforms in the surface normal, longitudinal and shear horizontal directions at various locations along the delay path including the output transducer fingers. The voltage waveforms analyzed at the output transducer are used to gain insights into the extent of wave attenuation. The wave propagation into the depth of the substrate is analyzed to understand the acoustic energy confinement as well as wave conversion into the bulk mode.

10.6.2.1 Effect of degree of arc of F-IDT

AC analysis of F-SAW devices with varying degrees of arc of F-IDTs ranging from 120° to 60° was carried out to investigate the focusing property and propagation characteristics of F-SAWs. An increase in the degree of arc also causes an increase in the aperture width of the F-IDT fingers. The simulated amplitude field obtained after the wave has stabilized (after 40 ns) is shown in Fig. 10-8. It can be clearly seen that the amplitudes attain maxima at regions close to the focal point. The displacement amplitudes at the focal point decrease with degree of arc of the FIDTs. The maximum in case of Designs 6 and 1 (*i.e.* with Da=90° and 120°) appears to be shifted away from the focal point. The deviation results from SAW diffraction and is attributed to the anisotropy of the piezoelectric substrate. The SAW diffraction effect increases with the degree of arc. As a result, the frequency response of devices with larger degrees of arc shows higher insertion loss.

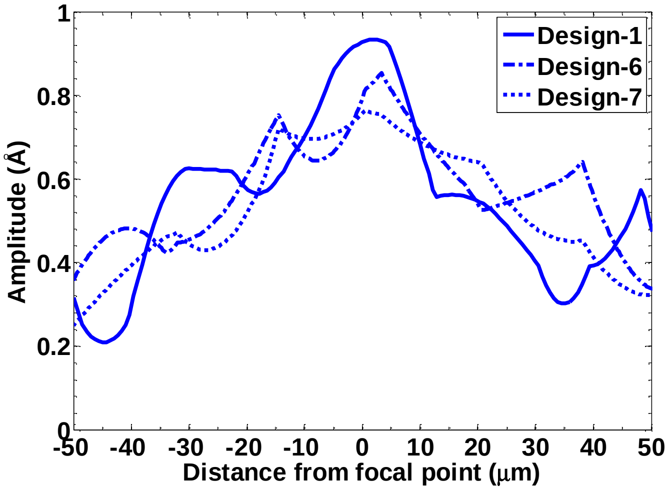

Figure 10-8. Simulated amplitude field for F-SAWs with varying degrees of arc.

The snapshots obtained at the end of 70 ns of simulation time for the three FIDT designs are shown in Fig. 10-9. The amplitude fields appear to converge to the focal point as the degree of arc increases from 60° to 120°. Hence, it can be observed that FIDTs with larger degree of arc produce a smaller focal point. Therefore, the focusing property becomes better as we increase the degree of arc, with the amplitude field approaching the focal point. For devices having sufficiently larger degree of arc, *i.e.*, greater than 90°, it can be seen that the variations in the azimuthal direction are negligible, especially at regions near the focal point. As we move away from the focal region, *i.e.*, distances greater than 4λ, variations in the azimuthal direction become significant as seen from the displacement contours shown in Fig. 10-9. The acoustic wave propagation characteristics in devices having FIDTs with smaller degree of arc approach that of a conventional SAW device. At longer simulation times, wave reflections from the edge of the substrates are also captured by these coupled field finite element models.

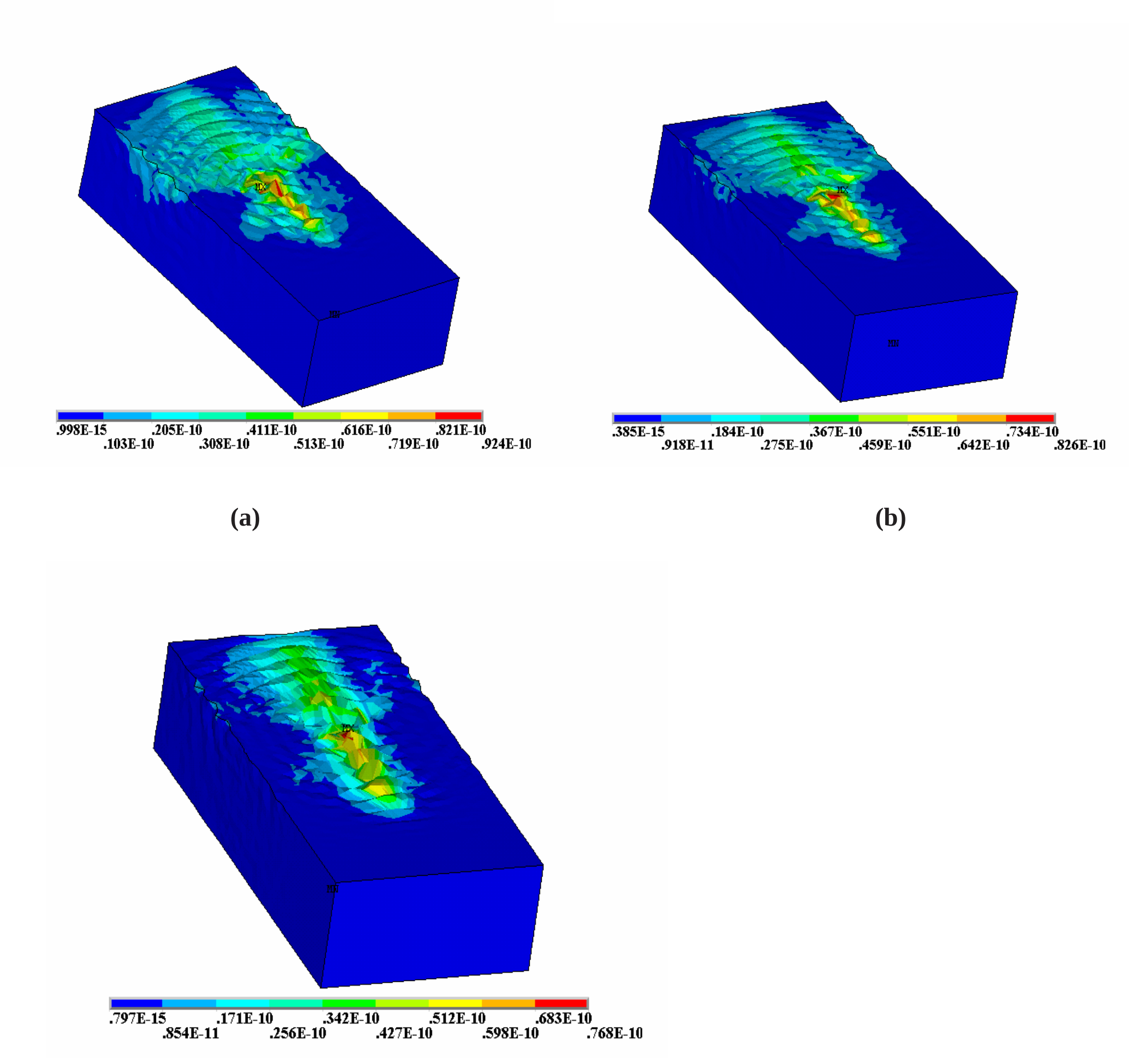

(a)

(b)

(c)

Figure 10-9. Simulated displacement contours for F-SAW devices having F-IDTs with various degrees of arc (a) Design-1 (b) Design-6 (c) Design-7.

We further analyze the displacement profiles along the depth of the piezoelectric substrate for a section cut through the region close to the focal point of the F-SAW device as shown in Fig. 10-10. Insights into the acoustic energy confinement at regions near the focal point and substrate surface can be obtained using Fig. 10-10. The waves are confined within one to two wavelengths from the device surface. The acoustic intensity rapidly attenuates with depth into the device surface for the three designs shown. However, we find higher acoustic wave penetration into the substrate surface for F-SAW devices having larger degree of arc. As brought out earlier, the displacement amplitudes are higher for devices having FIDTs with larger degrees of arc.

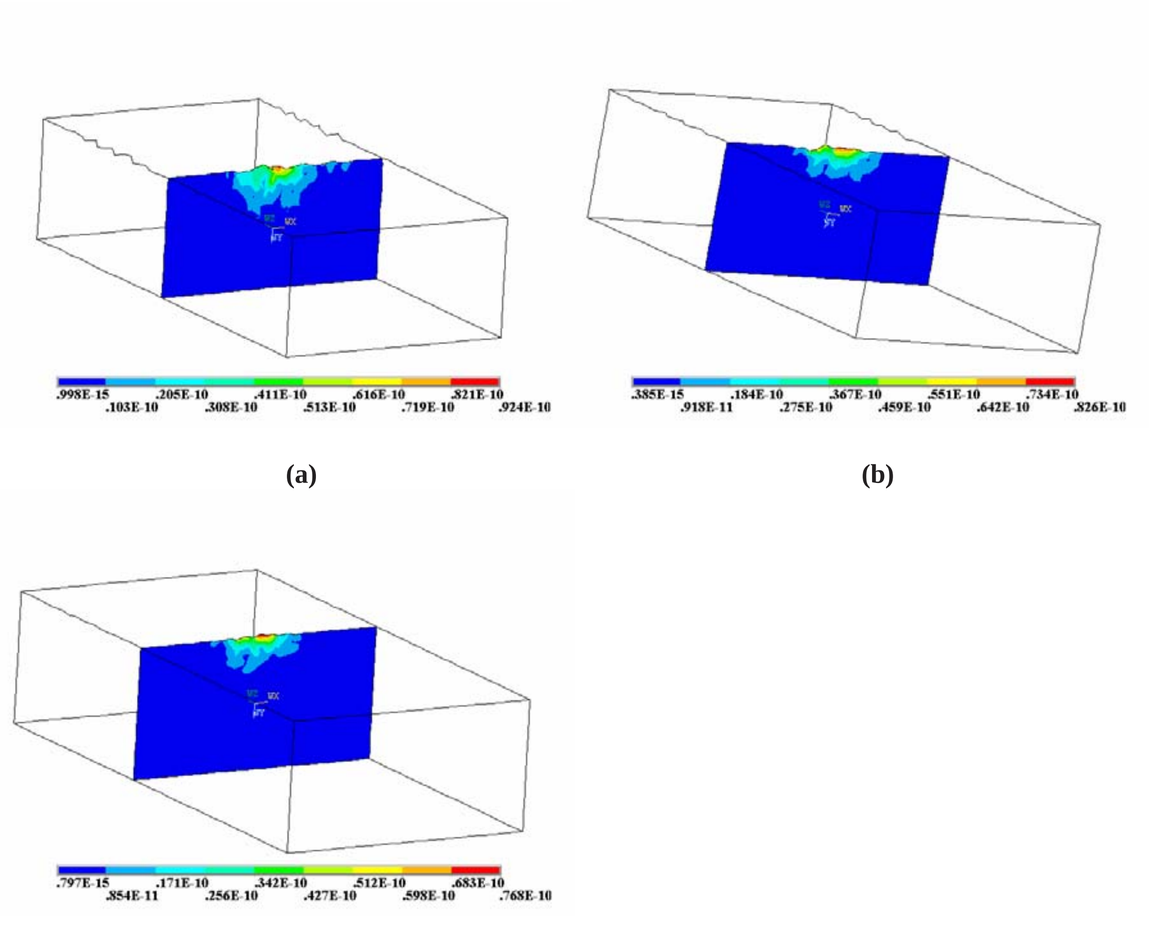

(a) **(b)**

(c)

Figure 10-10. Simulated displacement profiles along the depth of the piezoelectric substrate for a section cut through a region close to the center of delay path and normal to the propagation direction for (a) Design-1 (b) Design-6 (c) Design-7.

Based on the findings of the AC and impulse analysis, it appears difficult to design F-SAW devices having degree of arc that results in best possible focusing properties and lowest insertion loss at the same time. Amongst the various simulated designs, F-IDTs with Da=90° appears to be the optimum transducer configuration for use in both microfluidic and sensing applications. On the other hand, FIDTs with Da=120° have better focusing property, but higher insertion loss and are most suitable for use in actuation or excitation. FIDTs with Da=60° have moderate focusing property, but smaller insertion loss and hence are most suitable for sensing applications.

Furthermore, comparison of propagation characteristics of an F-SAW device (Design-1) with a conventional SAW device having uniform transducer fingers can also be carried out. In Ref. (29), we simulated a 100 MHz conventional SAW device having a finger periodicity of 40 microns, an aperture width of 200 microns and delay-line equivalent to twice the focal length in Design-1. An AC electrical input of 5 V (peak-peak) was applied at its transmitting fingers. We analyzed the displacement contours as well as the amplitude field at various locations along the device delay-line as well as at the output transducer fingers after the system had stabilized (after 70ns). Our simulation results indicated that the surface waves generated in a conventional SAW device with uniform fingers and aperture width has smaller amplitudes of particle displacement compared to F-SAWs. The analysis of particle displacement profiles indicated that the depth penetration of the surface waves in a conventional SAW is smaller than that observed for a focused SAW device. Additionally, the localized variations observed near the focal point in an F-SAW device are absent in conventional SAWs. Our analysis of the voltage profiles obtained at the receiving IDT fingers indicates the propagation losses in the conventional SAW are lower than that in F-SAW, owing to reduced second order effects such as SAW diffraction, refraction and beam steering. More details on the generation and propagation characteristics of F-SAW and its comparison to a conventional SAW can be found in [304]. We found that the conventional SAW devices are better suited for sensing applications than for actuation and microfluidic application. On the other hand, depending on the design specifications, F-SAW devices can be applied for both sensing as well as actuation and microfluidic applications.

10.6.2.2 Effect of geometric focal length (f_L)

AC analysis, as brought out in the above sub-section, of F-SAW devices with varying geometric focal length (45, 85 and 125 microns) was carried out to investigate its effect on the propagation characteristics of F-SAWs. The amplitude fields obtained near the focal point for the three designs are qualitatively similar. The simulated displacement contours obtained for the three designs, *i.e.*, Designs 1, 4 and 5 shown in Fig. 10-9 (a), 10-7 and 10-11, respectively, were analyzed to study the dependence of the focusing property on the geometric focal length. Our analysis indicated that the displacement amplitudes attain a maximum near the focal point, which increases with F-IDT focal length. At first sight, this might appear counter-intuitive as one would expect higher propagation losses and smaller displacement amplitudes for devices with longer geometric focal length. However, for the same degree of arc and number of finger pairs, the aperture width of the F-IDT fingers would increase with distance from the focal point (Fig. 10-1 (b)). Hence, the increased propagation losses are compensated by a corresponding increase in the aperture width and therefore, higher displacement amplitudes as well as increased focusing property result in devices with increased geometric focal length. For the same reason, our analysis of displacement profiles along the depth of the substrate for a section cut through the focal point also indicated higher acoustic energy penetration for F-SAW devices having longer geometric focal length.

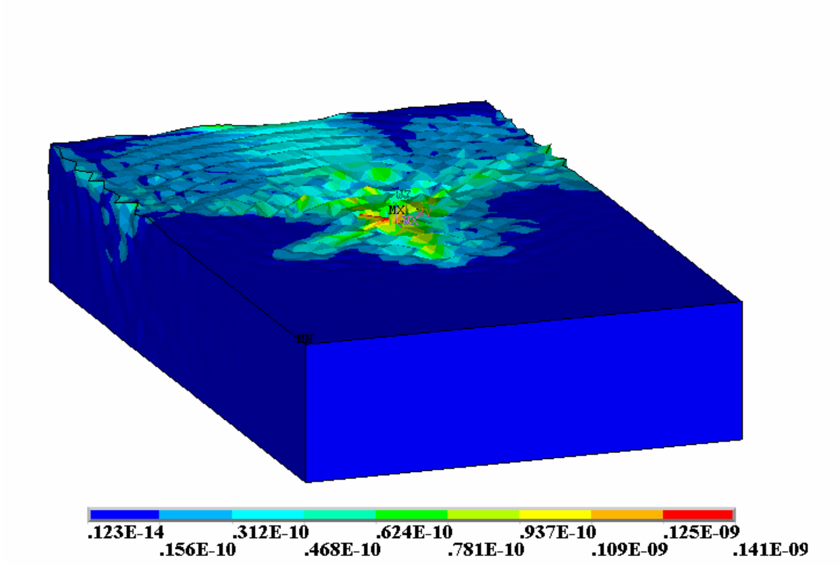

Figure 10-11. Simulated displacement contours for Design-5, i.e., F-SAW device having F-IDTs with focal length of 125 microns and degree of arc of 120°.

Although the current simulations suggest that longer focal lengths might be needed (typically 20λ) for the amplitude field to approach a concise focal point, the scale of the device would also increase significantly, making the simulation computationally intensive. This, and other limitations of the finite element simulations can be found in Ref. (305).

10.6.2.3 Effect of wavelength (λ)

AC analysis of F-SAW devices with varying F-IDT finger spacing was carried out to understand the effect of F-SAW wavelength on its propagation characteristics, in particular, the focusing property. An applied voltage of 5 V (peak-peak) with frequency determined from the frequency response shown in Fig. 10-3 was input at the transmitting F-IDTs. The amplitude fields obtained for the three designs are shown in Fig. 10-12. Although the F-SAW amplitude at the focal point is not very different for the three designs, the distribution of the F-SAW amplitude field shows significant differences. Comparison of the peak amplitudes of the F-SAW crest at regions near the focal point for the three different wavelengths (Fig. 10-12) suggests that the focusing effect is enhanced for devices with smaller wavelengths and higher frequency. The localized variations are more prominent in Design-1, whereas Design-3 appears to have a more uniform particle displacement near the focal point.

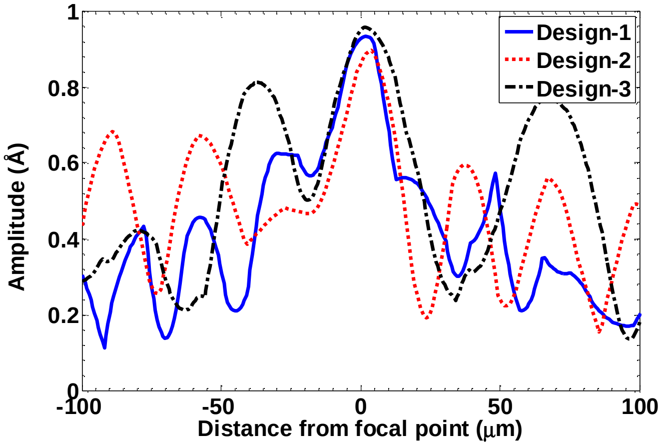

Figure 10-12. Simulated amplitude fields for F-SAWs with varying wavelengths.

The simulated displacement contours for Designs 1, 2 & 3 obtained after the system has stabilized (70 ns) is shown in Fig. 10-9 (a) and 10-13 (a) and (b), respectively. We find that the scattering of the waves after the focal point reduces with increase in the wavelength and the amplitude field becomes more uniform. The size of the focal area increases with the increase in F-SAW wavelength. For larger wavelengths, the amplitude field has no concise focal point. Instead, the F-SAW propagates as a narrow, long, strong SAW beam as shown in Fig. 10-13 (b).

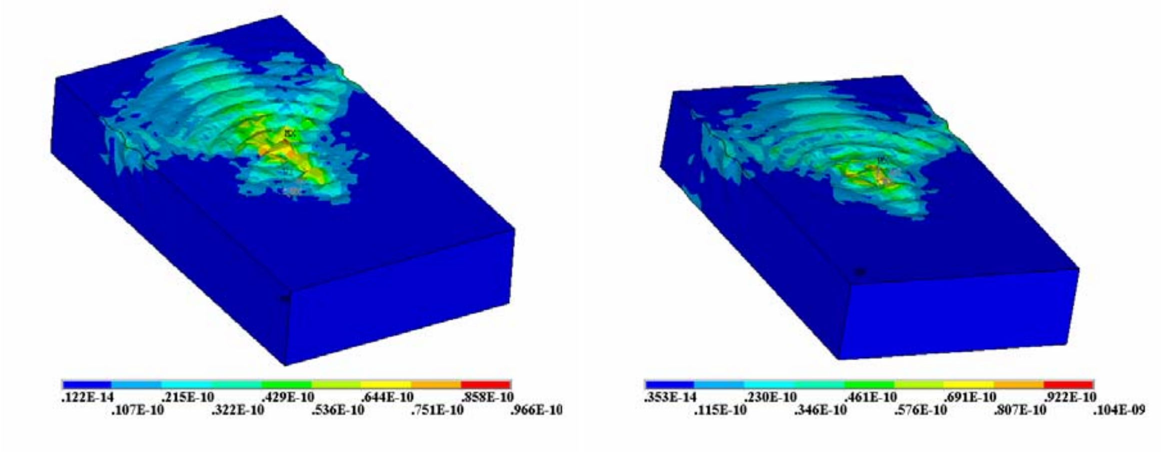

(a) **(b)**

Figure 10-13. Simulated displacement contours for (a) Design-2 (b) Design-3; *i.e.*, F-SAW device having F-IDTs with wavelengths of 60 & 80 microns, respectively.

Our simulation results indicate that the focusing properties increase with decrease in the wavelength of the F-SAW. Additionally, F-SAW devices operating at higher frequencies or smaller wavelengths also incur smaller propagation losses. Hence, for both sensing and microfluidic applications, devices operating at higher frequencies or generating F-SAWs with smaller wavelengths are preferred.

10.6.3 Effect of applied input voltage

The simulations results reported above for the various F-IDT designs were obtained for an applied AC electrical input of 5 V (peak-peak) at the transmitter F-IDT fingers. To investigate the effect of voltage intensity on the propagation characteristics of the wave, we simulated a F-SAW device with transducer design parameters corresponding to Design-1 and operating at 100 MHz, but with varying applied input voltages of 5, 10, 20 and 30 V (peak-peak). Our simulation results indicated that the propagation characteristics and displacement contours generated for the various power inputs were qualitatively similar, but quantitatively different. As brought out earlier, the maximum amplitudes were obtained at the focal point of the F-SAW device. The amplitudes of the wave generated at the focal point in the F-SAW device for the various simulated voltage inputs are shown in Fig. 10-14. We find that the amplitude of the generated focused wave varies linearly with the applied input voltage.

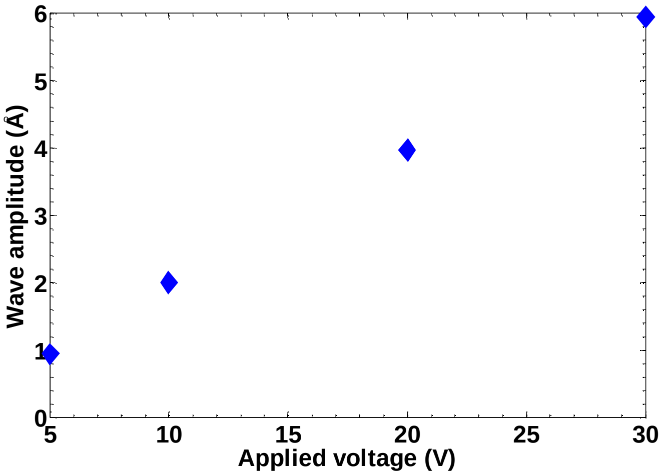

Figure 10-14. Effect of applied input voltage on the wave amplitudes at the focal point in an F-SAW device.

Similar linear variation was observed theoretically for conventional SAW devices simulated in our previous investigations and was also reported experimentally by Chono et al. for SAW devices operating at 50 MHz frequency. The SAW amplitudes in these experiments were measured using optical methods for varying input voltages [306]. When in contact with the fluid medium, the increased wave amplitudes are expected to result in enhanced streaming forces and increased streaming velocities.

10.7 Conclusions

A three dimensional coupled field finite element (FE) model of F-SAW devices was developed in this work. The F-IDTs were modeled as concentric circular arcs patterned on the surface of YZ-$LiNbO_3$ The model was used to investigate the effect of geometric shape of transducers on the focusing property of F-

IDTs. The effect of several F-IDT design parameters such as number of finger pairs, degree of arc, geometric focal length as well as the wavelength of F-SAW on its propagation characteristics as well as focusing property was studied in detail. An impulse and AC electrical input was applied at the transmitting F-IDT fingers to evaluate the device frequency response and F-SAW propagation characteristics, respectively. The frequency of the simulated devices ranged from approximately 55 to 100 MHz.

The displacement contours as well as the variations in amplitude field at various locations around the focal region obtained in an AC analysis were used to evaluate the focusing property for the various transducer designs. The results indicate that the focusing property is significantly influenced by the geometric shape of the transducers. F-SAW devices with larger degree of arc of F-IDTs and operating at higher frequencies, *i.e.*, generating waves with smaller wavelength, are needed to obtain better focusing. Also, there exists an optimal geometric focal length for the F-SAW devices which depends on a compromise between the focusing property and the associated insertion loss. Longer geometric focal length gave better focusing characteristics and increased insertion losses. The wavelength of F-SAWs also significantly affected the focusing property. Larger wavelength F-SAWs generate long, narrow, strong SAW beams, but the amplitude field is unable to approach a precise focal point. Shorter wavelength F-SAWs which are generated in devices operating at higher frequencies are able to achieve the same.

Based on the FE simulation results, we have attempted to identify transducer configurations that are best suited for sensing and microfluidic applications. We find that F-SAW devices operating at higher frequencies and with high applied input voltages, optimal geometric focal length, and larger degree of arc are best suited for actuation and microfluidic applications whereas F-SAW devices with shorter geometric focal length and smaller degree of arc of F-IDTs are better suited for sensing. Additionally, in comparison with the conventional SAW devices fabricated with uniform interdigital transducers, we find that the focused SAW devices are more sensitive to variations in the focal area instead of the whole delay-line region. This makes them suitable for application requiring detection or manipulation of localized variations, such as those utilizing acousto-optic or acousto-electric effects. The findings of our study have laid the groundwork for further investigation into the propagation characteristics and focusing property of F-SAW devices fabricated on multilayered substrates and/or with more complicated transducer designs.

Chapter Eleven

Conclusions and future work

11.1 Conclusions

In the first part of the thesis, the nanoscale material behavior of transition metal alloys in the form of clusters and wires was investigated using classical molecular dynamics simulations. The thermodynamic, structural and mechanical properties of Pd-Pt nanoclusters and nanowires having diameter of approximately 2.3 nm and varying compositions was studied. The melting behavior of Pd-Pt nanoclusters is characterized by pre-melting of surface segregated Pd atoms followed by homogeneous melting of Pt core. The simulated melting point of nanoclusters calculated from our simulations is much lower than the corresponding bulk Pd and Pt crystals. Comparisons to same sized bimetallic nanowires are also carried out. The simulated phase diagram of bimetallic nanowires is quite different from that of same-diameter nanoclusters as well as that of bulk Pd-Pt alloy. Nanowires undergo solid-solid transition from fcc to hcp resulting in the existence of metastable hcp phase over temperature ranges which vary with the wire composition. The phase boundaries (fcc-hcp and solid-liquid) in nanophase alloys are dictated by two competing processes *i.e.* surface melting and solid-solid transformation. The observed differences in the surface melting mechanism of wires and clusters as well as the strength of the metal-metal interactions for a given segregation profile dictate the onset of solid-solid transition from fcc-hcp for a particular nanowire composition. A melting theory developed for nanoclusters was extended to nanowires to facilitate comparisons with the same. The simulated nanowire and nanocluster melting temperatures over a range of alloy composition are in moderate agreement with the predictions of the phenomenological models. We have discussed possible sources of discrepancies. A linear variation of melting point with reciprocal nanowire diameter was found. The size and composition dependence of nanowire melting temperatures are thus consistent with the available melting theories.

The influence of substrate interactions on the thermal characteristics of bimetallic nanoclusters was also studied. Our simulations indicate that the effect of the weak graphite support is to delay the onset of melting leading to higher transition temperatures compared with isolated nanoclusters, but still lower than bulk melting points. Structural transformations are found to occur at temperatures much below the phase transition. The graphite field causes a rapid rearrangement of atoms located close to the substrate. The dynamic properties associated with substrate-supported cluster melting were studied using deformation parameters, diffusion coefficients, velocity auto-correlation functions and analysis of density profiles. Components of velocity auto-correlation function characterizing diffusion of the constituent atoms in the bimetallic nanoclusters suggest greater out-of-plane movement in comparison to in-plane which increases with increasing composition of Cu in Pd-Cu and Pd in Pd-Rh and Pd-Pt.

Our studies indicate wetting behavior which is influenced by the weak metal-graphite, and the metal-metal interactions. Influence of the graphite field is restricted to a few monolayers of atoms and has a more prominent effect on surface melted atoms. Shell-based diffusion coefficients indicate greater surface melting in shells located farther away from the graphite substrate. We find the cluster to diffuse as a single entity on the graphite surface. All the three nanoclusters studied exhibit high diffusivities on the graphite substrate, consistent with experimental observations. The forces exerted by the graphite field are relatively lower when compared to actual piezoelectric substrates that are present in SAW sensors. Therefore, our findings indicate that the effect of piezoelectric substrate would have a profound effect on the structure and dynamics of nanoclusters and wires employed as sensing layers.

The mechanical properties of the transition metal alloy nanowires were estimated under varying strain rates and temperatures. The deformation and rupture mechanism of alloy nanowires were found to be similar to those observed for single component wires. The yielding and fracture mechanisms depend on the applied strain rate as well as atomic arrangement, and temperature. At low temperature and strain rate, where crystal order and stability are highly preserved, the calculated stress-strain response of pure Pt and Pd as well as Pd-Pt alloy nanowires showed clear periodic, stepwise dislocation-relaxation behavior. Crystalline to amorphous transformation takes place at high strain rates (5% ps^{-1}), with amorphous melting detected at

300 K. Due to higher entropy of the nanowire at higher temperature and strain rate, periodic stress-strain behavior is absent, and superplasticity behavior is observed. Deformation of nanowires at higher strain rates and low temperature, where the superplasticity characteristic is significantly enhanced, results in the development of a multishell helical structure.

Mechanical properties of the alloy nanowires are significantly different from those of bulk phase and are dictated by the applied strain rate, temperature, alloy composition as well as the structural rearrangement associated with nanowire elongation. We find that the Young's modulus of both the single component as well as alloy nanowires depends on the applied strain rate and is about 70-75% of the bulk value. Ductility of the studied nanowires showed a non-monotonic variation with Pd composition at low strain rates and was significantly enhanced for wires developing and rearranging into a multishell helical structure which occurred at higher strain rates. The Poisson ratio of Pd rich alloys is 60-70% of its bulk value whereas that of Pt rich alloys is not significantly changed at the nanoscale. The calculated differences in the nanowire mechanical properties are shown to have significant effect on their applicability in areas such as sensing and catalysis. The propagation characteristics of SAW with nanomaterial sensing layer would be significantly different from those calculated using properties of thin films. The morphological and structural changes in metallic nanowires induced by uniaxial stretching can also be expected to play an important role when used as sensing layers in high frequency SAW devices.

The second part of the thesis utilizes 3-D and 2-D coupled field finite element models to study wave propagation characteristics in a typical SAW gas sensor as well as in a novel SAW biosensor. The response of a SAW H_2 gas sensor was simulated by using material properties of Pd and Pd-H sensing layers. Changes in the Young's modulus of elasticity and density of the palladium film upon gas adsorption were introduced into the simulations. The displacement and voltage profiles obtained at the output transducer were used to derive the gas sensor response. The finite element model reveals that the Rayleigh mode (z-direction displacement) is the most suitable for gas sensing. A time shift of approximately 3 ns and an insertion loss of 1.8 dB were observed when the gas sensor with thin Pd film was exposed to 3% H_2. The finite element modeling and simulation provides a powerful means to study surface acoustic wave propagation characteristics.

Fluid-structure interaction models are developed for biosensing applications. A coupled field finite element fluid-piezoelectric interaction model is developed and solved to gain insights into the acoustic streaming induced flow in SAW devices. The developed model is more accurate and represents a significant improvement over the existing numerical techniques utilized to model the SAW streaming phenomenon. Fluid domain was modeled using the Navier Stokes' equation; the arbitrary Lagrangian Eulerian approach was employed to handle the mesh distortions arising from the motion of the solid substrate. The fluid-solid coupling was established by maintaining stress and displacement continuity at the fluid-structure interface. To our knowledge, this is the first presentation of a coupled field finite element fluid-piezoelectric interaction model in the literature. Experimental investigations demonstrate the validity of the model. The results demonstrate the use of acoustic streaming in removal of non-specifically bound proteins, thereby improving sensor response and sensitivity.

The developed 3-D finite element structural models are extended to study wave propagation in a novel hexagonal SAW device, which finds applications in materials characterization as well as chemical and biological sensing. The wave propagation characteristics along the different delay paths in a hexagonal SAW device are studied. Our simulation results indicate that the hexagonal SAW device based on $LiNbO_3$ can be utilized for rapid and simultaneous extraction of multiple film parameters (film material density, Lamé and shear modulii, sheet conductivity) of a thin film material and achieve a more complete characterization in comparison to a conventional SAW device. Furthermore, our results indicate that in hexagonal devices based on $LiTaO_3$, one of the delay paths can be used for detection whereas the other delay paths can be used to simultaneously remove the non-specifically bound proteins using acoustic streaming phenomenon in biosensing application. The developed models are extended to investigate the acoustic wave propagation and generation in focused SAW devices with transducers shaped as concentric circular arc. Optimization of design parameters leading to enhanced amplitude fields & lower propagation losses, thereby increased device sensitivity is carried out. In comparison to conventional SAW devices with uniform transducer fingers, the variations in amplitude field at regions close to the focal point are significantly enhanced. Our results indicate that focused SAW devices operating at higher device frequencies and with smaller degree of arc are most suitable for sensing applications.

11.2 Major contributions

Computational models are developed to design SAW sensors employing nanomaterial sensing layers for chemical and biological species detection. The material properties of nanomaterial sensing layers are explored in detail. The differences that exist between the nanoscale and bulk materials are brought to the forefront. The findings of this research in not only beneficial for sensing applications, but also provide a good platform for the study of other transition metal nanostructures which are useful in catalysis and fuel cell applications.

At the macro-scale, the wave propagation characteristics in SAW devices operating in air and liquid media are studied using coupled field finite element models. Novel multi-frequency SAW transducer designs for enhanced response in chemical and biological sensing applications are modeled. Fundamental understanding of the acoustic wave generation and propagation in SAW sensors with complicated transducer configurations is achieved using the developed models. This research enables the consideration of more complicated configurations and allows for extending the developed models to analyze propagation characteristics in hexagonal SAW device fabricated on other bare and multi-layered piezoelectric substrates. Finally, the current research would result in improved, solid-state chemical and biological micro-sensors which will have a broad impact on industrial process monitoring, safety and control, monitoring of human health and the environment, and on national security.

11.3 Future work

Based on the findings of the current research the following possibilities exist which could lead to improvements in future sensor designs. The details are discussed in this section.

1) Molecular simulations of multi-component alloys

The bond order simulation model developed in this work for binary transition metal alloys can be extended to obtain the microstructure of multi-component alloys. These could be utilized as starting configurations for subsequent MD simulations to investigate their material properties for possible use in sensing and catalytic applications.

2) Ab-initio simulations of gas molecule-nanoalloy interactions

Knowledge of the site preference and relative densities of different surface sites in the bimetallic nanoclusters and nanowires simulated at different temperatures using MD, can give useful insights into the extent of adsorption or mass loading of the gases in a given nanocluster. The same can be used to investigate the mechanism of sensor response occurring at nanoscale. Manipulation of the variables such as temperature, pressure, molecular orientation can be carried out to maximize sensor response towards a particular gas (selectivity). Adsorption of gases like CO, H_2 and O2 on different surfaces (fcc (110), fcc (111), fcc (211)) of metals like Pt, Ni, and Pd can be investigated by density functional theory (DFT) methods. Adsorption energies and structures of the gases on these surfaces could be investigated by considering multiple possible adsorption sites, and comparing them with the available experimental data at low coverage. The differences in the site-preference and adsorption structures (for e.g. tilt angle, C-O bond length, metal-C distance in case of CO) among the different surfaces can also be investigated. Identification of stable adsorption sites and maximizing the densities of same in the nanomaterials employed as sensing layers would result in enhanced mass loading. It is expected that the increased mass loading would further result in higher frequency shifts, thereby giving increased sensitivity of the SAW sensors.

3) 3-D fluid-solid interaction model of SAW biosensor

The 2-D fluid-solid interaction model developed for Rayleigh wave interaction with liquid medium can be extended to develop a 3-D model of hexagonal SAW device based on $LiTaO_3$ substrate. Based on the crystallographic directions, one of the delay paths would involve SH wave interactions with liquid medium as in typical SAW biosensor applications. The other delay path would generate Rayleigh waves which would be used for simultaneous removal of non-specifically bound proteins. The developed 3-D model would give insights into the induced flow fields which can be used to evaluate the functioning of the SAW biosensor as well as optimize the design parameters to obtain improved sensor response.

4) High frequency SAW biosensors based on diamond substrate

The simulation results obtained in this research indicate that the devices operating at higher frequencies can more effectively remove the non-specifically bound proteins and thus lead to improved sensitivity. Recent experimental studies indicate that SAW devices fabricated on diamond substrates operate in the high frequency regime[307]. Diamond is especially attractive because, in addition to having good electrical and chemical properties, it is widely considered to be biocompatible, and can be used as a waveguide in layered SAW devices. The high density of diamond layer helps achieve higher acoustic wave propagation velocity and realize GHz frequency devices with transducer finger spacing achievable by optical lithography. The 3-D structural and 2-D fluid solid interaction finite element models developed in this work can be extended to study the wave propagation characteristics in hexagonal diamond layered piezoelectric surface acoustic wave devices under the influence of a fluid loading. The models would help design SAW sensors with improved sensitivity and speed of response.

5) Microfluidic applications

The fluid-solid interaction model developed in this work can be used to determine the utility of SAW devices in potential microfluidic applications. SAWs can be used to actuate and process smallest amounts of fluid on the planar surface of a piezoelectric chip [308,309]. The small size of these pumps or devices can minimize the dead volume of fluid in the system. This feature is especially useful when the reagents or products are precious or when the device needs to be cleaned or reused. Potential applications of the developed microfluidic systems include biological or chemical analysis and synthesis, micromixing, micro-dispensing, and precision chemical dilution and mixing.

References

1 D. S. Ballantine, R. M. White, S. J. Martin, A. J. Ricco, G. C. Frye, E. T. Zellers, and H. Wohltjen, *Acoustic wave sensors: Theory, design, and physico-chemical application*, (Academic Press, New York, 1997).

2 W. F. Cady, *Piezoelectricity*, Vol. 1 and 2 (Dover, New York, 1964).

3 A. J. Slobodnik, E. D. Conway, and R. T. Delmonico, *Microwave acoustics handbook, surface wave velocities*, Vol. 1A (1974).

4 A. J. Slobodnik, E. D. Conway, and R. T. Delmonico, *Microwave acoustics handbook, surface wave velocities*, Vol. 2 (1974).

5 T. Numura and A. Minemura, *Behavior of a piezoelectric quartz crystal in an aqueous solution and its use for the determination of minute amounts of cyanide.* Nippon Kagaku Kaishi, 1621, 1-4 (1980).

6 R. M. White and F. W. Volltmer, *Direct piezoelectric coupling to surface elastic waves.* Applied Physics Letters 7, 314-316 (1965).

7 A. J. Ricco, S. J. Martin, T. M. Niemczyk, and G. C. Frye, *Liquid-phase sensors based on acoustic plate mode devices.* Proceedings of ACS Symposium Series, p. 191-207 (1989).

8 J. W. Grate, S. W. Wenzel, and R. M. White, *Flexural plate wave devices for chemical analysis.* Analytical Chemistry 63(15), 1552-61 (1991).

9 H. Wohltjen, *Mechanism of operation and design considerations for surface acoustic wave device vapor sensors.* Sensors and Actuators 5, 307-25 (1984).

10 H. Wohltjen; *Patent Number 4,312,228* (US, January 26 1982).

11 M. Hoummady, A. Campitelli, and W. Wlodarski, *Acoustic wave sensors: Design, sensing mechanisms and applications.* Smart Materials & Structures 6, 647-657 (1997).

12 F. Josse, F. Bender, and R. W. Cernosek, *Guided shear horizontal surface acoustic wave sensors for chemical and biochemical detection in liquids.* Analytical Chemistry 73, 5937-44 (2001).

13 F. Josse, F. Bender, R. W. Cernosek, and K. Zinszer, *Guided SH-SAW sensors for liquid-phase detection.* Proceedings of IEEE International Frequency Control Symposium and PDA Exhibition, p. 454-461 (2001).

14 S. Shiokawa and J. Kondoh, *Surface acoustic wave sensor for liquid-phase application.* Proceedings of IEEE Ultrasonics Symposium, p. 445-452 (1999).

15 S. Shiokawa and J. Kondoh, *Surface acoustic wave sensors.* Japanese Journal of Applied Physics, Part 1: Regular Papers, Short Notes & Review Papers 43, 2799-2802 (2004).

16 K. Nakamura, M. Kazumi, and H. Shimizu, *SH-type and Rayleigh-type surface waves on rotated Y-cut LiTaO*$_3$. Proceedings of IEEE Ultrasonics Symposium, p. 819-22 (1977).

17 Lord Rayleigh, *On waves propagated along the plane surface of an elastic solid.* Proceedings of London Math Society, p. 4-11 (1885).

18 J. F. Rosenbaum, *Bulk acoustic wave acoustic theory and devices*, (Artech House Boston, London, 1988).

19 R. Daniel and D. Eugene, *Elastic waves in solids*, Vol. I (Springer, New York, 1999).

20 R. Daniel and D. Eugene, *Elastic waves in solids*, Vol. II (Springer, New York, 1999).

21 F. Martin, M. I. Newton, G. McHale, K. A. Melzak, and E. Gizeli, *Pulse mode shear horizontal-surface acoustic wave (SH-SAW) system for liquid based sensing applications.* Biosensors and Bioelectronics 19, 627-32 (2004).

22 S. J. Martin, A. J. Ricco, T. M. Niemczyk, and G. C. Frye, *Characterisation of SH acoustic plate mode liquid sensors.* Sensors and Actuators 20, 253-268 (1989).

23 J. Kondoh and S. Shiokawa, *A liquid sensor based on a shear horizontal SAW device.* Electronics and Communications in Japan Part II 76, 69-82 (1993).

24 J. W. Grate, S. J. Martin, and R. M. White, *Acoutic wave microsensors Part I.* Analytical Chemistry 65 (1993).

25 J. W. Grate, S. J. Martin, and R. M. White, *Acoutic wave microsensors Part II.* Analytical Chemistry 65 (1993).

26 A. D'Amico and E. Verona, *SAW sensors.* Sensors and Actuators 17 (1989).

27 Z. P. Khlebarov, A. I. Stoyanova, and D. I. Topalova, *Surface acoustic wave sensors.* Sensors and Actuators: B 8, 33-40 (1992).

28 J. J. McCallum, *Piezoelectric devices for mass and chemical measurements: An update.* Analyst 114, 1173-89 (1989).

29 A. R. Marrion, *The chemistry and physics of coatings*, (Lewis Publishers, Boca Raton, 1993).

30 J. J. Pesek, *Chemically modified surfaces*, (Lewis Publishers, Boca Raton, 1994).

31 J. P. Sibilia, *A guide to materials characterization and chemical analysis*, (VCH Publishers, New York, 1988).

32 M. Thompson and D. C. Stone, *Surface-launched acoustic wave sensors (Chemical sensing and thin-film characterization)*, (John Wiley and Sons, New York, 1997).

33 C.-Y. Shen, C.-L. Hsu, K.-C. Hsu and J.-S. Jeng, *Analysis of shear horizontal surface acoustic wave sensors with the coupling of modes theory.* Japanese Journal of Applied Physics, Part 1: Regular Papers, Short Notes & Review Papers 44, 1510-1513 (2005).

34 P. Ventura, J. M. Hode, J. Desbois, and H. Solal, *Combined FEM and green's function analysis of periodic SAW structure: Application to the calculation of reflection and scattering parameters.* Proceedings of IEEE Transactions on Ultrasonics, Ferroelectrics and Frequency Control 48, 1259-1274 (2001).

35 S. Yoon, J.-D. Yu, S. Kanna, M. Oshio, and M. Tanaka, *Finite element analysis of the substrate thickness effect on traveling leaky surface acoustic waves*. Proceedings of IEEE Ultrasonics Symposium, p. 1696-1699 (2003).

36 B. A. Auld, *Acoustic fields and waves in solids*, Vol. 1 (John Wiley and Sons, New York, 1973).

37 B. A. Auld, *Acoustic fields and waves in solid*s, Vol. 2 (John Wiley and Sons, New York, 1973).

38 S. J. Martin, G. C. Frye, and S. D. Senturia, *Dynamics and response of polymer-coated surface acoustic wave devices: Effect of viscoelastic properties and film resonance*. Analytical Chemistry 66, 220-2219 (1994).

39 J. Kondoh and S. Shiokawa, *Measurements of conductivity and pH of liquid using surface acoustic wave devices*. Japanese Journal of Applied Physics, Part 1: Regular Papers, Short Notes & Review Papers 31, 82-4 (1992).

40 R. C. Peach, *A general green function analysis for saw devices*. Proceedings of IEEE Ultrasonics Symposium, p. 221–225 (1995).

41 V. P. Plessky and T. Thorvaldsson, *Rayleigh waves and leaky SAW's in periodic systems of electrodes: Periodic green functions analysis*. Electronics Letters 28, 1317-1319 (1992).

42 W. P. Mason, *Electromechanical transducers and wave filters*. 3rd ed. (D. van Nostrand, Princeton, 1948).

43 S. Datta, *Surface acoustic wave devices*, (Prentice-Hall, Englewood Cliffs, 1986).

44 T. D. Kenny, T. B. Pollard, E. J. Berkenpas, and M. Pereira da Cunha, *FEM/BEM impedance and power analysis for measured lgs SH-SAW devices*. Proceedings of IEEE Ultrasonics Symposium, p. 1371-1374 (2004).

45 N. Finger, G. Kovacs, J. Schoberl, and U. Langer, *Accurate FEM/BEM simulation of surface acoustic wave filters*. Proceedings of IEEE Ultrasonics Symposium, p. 1680-85, (2003).

46 A. D'Amico, A. Palma, and E. Verona, *Palladium-surface acoustic wave interaction for hydrogen detection*. Applied Physical Letters 41, 300-1 (1982).

47 C. Caliendo, A. D'Amico, P. Varadi, and E. Verona, *Surface acoustic wave H_2 sensor on silicon substrate*. Proceedings of IEEE Ultrasonics Symposium, p. 569-574 (1988).

48 H. Muramatsu, T. Watanabe, and M. Hikuma, *Piezoelectric crystal biosensor system for detection of escherichia-coli*. Analytical Letters 22, 2155-2166 (1989).

49 S. H. Si, Y. S. Fung, and D. R. Zhu, *Improvement of piezoelectric crystal sensor for the detection of organic vapors using nanocrystalline TiO_2 films*. Sensors and Actuators B: Chemical B108, 165-171 (2005).

50 J. H. Sinfelt, *Bimetallic catalysts-discoveries, concepts, and applications*, (John Wiley and Sons, New York, 1983).

51 F. Favier, E. C. Walter, M. P. Zach, T. Benter, and R. M. Penner, *Hydrogen sensors and switches from electrodeposited palladium mesowire arrays*. Science 293, 2227-2231 (2001).

52 A. Chaudhari, M.S. Thesis, University of South Florida (2004).

53 J. P. Borel, *Thermodynamical size effect and the structure of metallic clusters*. Surface Science 106, 1-9 (1981).

54 Z. L. Wang, J. M. Petroski, T. C. Green, and M. A. El-Sayed, *Shape transformation and surface melting of cubic and tetrahedral platinum nanocrystals*. Journal of Physical Chemistry B 102, 6145-6151 (1998).

55 R. Kusche, T. Hippler, M. Schmidt, B. von Issendorff, and H. Haberland, *Melting of free sodium clusters*. European Physical Journal D 9, 1-4 (1999).

56 M. Schmidt, R. Kusche, W. Kronmuller, B. von Issendorff, and H. Haberland, *Experimental determination of the melting point and heat capacity for a free cluster of 139 sodium atoms*. Physical Review Letters 79, 99-102 (1997).

57 J. M. Petroski, Z. L. Wang, T. C. Green, and M. A. El-Sayed, *Kinetically controlled growth and shape formation mechanism of platinum nanoparticles*. Journal of Physical Chemistry B 102, 3316-3320 (1998).

58 P. Buffat and J. P. Borel, *Size effect on melting temperature of gold particles*. Physical Review A 13, 2287-2298 (1976).

59 F. Ercolessi, W. Andreoni, and E. Tosatti, *Melting of small gold particles - mechanism and size effects*. Physical Review Letters 66, 911-914 (1991).

60 C. L. Cleveland, W. D. Luedtke, and U. Landman, *Melting of gold clusters: Icosahedral precursors*. Physical Review Letters 81, 2036-2039 (1998).

61 F. Calvo and F. Spiegelmann, *Mechanisms of phase transitions in sodium clusters: From molecular to bulk behavior*. Journal of Chemical Physics 112, 2888-2908 (2000).

62 H. Lei, *Melting of free copper clusters*. Journal of Physics-Condensed Matter 13, 3023-3030 (2001).

63 M. P. Allen and D. J. Tildesley, *Computer simulation of liquids*, (Oxford University Press, Oxford, 1987).

64 F. Baletto, C. Mottet, and R. Ferrando, *Growth of three-shell onionlike bimetallic nanoparticles* Physical Review Letters 90 (2003).

65 E. E. Walter, *Metal clusters, in Wiley series in theoretical chemistry* (John Wiley and Sons, New York, 1999).

66 L. J. Lewis, P. Jensen, and J. L. Barrat, *Melting, freezing, and coalescence of gold nanoclusters*. Physical Review B 56, 2248-2257 (1997).

67 Y. Qi, T. Cagin, W. L. Johnson, and W. A. Goddard, *Melting and crystallization in Ni nanoclusters: The mesoscale regime*. Journal of Chemical Physics 115, 385-394 (2001).

68 Y. G. Chushak and L. S. Bartell, *Melting and freezing of gold nanoclusters*. Journal of Physical Chemistry B 105, 11605-11614 (2001).

69 Y. J. Lee, E. K. Lee, S. Kim, and R. M. Nieminen, *Effect of potential energy distribution on the melting of clusters*. Physical Review Letters 86, 999-1002 (2001).

70 A. A. Shvartsburg and M. F. Jarrold, *Solid clusters above the bulk melting point*. Physical Review Letters 85, 2530-2532 (2000).

71 S.-P. Huang and P. B. Balbuena, *Melting of Cu-Ni nanoclusters*. Journal of Physical Chemistry B 106 (2002).

72 M. J. Lopez, P. A. Marcos, and J. A. Alonso, *Structural and dynamical properties of Cu-Au bimetallic clusters*. Journal of Chemical Physics 104, 1056-1066 (1996).

73 Z. H. Jin, H. W. Sheng, and K. Lu, *Melting of Pb clusters without free surfaces*. Physical Review B 60, 141-149 (1999).

74 Y. G. Chushak and L. S. Bartell, *Freezing of Ni-Al bimetallic nanoclusters in computer simulations*. Journal of Physical Chemistry B 107, 3747-3751 (2003).

75 Y. Qi, T. Cagin, Y. Kimura, and W. A. Goddard, *Molecular-dynamics simulations of glass formation and crystallization in binary liquid metals: Cu-Ag and Cu-Ni*. Physical Review B 59, 3527-3533 (1999).

76 L. Zhu and A. E. DePristo, *Microstructures of bimetallic clusters: Bond order metal simulator for disordered alloys*. Journal of Catalysis 167, 400-407 (1997).

77 L. Zhu and A. E. DePristo, *Bond order simulation-model-coordination dependent bimetallic bonds*. Journal of Chemical Physics 102, 5342-5349 (1995).

78 L. Zhu, R. P. Wang, T. S. King, and A. E. DePristo, *Effects of chemisorption on the surface composition of bimetallic catalysts*. Journal of Catalysis 167, 408-411 (1997).

79 D. S. Mainardi and P. B. Balbuena, *Monte Carlo simulation of Cu-Ni nanoclusters: Surface segregation studies*. Langmuir 17, 2047-2050 (2001).

80 J. P. K. Doye and D. J. Wales, *Global minima for transition metal clusters described by Sutton-Chen potentials*. New Journal of Chemistry 22, 733-744 (1998).

81 J. K. Strohl and T. S. King, *A multicomponent, multilayer model of surface segregation in alloy catalysts*. Journal of Catalysis 118, 53-67 (1989).

82 J. K. Strohl and T. S. King, *Monte-carlo simulations of supported bimetallic catalysts*. Journal of Catalysis 116, 540-555 (1989).

83 L. Q. Yang and A. E. Depristo, *On the compact structure of small fcc metal-clusters*. Journal of Catalysis 149, 223-228 (1994).

84 L. Q. Yang and A. E. Depristo, *Surface segregation in bimetallic clusters - statistical-mechanical modeling using cluster site energies*. Journal of Catalysis 148, 575-586 (1994).

85 S. M. Foiles, M. I. Baskes, and M. S. Daw, *Embedded-atom-method functions for the fcc metals Cu, Ag, Au, Ni, Pd, Pt, and their alloys*. Physical Review B 33, 7983-7991 (1986).

86 A. P. Sutton and J. Chen, *Long-range Finnis Sinclair potentials*. Philosophical Magazine Letters 61, 139-146 (1990).

87 T. Cagin, Y. Kimura, Y. Qi, H. Li, H. Ikeda, W. L. Johnson, and W. A. I. Goddard, *Bulk metallic glasses*. Proceedings of Materials Research Society Symposium, p. 43-48 (1999).

88 Y. Qi, T. Cagin, Y. Kimura, and W. A. Goddard, *Viscosities of liquid metal alloys from non-equilibrium molecular dynamics.* Journal of Computer-Aided Materials Design 8, 233-243 (2002).

89 S. O. Kart, M. Tomak, M. Uludogan, and T. Cagin, *Liquid properties of Pd-Ni alloys.* Journal of Non-Crystalline Solids 337, 101-108 (2004).

90 H. Rafiitabar and A. P. Sutton, *Long-range Finnis-Sinclair potentials for fcc metallic alloys.* Philosophical Magazine Letters 63, 217-224 (1991).

91 H. J. C. Berendsen, J. P. M. Postma, W. F. Vangunsteren, A. Dinola, and J. R. Haak, *Molecular-dynamics with coupling to an external bath.* Journal of Chemical Physics 81, 3684-3690 (1984).

92 H. Reiss, P. Mirabel, and R. L. Whetten, *Capillarity theory for the coexistence of liquid and solid clusters.* Journal of Physical Chemistry 92, 7241-7246 (1988).

93 R. Kofman, P. Cheyssac, A. Aouaj, Y. Lereah, G. Deutscher, T. Bendavid, J. M. Penisson, and A. Bourret, *Surface melting enhanced by curvature effects.* Surface Science 303, 231-246 (1994).

94 T. Morishita, *Fluctuation formulas in molecular-dynamics simulations with the weak coupling heat bath.* Journal of Chemical Physics 113, 2976-2982 (2000).

95 P. J. Steinhardt, D. R. Nelson, and M. Ronchetti, *Bond-orientational order in liquids and glasses.* Physical Review B 28, 784-805 (1983).

96 S. P. Huang and P. B. Balbuena, *Melting of bimetallic Cu-Ni nanoclusters.* Journal of Physical Chemistry B 106, 7225-7236 (2002).

97 L. Z. Mezey and J. Giber, *The surface free-energies of solid chemical-elements - calculation from internal free enthalpies of atomization.* Japanese Journal of Applied Physics Part 1: Regular Papers Short Notes & Review Papers 21, 1569-1571 (1982).

98 J. M. Haile, *Molecular dynamics simulations: Elementary methods*, (John Wiley and Sons, New York, 1992).

99 H. Goldstein, *Classical mechanics.* (Narosa Publishing House, New Delhi, 1985).

100 B. Zhou, S. Hermans, and G. A. Somarjai, *Nanotechnology in catalysis*, Vol. 1-2 (Kluwer Academic Publishers, New York, 2004).

101 K. H. Hansen, Z. Sljivancanin, E. Laegsgaard, F. Besenbacher, and I. Stensgaard, *Adsorption of* O_2 *and NO on Pd nanocrystals supported on* Al_2O_3*/NiAl(110): Overlayer and edge structures.* Surface Science 505, 25-38 (2002).

102 D. S. Ivanov and L. V. Zhigilei, *Effect of pressure relaxation on the mechanisms of short-pulse laser melting.* Physical Review Letters 91 (2003).

103 B. Rethfeld, K. Sokolowski-Tinten, and D. von der Linde, *Ultrafast thermal melting of laser-excited solids by homogeneous nucleation.* Physical Review B 65 (2002).

104 U. Landman, W. D. Luedtke, N. A. Burnham, and R. J. Colton, *Microscopic mechanisms and dynamics of adhesion, micro-indentation and fracture.* Science 248 (1990).

105 M. F. Crommie, C. P. Lutz, and D. M. Eigler, *Imaging standing waves in a 2-dimensional electron gas.* Nature 363, 524 (1993).

106 Y. Hasegewa and P. Avouris, *Direct observation of standing wave formation at surface steps using scanning tunneling spectroscopy*. Physical Review Letters 71 (1993).

107 F. J. Himpsel and J. E. Ortega, *Edge state and terrace state for Cu on W (331) and W (110)*. Physical Review B 50 (1994).

108 O. G. Biedermann, W. Hebenstreit, M. Shmid, J. Redinger, R. Podloucky, and P. Varga, *Scanning tunneling spectroscopy of one-dimensional surface states on a metal surface*. Physical Review Letters 76 (1996).

109 J. Li, W. D. Schneider, and R. Bemdt, *Local density of states from spectroscopic scanning-tunneling-microscope images: Ag (111)*. Physical Review B 56 (1997).

110 L. Burgi, O. Jeandupeux, A. Hirstein, H. Brune, and K. Kern, *Confinement of surface state electrons in fabry-pérot resonators*. Physical Review Letters 81 (1998).

111 B. J. V. Wees, H. V. Houten, C. W. J. Beenakker, J. G. Williamson, L. P. Kouvenhoven, D. V. d. Marel, and C. T. Foxon, *Quantized conductance of point contacts in a two-dimensional electron gas*. Physical Review Letters 60 (1988).

112 G. Binasch, P. Grunberg, F. Saurenbach, and W. Zinn, *Enhanced magnetoresistance in layered magnetic structures with anti-ferromagnetic interlayer exchange*. Physical Review B 39 (1989).

113 S. S. P. Parkin, N. More, and K. P. Roche, *Oscillations in exchange coupling and magnetoresistance in metallic superlattice structures: Co/Ru, Co/Cr, and Fe/Cr*. Physical Review Letters 64 (1990).

114 K. Tokushi, *Atomic process of point contact in gold studied by time-resolved high-resolution transmission electron microscopy*. Physical Review Letters 81, 4448 (1998).

115 K. Tokushi, *Direct atomistic observation of a contact process between crystalline silicon surfaces at room temperature*. Physical Review B 63, 033309 (2001).

116 C. M. Doudna, M. F. Bertino, F. D. Blum, A. T. Tokuhiro, D. Lahiri-Dey, S. Chattopadhyay, and J. Terry, *Radiolytic synthesis of bimetallic Ag-Pt nanoparticles with a high aspect ratio*. Journal of Physical Chemistry B 107, 2966-2970 (2003).

117 E. C. Walter, B. J. Murray, F. Favier, and R. M. Penner, *Beaded bimetallic nanowires: Wiring nanoparticles of metal 1 using nanowires of metal 2*. Advanced Materials 15, 396-399 (2003).

118 L. Hui, F. Pederiva, B. L. Wang, J. L. Wang, and G. H. Wang, *How does the nickel nanowire melt?* Applied Physical Letters 86, 011913/1-011913/3 (2005).

119 L. Hui, B. L. Wang, J. L. Wang, and G. H. Wang, *Evidence of a melt like super-cooled liquid during a solid to liquid transition of titanium nanowire*. Chemical Physical Letters 399, 20-25 (2004).

120 L. Hui, B. L. Wang, J. L. Wang, and G. H. Wang, *Local atomic structures of palladium nanowire*. Journal of Chemical Physics 121, 8990-8996 (2004).

121 L. Hui, B. L. Wang, J. L. Wang, and G. H. Wang, *Melting behavior of one-dimensional zirconium nanowire*. Journal of Chemical Physics 120, 3431-3438 (2004).

122 Y.-H. Wen, Z.-Z. Zhu, R. Zhu, and G.-F. Shao, *Size effects on the melting of nickel nanowires: A molecular dynamics study*. Physica E: Low-Dimensional Systems & Nanostructures 25, 47-54 (2004).

123 B. Wang, G. Wang, X. Chen, and J. Zhao, *Melting behavior of ultra thin titanium nanowires.* Physical Review B 67, 193403/1-193403/4 (2003).

124 J. Wang, X. Chen, G. Wang, B. Wang, W. Lu, and J. Zhao, *Melting behavior in ultrathin metallic nanowires*. Physical Review B 66, 085408/1-085408/5 (2002).

125 H. J. Hwang and J. W. Kang, *Melting and breaking of ultrathin copper nanobridges*. Surface Science 532-535, 536-543 (2003).

126 P. Nguyen, H. T. Ng, J. Kong, A. M. Cassell, R. Quinn, J. Li, J. Han, M. McNeil, and M. Meyyappan, *Epitaxial directional growth of indium-doped tin oxide nanowire arrays*. Nano Letters 3, 925-928 (2003).

127 T. Y. L. Tan, Na; Gosele, Ulrich., *Is there a thermodynamic size limit of nanowires grown by the vapor-liquid-solid process?* Applied Physics Letters 83, 1199-1201 (2003).

128 A. I. Hochbaum, R. Fan, R. He, and P. Yang, *Controlled growth of Si nanowire arrays for device integration.* Nano Letters 5, 457-460 (2005).

129 C.-X. Wang, B. Wang, Y.-H. Yang, and G.-W. Yang, *Thermodynamic and kinetic size limit of nanowire growth*. Journal of Physical Chemistry B 109, 9966-9969 (2005).

130 W. H. Qi, M. P. Wang, M. Zhou, and W. Y. Hu, *Surface-area-difference model for thermodynamic properties of metallic nanocrystals*. Journal of Physics D: Applied Physics 38, 1429-36 (2005).

131 E. Ongi, C. Dane, K. Jongbaeg, and L. Liwei, *Electric-field assisted growth and self-assembly of intrinsic silicon nanowires.* Nano Letters 5, 705-8 (2005).

132 S. Volker, S. Stephan, and G. Ulrich., *Diameter-dependent growth direction of epitaxial silicon nanowires*. Nano Letters 5, 931-5. (2005).

133 S.-W. Cheng and H.-F. Cheung, *Temperature profile and pressure effect on the growth of silicon nanowires*. Applied Physics Letters 85, 5709-5711 (2004).

134 K. A. Dick, K. Deppert, T. Martensson, B. Mandl, L. Samuelson, and W. Seifert, *Failure of the vapor-liquid-solid mechanism in Au-assisted MOVPE growth of InAs nanowires*. Nano Letters 5, 761-4 (2005).

135 L. Miao, V. R. Bhethanabotla, and B. Joseph, *Melting of Pd clusters and nanowires: A comparison study using molecular dynamics simulation.* Physical Review B 72, 134109/1-134109/12 (2005).

136 D. Lahiri, B. Bunker, B. Mishra, Z. Zhang, D. Meisel, C. M. Doudna, M. F. Bertino, F. D. Blum, A. T. Tokuhiro, S. Chattopadhyay, T. Shibata, and J. Terry, *Bimetallic Pt-Ag and Pd-Ag nanoparticles*. Journal of Applied Physics 97, 094304/1-094304/8 (2005).

137 S. K. R. S. Sankaranarayanan, V. R. Bhethanabotla, and B. Joseph, Proceedings of AIChE Symposium, p. 1-4 (2005).

138 S. K. R. S. Sankaranarayanan, V. R. Bhethanabotla, and B. Joseph, *Molecular dynamics simulations of the structural and dynamic properties of graphite-supported bimetallic transition metal clusters*. Physical Review B 72 (2005).

139 W. Smith and T. R. Forester, *Dl_Poly: A general purpose parallel molecular simulation package.* Journal of Molecular Graphics 14, 136 (1996).

140 S. K. R. S. Sankaranarayanan, V. R. Bhethanabotla, and B. Joseph, *Molecular dynamics simulation study of the melting of Pd-Pt nanoclusters*. Physical Review B 71, 195415/1-195415/15 (2005).

141 C. W. Hills, N. H. Mack, and R. G. Nuzzo, *The size dependent strcutural phase behaviors of supported bimetallic (Pt-Ru) nanoparticles*. Journal of Physical Chemistry B 107, 2626-2636 (2003).

142 W. A. Jesser, R. Z. Shneck, and W. W. Gile, *Solid-liquid equilibra in nanoparticles of Pb-Bi alloys* Physical Review B 69, 144121 (2004).

143 FSnobl Nobel metal database, Spencer group (New York)

144 M. Jose-Yacaman, R. Herrera, A. G. Gomez, S. Tehuacanero, and P. Schabes-Retchkiman, *Decagonal and hexagonal structures in small gold particles*. Surface Science 237, 248-56 (1990).

145 S. K. R. S. Sankaranarayanan, V. R. Bhethanabotla, and B. Joseph, *Molecular dynamics simulation study of the melting of Pd-Pt nanoclusters*. Physical Review B: Condensed Matter and Materials Physics 71, 195415/1-195415/15 (2005).

146 A. S. Edelstein and R. C. Cammarata, *Nanomaterials: Synthesis, properties and applications*. (Institute of Physics, Bristol, 1996).

147 S. P. Huang, D. S. Mainardi, and P. B. Balbuena, *Structure and dynamics of graphite-supported bimetallic nanoclusters*. Surface Science 545, 163-179 (2003).

148 R. C. Longo, C. Rey, and L. J. Gallego, *Structure and melting of small Ni clusters on Ni surfaces.* Surface Science 424, 311-321 (1999).

149 A. Antonelli, S. N. Khanna, and P. Jena, *Thermal-stability of supported metal-clusters.* Physical Review B 48, 8263-8266 (1993).

150 L. J. Lewis, P. Jensen, N. Combe, and J. L. Barrat, *Diffusion of gold nanoclusters on graphite.* Physical Review B 61, 16084-16090 (2000).

151 L. Bardotti, B. Prevel, P. Melinon, A. Perez, Q. Hou, and M. Hou, *Deposition of Au-Ni clusters on Au(111) surfaces. Experimental results and comparison with simulations.* Physical Review B 62, 2835-2842 (2000).

152 B. Prevel, L. Bardotti, S. Fanget, A. Hannour, P. Melinon, A. Perez, J. Gierak, G. Faini, E. Bourhis, and D. Mailly, *Gold nanoparticle arrays on graphite surfaces.* Applied Surface Science 226, 173-177 (2004).

153 W. Vervisch, C. Mottet, and J. Goniakowski, *Theoretical study of the atomic structure of Pd nanoclusters deposited on a MgO(100) surface*. Physical Review B 65 (2002).

154 Y. F. Zhukovskii, E. A. Kotomin, D. Fuks, S. Dorfman, and A. Gordon, *Hartree-fock study of adhesion and charge redistribution on the Ag/MgO(001) interface.* Surface Science 482, 66-72 (2001).

155 J. W. M. Frenken and J. F. Vanderveen, *Observation of surface melting.* Physical Review Letters 54, 134-137 (1985).

156 P. Stoltze, J. K. Norskov, and U. Landman, *Disordering and melting of aluminum surfaces.* Physical Review Letters 61, 440-443 (1988).

157 Q. Hou, M. Hou, L. Bardotti, B. Prevel, P. Melinon, and A. Perez, *Deposition of Au-N clusters on Au(111) surfaces. I. Atomic-scale modeling.* Physical Review B 62, 2825-2834 (2000).

158 J. Garcia-rodeja, C. Rey, L. J. Gallego, and J. A. Alonso, *Molecular-dynamics study of the structures, binding-energies, and melting of clusters of fcc transition and noble-metals using the Voter and Chen version of the embedded-atom model.* Physical Review B 49, 8495-8498 (1994).

159 D. Bazin, I. Kovacs, J. Lynch, and L. Guczi, *Ru-Co/Na$_y$ bimetallic catalysts: In situ EXAFS study at Co$_k$- and Ru$_k$-absorption edges.* Applied Catalysis A-General 242, 179-186 (2003).

160 D. Bazin, C. Mottet, and G. Treglia, *New opportunities to understand heterogeneous catalysis processes on nanoscale bimetallic particles through synchrotron radiation and theoretical studies.* Applied Catalysis A-General 200, 47-54 (2000).

161 D. Bazin, D. Sayers, J. J. Rehr, and C. Mottet, *Numerical simulation of the Platinum l-iii edge white line relative to nanometer scale clusters.* Journal of Physical Chemistry B 101, 5332-5336 (1997).

162 F. Rosei, *Nanostructured surfaces: Challenges and frontiers in nanotechnology.* Journal of Physics-Condensed Matter 16, S1373-S1436 (2004).

163 F. Besenbacher, I. Chorkendorff, B. S. Clausen, B. Hammer, A. M. Molenbroek, J. K. Norskov, and I. Stensgaard, *Design of a surface alloy catalyst for steam reforming.* Science 279, 1913-1915 (1998).

164 C. Mottet, J. Goniakowski, F. Baletto, R. Ferrando, and G. Treglia, *Modeling free and supported metallic nanoclusters: Structure and dynamics.* Phase Transitions 77, 101-113 (2004).

165 L. Bardotti, B. Prevel, M. Treilleux, P. Melinon, and A. Perez, *Deposition of preformed gold clusters on hopg and gold substrates: Influence of the substrate on the thin film morphology.* Applied Surface Science 164, 52-59 (2000).

166 S. P. Huang and P. B. Balbuena, *Platinum nanoclusters on graphite substrates: A molecular dynamics study.* Molecular Physics 100, 2165-2174 (2002).

167 L. Bardotti, P. Jensen, A. Hoareau, M. Treilleux, and B. Cabaud, *Experimental-observation of fast diffusion of large antimony clusters on graphite surfaces.* Physical Review Letters 74, 4694-4697 (1995).

168 V. Bhethanabotla and W. Steele, *Simulations of the thermodynamic properties of krypton adsorbed on graphite at 100-K.* Journal of Physical Chemistry 92, 3285-3291 (1988).

169 V. R. Bhethanabotla and W. A. Steele, *Molecular-dynamics simulations of oxygen monolayers on graphite.* Langmuir 3, 581-587 (1987).

170 V. R. Bhethanabotla and W. A. Steele, *Computer-simulations of monolayer and bilayer nitrogen films at low-temperature.* Journal of Chemical Physics 91, 4346-4352 (1989).

171 V. R. Bhethanabotla and W. A. Steele, *Computer-simulation study of melting in dense oxygen layers on graphite.* Physical Review B 41, 9480-9487 (1990).

172 P. M. Agrawal, B. M. Rice, and D. L. Thompson, *Predicting trends in rate parameters for self-diffusion on fcc metal surfaces.* Surface Science 515, 21-35 (2002).

173 T. Iida and R. I. L. Guthrie, *The physical properties of liquid metals*, (Clanderon Press, Oxford, 1988).

174 S. K. R. S. Sankaranarayanan, V. R. Bhethanabotla, and B. Joseph, *Molecular dynamics simulation study of the melting of Pd-Pt nanoclusters.* Physical Review B 71, 195415 (2005).

175 S. Gonzalez, C. Sousa, and F. Illas, *Theoretical study of the chemisorption of Co on bimetallic Rh-Cu surfaces and nanoparticles.* Surface Science 531, 39-52 (2003).

176 N. Lopez and J. K. Norskov, *Synergetic effects in co adsorption on Cu-Pd(111) alloys.* Surface Science 477, 59-75 (2001).

177 J. Diao, K. Gall, and M. L. Dunn, *Surface-stress-induced phase transformation in metal nanowires.* Nature Materials 2, 656-660 (2003).

178 S. K. R. S. Sankaranarayanan, V. R. Bhethanabotla, and B. Joseph, *Molecular dynamics simulation study of melting and structural evolution of bimetallic Pd-Pt nanowires.* Physical Review B 74, 155441 (2006).

179 C. Yang, Z. Zhong, and C. M. Lieber, *Encoding electronic properties by synthesis of axial modulation-doped silicon nanowires.* Science 310, 1304-7 (2005).

180 F. Patolsky, B. P. Timko, G. Yu, Y. Fang, A. B. Greytak, G. Zheng, and C. M. Lieber, *Detection, stimulation, and inhibition of neuronal signals with high-density nanowire transistor arrays.* Science 313, 1100-4 (2006).

181 J. C. Johnson, H.-J. Choi, K. P. Knutsen, R. D. Schaller, P. Yang, and R. J. Saykally, *Single gallium nitride nanowire lasers.* Nature Materials 1, 106-110 (2002).

182 L. Thilly, F. Lecouturier, and J. von Stebut, *Size-induced enhanced mechanical properties of nanocomposite copper/niobium wires: Nanoindentation study.* Acta Materialia 50, 5049-5065 (2002).

183 B. Wu, A. Heidelberg, and J. J. Boland, *Mechanical properties of ultrahigh-strength gold nanowires.* Nature Materials 4, 525-529 (2005).

184 A. Husain, J. Hone, H. W. C. Postma, X. M. H. Huang, T. Drake, M. Barbic, A. Scherer, and M. L. Roukes, *Nanowire-based very-high-frequency electromechanical resonator.* Applied Physics Letters 83, 1240-1242 (2003).

185 Z. L. Wang, *Nanowires and nanobelts – materials, properties and devices: Nanowires and nanobelts of functional materials*, Vol. II (Kluwer Academic Publisher, New York, 2003).

186 Z. L. Wang, *Nanowires and nanobelts – materials, properties and devices: Nanowires and nanobelts of functional materials*, Vol. I (Kluwer Academic Publisher, New York, 2003).

187 L. Kuipers and J. W. M. Frenken, *Jump to contact, neck formation, and surface melting in the scanning tunneling microscope.* Physical Review Letters 70, 3907-3910 (1993).

188 N. Agraït, J. G. Rodrigo, C. Sirvent, and S. Vieira, *Atomic-scale connective neck formation and characterization.* Physical Review B 48, 8499-8501 (1993).

189 K. H. Liu, W. L. Wang, Z. Xu, L. Liao, X. D. Bai, and E. G. Wang, *In situ probing mechanical properties of individual tungsten oxide nanowires directly grown on tungsten tips inside transmission electron microscope.* Applied Physical Letters 89, 221908/1 (2006).

190 J. Bettini, F. Sato, P. Z. Coura, S. O. Dantas, D. S. Galvao, and D. Ugarte, *Experimental realization of suspended atomic chains composed of different atomic species*. Nature Nanotechnology 1, 182-185 (2006).

191 S.-P. Ju, J.-S. Lin, and W.-J. Lee, *A molecular dynamic study of the tensile properties of ultrathin gold nanowires*. Nanotechnology 15, 1221-1225 (2004).

192 P. S. Branicio and J.-P. Rino, *Large deformation and amorphization of Ni nanowires: A molecular dynamics study*. Physical Review B 62, 16950 (2000).

193 E. A. Jagla and E. Tosatti, *Structure and evolution of metallic nanowire tip junction*. Physical Review B 64, 205412 (2001).

194 W. Liang and M. Zhou, *Pseudoelasticity of single crystalline Cu nanowires through reversible lattice reorientations*. Journal of Engineering Materials Technology 127, 423-433 (2005).

195 W. Liang, M. Zhou, and F. Ke, *Shape memory effect in Cu nanowires*. Nano Letters 5, 2039-2043 (2005).

196 K. Gall, J. Diao, and M. L. Dunn, *The strength of gold nanowires*. Nano Letters 4, 2431-2436 (2004).

197 H. S. Park and J. A. Zimmerman, *Modeling inelasticity and failure in gold nanowires*. Physical Review B 72, 054106/1-054106/9 (2005).

198 H. S. Park, K. Gall, and J. A. Zimmerman, *Deformation of fcc nanowires by twinning and slip*. Journal of the Mechanics and Physics of Solids 54, 1862-1881 (2006).

199 Y.-H. Wen, Z.-Z. Zhu, G.-F. Shao, and R. Z. Zhu, *The uniaxial tensile deformation of ni nanowire: Atomic-scale computer simulations*. Physica E: Low-Dimensional Systems & Nanostructures 27, 113-120 (2005).

200 S. J. A. Koh, H. P. Lee, C. Lu, and Q. H. Cheng, *Molecular dynamics simulation of a solid platinum nanowire under uniaxial tensile strain: Temperature and strain-rate effects*. Physical Review B 72, 085414/1-085414/11 (2005).

201 W. Bin, A. Heidelberg, and J. J. Boland, *Mechanical properties of ultrahigh-strength gold nanowires*. Nature Materials 4, 525-529 (2005).

202 D.-L. Chen and T.-C. Chen, *Mechanical properties of Au nanowires under uniaxial tension with high strain-rate by molecular dynamics*. Nanotechnology 16, 2972-2981 (2005).

203 J.-S. Lin, S.-P. Ju, and W.-J. Lee, *Mechanical behavior of gold nanowires with a multishell helical structure*. Physical Review B 72, 085448/1-085448/6 (2005).

204 J. Diao, K. Gall, and M. L. Dunn, *Yield strength asymmetry in metal nanowires*. Nano Letters 4, 1863-1867 (2004).

205 H. S. Park, *Stress-induced martensitic phase transformation in intermetallic nickel aluminum nanowires*. Nano Letters 6, 958-62 (2006).

206 H. S. Park, K. Gall, and J. A. Zimmerman, *Shape memory and pseudo elasticity in metal nanowires*. Physical Review Letters 95, 255504/1-255504/4 (2005).

207 J. C. Gonzalez, V. Rodrigues, J. Bettini, L. G. C. Rego, A. R. Rocha, P. Z. Coura, S. O. Dantas, F. Sato, D. S. Galvao, and D. Ugarte, *Indication of unusual pentagonal structures in atomic - size Cu nanowires*. Physical Review Letters 93, 126103/1-126103/4 (2004).

208 A. Cao and Y. Wei, *Atomistic simulations of the mechanical behavior of fivefold twinned nanowires*. Physical Review B 74, 214108/1-7 (2006).

209 H. Ikeda, Y. Qi, T. Cagin, K. Samwer, W. L. Johnson, and W. A. Goddard, III, *Strain rate induced amorphization in metallic nanowires*. Physical Review Letters 82, 2900-2903 (1999).

210 S. K. R. S. Sankaranarayanan, V. R. Bhethanabotla, and B. Joseph, *Phase diagram of alloy nanostructures*. Proceedings of AVS symposium, 2006.

211 S. K. R. S. Sankaranarayanan, V. R. Bhethanabotla, and B. Joseph, *Molecular dynamics simulation of mechanical properties of transition metal nanowires: Temperature and strain rate effects*. Proceedings of AIChE Symposium, p. 1-4 (2006).

212 G. M. Finbow, R. M. Lynden-Bell, and I. R. McDonald, *Atomistic simulation of the stretching of nanoscale metal wires*. Molecular Physics 92, 705-714 (1997).

213 S. J. A. Koh and H. P. Lee, *Shock-induced localized amorphization in metallic nanorods with strain-rate-dependent characteristics*. Nano Letters 6, 2260-2267 (2006).

214 Y. Oshima, H. Koizumi, K. Mouri, H. Hirayama, K. Takayanagi, and Y. Kondo, *Evidence of a single - wall platinum nanotube*. Physical Review B 65, 121401/1-121401/4 (2002).

215 D.-L. Chen and T.-C. Chen, *Mechanical properties of Au nanowires under uniaxial tension with high strain-rate by molecular dynamics*. Nanotechnology 16, 2972-2981 (2005).

216 K. Srinivasan, S. Cular, V. R. Bhethanabotla, S.-Y. Lee, M. T. Harris, and J. N. Culver, *Pd coated tobacco mosaic virus for H_2 sensing applications*. Proceedings of IEEE Ultrasonics Symposium, p 1-4 (2005).

217 S.-P. Daniel, U. Carlos, M. S. José, J. S. Juan, and A. Nicolás, *Nanocontacts: Probing electronic structure under extreme uniaxial strains*. Physical Review Letters 79, 4198 (1997).

218 V. Rodrigues, T. Fuhrer, and D. Ugarte, *Signature of atomic structure in the quantum conductance of gold nanowires*. Physical Review Letters 85, 4124 (2000).

219 M. R. Sørensen, M. Brandbyge, and K. W. Jacobsen, *Mechanical deformation of atomic-scale metallic contacts: Structure and mechanisms*. Physical Review B 57, 3283-3294 (1998).

220 V. Rodrigues, J. Bettini, A. R. Rocha, L. G. C. Rego, and D. Ugarte, *Quantum conductance in silver nanowires: Correlation between atomic structure and transport properties*. Physical Review B 65, 153402 (2002).

221 J. A. Torres and J. J. Saenz, *Conductance and mechanical properties of atomic-size metallic contacts: A simple model*. Physical Review Letters 77, 2245 (1996).

222 J. J. Campbell and W. R. Jones, *A method for estimating optimal crystal cuts and propagation directions for excitation of piezoelectric surface waves*. Proceedings of IEEE Transactions on Sonics and Ultrasonics 15, 209-218 (1968).

223 J. J. Campbell and W. R. Jones, *Propagation of surface waves at the boundary between a piezoelectric crystal and a fluid medium*. Proceedings of IEEE Transactions on Sonics and Ultrasonics 17, 71-77 (1970).

224 D. P. Morgan, *History of saw devices*. Proceedings of IEEE International Frequency Control Symposium, p. 439-460 (1998).

225 R. Lerch, *Finite element analysis of saw-transducers*. Proceedings of Circuits and Systems, IEEE International Symposium, p. 1399 - 1403 (1988).

226 R. Lerch, *Simulation of piezoelectric devices by two- and three-dimensional finite elements*. Proceedings of IEEE Transactions on Ultrasonics, Ferroelectrics and Frequency Control, 37, 233-247 (1990).

227 G. Xu, *Finite element analysis of second order effects on the frequency response of a SAW device*. Proceedings of IEEE Ultrasonics Symposium, p. 187-190 (2000).

228 G. Xu, *Direct finite element analysis of the frequency response of a Y-Z* $LiNbO_3$ *SAW filter*. Smart Materials Structures 9, 973-980 (2000).

229 S. J. Ippolito, K. Kalantar-Zadeh, D. A. Powell, and W. Wlodarski, *A 3-dimensional finite element approach for simulating acoustic wave propagation in layered saw devices*. Proceedings of IEEE Ultrasonics Symposium, p. 303-306 (2003).

230 S. J. Ippolito, K. Kalantar-zadeh, D. A. Powell, and W. Wlodarski, *A finite element approach for 3-dimensional simulation of layered acoustic wave transducers*. Proceedings of Optoelectronic and Microelectronic Materials and Devices, p. 541-544 (2002).

231 S. J. Ippolito, K. Kalantar-zadeh, W. Wlodarski, and G. I. Matthews, *The study of ZnO/XY* $LiNbO_3$*/sub-3/ layered saw devices for sensing applications*. Proceedings of IEEE Sensors Symposium, p. 539-542 (2003).

232 M. Z. Atashbar, B. J. Bazuin, M. Simpeh, and S. Krishnamurthy, *3-d finite element simulation model of SAW palladium thin film hydrogen sensor*. Proceedings of IEEE International Ultrasonics, Ferroelectrics and Frequency Control Joint 50th Anniversary Conference, p. 1-4 (2004).

233 A. Fabre, E. Finot, J. Demoment, and S. Contreras, *In situ measurement of elastic properties of PdHx, PdDx, and PdTx*. Journal of Alloys and Compounds 356-357, 372-376 (2003).

234 V. I. Anisimkin, I. M. Kotelyanskii, P. Verardi, and E. Verona, *Elastic properties of thin-film palladium for surface acoustic wave (SAW) sensors*. Sensors and Actuators B: Chemical B23, 203-8 (1995).

235 W. Nyborg, *Acoustic streaming* Vol. II B, (Academic Press, New York, 1965).

236 S. Shiokawa, Y. Matsui, and T. Moriizumi, *Experimental study on liquid streaming by SAW*. Japanese Journal of Applied Physics 28, 126-128 (1989).

237 Z. Guttenberg, A. Rathgeber, S. Keller, J. O. Raedler, A. Wixforth, M. Kostur, M. Schindler, and P. Talkner, *Flow profiling of a surface-acoustic-wave nanopump*. Physical Review E: Statistical, Nonlinear, and Soft Matter Physics 70, 056311/1-056311/10. (2004).

238 R. M. Moroney, R. M. White, and R. T. Howe, *Microtransport induced by ultrasonic lamb waves*. Applied Physics Letters 59, 774-776 (1991).

239 N. T. Nguyen and R. M. White, *Design and optimization of an ultrasonic flexural plate wave micropump using numerical simulation.* Sensors and Actuators A 77, 229-236 (1999).

240 N. T. Nguyen and R. M. White, *Acoustic streaming in micro-machined flexural plate wave devices: Numerical simulation and experimental verification.* Proceedings of IEEE Transactions on Ultrasonics, Ferroelectrics and Frequency Control 47, 1463-1471 (2000).

241 G. G. Yaralioglu, I. O. Wygant, T. C. Marentis, and B. T. Khuri-Yakub, *Ultrasonic mixing in microfluidic channels using integrated transducers.* Analytical Chemistry 76, 3694-3698 (2004).

242 R. H. Nilson and S. K. Griffiths, *Enhanced transport by acoustic streaming in deep trench-like cavities.* Journal of Electrochemical Society 149, G286-G296 (2002).

243 K. Bakhtari, R. O. Guldiken, P. Makaram, A. A. Busnaina, and J.-G. Park, *Experimental and numerical investigation of nanoparticle removal using acoustic streaming and the effect of time.* Journal of Electrochemical Society 153, G846-G850 (2006).

244 K. R. Nightingale and G. E. Trahey, *A finite element model for simulating acoustic streaming in cystic breast lesions with experimental validation.* Proceedings of IEEE Transactions on Ultrasonics Ferroelectrics and Frequency Control 47, 201-215 (2000).

245 J. Kondoh, N. Shimizu, Y. Matsui, and S. Shiokawa, *Liquid heating effects by saw streaming on the piezoelectric substrate.* Proceedings of IEEE Transactions on Ultrasonics, Ferroelectrics, and Frequency Control 52, 1881-1883 (2005).

246 M. Kurosawa, T. Watanabe, A. Futami, and T. Higuchi, *Surface acoustic wave atomizer.* Sensors and Actuators A: Physical 50, 69-74 (1995).

247 K. Miyamoto, S. Nagatomo, Y. Matsui, and S. Shiokawa, *Nonlinear vibration of liquid droplet by surface acoustic wave excitation.* Japanese Journal of Applied Physics 41, 3465-3468 (2002).

248 C. M. Gregorya, J. V. Hatfielda, S. Higginsa, H. Iacovidesb, and P. J. Vadgamac, *A novel open flow microflow sensor for reduced fouling of chemical sensors in physiological sampling environments.* Sensors and Actuators B: Chemical 65, 305-309 (2000).

249 N. Wisniewski and M. Reichert, *Methods for reducing biosensor membrane biofouling.* Colloids and Surfaces B: Biointerfaces 18, 197-219 (2000).

250 S. Sharma, R. W. Johnson, and T. A. Desai, *Xps and afm analysis of antifouling peg interfaces for microfabricated silicon biosensors.* Biosensors and Bioelectronics 20, 227-239 (2004).

251 S. Cular, V. R. Bhethanabotla, and D. W. Branch, *Hexagonal surface acoustic wave devices for enhanced sensing and materials characterization.* Proceedings of IEEE Ultrasonics Symposium, p. 2309- 2312 (2005).

252 L. A. Kuznetsova and W. T. Coakley, *Applications of ultrasound streaming and radiation force in biosensors.* Biosensors and Bioelectronics 22, 1567–1577 (2007).

253 J. D. Ballantine, R. White, S. Martin, A. Ricco, E. Zellers, G. Frye, H. Wohltjen, M. Levy, and R. Stern, *Acoustic wave sensors, theory, design, & physico-chemical applications.* (Academic Press, Boston, 1997).

254 F. Josse, F. Bender, and R. W. Cernosek, *Guided shear horizontal surface acoustic wave sensors for chemical and biochemical detection in liquids.* Analytical Chemistry 73, 5937-5944 (2001).

255 Z. Li, Y. Jones, J. Hossenlopp, R. Cernosek, and F. Josse, *Analysis of liquid-phase chemical detection using guided shear horizontal-surface acoustic wave sensors.* Analytical Chemistry 77, 4595-4603 (2005).

256 J. Kondoh and S. Shiokawa, *Investigation of streaming phenomenon in SAW devices.* Proceedings of IEEE Ultrasonics Symposium, p. 1-4 (1995).

257 S. Shiokawa, Y. Matsui, and T. Ueda, *Liquid streaming and droplet formation caused by leaky Rayleigh waves*. Proceedings of IEEE Ultrasonics Symposium, p. 643-646 (1989).

258 L. G. Olson, *Finite element model for ultrasonic cleaning*. Journal of Sound and Vibration 126, 387-405 (1988).

259 T. Xue, W. Lord, and S. Udpa, *Finite element simulation and visualization of leaky Rayleigh waves for ultrasonic NDE*. Proceedings of IEEE Transactions on Ultrasonics, Ferroelectrics and Frequency Control 44, 557-565 (1997).

260 K. Chono, N. Shimizu, Y. Matsui, J. Kondoh, and S. Shiokawa, *Novel atomization method based on SAW streaming.* Proceedings of IEEE Ultrasonics Symposium, p. 1786-1789 (2003).

261 K. Chono, N. Shimuzu, Y. Matsui, J. Kondoh, and S. Shiokawa, *Development of novel atomization system based on saw streaming.* Japanese Journal of Applied Physics 43, 2987–2991 (2004).

262 T. Uchida, T. Suzuki, and S. Shiokawa, *Investigation of acoustic streaming excited by surface acoustic waves.* Proceedings of IEEE Ultrasonics Symposium, p. 1-4 (1995).

263 S. Furukawat, T. Nomuraz, and T. Yasudaz, *Characteristic features of leaky surface acoustic waves propagating on liquid/piezoelectric film/glass structures.* Journal of Physics D: Appl. Phys. 24, 706713 (1991).

264 ANSYS, v.10 Trademark of ANSYS Inc. (www.ansys.com).

265 B. A. Auld, *Acoustic fields and waves in solids* Vol. I-II, (John Wiley and Sons, New York, 1965).

266 T. J. R. Hughes, W. K. Liu, and T. K. Zimmermann, *Lagrangian-Eulerian finite element formulation for incompressible viscous flows.* Computer Methods in Applied Mechanics and Engineering. 29, 329-349 (1981).

267 J. Donea, S. Giuliani, and J. P. Halleux, *An Arbitrary Lagrangian Eulerian finite element method for transient dynamic fluid structure analysis.* Computer Methods in Applied Mechanics and Engineering. 33, 689-723 (1982).

268 T. J. R. Hughes, *The finite element method linear static and dynamic finite element analysis.* (Prentice-Hall, Englewood Cliffs, 1987).

269 S. K. R. S. Sankaranrayanan, B. V. R., and B. Joseph, *A 3-D finite element simulation study of SAW sensor.* ECS Transactions 1 (2006).

270 M. K. Aktas and B. Farouka, *Numerical simulation of acoustic streaming generated by finite-amplitude resonant oscillations in an enclosure.* Journal of Acoustical Society of America 116, 2822-2831 (2004).

271 A. K.-H. Chu, *Linear stability of acoustic streaming flows in microchannels.* Physical Review E 72, 066311 (2005).

272 R. M. Moroney, Thesis, University of California Berkeley, (1995).

273 R. M. Moroney, R. M. White, and R. T. Howe, *Fluid motion produced by ultrasonic lamb waves*. Proceedings of IEEE Ultrasonics Symposium, p. 355-358 (1990).

274 M. S. Longuet-Higgins, *Mass transport in water waves*. Philosophical Transactions of the Royal Society of London. Series A, Mathematical and Physical Sciences 953, 535-581 (1953).

275 A. Sano, Y. Matsui, and S. Shiokawa, *A new manipulator based on surface acoustic wave streaming*. Proceedings of IEEE Ultrasonics Symposium, p. 1-4 (1997).

276 S. Cular, D. W. Branch, G. D. Meyer, and V. R. Bhethanabotla, *Acoustic manipulation of biological samples for improved sensors*. Proceedings of AIChE Symposium, p. 1-4 (2005).

277 L. Byoung-Gook, L. Dong-Ryul, and K. Kwon, *Acoustic streaming pattern induced by longitudinal ultrasonic vibration in an open channel using particle imaging velocimetry*. Applied Physics Letters 89, 183505 (2006).

278 Q. Qi and G. J. Brereton, *Mechanisms of removal of micron-sized particles by high frequency ultrasonic waves*. Proceedings of IEEE Transactions on Ultrasonics, Ferroelectrics and Frequency Control. 42, 619-629 (1995).

279 J. Israelachvili, *Intermolecular and surface forces*. (Academic Press Inc., London, 1992).

280 H. Krupp, *Particle adhesion theory and experiment*. Vol. 2 (Elsevier, New York, 1967).

281 D. A. Drew, *The lift force on a small sphere in the presence of a wall*. Chemical Engineering Science 43, 769-773 (1988).

282 M. Z. Atashbar, B. J. Bazuin, M. Simpeh, and S. Krishnamurthy, *3D FE simulation of* H_2 *SAW gas sensor*. Sensors and Actuators, B: Chemical B111-B112, 213-218 (2005).

283 V. I. Anisimkin, I. M. Kotelyanskii, V. I. Fedosov, C. Caliendo, P. Verardi, and E. Verona, *Analysis of the different contributions to the response of SAW gas sensors*. Proceedings of IEEE Ultrasonics Symposium, p. 515-518 (1995).

284 J. Kondoh, S. Shiokawa, M. Rapp, and S. Stier, *Simulation of viscoelastic effects of polymer coatings on surface acoustic wave gas sensor under consideration of film thickness*. Japanese Journal of Applied Physics, Part 1: Regular Papers, Short Notes & Review Papers 37, 2842-2848 (1998).

285 D. D. Stubbs, S.-H. Lee, and W. D. Hunt, *Molecular recognition for electronic noses using surface acoustic wave immunoassay sensors*. IEEE Sensors Journal 2, 294-300 (2002).

286 D. S. Ballantine and H. Wohltjen, *Surface acoustic wave devices for chemical analysis*. Analytical Chemistry 61, 704A-15A (1989).

287 A. J. Ricco, S. J. Martin, and Z. T.E., *Surface acoustic wave gas sensors based on film conductivity changes*. Sensors and Actuators 8 (1985).

288 Oliver A. Williams, Vincent Mortet, Michael Daenen, and K. Haenen, *Nanocrystalline diamond enhanced thickness shear mode resonator*. Applied Physics Letters 90, 063514 (2007).

289 S. Cular, V. R. Bhethanabotla, and D. W. Branch, *Hexagonal surface acoustic wave devices for enhanced sensing and material characterization*. Proceedings of IEEE Ultrasonics Symposium, (2005).

290 N. Rao, X. Xie, D. Wielizcka, and D.-M. Zhu, *Quartz crystal microbalance sample stage for in situ characterization of thickness and surface morphology of spin coated polymer films*. Review of Scientific Instruments 77, 116111/1-116111/3 (2006).

291 L. Qin, H. Cheng, J. M. Li, and Q.-M. Wang, *Characterization of polymer nanocomposite films using quartz thickness shear mode (TSM) acoustic wave sensor*. Sensors and Actuators, A: Physical A136, 111-117 (2007).

292 S. Cular, D. W. Branch, and V. R. Bhethanabotla, *Hexagonal saw devices for enhanced sensing*. Proceedings of AIChE Symposium, p. 1-4 (2005).

293 S. Cular, D. W. Branch, G. D. Meyer, and V. R. Bhethanabolta, *Removal of non-specifically bound proteins on microsensors using surface acoustic waves*. IEEE Sensors Journal, submitted (2005).

294 J. J. Campbell and W. R. Jones, *A method for estimating optimal crystal cuts and propagation directions for excitation of piezoelectric surface waves*. Proceedings of IEEE Transactions on Sonics and Ultrasonics 15, 209-217 (1968).

295 J. J. Campbell and W. R. Jones, *Propagation of surface waves at the boundary between a piezoelectric crystal and a fluid medium*. Proceedings of IEEE Transactions on Sonics and Ultrasonics 17, 71-76 (1970).

296 K. Hasegawa and M. Koshiba, *Finite-element solution of Rayleigh-wave scattering from reflective gratings on a piezoelectric substrate*. Proceedings of IEEE Transactions on Ultrasonics, Ferroelectrics and Frequency Control, 37, 99-105 (1990).

297 K.-Y. Hashimoto, T. Omori, and M. Yamaguchi, *Recent progress in modeling and simulation technologies of shear horizontal type surface acoustic wave devices*. International Symposium on Acoustic Wave Devices for Future Mobile Communication Systems, p. 169-178 (2001).

298 T.-T. Wu, H.-T. Tang, and Y.-Y. Chen, *Frequency response of a focused saw device based on concentric wave surfaces: Simulation and experiment*. Journal of Physics D: Applied Physics 38, 2986-2994 (2005).

299 S. K. R. S. Sankaranarayanan, S. Cular, V. R. Bhethanabotla, and B. Joseph, *Flow induced by acoustic streaming in surface acoustic streaming and its applications in biofouling removal: Numerical and experimental study*. Physical Review E submitted (2007).

300 S. Cular, D. W. Branch, V. R. Bhethanabotla, G. D. Meyer, and H. G. Craighead, *Removal of non-specifically bound proteins on microsensors using surface acoustic waves*. IEEE Sensors Journal, submitted (2005).

301 J. B. Green, G. S. Kino, and B. T. Khuri-Yakub, *Saw convolvers using focusing interdigital transducers*. Proceedings of IEEE Transactions on Sonics and Ultrasonics 30, 43-50 (1983).

302 J. Z. Wilcox and R. E. Brooks, *Time-fourier transform by a focusing array of phased surface acoustic wave transducers*. Journal of Applied Physics 58, 1148-1159 (1985).

303 J. Z. Wilcox and R. E. Brooks, *Frequency-dependent beam steering by a focusing array of surface acoustic wave transducers - experiment*. Journal of Applied Physics 58, 1160-1168 (1985).

304 S. K. R. S. Sankaranarayanan and V. R. Bhethanabotla, *Numerical analysis of wave generation and propagation in focused surface acoustic wave devices.* Proceedings of IEEE Transactions on Ultrasonics, Ferroelectrics, and Frequency Control, submitted (2007).

305 S. K. R. S. Sankaranarayanan, V. R. Bhethanabolta, and B. Joseph, *Finite element modeling of hexagonal surface acoustic wave device based on* $LiNbO_3$. Proceedings of IEEE Sensors Symposium, p. 6688 (1-4) (2007).

306 Katsumi Chono, Norifumi Shimizu, Yoshikazu Matsui, J. Kondoh, and S. Shiokawa, *Development of novel atomization system based on saw streaming.* Japanese Journal of Applied Physics, Part 1: Regular Papers, Short Notes & Review Papers 43, 2987–2991 (2004).

307 E. Dogheche, D. Remiens, S. Shikata, A. Hachigo, and H. Nakahata, *High-frequency surface acoustic wave devices based on* $LiNbO_3$ */diamond multilayered structure.* Applied Physics Letters 87, 213503/1-3 (2005).

308 U. Demirici, *Picoliter droplets for spinless photoresist deposition.* Review of Scientific Instruments 76, 065103-065108 (2005).

309 Z. Guttenberg, A. Rathgeber, S. Keller, J. O. Rädler, A. Wixforth, M. Kostur, M. Schindler, and P. Talkner, *Flow profiling of a surface acoustic wave nanopump.* Physical Review E 70, 056311 (2004).

About the Author

Subramanian K.R.S. Sankaranarayanan was born in Trichurapalli, India. He obtained his Bachelor's degree in Chemical Engineering at Nagpur University in May 2000, where he was awarded the gold medal for excellence in the College of Engineering. After completing his undergraduate studies, he worked with Professors K.S. Gandhi and Sanjeev Gupta on modeling the synthesis of nanoparticles in micellar systems in the Chemical Engineering Department at Indian Institute of Science, Bangalore and completed his Master's Degree in 2002. He worked for Invensys, India from 2002-2003 as an associate developer and was involved in development of process simulation software such as Pro-II and Sim4me. He began pursuing his Ph.D. degree in the Chemical Engineering Department at University of South Florida in 2003. During the course of his study at USF, he presented his work in many conferences and published several papers. He was awarded the outstanding researcher award for the academic year 2006-2007 by the Chemical Engineering department at USF for his contributions in the field of molecular and finite element modeling applied to SAW sensors employing nanomaterial sensing layers.